Chemically Engineered Metal Sulfides and Oxides as Electrode Materials for Li-Ion and Photochargeable Batteries

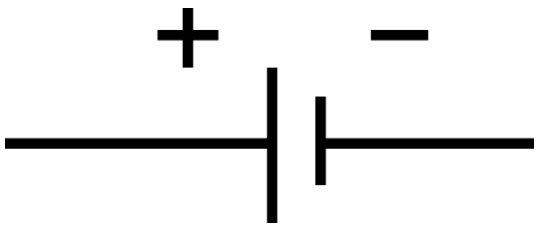

Inaugural-Dissertation

zur

Erlangung des Doktorgrades

der Mathematisch-Naturwissenschaftlichen Fakultät

der Universität zu Köln

vorgelegt von

Michael Wilhelm

aus Kassel

Universität zu Köln

Köln, 2023

Die vorliegende Arbeit wurde von der Mathematisch-Naturwissenschaftlichen Fakultät der Universität zu Köln als Dissertation angenommen.

Berichterstatter (Gutachter):

Prof. Dr. Dr. (h.c.) Sanjay Mathur	Universität zu Köln
Prof. Dr. Axel Klein	Universität zu Köln

Tag der mündlichen Prüfung:

14. Juni 2023

"If it disagrees with experiment – it's wrong. In that simple statement is the key to science. It doesn't make a difference how beautiful your guess is. It doesn't make a difference how smart you are who made the guess or what his name is. If it disagrees with experiment, it's wrong."

(Richard Feynman, The Feynman Lectures on Physics)

Abstract

Lithium-ion batteries have dominated battery technologies for portable electronic devices for decades, commanded by intercalation chemistry for electrochemical energy storage while pushing the limits of storage capacity worldwide to the terawatt-hour level. State-of-the-art intercalation cathodes for Li-ion batteries operate within the limits of transition metal oxide electrochemistry. However, conversion-redox processes have rich opportunities for substantially increasing energy densities. Due to the limitations of both the Li content and the extraction of one electron per transition metal, the target energy density of 500 Wh kg^{-1} of classical layered oxides at the cell level remains elusive. The diversity of compositions that exhibit high reversible capacities following a conversion redox reaction in the solid state has inspired the exploration of new materials for next-generation cathodes for lithium batteries and beyond. While thinking beyond, the electrification of the aviation sector is a game-changer for future transport. Therefore, the requirements on battery technologies must focus even more on high power density, high energy density with fast-charging capability and having low weight and compacted cell design. In addition, battery safety aspects and sustainability of energy materials are key challenges.

To address some of the challenges, synthesis and surface engineering of high energy density and fast-charging materials, as well as the development and comprehensive characterization of metal-sulfur batteries for Li-S, Mg-S, and hybrid Li/Mg-S systems, were studied in this thesis.

In terms of fast-charging electrode materials, $TiNb_2O_7$ was modified by a carbon-coating to improve the charge conduction and specific capacity at high current rates. Further, novel concepts towards photoresponsive cathode materials, such as vanadium pentoxide were investigated in a lithium-ion photo battery. This study reports on the optimization of dual functionality by chemical surface engineering of electrospun vanadium pentoxide fibers as photoresponsive cathodes in lithium-ion batteries. To meet the demand for high energy density in metal-sulfur batteries, lithium-sulfur and magnesium-sulfur batteries were explored. For Li-S system, a synthetic approach based on a new molecular precursor $[(LiSC_2H_4)_2NCH_3]$ to form lithium sulfide/carbon nanofibers as cathode was pursued. Suitable cathode materials based on metal sulfides, mainly copper, iron, and copper-iron-sulfides, were investigated in terms of their

suitability for rechargeable magnesium batteries due to their high theoretical capacities (Mg: 3,833 mAh/cm^3; 2,205 mAh/g) and high abundance in the earth's crust (23,300 ppm). The influence of their crystal structures, particle morphologies, and nano-sized effects were tested to elucidate and further understand the electrochemical behavior with Mg^{2+} as the active ion. Introducing a small amount of Li-containing salts to the magnesium electrolyte, resulted in a hybrid electrolyte that showed great potential to improve the electrochemical behavior in combination with metal sulfides following a conversion reaction mechanism.

Kurzzusammenfassung

Lithium-Ionen-Batterien dominieren seit Jahrzehnten die Batterietechnologien für mobile elektronische Geräte, die dem Mechanismus der Interkalationschemie zur elektrochemischen Energiespeicherung folgen. Moderne Interkalationskathoden für Li-Ionen-Batterien arbeiten innerhalb der Grenzen der Übergangsmetalloxid Elektrochemie. Aufgrund der Beschränkungen sowohl des Li-Gehalts als auch der Extraktion von nur einem Elektron pro Übergangsmetall, bleibt die angestrebte Energiedichte von 500 Wh kg^{-1} klassischer Übergangsmetalloxide auf Zellebene schwer zu erreichen. Die Vielfalt der Verbindungen, die eine Umwandlungs-Redox-Reaktion im Festkörper aufweisen, hat die Erforschung neuer Materialien für Kathoden der nächsten Generation durch hohe reversible Kapazitäten inspiriert. Darüber hinaus ist die Elektrifizierung des Luftfahrtsektors ein entscheidender Faktor für den Verkehr der Zukunft. Daraus ergeben sich veränderte Anforderungen an die Batterietechnologien, da die Zellen eine hohe Leistungsdichte, eine hohe Energiedichte, Schnellladefähigkeit, ein geringes Gewicht, eine kompakte Zellkonstruktion, hohe Batteriesicherheit und das Verwenden von nachhaltigen Ressourcen aufweisen müssen.

Aus diesem Grund wurden in der vorliegenden Arbeit die Synthese und Oberflächenchemie von energiedichten und schnellladenden Materialien sowie die Entwicklung und umfassende Charakterisierung von Metall-Schwefel-Batterien für z.B. Li-S, Mg-S und hybride Li/Mg-S Systeme durchgeführt.

In Bezug auf schnell ladende Materialien wurde $TiNb_2O_7$ durch Modifikationen aus Kohlenstoff-Verbundwerkstoffen weiterentwickelt, um die spezifische Kapazität bei hohen Lade- und Entladeströmen zu verbessern. Weiterhin standen neuartige Konzepte von photoempfindlichen Kathodenmaterialien wie beispielsweise Vanadiumpentoxid für den Einsatz in einer Lithium-Ionen-Solarbatterie im Fokus. Ausgehend von elektroversponnenen Vanadiumpentoxid-Fasern als photoempfindliches Kathodenmaterial konnte durch gezielte modifizierte Oberflächen einer Kohlenstoffbeschichtung eine verbesserte Leistungsfähigkeit erreicht werden. Zum Erreichen einer höheren Energiedichte in Batterien wurden Metall-Schwefel-Systeme für Lithium-Schwefel und Magnesium-Schwefel Batterien untersucht. Für Li-S-Systeme wurde ein synthetischer Ansatz zur einfachen Herstellung von Lithiumsulfid/Kohlenstoff-Fasern durch die Verwendung eines neuartigen molekularen ‘Single-Source-Präkursors‘ $[(LiSC_2H_4)_2NCH_3]$ gewählt. Geeignete Kathodenmaterialien basierend auf Übergangsmetallsulfiden,

hauptsächlich Kupfersulfiden, Eisensulfiden und Kupfer-Eisensulfiden, wurden aufgrund ihrer hohen theoretischen Kapazitäten (Mg: 3.833 mAh/cm^3; 2.205 mAh/g) und der hohen Verfügbarkeit in der Erdkruste (23.300 ppm) für wiederaufladbare Magnesiumbatterien untersucht. Der Einfluss ihrer Kristallstrukturen und Morphologie sowie nanoskalige Effekte wurden untersucht, um das elektrochemische Verhalten in Wechselwirkung mit Mg^{2+} als aktivem Ion besser zu verstehen. Das Einbringen einer geringen Menge von Li-haltigen Salzen in den Magnesium-Elektrolyten (Hybrid-Elektrolyten) besitzt großes Potenzial, das elektrochemische Verhalten in Kombination mit Übergangssulfiden für Umwandlungskathoden zu verbessern.

Acknowledgment

First, I would like to thank my mentor and supervisor, Prof. Sanjay Mathur, for his trust, guidance, and everlasting support. I appreciate the challenges and the freedom he provided to unfold this topic to its full extent. I am very grateful for all the opportunities he offered me to transition into scientific research and beyond. I am incredibly thankful for the various options of joining international conferences (virtual and in-person) and academic activities to connect to people around the globe throughout various societies.

I greatly acknowledge Prof. Dr. Axel Klein for being the second reviewer and examiner, Prof. Dr. Guenter Schwarz for taking over the chair of the theses defense committee, and Dr. Volker von der Gönna as the minutes taker.
I want to thank Prof. Ulrich Simon (RWTH Aachen) for his co-supervision and helpful support during my Ph.D. time.
Furthermore, I was enriched by many collaboration partners in joining various research projects. Much of the results presented in this work would not have been possible without the various cooperation partners, for which I am sincerely grateful.
In this context, I would like to thank Prof. Ravi Kumar and Dr. Ganesh Babu Thiyagarajan (IIT Madras, India) for their valuable collaboration and unceasing support regarding the $TiNb_2O_7$ studies. Furthermore, I am sincerely grateful to Sung Hun Cho, Prof. Yuki Yamada, Prof. Tohru Sekino (SANKEN, Osaka University, Japan), Jianming Tao, and Prof. Zhensheng Hong (Fujian Normal University, China) for their excellent support during the V_2O_5 photo battery study. I want to thank our collaboration partners at ZBT Duisburg (Germany), Sebastian Hirt, Dr. Sebastian Wennig, and Bernd Oberschachtsiek, for their assistance with the electrochemical measurements of Li_2S-nanofibers for Li-S batteries. In this context, I would also like to thank Dr. Veronika Brune, Dr. Christoph Bohr, and Dr. Tim Ludwig for letting me join this project. I acknowledge the Federal Ministry for Economic Affairs and Energy funding based on the German Parliament's decision (Project IGF 15EWN).

Furthermore, I am sincerely grateful to Dr. Dirk Roller (Orion Engineered Carbons, Germany) for his collaboration and the helping me in my transition from academia to industry.

Many thanks to the Cologne Summer School of the University of Cologne and Team Kraków (Dr. Veronika Brune, Dr. Aida Raauf, Andreas Lichtenberg, Ziyaad Aytuna, David Patrun, Benedict Witulski, Anna Schmidt-Verma, Seulgi Ji, Niusha Heshmati, Sumiya Iqbal, Hyeonkwon Lee, Simon Diel, Dr. Aman Bhardwaj, and Dr. Kruti Halankar) as well as the members of our partner universities who made this trip a huge success. Special thanks to Dr. Veronika Brune for supporting the summer school; without her, it would not be that successful.

I want to thank Lorri Smiley and Natalie Larocco from the MRS stuff (Materials Research Society), as well as the Chairs, Prof. Eva Hemmer and Dr. Isabel Gessner, for supporting the events of the Student Engagement Subcommittee as well as the Focus on Sustainability - Task Force Subcommittee.
Dr. Feray Ünlü and Khan Lê for being excellent colleagues and supporting me in perovskites and solar cells. I want to thank Dr. Thomas Fischer for his genius and helpfulness, however busy he is. I am incredibly thankful to Anja Sutorius for her mental support and funny moments.
Jean Thibaut (Euroscan Instruments SA) for his continuous support in keeping the “old lady” (X-Ray photoelectron spectrometer) alive for the last four and a half years. This includes Dr. Tim Ludwig and Robert Frohnhoven, who introduced me to the beautiful machine. Their operator training at the beginning of my Ph.D. is the basis of the massive success in publishing with the device in recent years.
I would also like to thank the mechanical, electronic, and glass blower workshops of the Institute of Inorganic Chemistry and the Department of Chemistry for their support whenever needed.
I want to thank Dr. Thomas Fischer and Nurgül Tosun for the TEM measurements and the XRD operators Dr. Pantenburg, Daniel Moog, and Silke Kremer for the XRD measurements. Moreover, I am thankful to Dirk Pullem for measuring CHNS and Dr. Corrina Hegemann and Amadi Kingsley Chijioke for thermogravimetric analysis. For her open ears and great conversations, as well as her help in various administrative situations, I would like to thank Kelly Brinkmann. For the outstanding education during my Bachelor, Master's, and the support during the transition to the Ph.D., I am very grateful to Dr. Volker von der Gönna.

The continuing support and collaboration of past and present members of the Research group Mathur are highly acknowledged. Special thanks to Dr. Tim Ludwig, Dr. Isabel Gessner, Dr. Veronika Brune, and Dr. Eva Krakow for everything you helped me with at the beginning of my Ph.D. I will never regret these times!

Thanks to the Kegelklub *"Zum goldenen Fässchen*", especially the old and the new members. I am very thankful for the experience of traveling to the 2022 MRS Spring Meeting and the opportunity to meet Prof. Stanly Whittingham in Hawai'i. Even when your luggage does not arrive, it could be worse to go shopping with four girls in Honolulu. Thank you, Dr. Veronika Brune, Dr. Shaista Ilyas, Anna Schmidt-Verm, and Anja Sutorius, for sharing this trip with me and climbing up the Koko Head with our laptops. It felt already like getting through a Ph.D.

Furthermore, I would like to thank Team Pittsburgh (Dr. Aman Bhardwaj, Dr. Thomas Fischer, Dr. Veronika Brune, and Ruth Adam) for a beautiful trip to the MS&T 22 while celebrating Aman's 30th birthday for 30 hours in four different cities. I would like to also thank Prof. Sanjay Mathur for having me with him when taking over the presidency (2022-2023) of The American Ceramic Society. I thank my lab mates Fabian Hartl and Ruth Adam for fruitful discussions and synthetic help in the laboratory. Special thanks to Ruth, Anja, David, Tim, Veronika, and Khan for proofreading parts of my thesis.

I want to thank David and Kristina Sonnabend for supporting me outside of the university.

Finally, I would like to thank my family, especially my parents, Maria and Stefan, my brother Dominik, his wife Julia, and my nephew Karl Leo for their continuous and everlasting support in every problematic situation. Eva, without you, I could not have done this. Thank you for keeping my back free whenever possible and for being my daily motivator!

This thesis belongs to you as it belongs to me! Thank You!

List of publications included in this thesis

1. **Wilhelm, M.**, Adam, R., Bhardwaj, A., Neumann, I., Cho, S. H., Yamada, Y., Sekino, T., Tao, J., Hong, Z., Fischer, T., & Mathur, S. Carbon-Coated Electrospun V_2O_5 Nanofibers as Photoresponsive Cathode for Lithium-Ion Batteries. *Adv. Eng. Mater.* 2200765, (**2022**).
2. Brune, V., Bohr, C., Ludwig, T., **Wilhelm, M.**, Hirt, S. D., Fischer, T., Wennig, S., Oberschachtsiek, B., Ichangi, A., & Mathur, S. A novel molecular synthesis route to Li_2S loaded carbon fibers for lithium-sulfur batteries. *J. Mater. Chem. A* 10, 9902–9910 (**2022**).
3. Yang, Y., Hoang, M. T., Bhardwaj, A., **Wilhelm, M.**, Mathur, S., & Wang, H. Perovskite solar cells based self-charging power packs: Fundamentals, applications and challenges. *Nano Energy* 94, 106910 (**2022**).
4. Thiyagarajan, G. B., Shanmugam, V., **Wilhelm, M.**, Mathur, S., Moodakare, S. B., & Kumar, R. $TiNb_2O_7$-Keratin derived carbon nanocomposites as novel anode materials for high-capacity lithium-ion batteries. *Open Ceram.* 6, 100131 (**2021**).
5. Hong, Z., Maleki, H., Ludwig, T., Zhen, Y., **Wilhelm, M.**, Lee, D., Kim, K.-H., & Mathur, S. New insights into carbon-based and MXene anodes for Na and K-ion storage: A review. *J. Energy Chem.* 62, 660–691 (**2021**).

Other works not included in this thesis

1. Hartl, F., Brune, V., Lüggert, S., Hegemann, C., van Gerven, D., **Wilhelm, M.**, Ji, S., Choi, H., Mathur, S. Direct Synthesis of Two Dimensional SnSe and $SnSe_2$ Through Molecular Scale Preorganization. *Submitted manuscript*.
2. Dmonte, D.J., Bhardwaj, A., **Wilhelm, M.**, Fischer, T., Kuřitka, I., Mathur, S. Sub ppm Detection of NO_2 Using Strontium Doped Bismuth Ferrite Nanostructures. Micromachines, 14, 644, (**2023**).
3. Drexelius, M., Arnold, R., Meinberger, D., **Wilhelm, M**., Mathur, S., Neundorf, I. Rational design of bifunctional chimeric peptides that combine antimicrobial and titanium binding activity. J. Pept. Sci., e3481 (**2023**).
4. Cuzzupè, D. T., Ünlü, F., Lê, K., Bernhardt, R., **Wilhelm, M.**, Grosch, M., Weißing, R., Fischer, T., van Loosdrecht, P. H. M., & Mathur, S. Thermally-induced drift of A-site cations at solid–solid interface in physically paired lead halide perovskites. *Sci. Rep.* 12, 10241 (**2022**).
5. Brune, V., Hegemann, C., **Wilhelm, M.**, Ates, N., & Mathur, S. Molecular Precursors to Group IV Dichalcogenides MS_2 (M=Ti, Zr, Hf). *Zeitschrift für Anorg. und Allg. Chemie* 648, e202200049 (**2022**).
6. Mukkavilli, R. S., Ichangi, A., Thiyagarajan, G. B., Vollnhals, F., **Wilhelm, M.**, Bhardwaj, A., Christiansen, S., Neelakantan, L., Mathur, S., & Kumar, R. Electrospun 1D Ta_3N_5-(O) nanofibers as advanced electrocatalysts for hydrogen evolution reaction in proton exchange membrane water electrolyser. *Open Ceram.* 10, 100267 (**2022**).
7. Thiyagarajan, G. B., Mukkavilli, R. S., Graf, D., Fischer, T., **Wilhelm, M.**, Christiansen, S., Mathur, S., & Kumar, R. Self-supported amorphous $TaN_x(O_y)$/nickel foam thin film as an advanced electrocatalyst for hydrogen evolution reaction. *Chem. Commun.* 58, 3310–3313 (**2022**).
8. Christoffels, R., Breitenbach (née Stastny), C., Weber, J. P., Körtgen, L., Tobeck, C., **Wilhelm, M.**, Mathur, S., Neudörfl, J.-M., Farid, M. S. Z., Maslo, M., Strub, E., & Ruschewitz, U. UoC-3: A Metal–Organic Framework with an Anionic Framework Based on Uranyl UO_2^{2+} Nodes and Partly Fluorinated Benzene-1,3,5-Tribenzoate Linkers. *Cryst. Growth Des.* 22, 681–692 (**2022**).
9. Brune, V., Raydan, N., Sutorius, A., Hartl, F., Purohit, B., Gahlot, S., Bargiela, P., Burel, L., **Wilhelm, M.**, Hegemann, C., Atamtürk, U., Mathur, S., & Mishra,

S. Single source precursor route to nanometric tin chalcogenides. *Dalt. Trans.* 50, 17346–17360 (**2021**).

10. **Wilhelm, M.**, Ludwig, T., Fischer, T., Yu, W., Singh, D., & Mathur, S. Functionalized few-layered graphene nanoplatelets for superior thermal management in heat transfer nanofluids. *Int. J. Appl. Ceram. Technol.* 19, 803–812 (**2022**).
11. Krakor, E., Saniternik, S., Gessner, I., Frohnhoven, R., **Wilhelm, M.**, Drexelius, M., Tosun, N., Neundorf, I., & Mathur, S. Hollow mesoporous silica capsules loaded with copper, silver, and zinc oxide nanoclusters for sustained antibacterial efficacy. *J. Am. Ceram. Soc.* 105, 1685–1696 (**2022**).
12. Raauf, A., Leduc, J., Frank, M., Stadler, D., Graf, D., **Wilhelm, M.**, Grosch, M., & Mathur, S. Magnetic Field-Assisted Chemical Vapor Deposition of UO_2 Thin Films. *Inorg. Chem.* 60, 1915–1921 (**2021**).
13. Krakor, E., Gessner, I., **Wilhelm, M.**, Brune, V., Hohnsen, J., Frenzen, L., & Mathur, S. Selective degradation of synthetic polymers through enzymes immobilized on nanocarriers. *MRS Commun.* 11, 363–371 (**2021**).
14. Frank, M., Bulut, Y., Czympiel, L., Weißing, R., Nahrstedt, V., **Wilhelm, M.**, Grosch, M., Raauf, A., Verma, A., Fischer, T., & Mathur, S. Piezo-enhanced activation of dinitrogen for room temperature production of ammonia. *Nanotechnology* 32, 465601 (**2021**).
15. Chernozem, R. V, Romanyuk, K. N., Grubova, I., Chernozem, P. V, Surmeneva, M. A., Mukhortova, Y. R., **Wilhelm, M.**, Ludwig, T., Mathur, S., Kholkin, A. L., Neyts, E., Parakhonskiy, B., Skirtach, A. G., & Surmenev, R. A. Enhanced piezoresponse and surface electric potential of hybrid biodegradable polyhydroxybutyrate scaffolds functionalized with reduced graphene oxide for tissue engineering. *Nano Energy* 89, 106473 (**2021**).
16. Bandar Abadi, M., Weissing, R., **Wilhelm, M.**, Demidov, Y., Auer, J., Ghazanfari, S., Anasori, B., Mathur, S., & Maleki, H. Nacre-Mimetic, Mechanically Flexible, and Electrically Conductive Silk Fibroin-MXene Composite Foams as Piezoresistive Pressure Sensors. *ACS Appl. Mater. Interfaces* 13, 34996–35007 (**2021**).
17. Schmidt-Verma, A.K., Renner, A.M., **Wilhelm, M.**, Bohr, C., Goenuellue, Y., Rudigier-Voigt, E. and Mathur, S., High-Temperature Ultrahydrophobic Ceramic

Coatings from Surface-Functionalized $MgAl_2O_4$ Nanoparticles. Adv. Eng. Mater., 23, 2000738 (**2021**).

18. Sekhar, P. K., Ludwig, T., **Wilhelm, M.**, Graf, D., Riheen, M. A., & Mathur, S. Potentiometric Ethene Sensor for Postharvest Detection Applications. *J. Electrochem. Soc.* 166, B1477–B1482 (**2019**).

Table of Contents

1 Motivation

"**B**uilding **B**etter **B**atteries" was the central message in a publication used by Armand and Tarascon in 2008 that was an appeal to motivate researchers from a range of disciplines to cross-fertilize solutions for addressing the remaining challenges of reaching the application demands, the further development of battery-driven cars and the rethinking of sustainable technology for the future.[1] This is almost supplied by the most commercialized lithium-ion battery (LIB), although LIBs are not necessarily sustainable by today's standards.[2,3] The predominant use of the technology in areas such as e-mobility, mobile electronic devices, or home batteries, cannot hide the fact that it is questionable whether the technology will also be able to meet the requirements in terms of energy demand.[2,4] It is only a matter of time before battery-driven trucks and airplanes reach market maturity.[5,6] Some leading companies, e.g., CUSTOMCELLS®, are already developing serial production of state-of-the-art lithium-ion battery cells to let their battery technology become viable for the aviation sector. With their article "High Voltage in the Clouds", published in Master of Batteries end of 2022, it became clear that the electrification of the aviation sector is going to be a game-changer for future transport.[7]

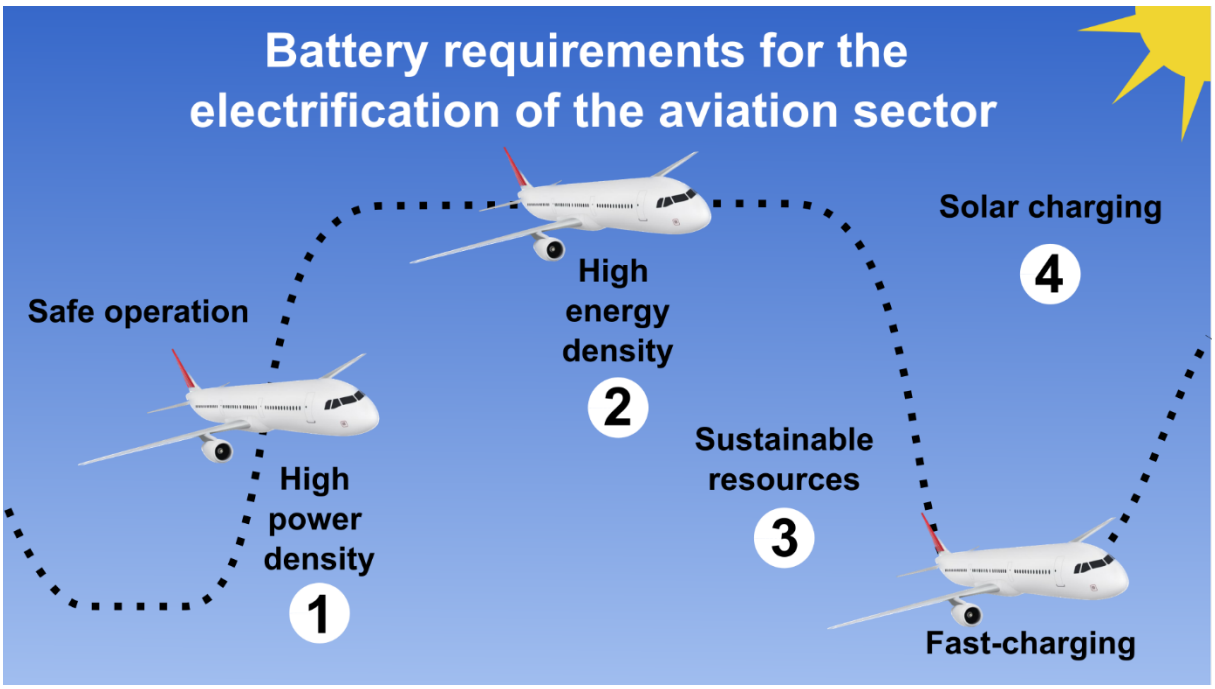

Figure 1: Illustration of battery requirements for the electrification of the aviation sector.

Thinking about battery technology for the aviation sector, the requirements in design and cell chemistry are entirely different from current standards, as illustrated in Figure 1. While high power density is required for a quick take-off (1), a high energy density is highly consequential for the actual flight distance (2). Low weight and compacted cell design are decisive in securing energy during the flight. In addition, battery safety and the use of sustainable resources (3) to meet the demand for materials for such batteries are of crucial importance. Finally, fast-charging capability after a flight or alternative ways of charging the batteries, such as solar power (4) during a flight, are essential for the frequent schedules of airlines.

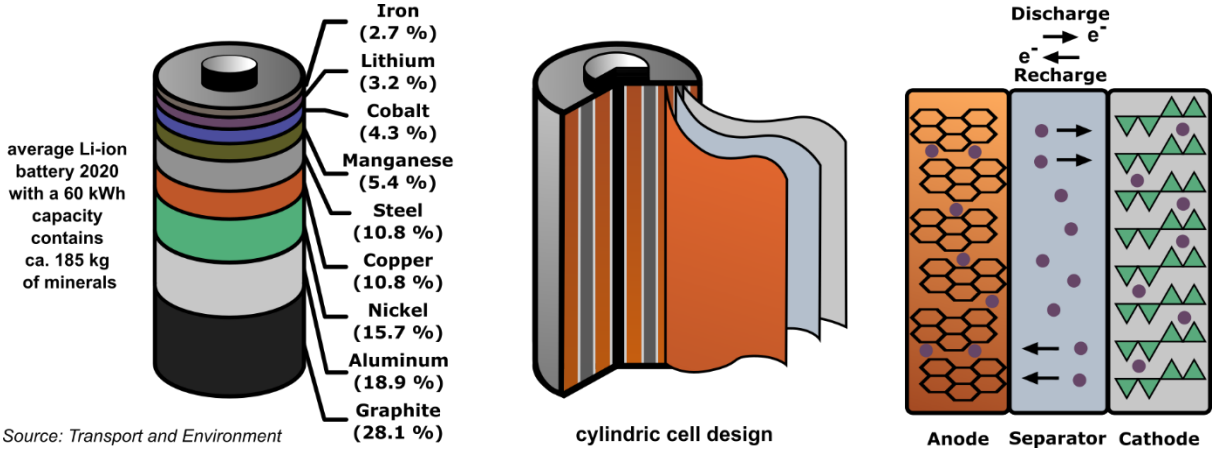

Figure 2: Average amount of minerals in a 2020 Li-ion battery of an EV car, its cell architecture, and its general working mechanism.

A brief look at the number of minerals currently used in a battery for an electric-driven passenger car (Figure 2) demonstrates how much material is needed to satisfy the upcoming demand, not only in the field of electric vehicles (Figure 3). Stationary batteries will emerge in the growing market continuously, which will be challenging with limited availability and accessibility of raw materials (e.g., lithium or cobalt).[8]

However, the requirements for mobile and stationary battery technologies are slightly different. Light weight and compact cell design are the main requirements for mobile applications. This is a challenge when thinking about increasing the capacity of the cell without increasing the weight or volume of the battery. Light weight and compact cell design is desirable but not mandatory for stationary battery systems. Instead, high energy density and constant power supply are key when other power sources are not usable. Therefore, Li-ion batteries are dominating the global market for mobile applications due to light weight and small cell design. The need for technologies beyond Li-ion batteries opens for the future of stationary electrochemical energy storage systems. Additionally, the rechargeability of the cells depends on the application's requirements.

It is to be considered that not every material has the capability for being suitable for fast charging.

To date, there is a need for optimization in the lifetime, cost, weight, and sustainability of battery powered electrical devices. Although some progress has been made since the "**BBB**" call in 2008, especially with regard to the energy density of the electrochemical cell, there is still room for improvement.[9,10] In 2014, Richard van Noorden in his publication entitled "The **R**echargeable **R**evolution - a **B**etter **B**attery" discussed the importance of chemists reinventing rechargeable batteries to lower the costs and boost the capacity.[11] Comparing Li-ion batteries with other cell technologies, there is plenty of room for improvement, which, e.g., begins with a radical redesign of the battery cell (Figure 2). Examples of these redesigns could be solid-state electrolytes, lithium-sulfur, lithium-oxygen, or rechargeable magnesium batteries (RMB).[11]

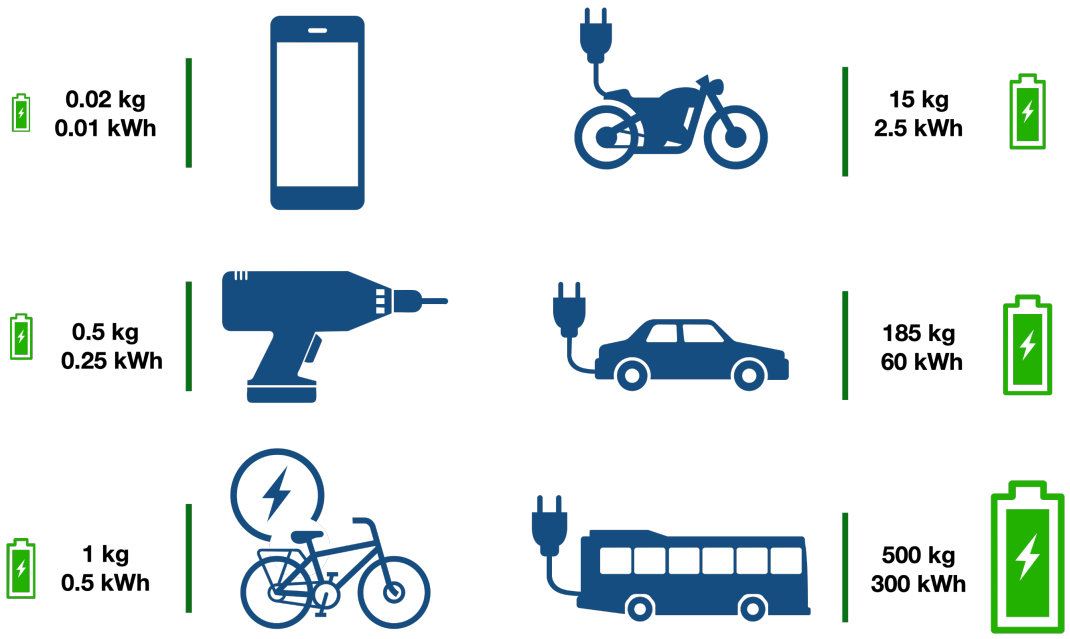

Figure 3: Battery weights and energies for different types of applications.

In addition, the nanotechnology revolution also played a significant role in the improvements of the battery sector regarding capacity, power, cost, and materials sustainability.[1,12] For instance, high-surface areas and nanosized materials of metal oxides, metal sulfides, or carbon-based materials can improve the electrochemical performances of the batteries. This effect can be adapted to the next generation of battery technology.[13,14]

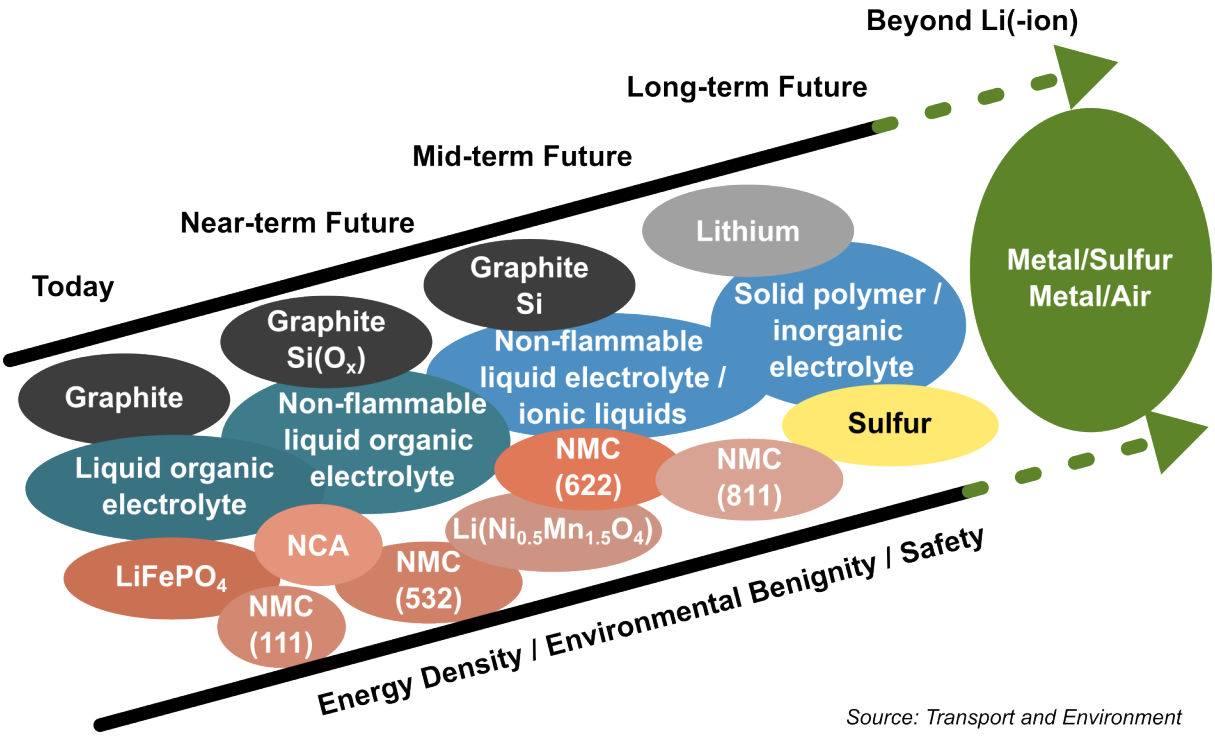

Figure 4: Transition from today's battery inner life towards beyond lithium-ion batteries.

High performance and efficiency are of high importance for future batteries. Battery powered mobile devices are indispensable nowadays. One needs to imagine, would be impossible without batteries: Starting a car or carrying portable devices such as mobile phones, laptops, watches, and many more. By default, they would become *immobile*. Further, storing energy from renewables, both on and off-grid, such as solar, wind, or water, to recall it at a later stage when no renewable energy sources are available is prime for energy sustainability. For example, stationary applications ensure backup power in case of power outages in critical facilities such as hospitals and telecom installations.

Increased CO_2 emissions have led to global warming with rising risks for humanity and nature. Batteries are seen as one of the key enablers of a low-carbon society. Batteries also help reduce greenhouse gas emissions by efficiently storing electricity generated from both conventional and renewable energy sources and providing a power source for different mobile electrical applications. Batteries ensure a stable and sustainable energy supply and support the creation of a net-zero emission society by 2050.[15]

2 Scientific objectives

The primary aim of this work was the development of electrode materials for the next generation of batteries considering the demands of high power and energy density, safety, enhanced charging ability, and sustainable resources (Figure 5).
Based on fundamental concepts applied in the battery sector, the improvement of electrode materials by chemically engineered surface modifications was the first target of this study. Advanced characterization techniques were applied, allowing precise analysis of electrochemical properties and mechanisms. Different synthesis routes of $TiNb_2O_7$ – carbon composites were tested to investigate their influence on the charging performance and cyclic stability of the electrode materials for lithium-ion batteries.
Moreover, the establishment of new concepts for synergistic harvesting and storing of energy from solar power was targeted. Further, optimization by surface engineering of vanadium pentoxide as photoresponsive cathode material in lithium-ion batteries was another scientific objective of this work.

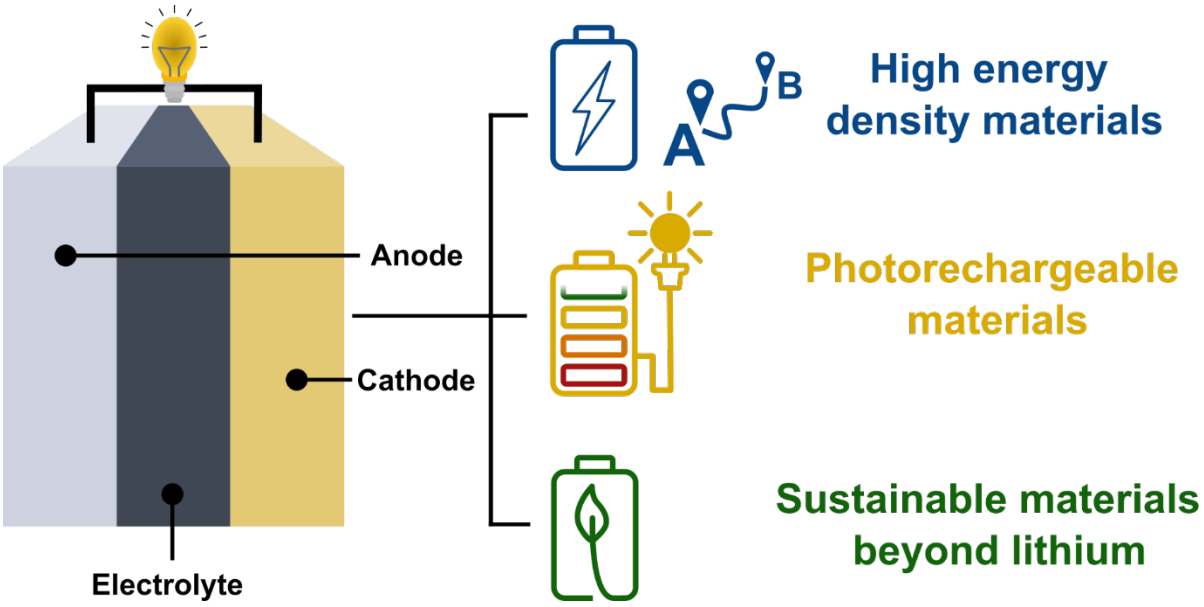

Figure 5: The future of electrode materials for the next generation of batteries.

Furthermore, metal-sulfur systems for lithium-sulfur and magnesium-sulfur batteries were targeted to meet the demand for high energy density for application in the electric vehicle market. For Li-S systems, a new synthetic approach for improving material production needed to be investigated. To employ sustainable and safe electrode materials, research beyond lithium-ion batteries was among the primary goals. Rechargeable magnesium batteries are promising candidates to replace lithium due to their

comparable standard redox potential (-2.37 V vs. SHE) and higher theoretical volumetric capacity (3,833 mAh g^{-1}). Suitable cathode materials based on transition metal sulfides, their crystal structures, morphology, and nano-sized effects, were to be studied to elucidate and further understand the electrochemical behavior in interaction with Mg^{2+} as the active ion.

The primary goal and structure of this work can be summarized as the following:

- Synthesis of new active materials for Li-ion batteries and beyond
- Optimization of active materials by surface engineering and additive manufacturing for electrode materials in batteries
- Development of new synthetic approaches for an improved battery manufacturing
- Advanced characterization of the electrode materials for an enhanced application in energy storage systems

3 Introduction

3.1 Know-how on batteries

The history of electrochemical reactions is embossed by the finding of Frederic Daniell in 1836 with the famous Daniell-cell.[16] In the typical setup, two electrodes of copper and zinc are placed in their corresponding sulfate salt solutions, which are divided by a diaphragm (Figure 6). By closing the circuit between the electrodes, Zn^{2+} dissolves in the $ZnSO_4$ solution while its electrons are conducted around the circuit to the positive electrode. The two electrons are consumed by the Cu^{2+}, which is dissolved in the electrolyte, to form the reduced state (Cu^0) at the copper electrode. This conversion redox reaction could achieve an operating voltage of 1.1 V and a max current of 100 mA.
Since this system only applies to primary batteries due to its irreversible reaction, a different approach had to be made for secondary batteries. TiS_2 – a transition metal chalcogenide – was found to have a 2D structure, which can store and release ions between the interlayers reversibly without changing its crystal structure. Whittingham employed this technique of intercalation/deintercalation of Li^+ in TiS_2 for the use as cathode material for LIBs, which was honored together with Goodenough and Yoshino with the Nobel prize in chemistry in 2019.[17–19]

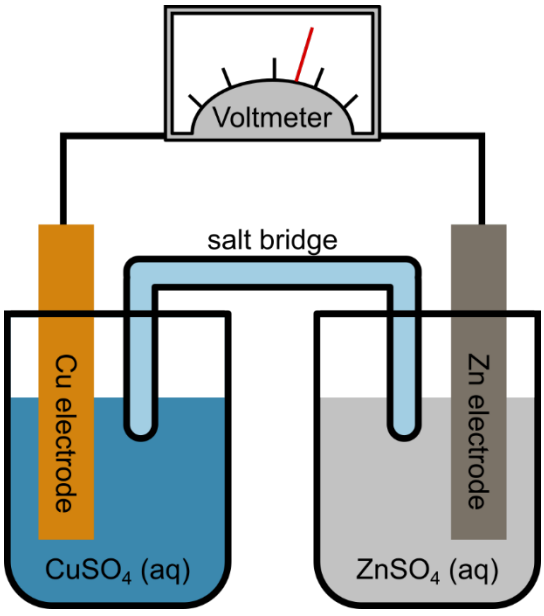

Figure 6: Daniell-cell represents an electrochemical cell of a copper/copper sulfate solution and a zinc/zinc sulfate solution connected by a salt bridge and an external circuit.

A battery is a source of energy that primary can convert chemical energy into electrical energy consisting of one or more electrochemical cells with external connections that provides power for electrical devices. During the operation of a galvanic cell, the electrical energy is supplied by the chemical redox reactions at the electrodes. In the simplest term of a battery, the cell consists of three parts: the cathode, the anode, and the electrolyte. When a battery is connected to an external electric load, ions are transported from the anode to the cathode supported by the electrolyte. In redox reactions, high-energy reactants are converted to lower-energy products, while the free-energy difference is delivered via an external circuit as electrical energy.

Batteries can be mainly categorized into two groups: primary and secondary batteries. A **primary** or ‘single-use’ cell can be only discharged once since the redox reactions on the electrodes are irreversible. These cells are designed to be used until exhausted of energy before they are discarded. The most common examples are alkaline and zinc-carbon batteries. Both produce a cell voltage of around 1.5 V.

Secondary batteries are rechargeable and can be discharged and recharged multiple times using an external power supply. The electrode compositions undergo reversible redox reactions meaning that the initial phase before and after one cycle can be restored. Both battery types can be connected in parallel or series to higher the cell voltage or the current output. Batteries can be further categorized by their performance depending on the cells' architecture, materials, and cell types. Within the field of secondary batteries are **ternary batteries**, which are batterie using three transition metal oxides as positive electrode. The most prominent electrodes are nickel, cobalt, and manganese, which combine the good cycle performance of lithium cobaltate, the high specific capacity of lithium nickelate, and the high safety and low cost of lithium manganate. Most common used battery types are summarized, and advantages and disadvantages are discussed in Table 1.

Table 1: Most common used batteries used today.

Battery Size	Electrochemical System	Nominal Voltage	Type	Advantage	Disadvantage
AA, AAA, C, D	Zinc-Manganese Dioxide, Zinc-Carbon	1.5V	Primary (non-rechargeable)	Decent Power density, Low cost	Susceptible to natural rupture, short lifetime
	Nickel-Metal Hydride	1.2V	Secondary (rechargeable)	High current ability, less susceptible to memory issues, low costs	Short storage life, Susceptible to overcharge
Coin Cell	Lithium-Manganese Dioxide	3V	Primary (non-rechargeable)	Long-term reliability, stable discharge capability, Wide temperature range	Susceptible to natural rupture
Flat Pack (e.g., Cell phone)	Lithium-Ion (Li-Ion), Lithium polymer (LiPo)	3.7V	Secondary (rechargeable)	Very high energy density, limited memory effect, long life,	High cost, Vulnerable to stress, Safety issues
Car battery	Lead-Acid	12V	Secondary (rechargeable)	High power density, Durable, Wide temperature range	Low energy density, Heavy, Large size, Toxic
Electromotive	Li-ion with Nickel-Manganese-Cobalt (NMC)	Depending on the structure	Ternary (rechargeable)	Very high energy density, lower costs, long life,	High cost, Vulnerable to stress, Safety issues

3.2 Lithium-ion batteries

The central part of this section is published in the following review article, which includes the preparation of the specific section related to lithium-ion batteries. For the reproduction in this thesis/dissertation as an author, permission is not required [20]*:*

Yang, Y., Hoang, M. T., Bhardwaj, A., Wilhelm, M., Mathur, S., & Wang, H. Perovskite solar cells based self-charging power packs: Fundamentals, applications and challenges. *Nano Energy* 94, 106910 (**2022**).

A lithium-ion battery generally consists of an anode (Li metal, carbon materials, $Li_4Ti_5O_{12}$, *etc.*), a cathode ($LiFePO_4$, $LiCoO_2$, $LiMnO_2$, *etc.*), a separator, and a lithium-ion conducting electrolyte (lithium salt in an organic solvent).[21] The working mechanism of a LIB is illustrated in Figure 7a. On discharge, Li-ions and electrons flow from the anode to the cathode via the electrolyte carrier and the external circuit while the anode is getting oxidized, and the cathode is reduced. During charging, the Li-ions and electrons are forced by an external power to flow from the cathode to the anode while the cathode is oxidized and the anode is reduced. It is worth noting that the voltage of LIBs is determined by the difference in chemical potential between the anode and cathode.[22]

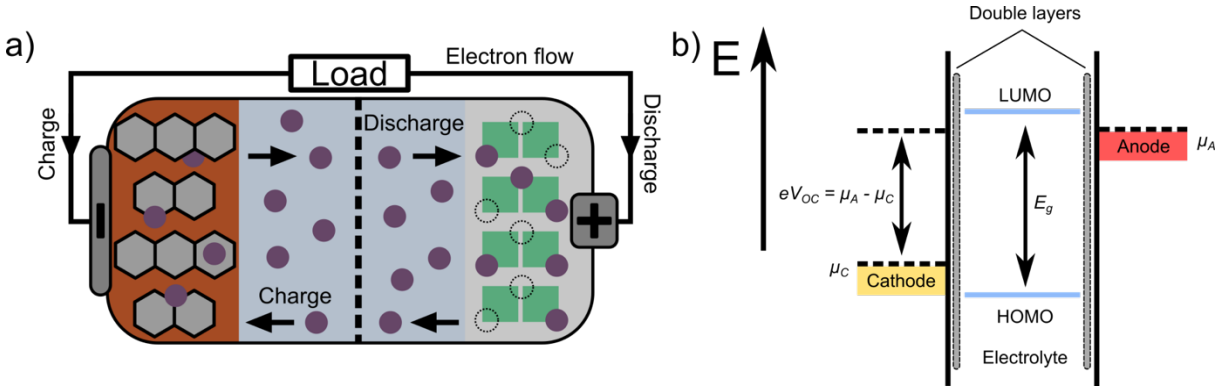

Figure 7: a) General scheme of a lithium-ion battery and b) relative energy levels LUMO-HOMO window of the electrolyte and the relationship between the electrochemical potentials of the anode (μ_A) and cathode (μ_C).

Moreover, the output voltage is reduced by internal resistance to the ionic current. The charging voltage is increased by an overvoltage, which accounts for internal losses due to electrical and ionic conduction through the different components of the cell. The choice of the electrode and the electrolyte depends on their relationship in electrochemical potential values (μ_A = anode, μ_C = cathode) and energy positions of the

HOMO-LUMO (E_g) of the electrolyte. If the μ_A is higher in energy, then the LUMO of the electrolyte will be reduced, and on the other hand, if μ_C is lower in energy, then the HOMO of the electrolyte inhibits the oxidation of the electrolyte, as shown in Figure 7b.[23]

3.2.1 Intercalation vs. conversion mechanisms

In **intercalation** cathodes (Figure 8), primarily transition metal oxides and sulfides, the oxidation state of the metal compensates for the charge of the guest molecules and ions, whereas the structural phase of the solid host is not changing.[24] In general, this process is not different among monovalent (Li^+, Na^+, K^+) and multivalent (Mg^{2+}, Ca^{2+}, Al^{3+}) working ions. Depending on the charge and the size of the active ion, the insertion/extraction can be inhibited, resulting in poor performance of the material. The most prominent candidates for the most commercially exploited cathodes for Lithium-Ion batteries are TiS_2 and $LiCoO_2$.[25]

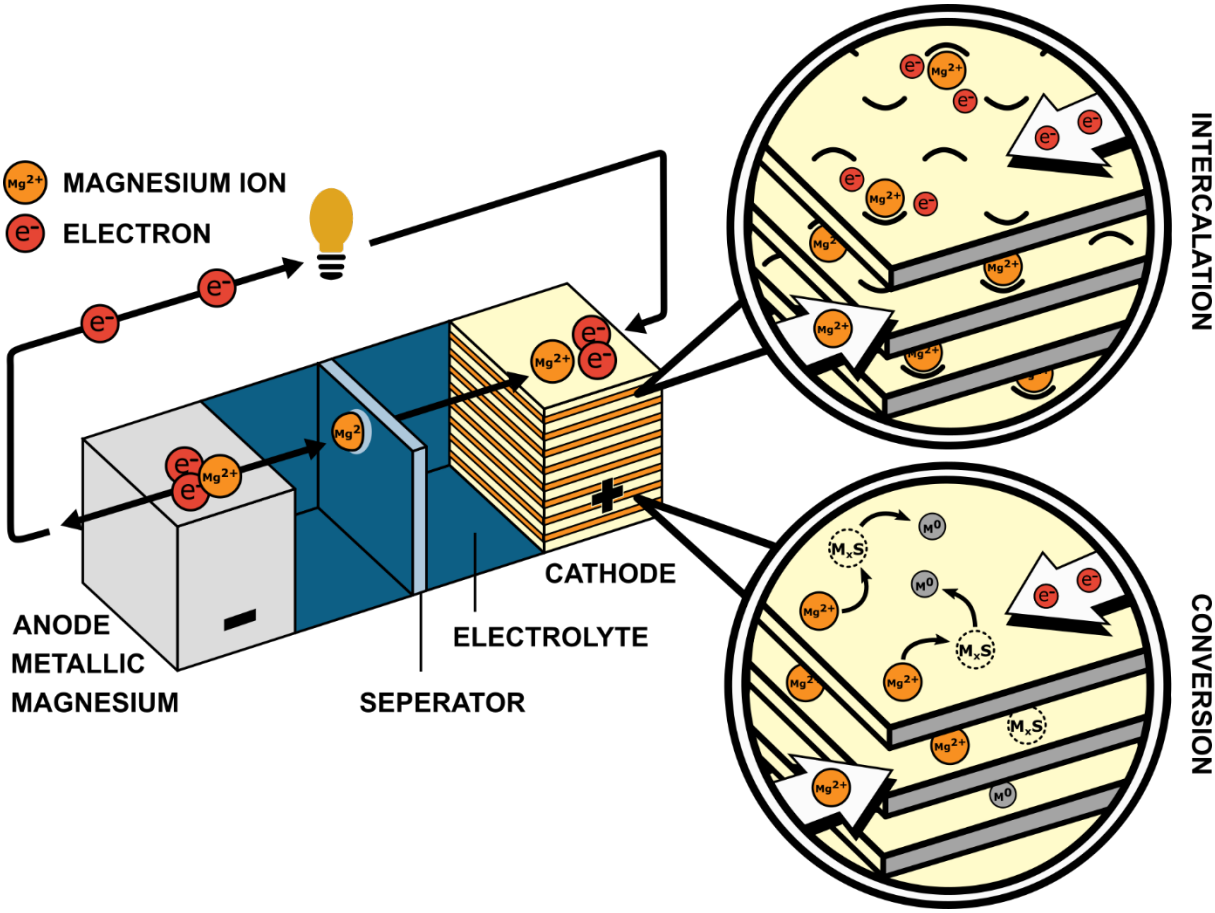

Figure 8: Illustration of a rechargeable magnesium battery with a metallic magnesium anode and an intercalation or conversion cathode based on a transition metal sulfide. Adapted from [19].

Electrode materials follow a **conversion** reaction mechanism involving breaking and creating chemical bonds. The conversion-type cathode materials react with the active ion to form a working ion compound by reducing the cathode material. Here, compared to the intercalation type materials, the active material undergoes a structural deformation by mostly a change of the crystal structure.[26–28] Prominent examples of explored cathode materials for use with lithium metal anodes include sulfur, oxygen, and metal halides.[29,30] Figure 8 illustrates the working principle of a magnesium ion battery using a metallic magnesium anode and a transition metal sulfide cathode. Depending on the material, an intercalation or conversion reaction is preferred.

Table 2 summarize timely applied cathode materials/battery types following an intercalation mechanism with lithium-ions in the electroautomotive sector. These parameters can be seen as the current state-of-the-art values. In the field of intercalation chemistry, the goal is to increase these, whereas the primary target for the conversion type materials is to meet these values to make battery manufactoring cheaper and more sustainable.

Table 2: Timely used cathode materials/battery types of lithium-ion batteries and their current performance parameters.

Type	Voltage Window (Norminal Voltage)	Specific Energy	Charge Rate	Cycle Life
NCA	3-4.2V (3.6V)	200-300 Wh kg^{-1}	0.7C	500 cycles
NMC	3-4.2V (3.7V)	150-220 Wh kg^{-1}	1C	1500 cycles
LTO	1.8-2.85V (2.4V)	50-80Wh kg^{-1}	1-10C	3500 cycles
LMO	3-4.2V (3.7V)	100-150 Wh kg^{-1}	0.7-1C	350 cycles
LFP	2.5-3.65V (3.3V)	90-120 Wh kg^{-1}	1C	2000 cycles

NCA = Nickel-Cobalt-Aluminum, NMC = Nickel-Manganese-Cobalt, LTO = Lithium Titanate, LMO = Lithium Manganese Dioxide (spinel), LFP = Lithium-Iron-Phosphate

3.2.2 Titanium niobium oxides ($TiNb_2O_7$) as anode materials for LIB

The central part of this section is published in the following article, which includes support in manuscript preparation. Further, in this study, formal XPS characterization, analysis, evaluation, and preparation of the scientific section related to TNBO and TNBO/KC, as well as their influence on the electrochemical properties of their materials, were done. The chemical synthesis of the material was done by the first and co-authors. For the reproduction in the thesis/dissertation as an author, permission is not required [31]*:*

Thiyagarajan, G. B., Shanmugam, V., Wilhelm, M., Mathur, S., Moodakare, S. B., & Kumar, R. $TiNb_2O_7$-Keratin derived carbon nanocomposites as novel anode materials for high-capacity lithium-ion batteries. *Open Ceram.* 6, 100131 (**2021**).

The performance of conventional lithium-ion technologies with graphite as an anode material is limited by its low working potential (~0.1 V vs. Li/Li^+), which leads to the formation of passivating solid-electrolyte interphase (SEI), resulting in poor cycle life and safety related issues (Figure 10b).[32] Moreover, graphite-based anode chemistry requires a formation cycle prior to the application, which directly impacts the cost and time of the production line. Owing to the challenges posed by graphite anodes, exploring alternative anode materials with high energy storage capabilities is in order.

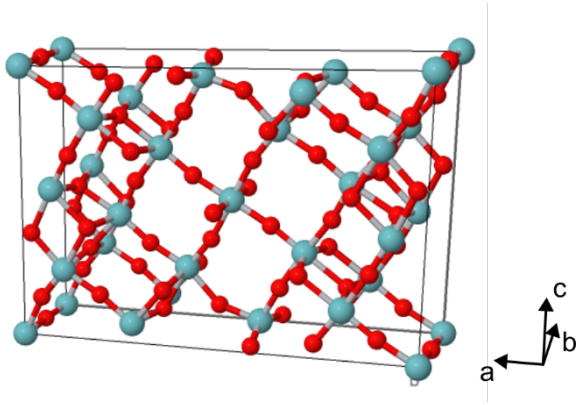

Figure 9: Crystal structure of monoclinic $TiNb_2O_7$ (Blue = Ti/Nb, red =O).

Recently, monoclinic $TiNb_2O_7$ (Figure 9) was proposed as potential alternative anode material for LIB owing to its large theoretical capacity of 387 mAh g^{-1} and high working potential of ~1.6 V, preventing the formation of SEI layers and lithium dendrites.[33–37] Albeit the aforementioned advantages, TNO possesses low electronic (< 10^{-9} S cm^{-1}) and ionic conductivity.[38] It also suffers from a low Li^+-ion diffusion coefficient ($D_{Li\ in\ TNO}$

= 10^{-12} cm^2 s^{-1}), resulting in poor rate capability ($D_{Li\ graphite\ between\ planes}$ = 10^{-12} cm^2 s^{-1} and $D_{Li\ in\ plane}$ = 10^{-6} cm^2 s^{-1}). The enhancement of the rate capability of TNO has been explored through nano-structured forms of TNO (particles, fibers, rods, and porous), doped TNO (Mo, V), and TNO carbon composites (CNT, graphene, and graphene oxide) which are reported widely in the literature.[34,39–46] The nano-structuring of TNO is reported to facilitate the fast diffusion of lithium-ions between the electrode-electrolyte interface boosting electrochemical performance. In the case of doped TNO and TNO-carbon composites, dopants and carbon components, respectively, contribute towards an increase in the ionic and electronic conductivity of TNO. The comparison of the rate capabilities of these materials is shown in the Ragone chart (Figure 10a). The superior performance of TNO/carbon composites is imperative in contrast to doped TNO and nano-structured forms of TNO. Most of the earlier work reports the fabrication of TNO/carbon composites employed carbon-nanotubes, graphene, and graphene oxide as carbon sources which, besides being expensive, also involve complex and specialized preparation routes limiting their scalability for possible use in LIBs.

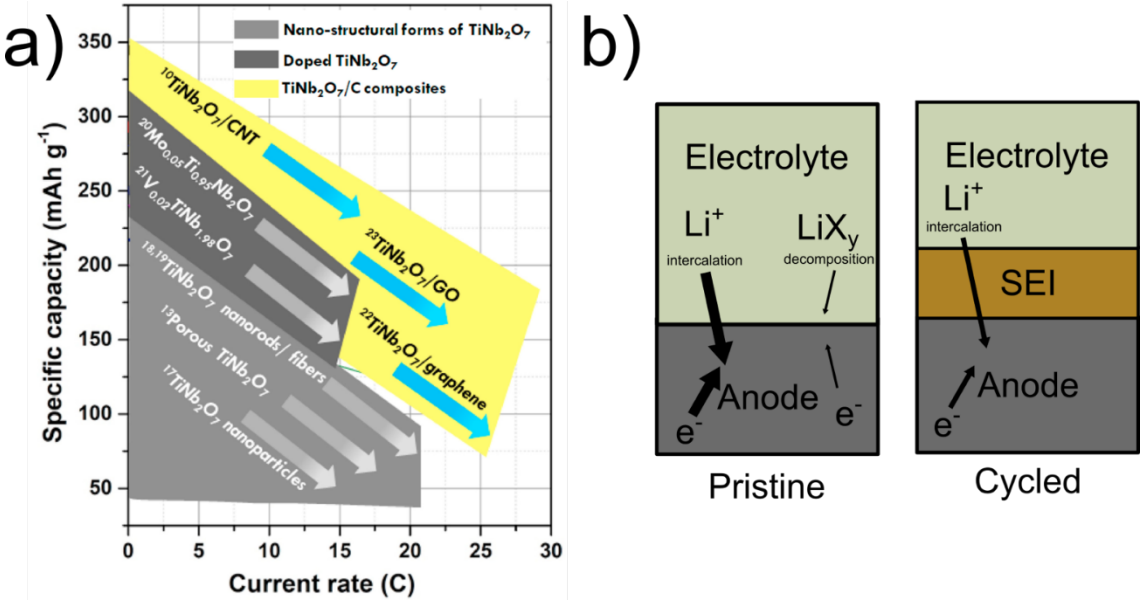

Figure 10: a) Ragone chart showing rate capabilities comparison of earlier works on different forms of $TiNb_2O_7$ materials. Reprinted and modified with permission [31]. b) Illustration of the formation of a solid electrolyte interface upon cycling of the negative electrode at low working potentials.

Although the presence of carbon in TNBO/carbon composites contributes towards performance enhancement of LIBs *via* improved electrical and ionic conductivities, the role of nano-structuring in the improvement of the electrochemical performance and conversion efficiency cannot be undermined.

In this context, it is expected that a hybrid, nano-structured TNBO/carbon composite as anode materials will synergistically combine good electrochemical interactions concomitant with improved electronic and ionic conductivities resulting in high-performing LIBs.

3.2.3 Electrode design and preparation

In the classical electrode preparation method, the active material is mixed with a binder, a conductive additive, and a solvent together to form a slurry. This slurry is then coated on a current collector, mostly copper and aluminum, and afterward dried to form the desired electrode. The bottleneck with these coated slurries is that the binder and the conductive carbon, as well as the current collectors, are inert materials for the electrochemical redox reactions and just increase the weight of the cell (
Figure 11). Additionally, the most common solvent N-Methyl-2-pyrrolidone (NMP) has environmental issues and is unfavorable for human health.

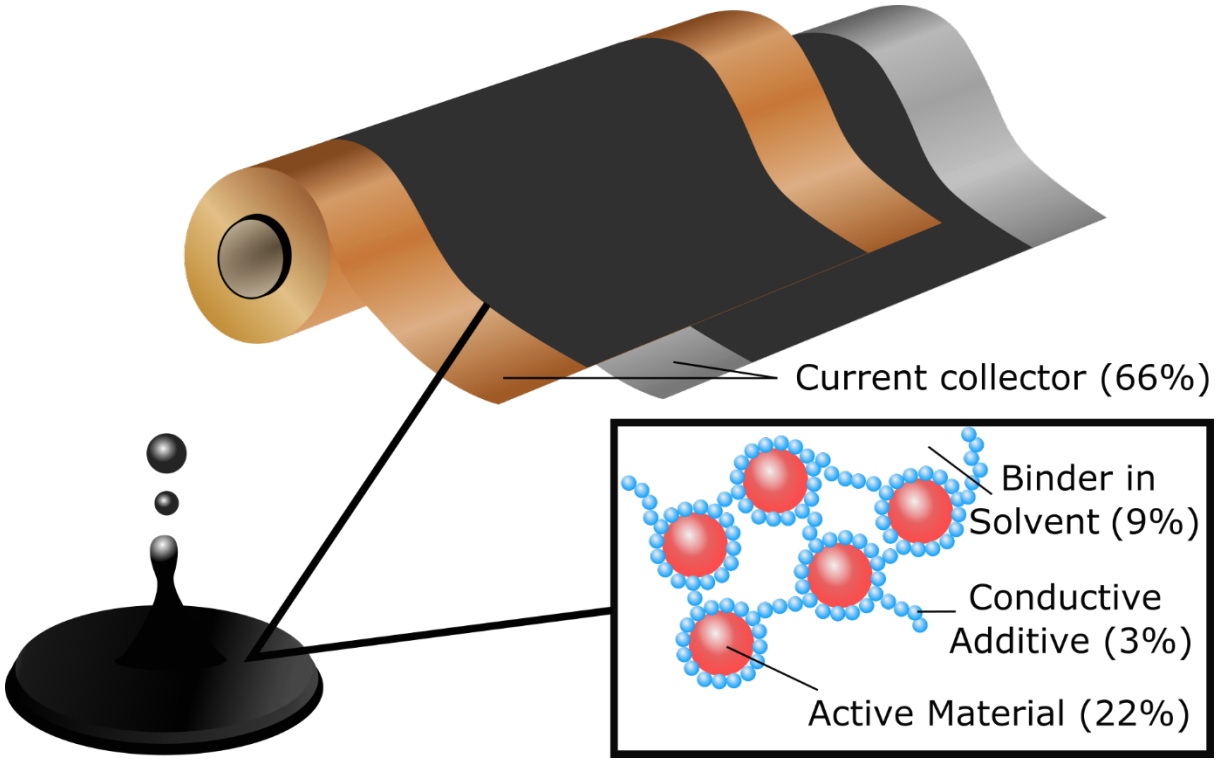

Figure 11: Active material suspended in a battery slurry and coated on current collectors. Allocation of material in the electrode preparation.

With the increased demand for energy storage in different sectors, flexible devices are getting more attention.[47] Therefore, it is of great interest to achieve flexible electrodes to enable the application of flexible batteries, as illustrated in Figure 12. With the achievement of flexible solid-state electrolytes, the potential for flexible all-solid-state-batteries is rising.[48,49]

Using flexible electrodes requires thin metal current collectors, which are expensive in production (Cu = 8-9 €/kg, Al = 2.5-3.5 €/kg). Therefore, another advantage would be to waive the metal foils as current collectors and achieve directly free-standing electrodes during the synthesis.

Flexible and free-standing anode materials are already known, mainly consisting of graphene and graphene-like structures. The architectures have a variation of different dimensions of 2D and 3D electrodes. Foams of carbon allotropes or film-like structures have found the most application so far.[50] Moreover, the deposition of active materials such as metal oxides and sulfides on flexible carbon fibers, e.g., carbon-clothes or electrospun fibers, have been investigated as flexible and binder-free electrodes for different types of batteries.[51–56]

Figure 12: Illustration of a flexible battery in a bendable smartphone. Reprinted with permission from [56].

Free-standing graphene-based films also have the potential to serve as free-standing, flexible, and binder-free electrodes. For these graphene-based films, mainly graphene oxide is used due to its surface functional groups, which build stable dispersions and have the potential to connect to giant graphene oxide films upon drying. Additional to the self-supported properties, it is possible to incorporate other electrochemically active materials between or onto the graphene layers.[57–62] After the reduction of the GO-films, highly electrical conductive films can be obtained after the calcination in a reductive atmosphere. Depending on the reduction procedure, different electrical conductivities can be achieved for the free-standing films, influencing the electrochemical performance of the cell.[57]

3.3 Beyond lithium-ion batteries

3.3.1 Lithium-sulfur batteries

The following chapter includes parts that are published in the following article, including the support of writing the specific part in the paper related to lithium-sulfur batteries and sketching of figures in this chapter. For the reproduction in the thesis/dissertation as an author, permission is not required [63]*:*

Brune, V., Bohr, C., Ludwig, T., Wilhelm, M., Hirt, S. D., Fischer, T., Wennig, S., Oberschachtsiek, B., Ichangi, A., & Mathur, S. A novel molecular synthesis route to Li_2S loaded carbon fibers for lithium-sulfur batteries. *J. Mater. Chem. A* 10, 9902–9910 (**2022**).

The rapid global consumption of fossil fuels is directly linked to huge CO_2 emissions. Therefore, the energy obtained from renewable sources like wind and solar is crucial for a sustainable energy supply.[64,65]
In this context, large-scale energy storage will play a key role in future energy technologies.[66] In general, batteries as electrochemical storage devices for different applications should meet several requirements of safety, high energy and power density, fast charging capability, sustainability, and natural abundance of raw materials.[64] Among the innumerable energy-storage technologies, the lithium-sulfur battery has emerged as a promising alternative because of its high theoretical gravimetric energy density (about 2600 W h kg^{-1}).[67] Furthermore, sulfur is highly abundant, economically priced, and non-toxic.[68–70] However, the low electrical conductivity of sulfur and lithium sulfide leads to limited high-rate capability.[71] Additionally, the polysulfide shuttle effect and the volume change of about 80% during cell operation are further challenges of this battery system that have prevented its commercialization so far.[72–74] The volume change leads to mechanical stress within the cathode, which can result in electrode cracking and electrode pulverization as well.[75] The shuttle effect involves the dissolution of higher-ordered polysulfides (Li_2S_4–Li_2S_8) in the electrolyte, their migration to the anode, and their electrochemical reduction on the anode's surface, which result in the formation of an additional passive layer composed of solid lithium sulfides such as Li_2S and Li_2S_2 (Figure 13).[76] This leads to increased cell resistance. Lower-ordered lithium

polysulfides diffuse back to the cathode, provoking chemical reactions with the cathode resulting in a decreased coulombic efficiency.[73] Finally, the shuttle effect causes a loss of the active material at the cathode, resulting in capacity fading.[77,78]

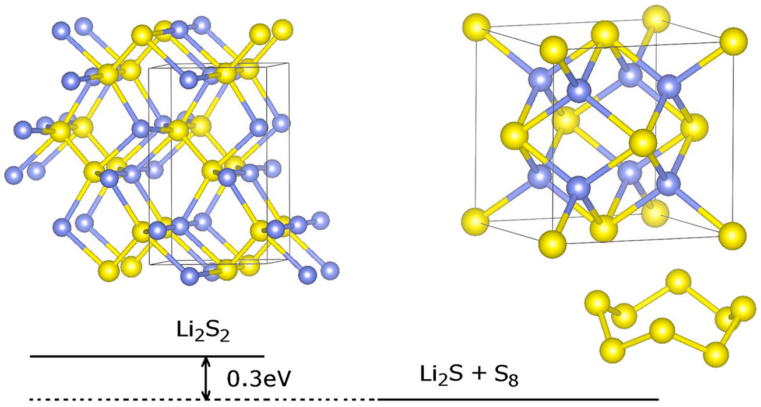

Figure 13: Crystal structure of Li_2S_2 (left) and Li_2S (right). Reprinted with permission from [76].

Applying elemental sulfur as the cathode material requires the deployment of elemental lithium as the anode. Lithium anodes can cause serious safety concerns since lithium dendrites can grow through the separator leading to short-circuits, which can result in a thermal runaway, as illustrated in Figure 14.[79]

Recently, lithium sulfide (Li_2S) has received much attention as an electrochemically active cathode material in lithium-sulfur batteries because a lithium-free anode can be used, and thus a higher level of safety can be ensured.[79] Li_2S also has a higher melting point than elemental sulfur, enabling the synthesis of advanced materials at higher temperatures. Therefore, Li_2S establishes various strategies for the composite formation and surface modification to enhance the electrical conductivity of the cathode. A common method for achieving this purpose is the embedding of the active material in a carbon matrix, as illustrated in Figure 15.[80,81]

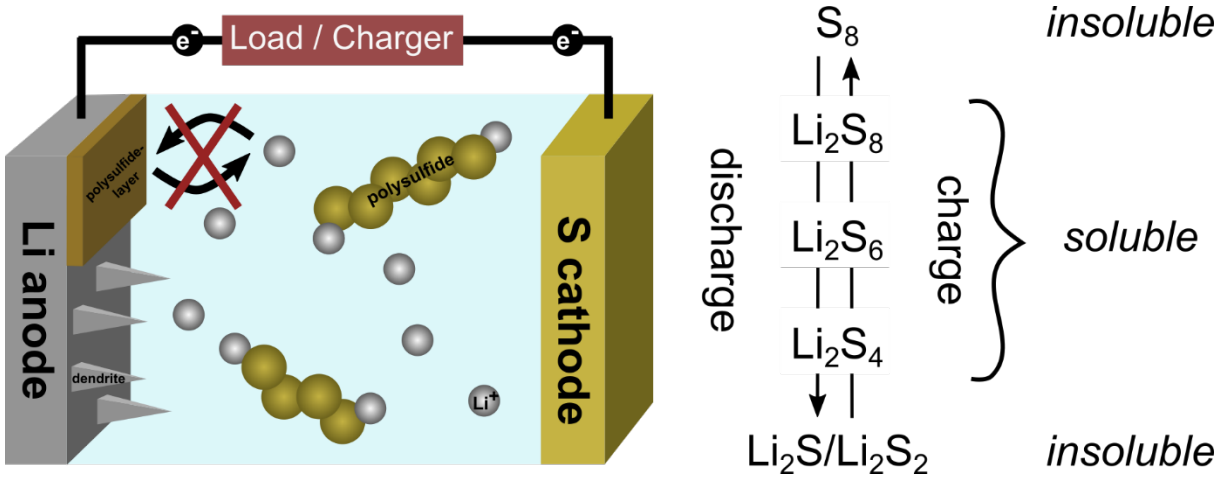

Figure 14: Working principle of a lithium-sulfur-battery.

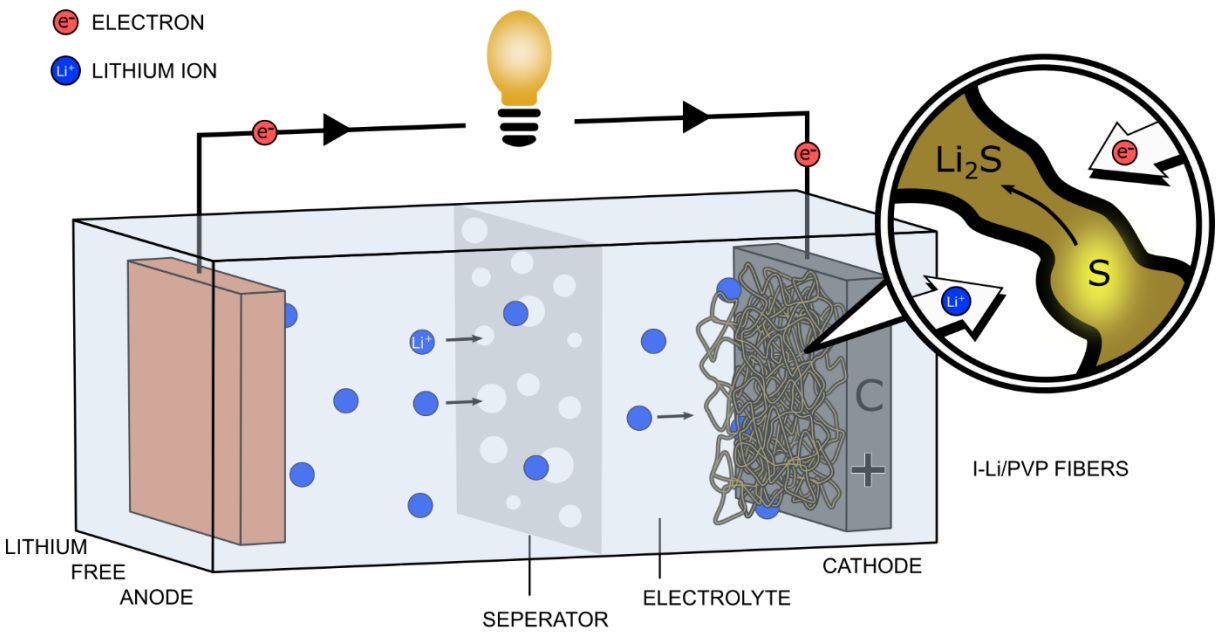

Figure 15: Illustration of the battery configuration with I-Li/PVP fibers as cathode material in a lithium metal-free anode.

The synthesis of hierarchically porous 1D structures by electrospinning methods reveals an alternative synthetic approach to embed the active material in a flexible, free-standing, and conductive carbon matrix to accelerate the electronic and ionic transfer of the active material for improving the cycling stability.[82] This synthesis enables the formation of 1D-fibers with varying diameters owing to the influence of changing process parameters such as the viscosity of the spinning solution, voltage, or kind of collector, among others.[83–85] Porous carbon nanofibers tend to be an ideal matrix due to their low weight, high electronic conductivity, and adjustable structural properties, meaning pore volume, pore size, and specific surface area.[54,80,86] Furthermore, carbon fibers can mitigate polysulfide dissolution by enhanced chemical adsorption of intermediate species and therefore reduce the shuttle effect significantly.[83,87–90] A simple synthetic access to lithium sulfide cathodes is hampered by the moisture sensitivity and reactivity of lithium.[91] So far, the electrospinning of Li_2S has been limited to inert electrospinning devices or the use of Li_2SO_4 as the precursor, which can be reduced to Li_2S by a carbon source and hydrogen, respectively.[55,92] Li_2SO_4 has the advantage of high stability against oxygen and moisture. As a drawback, the solubility of Li_2SO_4 is almost exclusive in aqueous solutions, which is a limiting factor in the choice of polymer for the electrospinning process.

By using different precursors instead of Li_2SO_4, Ye et al. achieved Li_2S/C fibers with high mass loading (72 wt%) by electrospinning a Li_2SO_4/PVP precursor solution under inert conditions. The disadvantage of this synthesis route is that precursor and material must always be under inert conditions, compared to the here presented molecular precursor.[93]

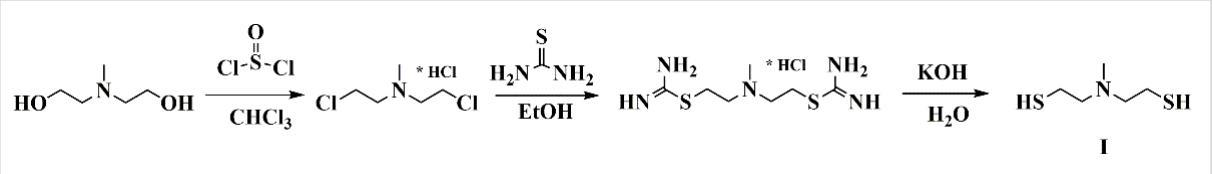

Figure 16: Synthesis of the ligand N-Methyldiethanthiolamine **I** ($(HSC_2H_4)_2NMe$). Reprinted with permission from[94].

Using presynthesized compounds combing lithium and sulfur already at a molecular level shows the advantages of preformed Li–S bonds and the opportunity to shield and protect the sensitive Li–S unit against oxidation by introducing a suitable ligand. This can be done by combining the dianionic, tridentate SNS ligand system ($(HSC_2H_4)_2NMe$) (Figure 16) with a suitable lithium source (e.g., butyllithium). The stabilizing properties and clear thermal decomposition of this ligand system have already been reported before in molecular precursor synthesis of transition metal dichalcogenides (TMDCs).[94,95] To overcome the current limitations in the synthesis of Li_2S electrospun fibers, a molecular approach towards a stable synthesized precursor can potentially guide the way to a successful composition. This molecular precursor enables the electrospinning of lithium sulfide-based fibers under ambient conditions from a single precursor solution, which is not limited to only aqueous solutions, ensuring a simple preparation of Li_2S/C nanofibers.

3.3.2 Sodium-ion batteries

The central part of this section is published in the following review article, which includes the writing of the following specific section and compilation of the graphics related to graphene-based anodes for sodium and potassium-ion batteries. For the reproduction in the thesis/dissertation as an author, permission is not required [13]*:*

Hong, Z., Maleki, H., Ludwig, T., Zhen, Y., Wilhelm, M., Lee, D., Kim, K.-H., & Mathur, S. New insights into carbon-based and MXene anodes for Na and K-ion storage: A review. *J. Energy Chem.* 62, 660–691 (**2021**).

Na-ion batteries and K-ion batteries are promising alternatives to vastly used lithium-ion batteries mainly due to the larger natural abundance of sodium and potassium resources. Carbon-based and MXene materials have received increasing attention due to their unique layered structure to accommodate the larger sodium and potassium ions. It's proposed that ionic size disparity (K^+: 1.38 Å; Na^+: 0.97 Å; Li^+: 0.76 Å) leads to sluggish intercalation and extraction kinetics in larger alkali metal ions. Nevertheless, the electrochemical inactivity of sodium intercalation in graphite suggests that different chemical properties of active materials and their interactions with carbon host and electrolytes are crucial for interfacial instability and irreversible capacity loss. Structural modifications by expanding interlayer spacing and defect engineering enable reduced diffusion barriers and enhanced insertion of sodium or potassium, but it blurs the electrochemical performance between the battery and capacitor.
The formation of thermodynamically unstable NaC_6 in graphite inhibits its potential Na-ion storage ability. The discrepancy of Na-ion size with respect to interlayer distance also reflects the poor efficiency of graphite as an anode material in sodium-ion batteries. Compared to the intercalation of Li-ions into a graphite host, the benefit of using few-layer graphene is mainly the larger interlayer distance between the individual carbon layers as the van der Waals interactions are weaker in few-layered graphene, also due to the presence of functional groups and defects. Furthermore, graphene-based materials have witnessed growing interest manly due to a higher gravimetric capacity and energy density favored by their high electrical conductivity, high specific surface area, and higher electrochemical activity for ion storage.[96,97]

The storage mechanism of Na-ions into graphene layers is still under research and it spawns a variety of advanced results.[98–101] Two known mechanisms for the storage of Na-ion in graphene-like host materials are referred to insertion and adsorption. The Na ion storage mechanism by adsorption is mainly driven by the presence of defects, nanovoids, and dopants.[102] In the case of sodium, the interlayer distance in graphite is unfavorable for the transition of Na-ions between the single carbon layers, which has been reported earlier.[97,103] Previous studies confirmed the formation of NaC_{64} during electrochemical intercalation of sodium in graphite instead of the assumed MC_6 structure.[104] In general, the mechanism of pore filling occurs at lower voltages (~0.1 V), while the insertion of Na ions between graphene layers takes place at higher voltages around 0.6 V from CV curve and displays capacitive-controlled behavior with slop sodiation potential profiles.[105–108]

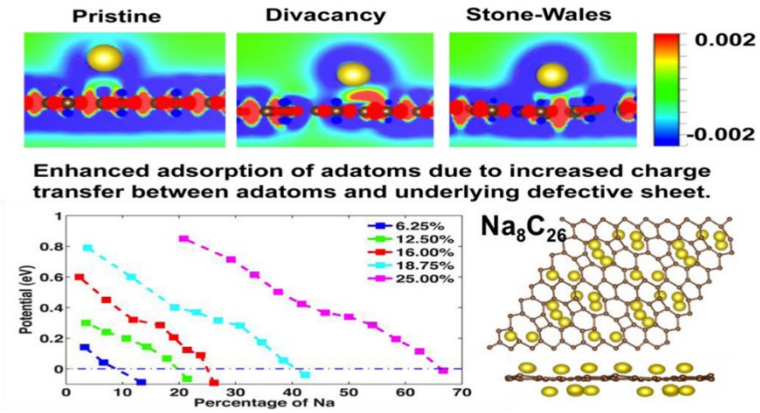

Figure 17: Adsorption of Na on graphene with divacancy and Stone-Wales defects in graphene. Reprinted with permission from [109]. Copyright 2014 American Chemical Society.

A single layer of pristine graphene showed lower adsorption of Na-ions on the surface compared to defect-rich materials, due to lower charge transfer between the graphene plane and the alkali metal ion. The adsorption and, therefore, the reachable capacities are affected by the presence of voids. DFT calculations indicated that divacancy and Stone-Wales defects with a higher charge transfer results in a capacity of 1450 mAh g^{-1} and 1071 mAh g^{-1} (Figure 17).[102,109] Despite the high insertion of the ions, the performance of these materials lacks high columbic efficiency.[110] Interestingly, depending on the synthesis route or even more on the quality of graphene, a different Na^+ storage mechanism can be observed. Graphene, which was synthesized at lower reaction temperatures, is comparable with reduced graphene oxide (rGO) in quality, storage mechanism, and electrochemical performance. Higher reaction temperatures yielded highly reduced graphene oxide that displayed an interlayer distance of 0.38 nm, which is beneficial for Na^+ insertion.[111] An interesting piece of work in the

field of sodium ion storage into rGO anode material was reported by Wang et al.[112] demonstrating a reversible capacity of 174.3 mAh g^{-1} at 0.2 C and 93.3 mAh g^{-1} at 1 C after 250 cycles. Due to higher electrical conductivity, with larger interlayer distances and a disordered structure, rGO enabled the storage of Na-ions and an irreversible loss after the first cycle. Similar to Li-ion batteries working with carbon-based anode materials with the formation of a characteristic SEI layer after the first cycle, a cathodic peak near low-voltage of 0.01 V is proposed in the adsorption of the ion to the active site of the host material.[112] Additionally, rGO-based anode materials are highly flexible and get along without any binder or conductive additives, which is practicable for battery applications.[58,111] Kang et al.[113] reported a high capacity of 930 mAh g^{-1} with the use of expanded graphite oxide (GO) as anode material. Furthermore, they studied the influence of different oxygen-containing functional groups like hydroxyls, carbonyls, and epoxides on the electrochemical properties to figure out that only epoxide groups with the absence of other oxygen functional groups enhances the electrochemical performance, mostly by the intercalation storage mechanism of Na^+.[109,113]

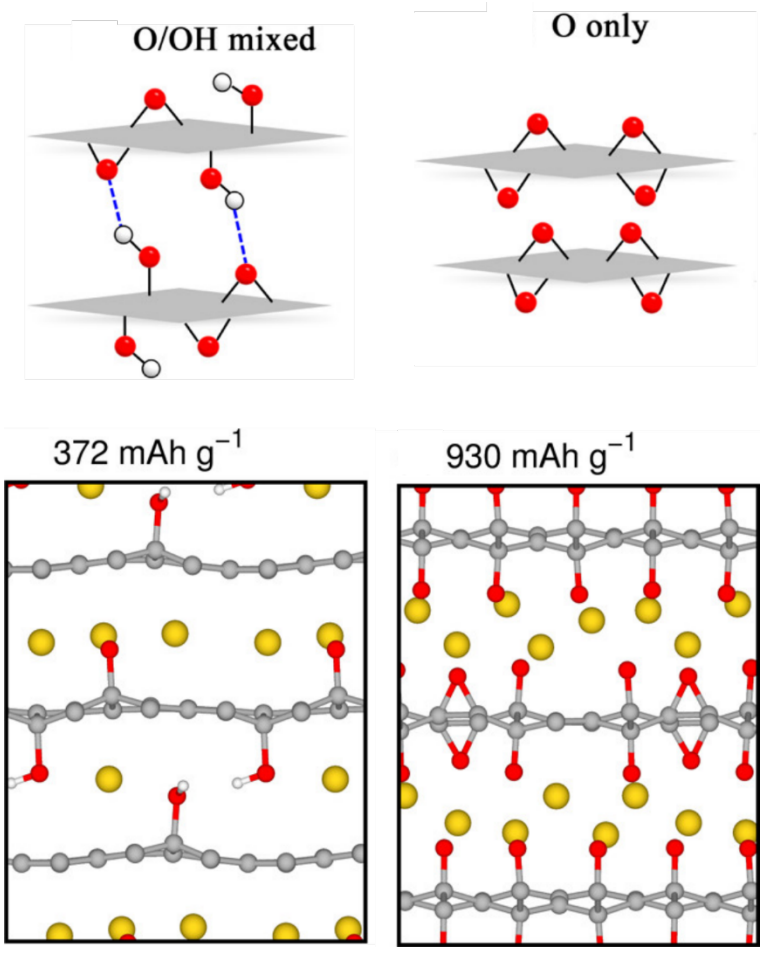

Figure 18: Fully sodiated stages of GO structures of 1:2 epoxide/hydroxyl mixed structures with a ration of 12.5% and the epoxide-only structure with an O/C ration of 50.0%. Yellow, red, white, and grey balls represent Na, O, H, and C atoms, respectively. Adapted with permission from [113]. Copyright 2015 American Chemical Society.

Heteroatom doping with atoms such as N, P, S, B, and F demonstrated a significant enhancement of electrochemical performance owing to the so-called pseudocapacitive action of the electrode material. In this mechanism, the doped surface acts as an electron donor to attract protons. Furthermore, the adsorption of alkali metal ions can be distinguished by surface hydrophilicity, charge transfer, and electrode-electrolyte interaction.[114–117] More recently, DFT calculations by Nijamudheen et al.[118] suggested that fluorine substitution at the uppermost layer of few-layer graphene not only modifies the electronic structure but also enables the thermodynamically favorable binding of Na within the carbon layer (Figure 19). Besides, the viability of K-ion intercalation into the graphene layer was also reported.[118] This study demonstrated the potential of graphene-based materials for metal-ion storage by heteroatom doping strategy and provided the fundamental guide for the structural design of carbon-based electrode material.

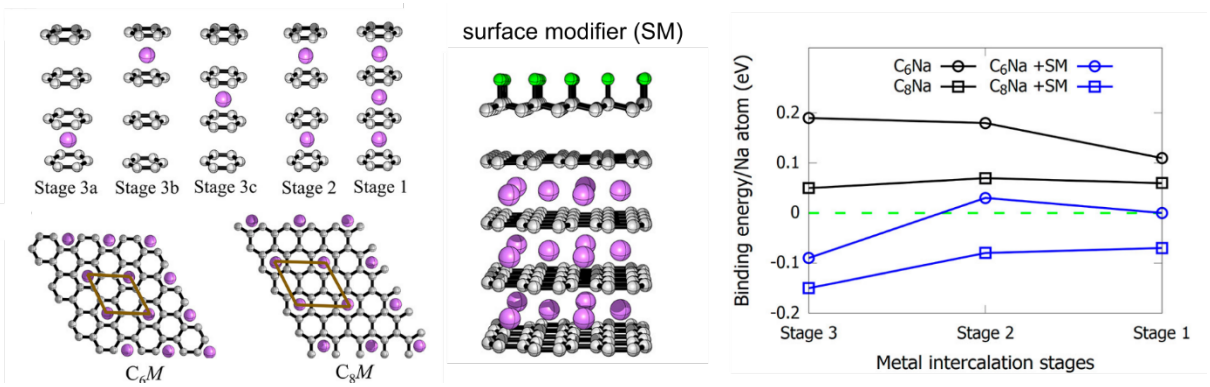

Figure 19: Models used to study the sodium intercalation chemistry in a four-layered graphene anode and the metal intercalation of 4LG with surface modifier (hydro fluorinated graphene. Adapted with permission from [118]. Copyright 2020 American Chemical Society.

In the case of nitrogen doping, the most commonly used dopant that can be easily integrated with three different types of nitrogen bonding to carbon atoms have been detected and designated as graphitic-N, pyrrolic-N, and pyridinic-N. An idea for this explanation of the improved electrical conductivity was given by Panchakarla et al., employing calculations of the electronic structure with the difference of the electronic bands within 1 eV of the Fermi energy. They revealed that doped graphene has the potential to exhibit the fascinating properties of pristine graphene justified by a positive shift of the Fermi energy at the apex of the Brillouin zone of graphene.[119] Especially, N-substitution enhances the electrical conductivity of the carbon structure by an additional fifth electron, donated by nitrogen, leading to strong valence bonds with carbon atoms and a higher positive charge.[120,121] Additionally, the density of states

calculations supports the high-rate capability of the doped graphene and suggests a metallic character for the $C_{46}N_3$ configuration, which is favorable for fast electron/ion transfer, superior rate capability, high capacity, and long cycling life for SIBs.[122]

It is known that pyridinic-N enhances the electric conductivity by raising the density of p states near the Fermi level and, hereinafter, the transfer of Na^+, leading to the improvement of the rate capability of the electrodes.[123,124] More recently, Huang et al.[125] prepared carbon nanosheets with high content of pyridinic-N and illustrated the enhanced Na (K) storage ability when compared to pyrrolic-N, as presented in Figure 20a.

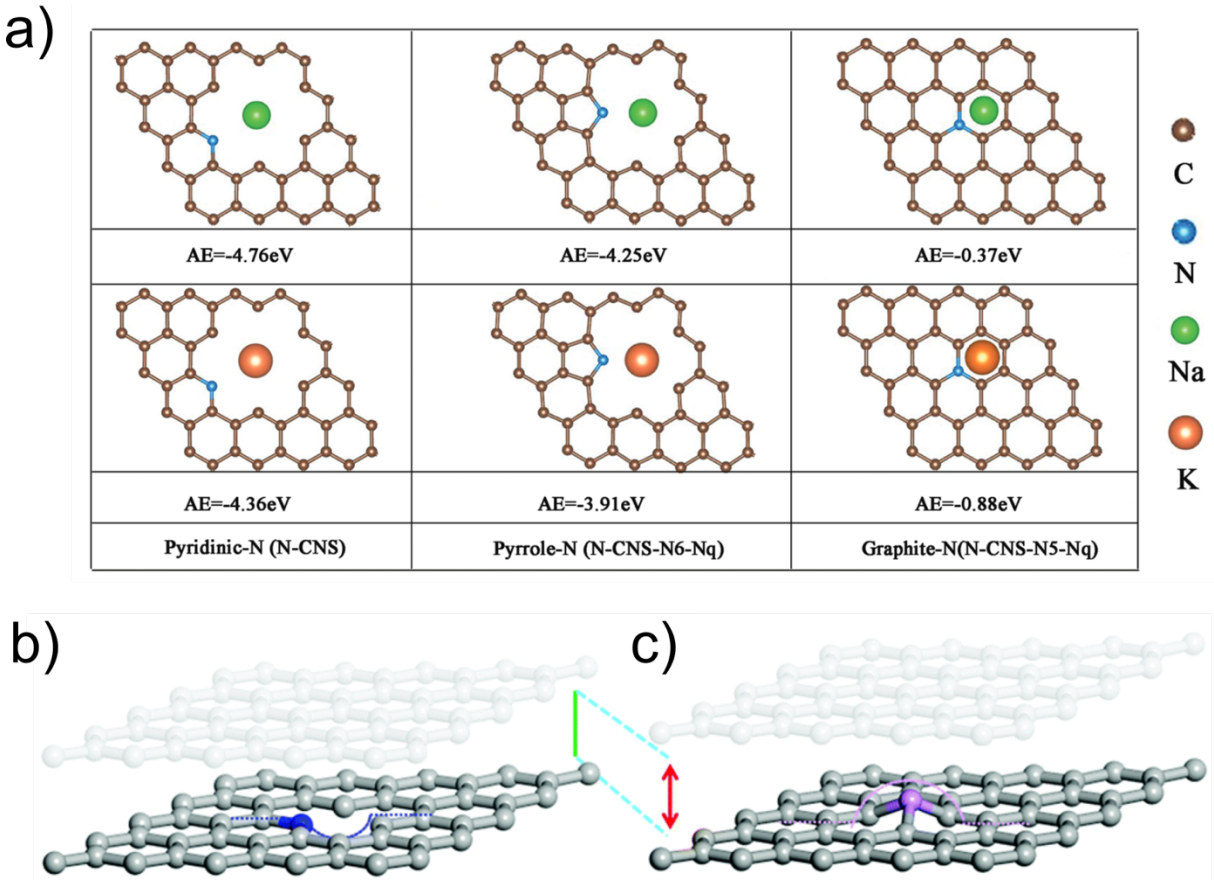

Figure 20: a) Schematic illustration of the three main bonding configurations of nitrogen in N-doped graphene and the different interaction of Na^+ and K^+ with the 2D structure based on the adsorption energy. Reproduced with permission from [125]. Copyright 2020, Wiley-VCH. b) An in-plane 'hole' defect produced by pyridinic nitrogen-doping (blue) and c) an out-of-plane 'protrusion' defect through phosphorus substitution (pink). Reproduced with permission [126]. Copyright 2017, Royal Society of Chemistry.

In this study, the defect structure further boosted the adsorption ability of metal ions. The adsorption energy of sodium(potassium) for pyridinic- and pyrrolic-N-doped carbon surfaces are 4.76 eV (4.36 eV) and 4.25 eV (3.91 eV), which are larger than

graphite N-doped structure of 0.37 eV (0.88 eV). Finally, this strategy enabled a high-performance carbon anode with unexpectedly high-rate capability and long cycling life of over 10,000 cycles due to the modification of local charge density distribution.

Graphene doping with sulfur yielded, besides the larger interlayer distance, two benefits for their usage as sodium anode material. Firstly, by exchanging carbon atoms with sulfur atoms, the highly ordered structure and translational symmetry in graphene were disordered, which led to a large number of active sides.[127] Secondly, the C-S-C interactions can react under a step-wise redox reaction with Na-ions at higher potential with the redox couples of 1.1/1.7 V and 1.6/2.0 V to form Na_2S_2 and Na_2S. The existence of the C-S-C bonding interactions before and after cycling was proved by XPS measurements and indicated no disruption in the chemical interactions.[123,127] Besides, the reaction between S and Na is significantly more reversible than that between O and Na.[127] Furthermore, covalent S-doping created nanopores that enabled a z-axial Na-ion diffusion pathway beneficial for the active sites that led to improved electrode kinetics.[128]

Phosphorous doping is another robust strategy to improve the structure and properties of graphene anode for NIBs.[129,130] Remarkably, it has an interesting electronic and structural effect when compared with N doping. Yang et al.[126] compared P- and N-doped graphene anodes showing an out-of-plane ‘protrusion’ and an in-plane ‘hole’, respectively. P-doped graphene anodes showed a remarkably higher electrochemical performance compared to N-doped graphene electrodes due to the much larger interlayer spacing. As displayed by the shadowed and solid layers (Figure 20b and c), the distance between the layers for the P-doping type was increased due to the introduction of a nonplanar configuration sandwiched between them, leading to an increased (0002) spacing and more Na^+-insertion active sites. Phosphorous atoms have a longer P-C bond length (1.76 Å) compared to N-C bonds (1.40 Å) as well as to the C-C bonds (1.38 Å), resulting in the puckering of the defect sites forming a quasi-trigonal pyramidal type, where the P atom is sitting 1.54 Å out of the plane. This configuration is more stable than the in-plane one, and the formation is driven by the rehybridization of the p_z states of the vacant C sites.[126]

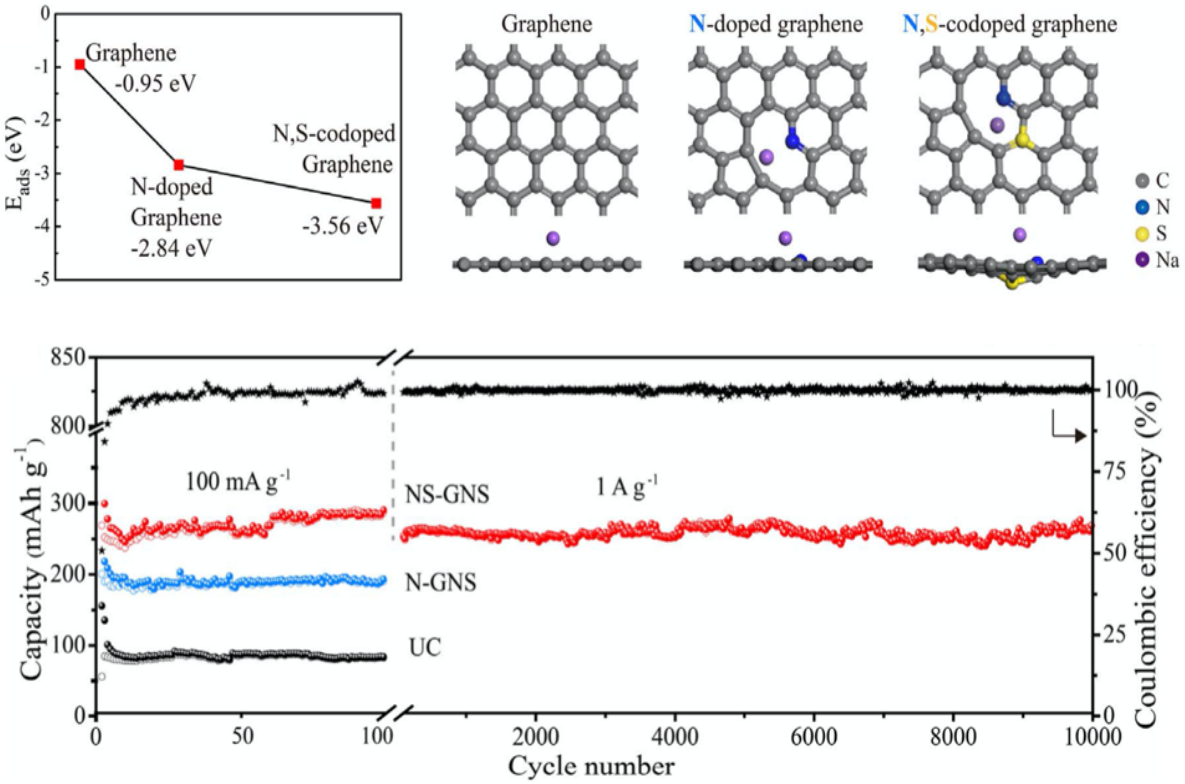

Figure 21: Adsorption energy of sodium electrochemically adsorbed onto the surface of the pristine graphene, N-doped, and N/S-co-doped graphene, along with corresponding geometry configurations (top). Electrochemical measurements of the undoped, N-doped, and N/S-co-doped materials and additional long-term cycling performance of the co-doped graphene (bottom). Reproduced with permission from [131]. Copyright, 2018 Elsevier.

Consequently, the P-doped graphene electrode displayed a higher capacity and faster energy storage with 210 mAh g^{-1}, while the N-doped graphene delivered only 52 mAh g^{-1} at 500 mA g^{-1}.[126] Furthermore, supported by in situ TEM performed during the charging/discharging cycles, they demonstrated the differences in the mechanism especially given by the insertion/exertion of Na-ions in addition to the surface adsorption at the 'protrusions' in graphene electrodes; whereas only Na-ion adsorption can take place on the surface of the N-doped graphene. One challenge in doping the graphene sheets when using graphene oxide as starting material lies in the presence of the oxygen-containing functional groups that invariably remain on the surface, even after strongly reductive treatment and thermal treatment at 700°C, which leads to an irreversible loss during the first cycles due to the formation of the SEI layer. Co-doping strategy with two different heteroatoms had also been tested for the improvement of the electrochemical behavior, for instance, by doping graphene nanosheets with nitrogen and sulfur via polymerization and carbonization method, and good electrochemical values were achieved.[123,132,133] Besides the expanded interlayer distance, the co-doping induced defects that eased the transfer of Na^+ and reduced the diffusion barrier.[123]

Ma et al. [131] investigated the adsorption energy of N/S-co-doped graphene and found that the N-doped species exhibited a lower negative value compared to the pristine graphene (Figure 21 (top)). For the N/S-co-doped graphene, even a lower value was determined, which is muchly favorable for the redox reactions located at/nearby the dopants. Further, N-doping introduces in-plane 'holey' defects, where Na ions can be adsorbed on the surface of the graphene network similar to the chelation in crown ether type ligands, which creates a spacious reservoir for storing more charges. Electrochemical measurements resulted in an increasing trend of the capacities from undoped to co-doped graphene (90 mAh g^{-1} for the undoped, 200 mAh g^{-1} for the N-doped, and 260 mAh g^{-1} for N/S-doped graphene after 100 cycles), which affirmed the similar trend to higher adsorption of Na ions on the surface driven by the different adsorption energies of the materials.[131] Coexisting of amorphous P and N dopants on the surface of graphene demonstrated an ultra-stable cyclic performance and excellent rate capability (809 mAh g^{-1} at 1500 mA g^{-1}) was achieved. In this system, the benefits of nitrogen and phosphorous doping were combined to create a highly conductive, defect-rich, and P-active graphene layer. Compared to the earlier described adsorption mechanism, the intercalation of Na^+ is suggested as a conversion reaction to form Na_3P.[122,134] Similarly, the co-doping of B, N has a synergistic effect, and its electrochemical performance is enhanced than that observed in single heteroatom doping.[135,136] Further, by changing the morphology of the co-doped graphene layers into nanotubes, fast diffusion kinetics and capacitive-controlled behavior, leading to an overall improved electrochemical performance, have been reported.[135] DFT calculations of the interaction of sodium atoms with boron and nitrogen-doped epoxy-graphene postulated an enhanced attraction of the doped materials compared to the pristine epoxy- graphene driven by the negatively charged epoxy group, however this model was not validated so far by experimental studies.[137,138]

3.3.3 Rechargeable magnesium batteries

The demand for safe energy storage systems with high energy density and long cycle life is growing up more and more. Among different monovalent alkaline and bivalent alkaline earth metals, magnesium has the highest theoretical volumetric capacity (3,833 mAh cm^{-3}) and outperforms the global player lithium in direct contrast. Magnesium keeps up in terms of gravimetric capacity and meets the demand of sulfur as one of the promising counter cathode materials for the next generation batteries, such as Li-S, Na-S, or Mg-S (Figure 22b).

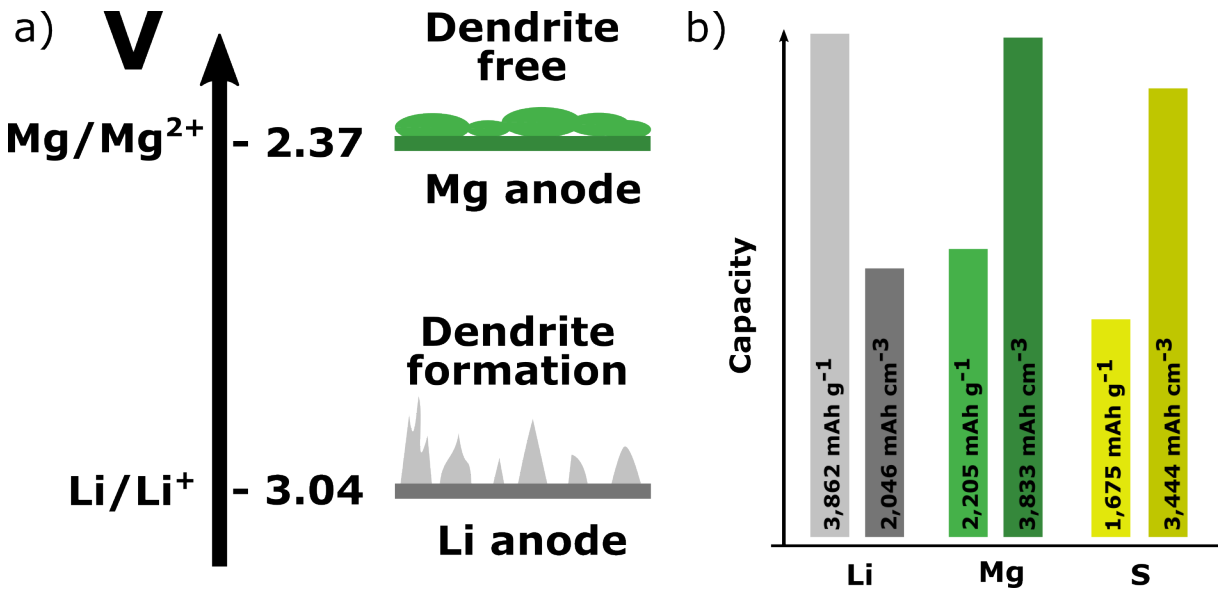

Figure 22: a) Standard redox potentials of magnesium and lithium and their electrochemical behavior as the metallic anode. b) Gravimetric and volumetric capacities of lithium, magnesium, and sulfur.

Secondary magnesium batteries have been regarded as promising candidates for large-scale storage systems with high safety, high energy density, and low production costs.[139–142] Furthermore, compared to lithium, magnesium is more available and much more accessible due to its higher abundance in the earth's crust, e.g., as carbonate derivates such as $MgCO_3$ (magnesite) and $CaCO_3 \bullet MgCO_3$ (dolomite). This is an essential advantage in cost and sustainability.[143,144] The environmental impact of using 'green chemicals', recycling, and a small carbon footprint plays an essential role in terms of battery production and sustainable energy harvesting and storage. Magnesium-based batteries could address these properties in the near future.[1] As Mg batteries are in their initial steps, different bottlenecks of the electrolyte and the cathode

materials must be addressed, considering the earth's abundance of the needed elements in the battery (Figure 23).[145]

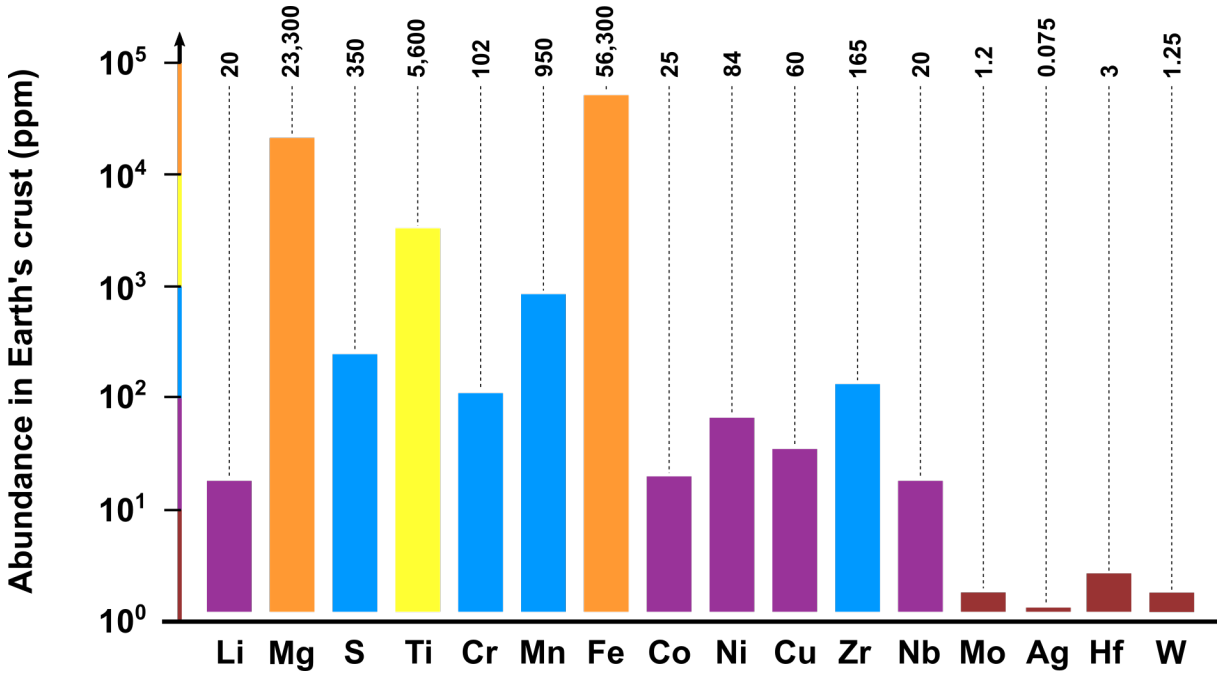

Figure 23: Abundance of Li, Mg, S in earth's crust and selective transition metals.

However, magnesium batteries profit from the use of a metal anode due to the dendrite-free deposition of magnesium ions. The dendrite-free deposition compared to elemental lithium can lead to a safe operation combined with a high negative reduction potential of -2.37 V vs. the standard hydrogen electrode, as illustrated in Figure 22a. The magnesium battery has a lower reactivity with air and rapid formation of a passivation layer MgO.[146,147] In addition to the challenge of finding suitable liquid or solid-state electrolytes, the hunt for viable cathode materials is a crucial success factor for battery fabrication. Beside the chevrel phase (Mo_6S_8), the interest in metal sulfur cathode materials is rising.[141,148–150] Depending on the transition metal, the reversible electrochemical reaction undergoes an intercalation or conversion reaction mechanism.[28,151] The systematic screening of transition metal sulfides as cathode materials for rechargeable magnesium batteries and the discussion of their mechanistic reactions is of great interest. Especially the influence of the crystal structure on the electrochemical performance of the host materials is significant for designing new electrodes. A sluggish diffusion of Mg^{2+} and slow kinetics led to elevated operation temperatures for Mg-ion batteries or require nano-structuring of the electrodes.[152] Even when the mobility of Mg^{2+} is accelerating with increased temperature, drawbacks in practical

application and disadvantages of, e.g., parasitic reactions hinder the commercialization.[148]

However, in order to realize rechargeable magnesium battery technology, a remaining challenge is to identify efficient cathode materials that are able to generate high voltage and energy capacity.[153] Aurbach was the first researcher who published a viable cathode material based on Mo_6S_8 in 2000. Based on an intercalation mechanism, Mo_6S_8 showed sustainable capacity retention when cycled vs. Mg^{2+}/Mg with a limited 1.4 V output voltage.[139]

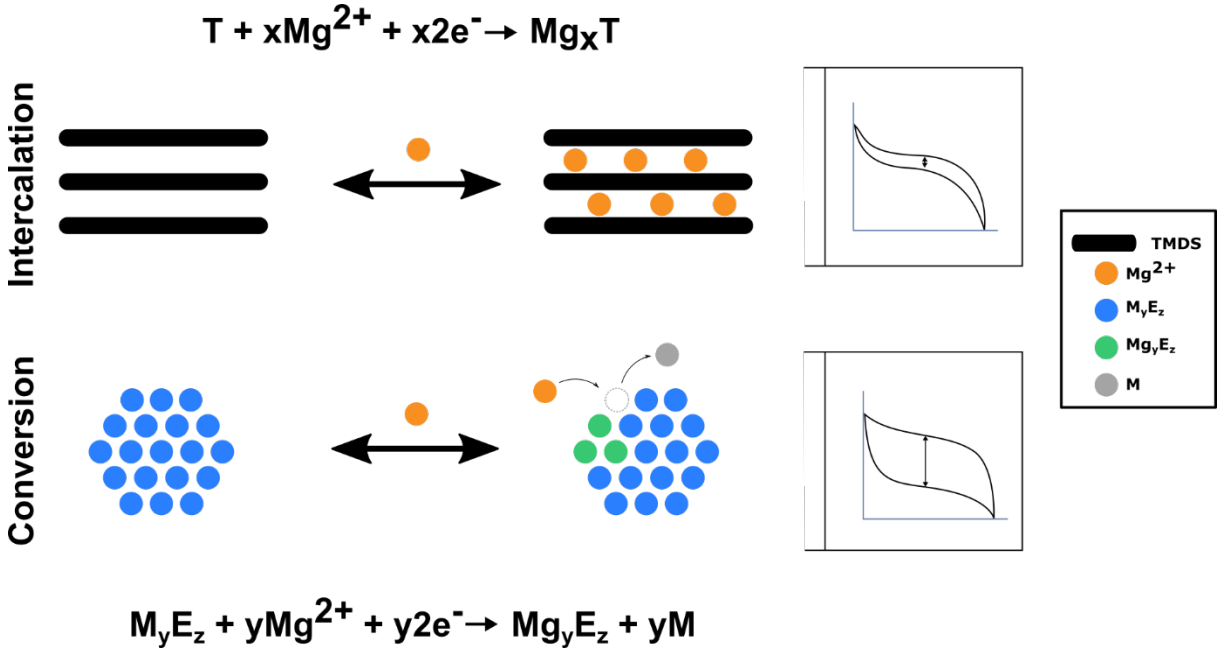

Figure 24: Schematic illustration of the intercalation (top) and the conversion (bottom) electrochemical reaction and their voltage profiles (right) for magnesium batteries.

Enhanced performance of the battery is possible when the cathodes include materials that exhibit higher theoretical capacities. Modern research of improved and suitable cathode materials for LIBs have driven the focus to the development of sulfur as active material in the cathode due to its high natural occurrence and theoretical gravimetric capacity (1,675 mAh g^{-1}).[154] Further, it is non-toxic and paired with a Mg metal anode, it offers a theoretical energy density of over 3,200 Wh cm^{-3}, based on the two-electron conversion reaction of $Mg^{2+} + S + 2\ e^- \rightarrow MgS$, which yields a theoretical cell voltage of 1.77 V.[141] MgS has a hypothetical power density of 46 Wh kg^{-1}.[155] Recent drawbacks of utilizing elemental sulfur as active material are the formation and dissolution of polysulfides in the electrolyte causing the failure of the electrochemical cell.[156,157] Sulfur-based compounds have the advantage that, based on the bonded metal, the material

can undergo a reversible intercalation or conversion reaction. The conversion vs. the intercalation mechanism for magnesium batteries is illustrated in Figure 24.

The advantages of this mechanism are higher capacities and higher energy densities. This mechanism also suffers some drawbacks, e.g., in the significant voltage difference between charge and discharge, resulting in poor efficiency and lower operating voltage compared to intercalation-based materials.[1] The structural deformation of the electrode material as a result of the conversion of the metal-based compound to the elemental form of the metal causes the dissolution of intermediates in the liquid electrolyte.

Especially for Mg^{2+} as the active ion, the conversion type reaction is thermodynamically favored and may circumvent the sluggish insertion and diffusion kinetics to go beyond intercalation chemistry.[152] In 2007, Amir et al. reported that for chalcogen cathode materials, e.g., layered Ti_2S_4, cubic Ti_2S_4, CuS, CoS, NiS, TiSSe, NiSSe, in a nonaqueous magnesium battery, the electrochemistry variates from intercalation and displacement reactions depending on the active material.[158]

One of the most promising candidates as a conversion-type cathode material is sulfur. The redox coupling of Mg and S is emerging in more and more interest due to their high abundance with high theoretical energy densities during the reversible reaction.[141,159–161] First investigation based on a sulfur cathode paired with a Mg-metal anode and a Mg-based electrolyte was made in 2011, showing the compatibility of the system.[162]

The first principal studies of the mechanism were reported by Robba et al. showing a multiple-step conversion of sulfur to polysulfides (high-voltage plateau) and polysulfides to MgS (low-voltage plateau) in a glyme-based electrolyte. This general mechanism is schematically shown in Figure 25.[163]

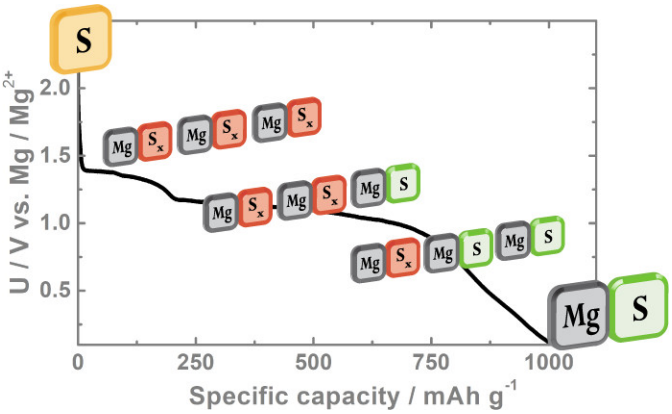

Figure 25: Mechanistic study of a magnesium-sulfur battery discharge. Reprinted with permission from [163]. 2017 Copyright American Chemical Society.

Interestingly, they could further show with investigations in XANES, RIXS, and NMR studies, that MgS discharges in a tetrahedral environment. This is particularly interesting since the chemically synthesized MgS crystallizes in octahedral coordination of magnesium in the well-known rock-salt structure. Robba et al. also showed the absence of diffraction peaks of MgS crystallized in the rock-salt structure during in-operando XRD, whereas they mentioned that MgS is present in another form of either nanoparticles or still in an amorphous form. Further investigations by RIXS and XANES showed differences in the electrochemically formed structure of MgS compared to the chemically synthesized MgS, but it was pointed out that a cubic phase has formed.[163] It was further predicted that the chemical shift observed by solid-state NMR is more similar to the MgS-wurtzite structure than to the MgS-zinc blende.[163]
The formation of nanocrystalline MgS is also supported by the observations made by Vinayan et al. by in-operando Raman spectroscopy.[164]

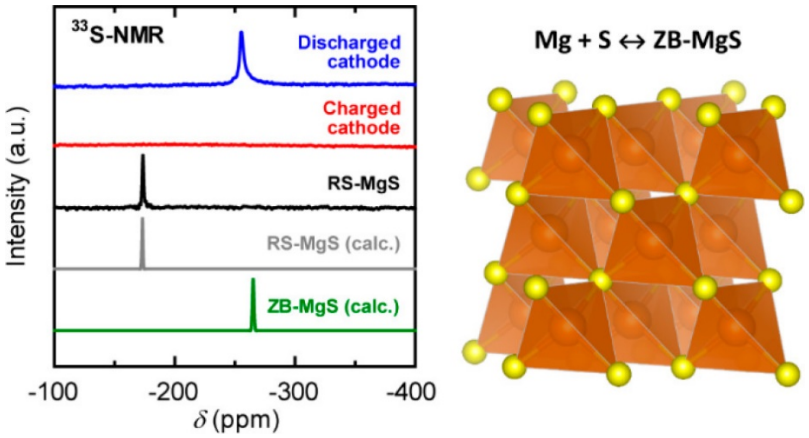

Figure 26: Solid-state ^{33}S-NMR of charged and discharged stages of a magnesium sulfur battery. Reprinted with permission from [165]. 2018 Copyright American Chemical Society.

Contrary to that, Nakayama et al. reported the zinc blende structure of the discharged MgS product by using similar characterization techniques, mainly ^{33}S-NMR (Figure 26). Moreover, they predicted no observation of the wurtzite structure. Even from starting with commercially available rock salt MgS, it was indicated that a much smaller electrochemical activation was observed, and a lower capacity was yielded. Further, the study resulted in an irreversible structural change regarding sulfur, which could not be observed as crystal phase in the XRD diffractometer after charging. The influence of the amorphous phase after the first cycle was further investigated by *ex situ* HE-XRD and pointed out that no S-S binding distances could be observed, indicating that the charged cathode does not return to the ordered S_8 structure for S_8

clusters or crystals.[165] Nakayama et al. described the mechanism as followed. During the initial cycle, Mg reacts with S_8 in a solid-state reaction, forming MgS_8 in the first step. In the second step, MgS_4 is formed by the further reduction of sulfur, which dissolves into the electrolyte. As the polysulfides are dissolved in the electrolyte, further reduction takes place to the final discharged product, whose microstructure is zinc blende MgS. In the charging reaction, the formed MgS in the zinc blende phase is oxidized completely to form amorphous sulfur or polysulfides.[165] Similar reaction mechanism was proposed by Zhao-Karger et al. Further, the improvement of capacity and electrochemical performance were made by modification of electrolyte, binder, preparation method, and carbon additives (several ways).[166]

However, some mechanistic investigations were made in the past, but the developments in Mg-S batteries are in their early stages and suffer drawbacks in coulombic efficiency and short cycle life caused by the well-known polysulfide shuttle, like in lithium-sulfur batteries.[167]

Similar results were found by Xu et al., which further pointed out that some of the formed polysulfides are electrochemically inert, causing capacity a rapid capacity decay in the successive cycles and shortening the cycle lifetime of the cell.[168] These findings were reconditioned by a theoretical study by Richter et al., not only looking at the cathode side but also including reactions that are taking place at the anode.[169]

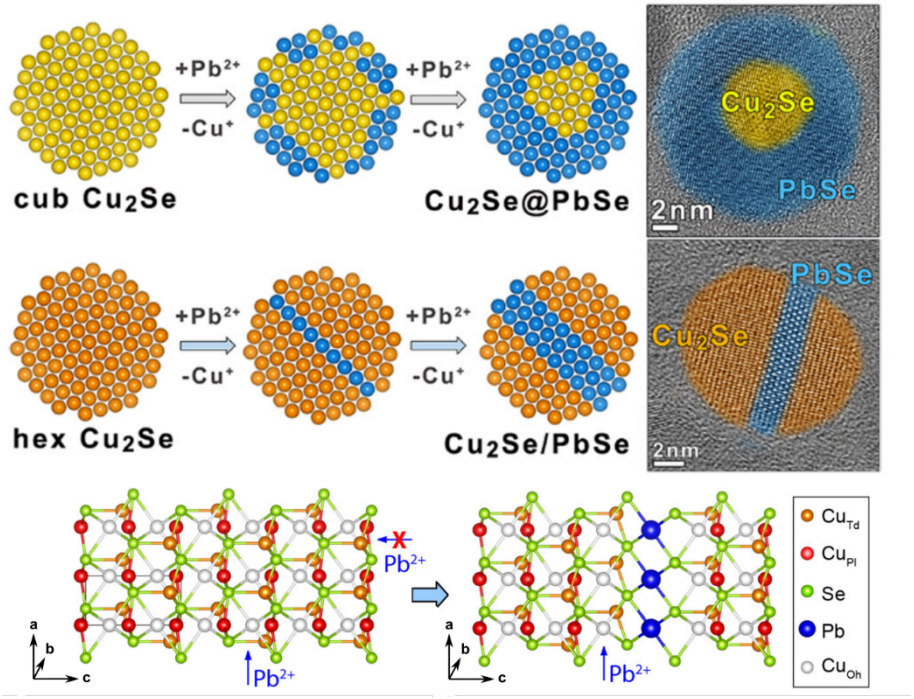

Figure 27: Crystal structure change depending on crystal structure This is an unofficial adaptation of an article that appeared in an ACS publication. ACS has not endorsed the content of this adaptation or the context of its use [170].

The fact that the role of the crystal structure for cation exchange is crucial has already been shown in the past. For example, Gariano et al. compared the cation exchange of Pb^{2+} with Cu^{+} starting from both the (metastable) hexagonal Cu_2Se and the cubic Cu_2Se phase. In their study, they could show that for both cases, the final crystalline phase was a cubic rock-salt PbSe structure (Figure 27). Interestingly, by starting from the cubic Cu_2S phase, PbSe nucleates randomly on the overall surface of the host material, which can be explained by the low diffusivity of Pb^{2+} ions coupled with the absence of preferred entry points in cubic Cu_2Se. While starting from the hexagonal Cu_2Se, Pb^{2+} ions could enter the nanocrystal along defined planes (*a, b*) to replace the host cations due to the almost empty octahedral sides of the Cu_2Se structure.[170]

For magnesium-based batteries, many researchers are recently in the search for suitable cathode materials with a high capacity, high energy density, high coulombic efficiency, and long cycle life. In this regard, oxygen and sulfur enable high theoretical capacities and energy densities. For oxygen, MgO or MgO_2 films lead to a large polarization and a highly irreversible capacity due to the poor thermodynamic and kinetic properties.[171]

Oxygen and sulfur, as cathode itself, follow the conversion type reaction mechanism. When oxygen or sulfur is bonded to a transition metal, forming a transition metal chalcogenide, an intercalation reaction is possible. For metal oxides, the intercalation is more likely observed than the conversion redox mechanism. Different types of layered (V_2O_5, MnO_2, MoO_3), spinel (Co_3O_4, Mn_3O_4, Mn_3O_4, $MgCo_2O_4$, $MgMn_2O_4$, $MgFe_2O_4$, $MgCr_2O_4$), and polyanionic ($MgMnSiO_4$, $(PO_4)^{3-}$, $(SiO_4)^{4-}$, and $(SO_4)^{2-}$) oxides materials have been investigated for LIBs and RMBs.[172,173] There energy densities for conversion-type and intercalation-type cathodes are compared in Figure 28a and b.

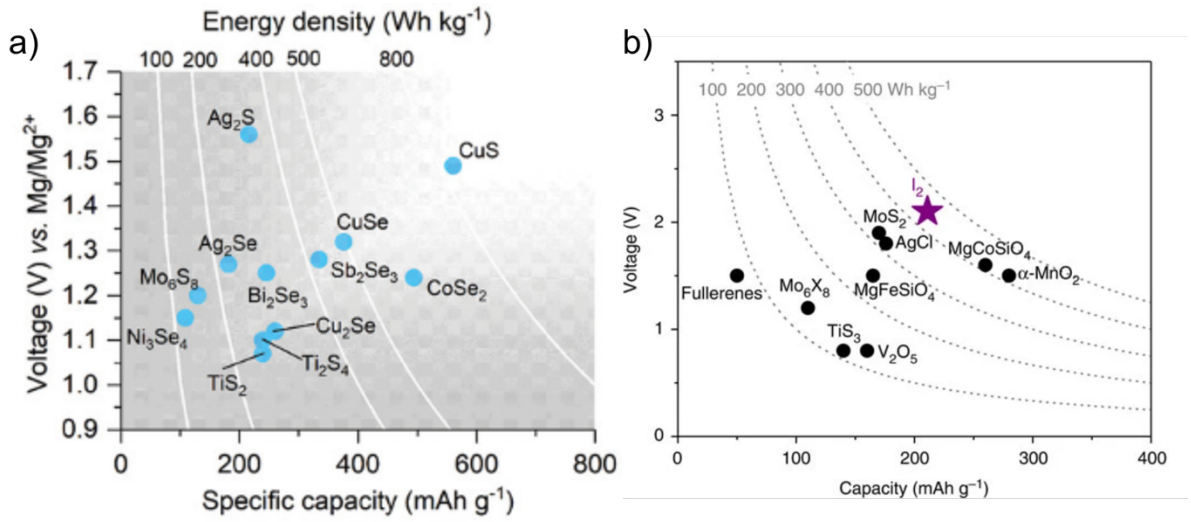

Figure 28: a) Theoretical operation voltages versus specific capacities of metal chalcogenide cathodes. Reproduced with permission from [148]. b) Reported energy densities of different cathode materials vs. Mg/Mg^{2+}. Reprinted with permission from [174].

Transition metal sulfides are the dominant metal sulfides as cathode material in rechargeable magnesium batteries, whereas the chemical bonds between the metal and sulfur are predominantly covalent in nature. The structure of transition metal sulfides depends on the interaction between the d-electrons of the metal with the p-electrons from the chalcogenide. Since the behavior of the d-electrons in solids differs between the oxides and sulfides, the d-electrons in chalcogenides participate in covalent binding, which reduces the formal charge on the transition metals.[175] These “softer” metal centers favor the formation of metal-metal bonds, which have an influence on the properties, e.g. enhancement of the electrical conductivity, of the metal sulfides.

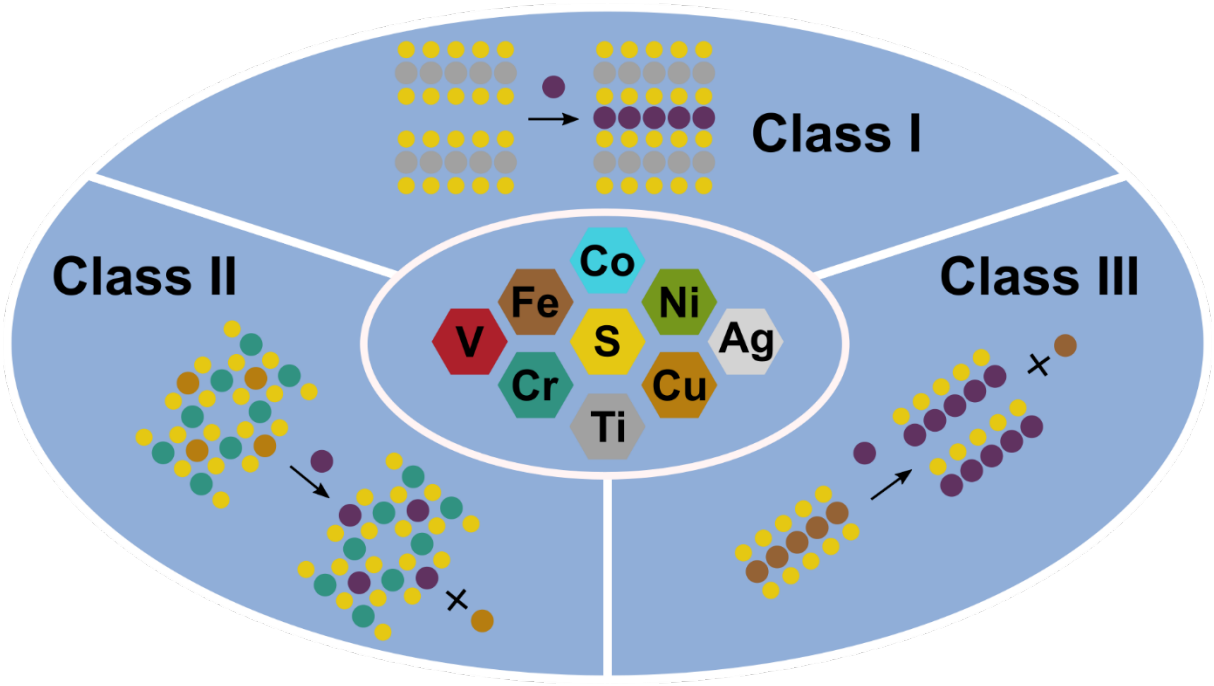

Figure 29: Overview of transition metal sulfide classes and their schematic working mechanism in rechargeable batteries.

In general, TMS can be divided into three categories based on their crystal structures namely: layered MS_2, thiospinels M_3S_4, and non-layered M_xS_y (Figure 29). The early transition metals in groups 4-7 (M = Ti, Mo, W, V, Zr, Hf, Nb, Ta, Tc, Re) can crystallize in layered structures that are stacked through van der Waals interactions, whereas the later transition metal sulfides in group 8-12 (M = Fe, Co, Ni, Cu, Zn) predominantly adopt non-layered structures.

Typically, the layered transition metal disulfides form covalent bonds between M and S consisting of a hexagonal layer of the transition metal atoms, which are sandwiched between two layers of sulfur atoms. The resulting atomic layer stacking of S-M-S is often referred to as mono- or single layer. Depending on the transition metal and the orientation of the sulfur atoms to the metal center, the layered MS_2 can be classified into different phases, namely, 1T, 2H, and 3R, which are further discussed elsewhere.[176] In this notation, the numeral donates the number of stacked layers in the unit cell, whereas the letter characterizes the lattices as trigonal prismatic, hexagonal, and rhombohedral.[177] In general, 2D transition metal sulfides can only exist when the valence state of the transition metal is +4 while the sulfur is in a -2 state.

For transition metal monosulfides, just as in transition metal oxides, a $3d^n$ manifold exists, which becomes more stable with respect to the 3s bands with an increasing atomic number until the shell is half-filled.

The larger covalency in the monosulfides implies greater screening of the cation electrons from their nuclear charge. This results in a small electrostatic energy. A smaller electrostatic energy results in a smaller transfer energy required for the formation of itinerant electrons, e.g., in TiS or VS. For heavier transition metal monosulfides, the d-band of d^{n+1} falls close to the top of the valence band due to the higher covalent characteristics. For CoS or NiS, this means that the σ^* bands have a reduced energy separation between high- and low-spin states. By moving further right in the periodic table, in CuS, a small value of the electrostatic energy brings the d^{10} manifold at a copper atom closer to the top of the valence band, which is why the valence state of the copper ions becomes ambiguous.[175]

3.3.3.1 Transition metal sulfide class I: layered sulfides

Among the transition metal sulfides, groups 4, 5, and 6 are known (except for Cr) to form layered structures with the common formula MX_2 (M^{4+} = transition metal, X^{2-} = sulfur). Those structures consist of S-M-S monolayers connected by weak van der Waals forces, meaning only every second gap in between the S-layers is occupied by a metal atom. The electron configuration of chalcogens in the valence shell can be expressed as $\mathrm{ns^2 p_x^1 p_y^1 p_z^2}$. The two paired electrons in the p_z orbital form a lone pair of electrons, which is chemically inactive, whereas the unpaired electrons in the p_x and p_y orbitals participate in the covalent bonding between the chalcogen and the metal atoms. The unoccupied gaps in the layered structure are possible hosts for other metals, such as Li or Mg, to intercalate.[178]

The coordination of the anions to the metal centers depends on the electronic structure of the transition metal, more precisely on the number of electrons located in the d-orbitals. Whereas the transition metals in the 4th group feature a d^0 configuration in an octahedral coordination sphere, the transition metals in the 5th group (d^1) can be found as both octahedral (d-electron in degenerated $\mathrm{d_{xy,\,xz,\,yz}}$) and trigonal prismatic (d-electron in $\mathrm{d_{z^2}}$). Group 6 elements (d^2) are primarily seen in trigonal prismatic geometry (both d-electrons filling $\mathrm{d_{z^2}}$). In the 7th group of the TMS, octahedral coordination is preferred (d^3). The octahedral splitting is preferred in d^0 because more orbitals have lower energy than in the trigonal prismatic. The different orbital splitting with respect to the Fermi energy is illustrated in Figure 30.

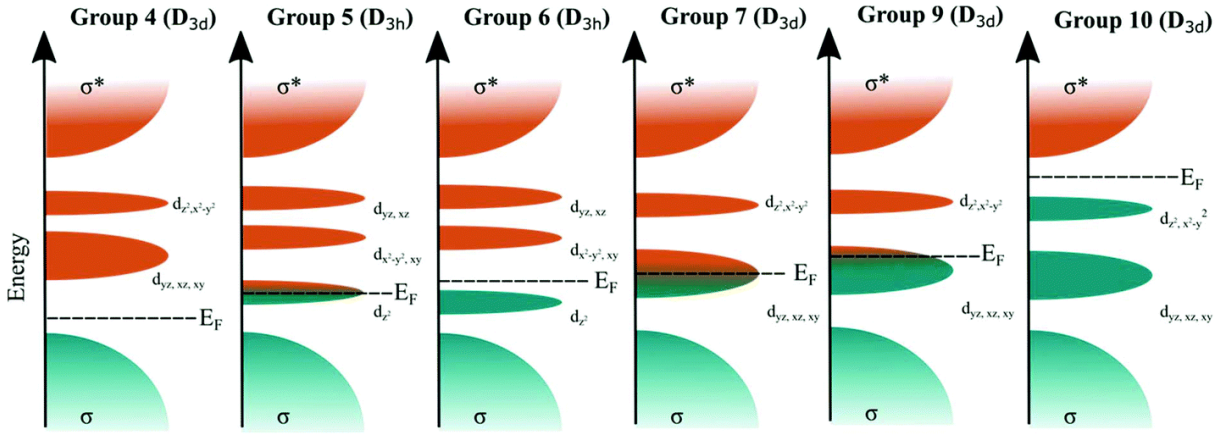

Figure 30: Schematic representation of the density of states due to d-orbital splitting of TMDCs (in parentheses the Schoenflies notation). The schematic representation is simplified and does not show accurate energy positions. Reproduced from [176] with permission from the Royal Society of Chemistry.

By having a closer look at the different phases of the TMS, in both the 1H (trigonal prismatic) and 1T (octahedral), the non-bonding d-bands are located within the gap between the bonding and antibonding bands of the M-X bonds. In an octahedrally co-ordinated transition metal center (D_{3d}), the orbitals split into t_{2g} (lower energy) and e_g (higher energy), whereas in trigonal prismatic coordination (D_{3h}), the orbitals split into a_1 (lower energy), e' (slightly lower energy) and e'' (higher energy) as illustrated in Figure 31. As a result, the different phases exhibit different band gaps.[179]

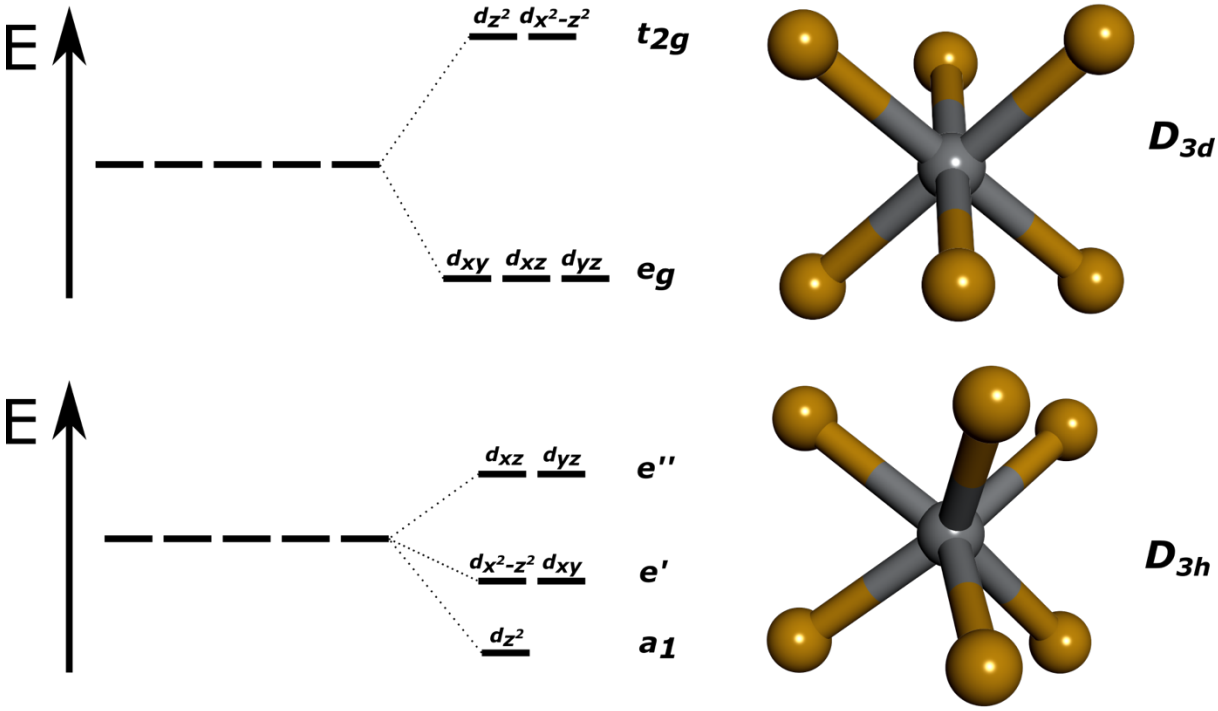

Figure 31: The atomic configurations of an octahedral (D_{3d}) and trigonal prismatic (D_{3h}) coordination and their corresponding energies due to their d-orbital splitting.

In most TMS, e.g., in MoS_2, the structural phase can be changed during the intercalation of alkali metals, which was also observed by the intercalation of Mg-ions in MoS_2, characterized by ex-situ XPS measurements of specific charge and discharge states (Figure 32).[180,181]

The phase change may be attributed to the change in the number of d-electrons occurring by the transfer of an electron from the s-orbital of the intercalated alkali metal into the d-orbital of the transition metal and a destabilization of the original phase.[179] Previous studies showed that the 1T phase of MoS_2 disordered at room temperature after intercalation of a cation. The driving force for such distortions in TMS is believed to be the 'Jahn-Teller instability' – in which the splitting of partially filled degenerate orbitals causes a reduction of the free energy.[182]

It was shown that the transition from trigonal prismatic (2H) to octahedral (1T) MoS_2 phase is possible by 0.2 Li^+ (corresponding to 0.1 Mg^{2+}) per MoS_2 unit.[183] This indicates that phase transitions are possible with intercalating Mg, just with a smaller amount because of its higher charge.[181]

Compared to monovalent working ions such as Li^+, Na^+, and K^+, the migration barriers for multivalent ion (Mg^{2+}, Ca^{2+}, Al^{3+}) diffusion can be reduced by changing the chalcogen anion. Using sulfur instead of oxygen as the chalcogenide, the increased covalency and larger volume per anion tend to decrease the electrostatic interactions between the working ion and the anion sublattice, thus reducing the migration barriers for Mg^{2+}.[184]

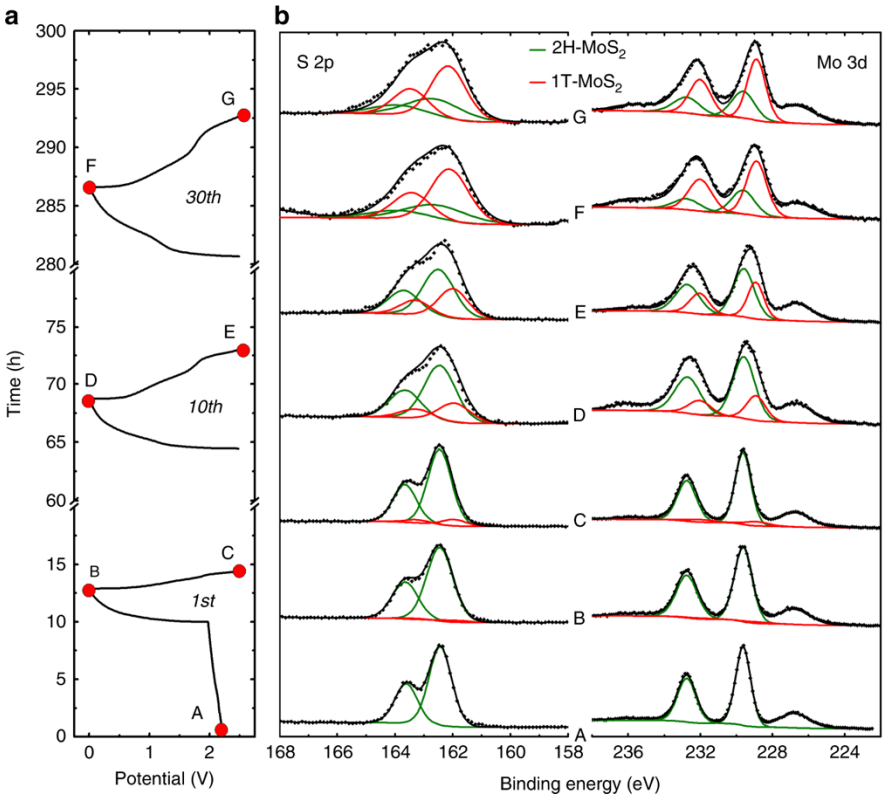

Figure 32: Ex-situ XPS analysis of MoS_2-carbon composite electrodes. a) Discharge/charge profile and b) the corresponding XPS spectra at specific stages. Reprinted with permission from [181].

Next to the electronic structure of an intercalation compound, the morphology and the size play essential roles in the intercalation behavior. It was shown by Yang et al. that MoS_2 nano ribbons obtain lower migration barriers for Mg^{2+} as comparable to bulk MoS_2. Mg^{2+} occupies either the octahedral (H) or tetrahedral (T) sites in MoS_2. Yang et al. investigated via the climbing image nudged elastic band method (determine the minimum energy path and saddle points between a given initial and final positions) that the diffusion of Mg^{2+} takes place between two adjacent T-sites through the nearest, energetic favorable H-site, leading to a zig-zag diffusions pathway (Figure 33).[185]

Layered MoS_2 as cathode material for rechargeable magnesium batteries could demonstrate cyclability vs. Mg/Mg^{2+} at relatively low current densities of 10-50 mA g^{-1}, achieving quite good capacities of 120-170 mAh g^{-1}.[186–188]

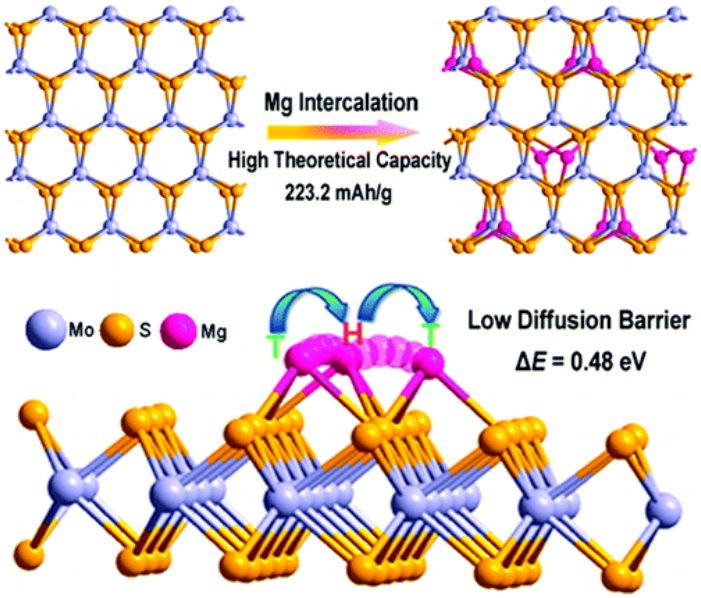

Figure 33: The intercalation of magnesium into MoS_2 resulting in a zig-zag diffusions pathway along the energetic favorable H-site. Reprinted with permission from [185]. Copyright 2012 American Chemical Society.

As known from lithium-ion batteries, layered TiS_2 is a suitable cathode material for the intercalation of Li-ions. Similar behaviors were investigated for Mg-ions which yield a capacity of 115 mAh g^{-1} at a C-rate of C/10 achieved by Sun et al. It is worth noting that evaluated temperatures (60°C) were necessary to achieve these values.[189]

The capacity could be further improved by the modification in structure, e.g., by changing the morphology to tube-like structures or the stepwise expansion of the interlayer distance from 5.69 Å to 18.63 Å. With these modified capacities of 236 and 239 mAh g^{-1} at current densities of 10 mA g^{-1} could be achieved. Moreover, at 60°C the expansion of the interlayer distances yields a capacity of 450 mAh g^{-1} at a current density of 24 mA g^{-1} due to the higher mobility evoked by low-migration energy barrier (0.18 eV) of the $MgCl^+$ (Figure 34).[190,191]

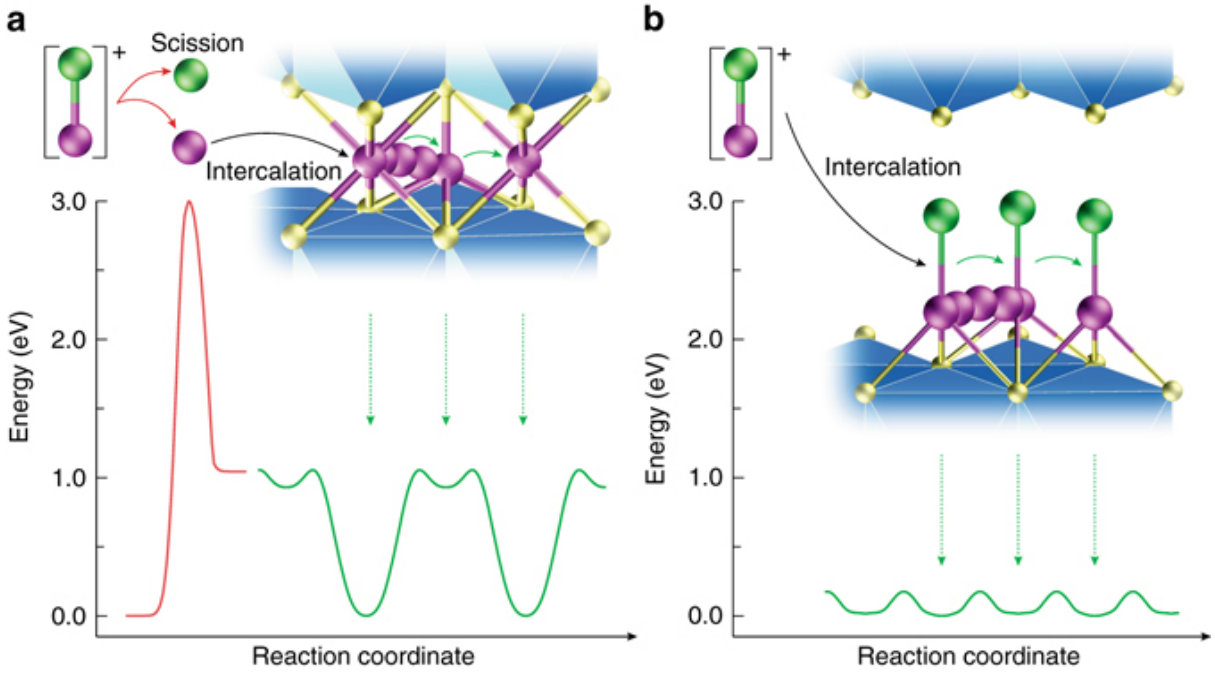

Figure 34: Energy diagrams and schematic illustrations for the intercalation of Mg^{2+} and $MgCl^{+}$ a) Activation needed and limited intercalation of Mg^{2+} (purple sphere) due to the scission of $MgCl^{+}$ ions into Mg^{2+} and Cl^{-} by small interlayer distance. b) Fast diffusion of $MgCl^{+}$ into the extended interlayers due to low-migration energy barrier. Reprinted with permission from [191].

Furthermore, layered vanadium sulfides (VS_2 and VS_4) could also be used as cathode materials for magnesium batteries. VS_2-nanoflowers with increased interlayer distance was achieved through a one-step solution-phase synthesis and in situ 2-ethylhexylamine intercalation process. This material was later tested under various current densities of 100 mA g^{-1} and 2000 mA g^{-1} vs. magnesium reaching capacities of 245 mAh g^{-1} and 103 mAh g^{-1}. Additionally, the nanoflower-like structure showed a stable cycle performance of 90 mAh g^{-1} at 1000 mA g^{-1} after 600 cycles.[192] Similar results were achieved by Jing et al., who could further improve the cyclability of VS_2 by using a hybrid Li^{+}/Mg^{2+} electrolyte.[193] By changing the morphology from nanoflowers to regular ordered plate-like nanosheets, higher capacities of 214 mAh g^{-1} at similar current densities were measured.[149]

For the familiar VS_4 layered structure, different attempts to use as cathode material for Mg-based batteries were performed. Compared to VS_2, where V_{ox} = +4 and S_{ox} = -2, it is evident that vanadium cannot come to an oxidation state +8, and therefore sulfur is forming dimeric structures of S_2 to maintain -2, while V_{ox} stays in +4. This allows the S_2^{2-} dimers to extend the coordination along the *c*-axis. These individual atomic chains of VS_4 are bonded by weak van der Waals forces. During the cycling process, the sulfur

dimers get partially reduced to S^{2-} while the V^{4+} oxidizes to V^{5+}, causing an irreversible loss after the first cycle because some Mg^{2+} remains in the lattice.[194]
Li et al. studied the influence of micro-morphology on electrochemical performance. Even here, flower-like structures showed the best performance with a capacity of 80 mAh g^{-1} at 50 mA g^{-1} and a 90 % capacity retention after 400 cycles.[195]
In the early 90s, the reversible insertion and extraction of Mg^{2+} into a ZrS_2 host material could be demonstrated by Gregory et al. surprisingly with a high cathodic voltage of 2.6 V and high capacity of 228 mAh g^{-1}.[196] Furthermore, recent studies have investigated ZrS_2 as cathode material for Li-ion systems. ZrS_2 prefers Li^+-intercalation electrochemistry at high operational voltages (~1.0 V), while at low discharge voltages (<0.3 V) the conversion reaction to Zr + 2 Li_2S (discharged) and ZrS_2 nanodomains (charged) is favored.[197] Similar has to be studied for Mg-based batteries.
Finally, WS_2, a typical 2D graphene-like material, has the potential for application in magnesium secondary batteries due to its electronic properties, high surface area, and sheet-like morphology. However, it has been investigated quite rarely in the literature so far.[198–200]

3.3.3.2 Transition metal sulfide class II: thiospinels

The spinel structure shows the general formula AB_2X_4 with the space group Fd3m, where the octahedral cation (B) is coordinated by the cubic anion (X) in the packed lattice (Figure 35). The octahedra share edges and extend in space, enabling 3D diffusion channels. In a normal spinel, cation 'A' occupies the tetrahedral sites to form the Fd3m symmetry.[201]
In oxide spinel, e.g., $MgAl_2O_4$, magnesium prefers the tetrahedral site.[202] However, by changing the anion from O^{2-} to the larger S^{2-}, surprisingly, Mg can adopt the inverse spinel structure, e.g., in $MgIn_2S_4$, with Mg and In sharing octahedral site.[203] This is primarily due to the ratio between the Mg^{2+} and S^{2-} ionic radii, which is ca. 0.4, where magnesium falls into a range that favors both octahedral and tetrahedral environments depending on the corresponding metal. For example, when Mg^{2+} interacts electrochemically with the cubic titanium disulfide, magnesium prefers to occupy the octahedral 16c sites rather than the tetrahedral 8a sites, as it would be expected for a normal spinel.[203–205]

Thiospinels can be classified into binary and ternary compounds. In both cases, sulfur forms the cubic closed packing. In binary thiospinels, both the tetrahedral and octahedral vacancies are occupied by the same metal ion. Hence it is clear that the metal in a binary spinel must have the potential to be stable in the oxidation states +2 and +3. Representatives for this class of compound are iron (Fe), cobalt (Co), and nickel (Ni).[206]

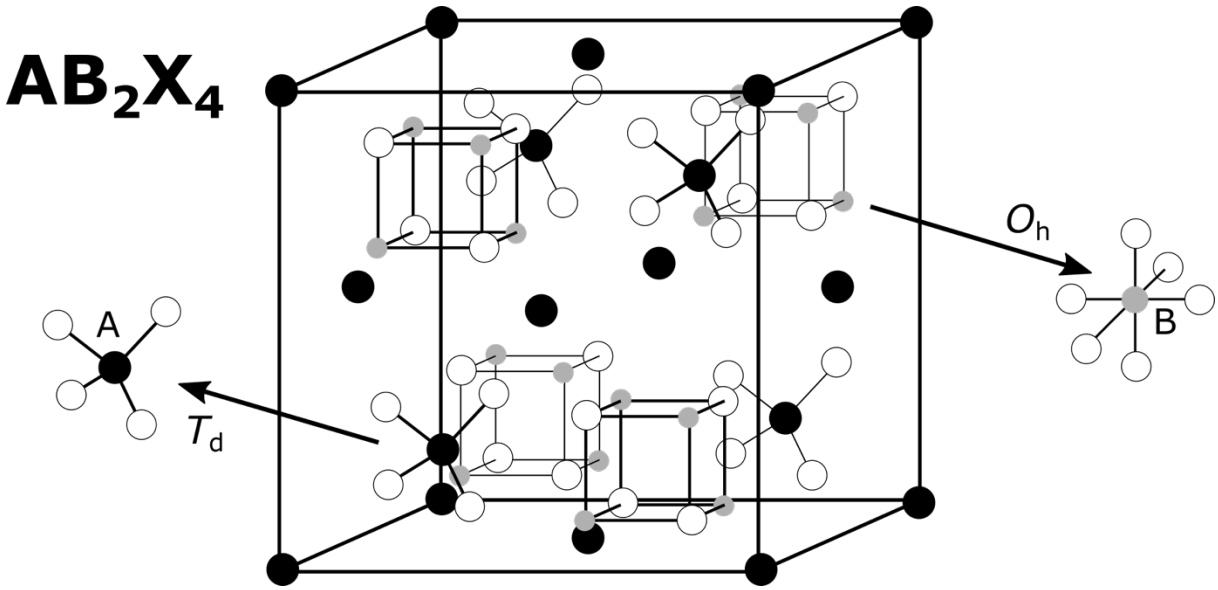

Figure 35: General crystal structure of an AB_2X_4 spinel.

Ternary thiospinels are characterized by two different metals in the tetra- and octahedral voids. Most compounds for ternary thiospinels are known with copper (Cu) at the A-site while the transition metal at the B-site can be vary (M = Ti, Zr, V, Cr, Rh) or indium (In) in the B-site while the A-site can be vary (M = Mn, Fe, Co, Ni). Interestingly, copper is not found in the valence state +2 as expected but in +1, whereas the transition metal must have a +4 charge.[207,208]

However, other known candidates in this class are chromium-based thiospinels, where Cr is occupied in the octahedral vacancies, mainly in the valence state +3, while the counter metal can be Mn, Fe, Co, Ni, Zn, or Cd in the valence state +2.

In the concern of cathode material in RMBs, the stabilities of the charged (without Mg) and discharged (with Mg) states were calculated and compared with the formation energy against the convex hull of ground state energies, so call ‘energy above hull’ (EAH). In general, a higher EAH indicates a thermodynamically more unstable phase. However, Hannah et al. investigated through thermodynamic analysis the presence of the driving forces for intercalation and conversion reactions in battery cathodes across a range of possible working ion, transition metal, and anion chemistries. These findings

showed that for a one-electron reduction, oxide polymorphs favor an intercalation reaction, while sulfides and selenides prefer a conversion reaction (Table 3). A two-electron reduction of the transition metal will always favor conversion reactions for $A(MX_2)_n$ compounds.[209]

Table 3: All reactions considered for the Mg-Cr-O, Mg-Cr-S, and Mg-Cr-Se systems and the associated voltages (in V). Adapted from [209]. (LDP = Lowest energy discharged polymorph; LCP = Lowest energy charged polymorph).

Reaction	LDP structure	V^{LDP}	LCP structure	V^{LCP}
	Mg-Cr-O			
$Mg + Cr(IV)_2O_4 \rightarrow MgCr(III)_2O_4$	Spinel	3.61	Rutile	2.68
$Mg + Cr_2O_4 \rightarrow MgO + Cr_2O_3$		3.36		2.78
	Mg-Cr-S		Layered	
$Mg + Cr_2S_4 \rightarrow MgCr_2S_4$	Spinel	1.65		1.24
$Mg + Cr_2S_4 \rightarrow MgS + Cr_2S_3$		1.64		1.58
	Mg-Cr-Se			
$Mg + Cr_2Se_4 \rightarrow MgCr_2Se_4$	Spinel	1.28	Layered	0.84
$Mg + Cr_2Se_4 \rightarrow MgSe + Cr_2Se_3$		1.30		1.21

For example, chromium has in the discharged phase a stable d^3 (Cr^{3+}) configuration were the t_{2g} is half-filled. Upon charging, Cr is oxidized to Cr^{4+} (d^2), which has an unstable electronic configuration and trends. Therefore, it oxidizes further to Cr^{6+} (d^0). This explains why it was not possible to reversibly extract Mg^{2+} from the lattice.[210] Blanc et al. observed similar behavior of an irreversible insertion/extraction of Mg^{2+} from the lattice and could further show the dissolution of the active material through polysulfide species in the electrolyte triggered by decomposition of the spinel through the oxidation of sulfur.[211]

By having a closer look at the 'low voltage' metals, more stable electronic configurations in the charged state can be observed. For example, Ti^{4+}, Mn^{4+}, and Ni^{4+} are very stable due to the d^0 configuration of half-filled and filled t_{2g} states. Upon the intercalation, one electron is added that resulting in a less stable electronic arrangement for the host materials, which results in a decreased stability through the filling of an antibonding orbital (e.g., Ni, Mn).[201]

By taking a closer look at the binary thiospinels, not many compounds are possible. Known binary thiospinels are Fe_3S_4, Ni_3S_4, Co_3S_4, Mo_3S_4. In a binary thiospinel, the

metal must be stable in valence states +2 and +3. Furthermore, when looking at a reversible insertion and extraction of the working ion in the host material, the metal must also be stable in an oxidation state +4. For conversion-type binary thiospinels, the oxidation state +4 must not be preferred because of the stepwise reduction from +2 or +3 to 0.

When looking at the electrochemical storage performance of these materials, Mo_3S_4 or Mo_6S_8 was the first cathode material reported for the prototype of a viable Mg-based battery.[139] For the iron-based thiospinels, previously a compound material combined with rGO synthesized by a simple in situ hydrothermal approach, showed outstanding cyclic and rate performance of 720 mAh/g after 880 cycles at a high current density of 1 A/g.[212] Some specific magnesium thiospinels ($MgSc_2S_4$, $MgIn_2S_4$) seems to be promising candidates as solid-state-electrolytes in magnesium solid-state batteries.[213,214]

3.3.3.3 Transition metal sulfide class III: other metal sulfides

Most metal-sulfides, which are not homed under the first two categories, follow a displacement reaction mechanism. During the displacement reaction, only the active ion (Mg^{2+}) is displaced from the host material, travels through the electrolyte where it further getting reduced to M^0. This mechanism is part of the conversion type compounds because the crystal structure of the cathode material is transformed during charging/discharging cycles. However, the foremost challenge of converting the charged and discharged materials is that this reaction suffers structural, morphological, and volume changes that influence the cell performance, leading to degradation or a collapse of the cathode material.[28] Further, large voltage hysteresis between charge and discharge results in low energy efficiency for conversion-type cathodes.[28,148]

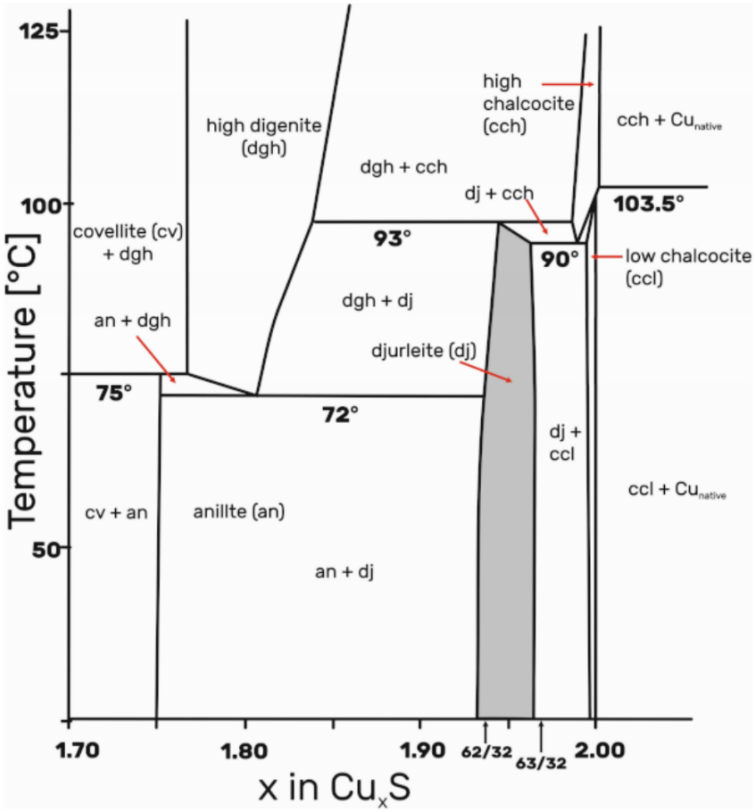

Figure 36: Phase diagram of CuS with different stoichiometries at different temperatures. Reprinted with the permission of [215].

Copper(II) sulfide as cathode material is the most reported 'conversion-type' cathode material for rechargeable magnesium batteries so far. Due to its high theoretical capacity of 560 mAh g^{-1} and high theoretical cell voltage of 2.7 V, resulting in a high theoretical energy density of 1,207 Wh kg^{-1} and 4,166 Wh L^{-1} seems copper sulfide to be the ideal candidate. Moreover, CuS is electrically conductive (10^3 S cm^{-1}), and both copper and sulfur are highly earth-abundant, enabling more sustainable batteries. In the past years, it could also be shown that a RMB based on a nanostructured CuS cathode is viable compared to its counterpart of bulk CuS, which can only be run at elevated temperatures.[27,151,216–224]

The phase diagram of the most straightforward binary Cu-S system with stoichiometric compositions and crystallographic phase has some very complex atomic arrangements, as shown in Figure 36.[225,226] The formula of copper sulfides is $Cu_{2-x}S$, with possible values for x ranging from 0 to 1. The main crystal phases are the hexagonal covellite (CuS), monoclinic low-temperature chalcocite ($Cu_{2.0\text{-}19997}S$), monoclinic djurleite ($Cu_{1.97\text{-}1.93}S$), triclinic roxbyite ($Cu_{1.81}S$), cubic digenite ($Cu_{1.8}S$), and orthorhombic anilite ($Cu_{1.75}S$) (Figure 37).

Depending on the amount of copper in the chalcocite, the crystal structure can differ, which is related to its properties. The hcp is formed by the sulfur atoms in chalcocite and djureleite, while in digenite, a ccp is observed.[175]

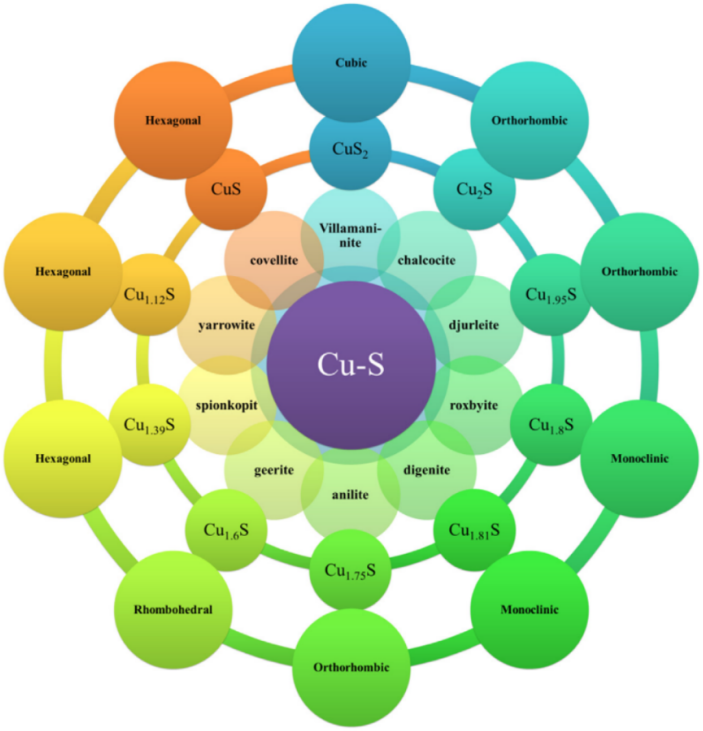

Figure 37: Overview of Cu-S compositions and their crystal structures. Reprinted with permission of [227].

Additionally, to the natural and synthesized phases of copper sulfides, several phase transitions for copper sulfide are well known. For example, chalcocite undergoes above 104°C a phase transition from its superstructure with monoclinic symmetry with metal atoms in triangular coordination to a hexagonal symmetry. Up to 435°C, the hexagonal chalcocite is stable before it inverts to high-temperature digenite of cubic symmetry. Interestingly, copper monosulfide is not the simple composition of Cu^{2+} and S^{2-} ions. Regarding the electronic structure of CuS, there is a converse discussion in the literature. CuS as a layered hexagonal structure consisting of alternating layers of CuS and Cu-S_2-Cu. This unusual structure is explained by the fact that S-S covalent bonds are energetically favorable over S-Cu bonds. Therefore, two of the six copper atoms in the unit cell have triangular coordination, and the other four have tetrahedral coordination. Copper can be found in valence states +1 and +2, whereas sulfur is in S_2^- and S^{2-}.[175] More detailed Pattrick et al. investigated the structures of copper sulfides during their X-ray adsorption study, which confirmed the presence of only Cu(I) and revealed that three types of S are present. Upon aging, the primitive structure transforms into one

with the characteristics of covellite, and this transformation involves the reordering of the S-S and Cu_3S-CuS_3 layers, as visualized in Figure 38.

Development of the primitive phase from either a wurtzite-like structure or planar Cu_3S-CuS_3-layers is possible, with the structural evolution driven by the antipathy of Cu(II) for tetrahedral coordination and anomalous electron densities in the metastable structures. Further, they describe the three different sulfur species as S^{2-}, S_2^{2-}, and S^{-*} with '*' as a positive hole which is possibly filled with H^+ to form a HS^- species.[228]

Similar findings for three different sulfur species were found by Nesbitt and Muir in the structure of pyrite. They consider the species as monosulfide (S^{2-} = 10%), disulfide (S_2^{2-} = 85%) and polysulfides (S_n^{2-}, n > 2, = 5%).[229]

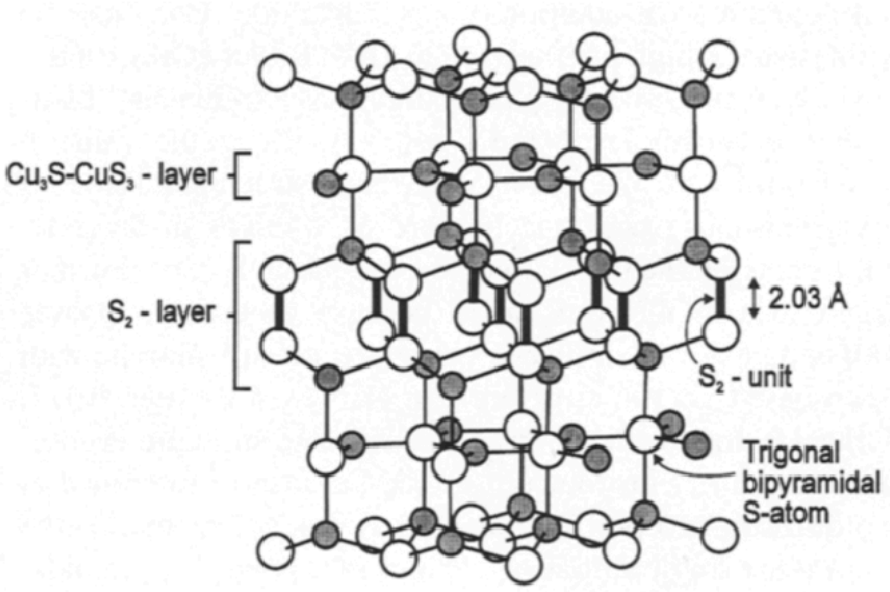

Figure 38: Crystal structure of CuS (covellite). Reprinted with permission from [228].

The redox mechanism of CuS in Mg-ion batteries was investigated by different ex-situ studies. All studies agree on the fact that the first cycles differ from the following cycles. During the first discharge, two plateaus can be measured under galvanostatic discharge measurements.[151,217,230] The first plateau starts at lower potentials and increases with time to a higher potential. This increase in potential is not visible under CV measurement due to the different working mechanisms of CV (control of voltage/measuring current) and galvanostatic (control of current/measuring voltage) measurements. Discrepancy in literature regarding the ongoing electrochemical reactions in the first cycle. Some mechanism studies report the reduction to Cu^0 in the first cycle[216,230,231], while others reporting by ex-situ XRD measurements of fully discharged electrodes that after the first cycle Cu_2S and no Cu^0 was detected.[215] The reports that

rely on the hypothesis of the full reduction to Cu^0 in the first discharge neglecting the changes in the oxidation state of sulfur. Ex-situ XPS measurements have shown that the oxidation state of sulfur is different for the pristine (contains S_2^{2-} and S^{2-}) and the discharged/charged (S^{2-}) states. The additional capacity in the first cycle has to come from the reduction of $S_2^{2-} + 2\ e^- \rightarrow 2\ S^{2-}$ since S^{2-} is playing only a passive role during the electrochemical reactions between copper and magnesium sulfides in the onward cycling ($Cu^+_2S^{2-} + Mg^0 \leftrightarrow Mg^{2+}S^{2-} + 2\ Cu^0$).[151] However, all studies agree to the fact that the peaks of CuS disappeared after total the 1st discharge.

Depending on the different mechanism studies the oxidation from $Cu^0 \rightarrow Cu^{2+} + 2e^-$ or no oxidation during the first charging step is observed. However, it is worth noting, depending on the electrolyte and the current collector, potentials higher than 2 V vs. Mg/Mg^{2+} can cause the decomposition of the electrolyte, especially for $AlCl_3$/THF or DME containing electrolytes.[232]

Long-term cycling performances of CuS/Mg systems show capacity losses in the first cycles. This loss is explained by some Mg^{2+} trapped in CuS as well as the dissolution of copper ions into the electrolyte.[233,234]

Tashiro et al. investigated the effect of the anion-sublattice on the displacement reaction in cubic digenite and chalcocite with the outcome that only the cubic structure of CuS enabled good reversibility versus magnesium. Further, the results suggested that a critical factor for a successful displacement reaction is that the charged and discharged products share the same anion sublattice structure.[224] Similar results of crystal structure depending capacities for copper sulfide (CuS, $Cu_{1.7}S$, $Cu_{1.9}S$) cathode materials were made by Wang et al.[220]

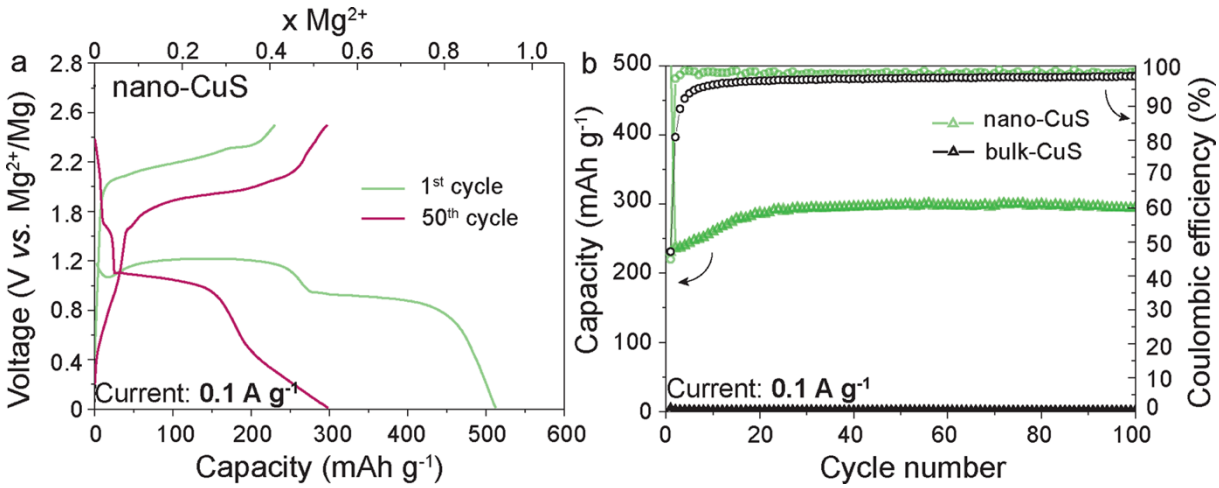

Figure 39: Effect of nano structuring copper sulfide on the electrochemical performance. a) Galvanostatic charge-discharge curves of CuS nanoparticles at the 1st and 50th cycle and b) cyclic stability measurement at a current density of 0.1 A g^{-1}. Reprinted with permission from [151].

Independent from the crystal structure Kravchyk et al. measured capacities which are close to the theoretical capacities of CuS and Cu_2S by nano structuring the cathode material (Figure 39).[151]

Silver sulfide is also a very prominent cathode candidate in the field of RMBs. The only stable compound in the Ag-S system is Ag_2S. The monoclinic β-form is stable up to 177°C and possesses a body-centered cubic structure of sulfur atoms in the range of 177°C and 600°C. At temperatures higher than 600°C, a fcc structure is formed. Furthermore, silver sulfide exhibits both ionic and electronic conductivity, depending on the sulfur content.[175]

Ha et al. demonstrated a reversible electrochemical reaction with Mg^{2+} on the base of a replacement reaction. The Ag_2S-carbon composite material delivered an initial capacity of 150 mAh g^{-1} at 0.1 C. Upon cycling, the active material showed a performance of 40 mAh g^{-1} at 1 C after 500 cycles.[235] Similar results were reported by Zhang et al.[236] A higher rate performance and improved cycle life was presented by Chen et al. by using α-Ag_2S-reduced graphene oxide as cathode material, which delivered a specific capacity of 46.3 mAh g^{-1} after 1000 cycles at 1 A g^{-1} (5 C).[237]

For ZnS, several polytypes exist. Due to its d^0 state in Zn^{2+}, zinc tends to fill the tetrahedral voids of the closed-packed anion structure, showing a (4,4)-coordination. In sphalerite, also known as zinc blende, the sulfur atoms form a fcc structure with the as-mentioned occupation of the zinc atoms in half of the tetrahedral holes. Likewise, ZnS undergoes a phase transition at about 1000°C, where sulfur atoms change the packing from cubic to hexagonal form (wurtzite).[175]

Other transition metal sulfides with a ratio of M:S = 1:1 crystalize in the nickel arsenide structure type. Examples of this group are TiS, VS, FeS, CoS as well as NiS.
The nickel arsenide structure is the hcp analog of the NaCl-structure, where the anions build the disordered hcp while the cations occupy the octahedral voids. The NiAs structure cannot be adopted by ionic compounds because of the eclipsing cations. The cation-cation repulsion would be internally destabilizing for an ionic compound because of no interaction of the neighbored octahedrons. Therefore, this structure is mainly adopted by covalent and polar covalent compounds (soft anion and low-valent transition metal cations). Therefore, monosulfides in the NiAs structure type are comparable with those of their intermetallic phase, which show metallic glaze and electrical conductivity.
He et al. studied the potential of CoS as cathode material in rechargeable magnesium batteries of different morphologies (flower-like and microspheres). The electrochemical tests show cycle stability and a specific capacity of 125 mAh g^{-1} for the flower-like structure, whereas the microsphere structured material suffered in capacity (105 mAh g^{-1}) and fading in cycling stability (60 mAh g^{-1} after 65 cycles at 50 mA g^{-1}).[238]
A better electrochemical performance was achieved by Pan et al. with the use of 3D hierarchical porous CoS spheres. As a result, good cycling stability (340 mA h g^{-1} after 88 cycles), a high capacity (up to 370 mA h g^{-1}), and a good rate performance (300 mA h g^{-1} at 50 mA g^{-1}) were achieved.[239]
Iron sulfides are, due to their low cost and non-harmful nature, also a promising active material for magnesium-ion batteries. The redox mechanism was studied by Wu et al. with the investigation of an iron-sulfur battery.[240] Interestingly, they could show the different Fe-S phase transitions from S $\leftrightarrow$ FeS_2 $\leftrightarrow$ Fe_3S_4 $\leftrightarrow$ FeS. During this phase transition, the active mass undergoes volume changes. In comparison, the volume shrinks from S $\rightarrow$ FeS_2 (77 vol.%), whereas volume expansions take place during the reactions from FeS_2 $\rightarrow$ Fe_3S_4 (118 vol.%) and from Fe_3S_4 $\rightarrow$ FeS (133 vol.%). When compared to Mg-S, Li-S, and Na-S redox chemistry, the overall volume change is nearly the same for Mg-S (24 vol.%) and Fe-S (32%), whereas the volume expansions for Li-S (72%) and Na-S (160%) are much higher.[240]
FeS was further used as cathode material in a magnesium/lithium hybrid configuration. A high-specific capacity and good cycling performance were demonstrated. A discharge capacity above 200 mAh g^{-1} could be obtained after 800 cycles with a

coulombic efficiency above 97%. Further findings resulted in an enhanced performance by increasing the amount of lithium in the cell, either by increasing the Li salt concentration or adding a Li source at the anode.[241]

A bimetallic sulfide, such as chalcopyrite ($CuFeS_2$), could combine the benefits of low cost, high earth-abundant, and high specific capacity.[242] Lithium-ions intercalate in the first step into the host structure. In a second step, Li_xCuFeS_2 undergoes with further addition of lithium-ions a conversion type redox reaction:

$$CuFeS_2 + x\ Li \rightarrow Li_xCuFeS_2$$
$$Li_xCuFeS_2 + (4-x)\ Li \rightarrow Cu + Fe + 2\ Li_2S$$

However, during the charging process, the crystal structure of $CuFeS_2$ cannot be obtained anymore, instead the formation of FeS_{1+x} and Cu_2S occurs.[243,244]

Natural $CuFeS_2$ has been tested as electrode material in Li-ion batteries, with reasonably good electrochemical performance exhibiting discharge capacities of around 1 Ah g^{-1} at a current density of 1 A g^{-1}.[245]

However, literature reports on the usage of $CuFeS_2$ as cathode material for magnesium batteries are rare.

3.4 Photo rechargeable batteries

3.4.1 Perovskites for self-charging batteries

The following part of this section is published in the following review article, which includes the preparation of the following specific section, support of writing, and the sketching of the TOC graphic. For the reproduction in the thesis/dissertation as an author, permission is not required [20]*:*

Yang, Y., Hoang, M. T., Bhardwaj, A., Wilhelm, M., Mathur, S., & Wang, H. Perovskite solar cells based self-charging power packs: Fundamentals, applications and challenges. *Nano Energy* 94, 106910 (**2022**).

Energy is essential for human beings. The energy demand has rapidly increased, driven by the requirement for global economic growth. Energy shortage caused by this constantly rising energy demand and limited resources has become an ongoing and pressing challenge for economic development. Traditional fossil fuels, including oil, natural gas, and coal, dominate the current energy system. However, burning them rise to the emission of carbon dioxide (CO_2) and other greenhouse gases, leading to environmental pollution, global warming, and climate change.[246,247]

Solar energy, with its abundance, clean and renewable features, is considered the most feasible solution to address this energy crisis effectively. To harvest solar power, photovoltaic (PV) technologies that convert solar energy into electricity have been developed, which can power the world from small electronic devices to domestic appliances and even large commercial plants. Since the first report of silicon solar cells in 1954, various types of PV technology have been developed, such as crystalline silicon cells,[248,249] copper indium gallium selenide thin-film cells (CIGS),[250,251] organic photovoltaics (OPV),[252,253] dye-sensitized solar cells (DSSCs),[254,255] perovskite solar cells (PSCs),[256–258], *etc.* Among them, PSCs have attracted tremendous attention as one of the cutting-edge and promising PV technologies to deliver cost-effective solar electricity due to their skyrocketing advancement of power conversion efficiency (PCE) achieved by low cost and simple fabrication processes.[259,260]

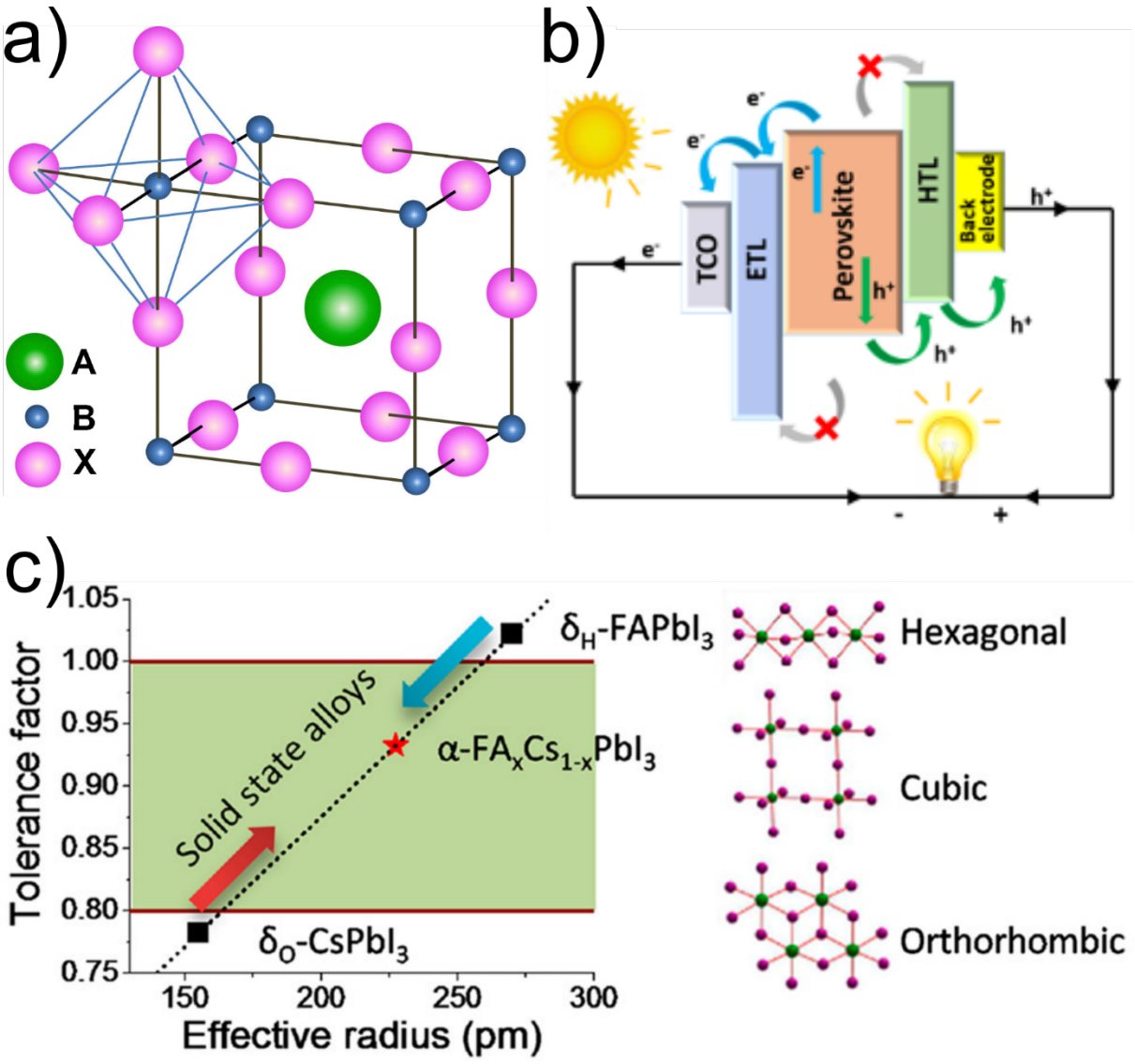

Figure 40: a) ABX_3 perovskite structure showing BX_6 octahedral and larger A cation occupied in the cubo-octahedral site. Reproduced with permission from [261] Copyright 2014 Elsevier. b) Correlations between tolerance factor and crystal structure of perovskite materials. Reproduced with permission from [262]. Copyright 2015 American Chemical Society. c) Working mechanism of perovskite solar cells. Reprinted with permission from [20]. Copyright 2022 Elsevier.

Since the first report on organometal halide perovskite as a visible-light absorber in a sensitized solar cell that achieved a PCE of 3.8% in 2009,[263] within 11 years, huge progress has been achieved for PSCs with a current world-record PCE of 25.7%.[264] This is already comparable with the state-of-the-art crystalline Si-based cells that dominate the current PV market. Nevertheless, similar to other PV technologies, the power generated by the independent PSC units heavily relies on the availability of illumination and its intensity, which is restricted by various environmental conditions such as weather, location, diurnal cycles, *etc.*[265] The discontinuous power output of a PV device fails to meet the requirement for sustainable and reliable electricity to external

loads in practice. Therefore, as a remedy, the integration of perovskite solar cells and electrochemical energy storage devices to make self-charging power packs (SCPPs) that can store the harvested solar energy and provide electricity has been proposed and developed. Upon exposure to light, the PSC part harvests solar irradiation and simultaneously generates electricity, which is instantly stored in the energy storage part. The photo-charged power pack releases the stored electricity to drive the external devices wherever and whenever needed, thereby completing the “photo-electrochemical-electricity” energy conversion (Figure 41).

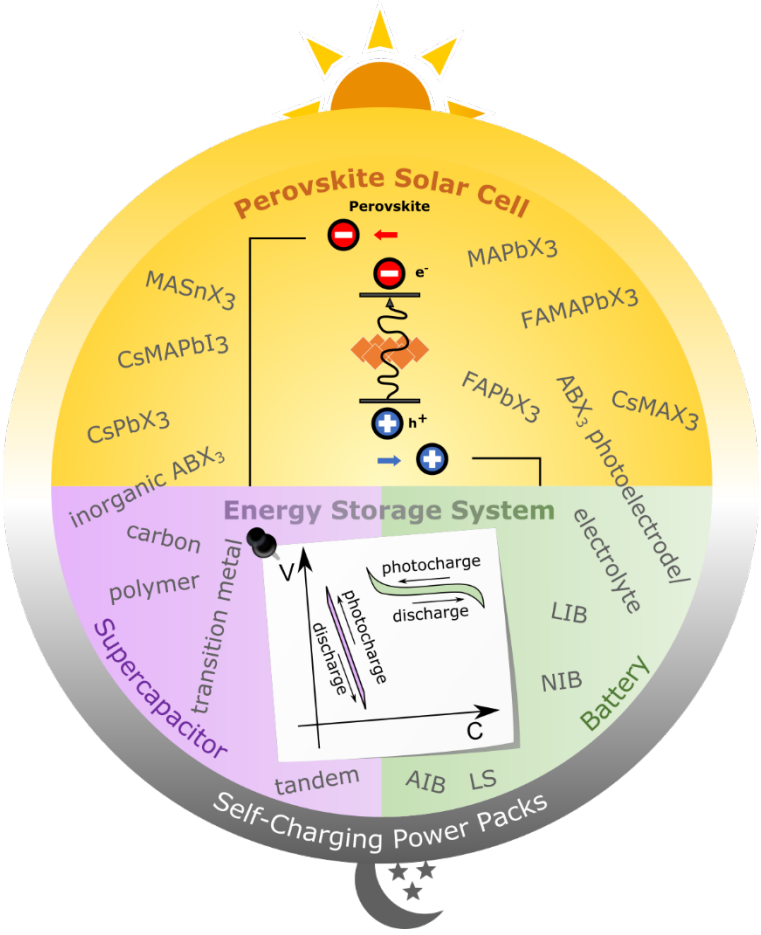

Figure 41: Self-charging power packs comprised of perovskite solar cells and energy storage systems, such as supercapacitors and lithium-ion batteries.

Figure 40c illustrates the working principle of a PSC. Upon exposure to illumination, photons pass through the transparent front electrode (TCO substrate) coated with ETL (regular structure) or HTL (inverted structure) to be absorbed by the perovskite layer, which instantly generates photo-excited charge carriers that are separated at the perovskite/ETL and perovskite/HTL interface. Owing to the energy band level alignment of the materials used in the PSC, the photo-generated electrons are extracted to the ETL while the photo-generated holes are injected into the HTL. The electrons and

holes are then collected by the current collector of the TCO substrate and back electrode, respectively. When the PSC connects with a load, the current flows through the external circuit to complete the circle. If the load is an energy storage system, different types of connections are imaginable.

The self-charging power packs can be assembled via the combination of light harvest part (PSC module) and energy storage part (battery) by means of either wire connection or wireless monolithic structure. In the wire-connected configuration, the individual PSC and energy storage device are directly linked via the external wires. By contrast, a shared electrode is used in the monolithic SCPPs to connect these two parts (Figure 42). This common electrode participates in the photoelectric energy conversion in the PSC part and electrochemical storage in the energy storage system. Therefore, properties of the shared electrode, such as conductivity, energy band level, work function and chemical compatibility with other materials in the devices, have significant impacts on the performance of the integrated SCPPs.

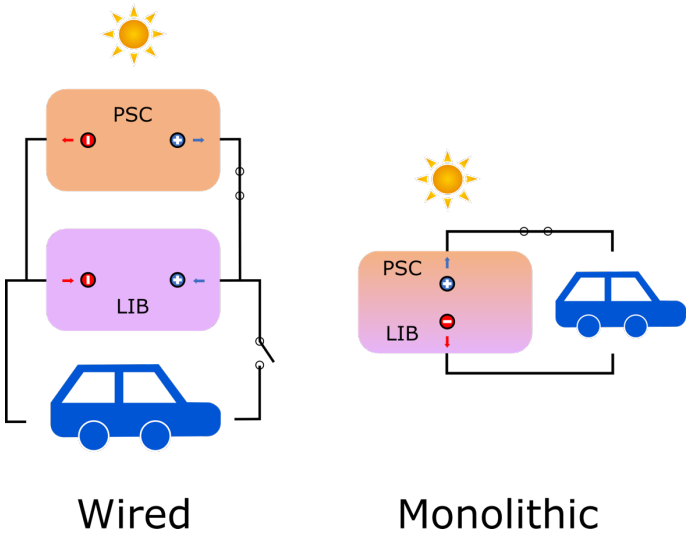

Figure 42: Illustration connection types of the wired and the monolithic SCPP.

Xu et al. presented already in 2015, the concept of using perovskite as energy harvester to charge a lithium-ion battery based on lithium-iron phosphate as cathode and lithium titanate as anode. However, this system was based on a wired connection and could be demonstrated in monolithic connection. Manly drawback of this system is, that four PSC units connected in series were needed to charge the lithium-ion battery.[266] Several research was done for perovskite as bifunctional electrode in lithium-ion and aluminum batteries, however, they reporting about stability issues of the cells.[267,268]

3.4.2 Inorganic materials as photoresponsive cathode for LIB

The following part of this section is published in the following peer-reviewed article with first author contribution, which includes the preparation of the manuscript, synthesis, graphics, and evaluation of the study. Post-mortem SEM measurements were conducted in collaboration with Prof. Yamada and Prof. Sekino SANKEN, Osaka university, Japan. Simulations of the band structures were done in collaboration with Prof. Hong, Fujian Normal University, Fuzhou, China. For the reproduction in the thesis/dissertation as an author, permission is not required [269]*:*

Wilhelm, M., Adam, R., Bhardwaj, A., Neumann, I., Cho, S. H., Yamada, Y., Sekino, T., Tao, J., Hong, Z., Fischer, T., & Mathur, S. Carbon-Coated Electrospun V_2O_5 Nanofibers as Photoresponsive Cathode for Lithium-Ion Batteries. *Adv. Eng. Mater.* 2200765 (**2022**).

An enormous amount of research efforts are dedicated to harvesting photo energy by direct (e.g., photovoltaics) and indirect (e.g., photocatalysis) approaches to demonstrate a sustainable energy cycle for industrial and community needs.[270–272] In addition, the energy harvested must be available for immediate use or should be stored in efficient energy storage devices, such as lithium-ion batteries.[273–277] For example, tandem systems such as an integrated set-up of photovoltaic and photoelectrochemical devices have been demonstrated with complementary dual functionality, however, these systems often suffer from large energy losses, poor energy densities, and high integration costs.[20] Therefore, improved integration strategies are needed to realize highly efficient self-charging power packs (SCPPs). In this context, the so-called “photo-battery” consisting of a shared electrode, working as both, an energy harvester and energy storage medium represents an innovative solution for the aforementioned challenges.[267,278–280]

The reversible redox reaction of intercalated Li-ions can be facilitated by applying photovoltage to the cathode (‘photocathode’). In the quest of dual-action electrode materials, various inorganic, organic, and inorganic-organic hybrid compositions serving as photoanode or -cathode have been recently investigated.[20,266,267,279–282] The synergistic effect of harvesting and storing energy within the same material requires certain prerequisites to be fulfilled such as suitable bandgap and a reversible redox active

behavior. Recently, vanadium pentoxide (V_2O_5) has been investigated as a cost-effective cathode material for lithium-ion batteries (LIBs) due to its high theoretical specific capacity values of 294 mAh g^{-1} and 441 mAh g^{-1} for a 2 and 3 Li-ion intercalation, respectively.[283] V_2O_5 as a host for the intercalation of Li-ions was first proposed by Whittingham et al. and is nowadays also investigated for Al^{3+} and Zn^{2+} batteries.[284–286] Many different morphologies of nanostructured V_2O_5 were investigated in the past that deliver excellent electrochemical properties.[287–290] Besides the abovementioned attractive electrochemical characteristics, V_2O_5 is a photoresponsive material with a suitable bandgap for light absorption in the visible range (Eg, ~2.35 eV) that enables its application as dual-action electrode material. Boruah et al. demonstrated for the first time, the light rechargeable properties of hydrothermally synthesized V_2O_5 for lithium and zinc batteries.[279,280] Figure 43 illustrates the differences between the photochemical and the electrochemical charging process.

$$V_2O_5 + 2\,Li^+ + 2\,e^- \leftarrow Li_2V_2O_5 + 2\,h^+ + 2\,e^- \xleftarrow{h\nu} Li_2V_2O_5$$

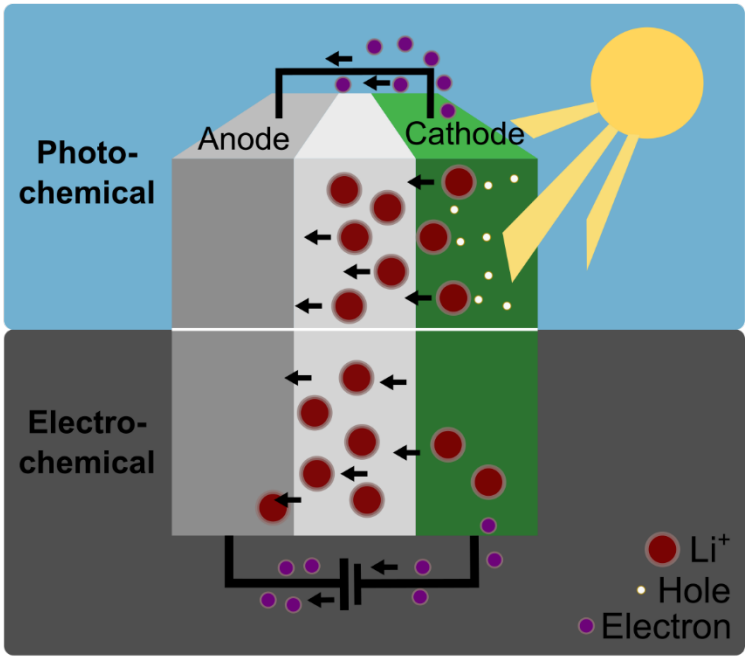

$$V_2O_5 + 2\,Li^+ + 2\,e^- \leftarrow Li_2V_2O_5$$

Figure 43: Photochemical and electrochemical charging of V_2O_5 as dual-functional electrode.

The enhancement in the electrochemical performance was explained through the following reaction that occurs under light illumination in which the photogenerated holes ease the extraction of Li^+ out of the lattice leading to an oxidation of the vanadium (Figure 44).

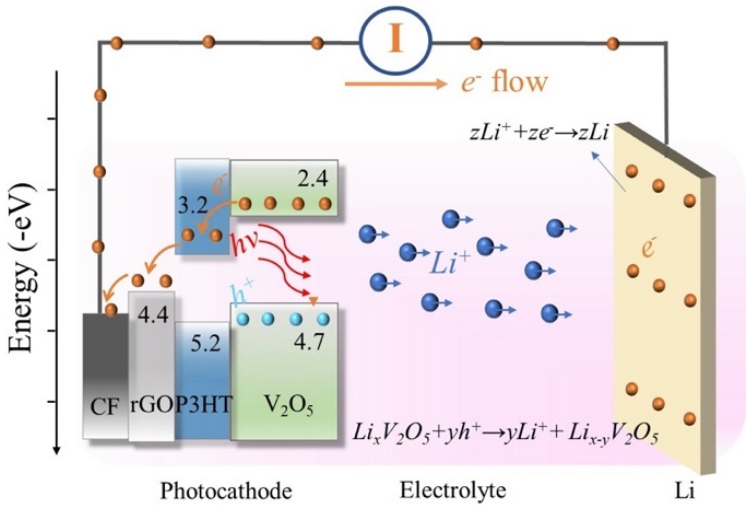

Figure 44: Schematic representing the photo charging mechanism of Photo-LIBs.

Moreover, the photogenerated electrons can be transferred through the external circuit to reduce lithium at the anode. Thus, the generated electron-hole pair reduces the energy barrier associated with the charging process, leading to a self-charging mechanism and/or enabling a longer operation of the battery by simple illumination.

Despite the successful demonstration of the proof-of-concept, the V_2O_5 photocathode could be further improved, especially in terms of conductivity, light absorption properties and mechanical stability by in-situ carbon-coating. We report here on vanadium pentoxide (V_2O_5) nanofibers fabricated through the electrospinning technique and coated with a sheath of conductive carbon through plasma-enhanced chemical vapor deposition (PECVD) of a carbon precursor (methane). The carbon-coated vanadium pentoxide (V_2O_5//C) materials [291–294] developed in this study served as cathode material for photo-rechargeable lithium-ion secondary batteries with better capacity retention over long-cycling due to seamless carbon coating that protects the active material from parasitic reactions of the electrolyte and by compensating for the volume change during the intercalation/deintercalation process, especially significant at higher applied voltages.[295] The carbon coating on electrode materials can effectively enhance electrical conductivity, improve surface chemistry of the active material as well as facilitate Li-ion diffusion, and also act as a protective overlayer on the electrodes to prevent direct contact with the electrolyte, ultimately improving the cell performance.[296] For example, hierarchically porous double-shell carbons prepared using polydopamine as carbon precursor showed an improved electrolyte ion diffusion toward redox active nitrogen species. Therefore, the porosity of materials needs to be carefully tuned while increasing the surface area to achieve maximum electrochemical efficiencies in

practical applications.[297] In this context, the nanostructuring of the electrode surface and the diffusion of the electrolyte ions at the surface are important parameters to tune the efficiency.

For example, by using KOH activation more nanopores could be created and the specific surface area could be significantly increased, which resulted in a synergetic effect with improved electrochemical performance of hollow activated carbons as superior supercapacitors and electrodes in lithium-ion batteries.[298,299] In terms of carbon coating from sustainable carbon sources achieving ultra-stable and fast-charging electrode materials, the use of biomass has attracted recent attention for both lithium as well as sodium-ion batteries.[31,300] Moreover, the interfacial modification by carbon coating is reported to enhance the stability of the electrodes during the photo charging effect by improving the charge extraction, as seen for example in graphene oxide.[301,302] In addition, the honeycomb-structured carbon architectures like carbon nanotubes or graphene can harvest sunlight, which is favorable for a synergetic effect of the carbon coating on the surface of vanadium pentoxide.[303]

4 Results and Discussion

4.1 $TiNb_2O_7$ – A fast-charging anode material

4.1.1 $TiNb_2O_7$-Keratin derived carbon nanocomposites as novel anode materials for LIB

The central part of this section is published in the following article, which includes support in manuscript preparation. Further, in this study, formal XPS characterization, analysis, evaluation, and preparation of the scientific section related to TNBO and TNBO/KC, as well as their influence on the electrochemical properties of their materials, were done. The chemical synthesis of the material was done by the first and co-authors. For the reproduction in the thesis/dissertation as an author, permission is not required [31]*:*

Thiyagarajan, G. B., Shanmugam, V., Wilhelm, M., Mathur, S., Moodakare, S. B., & Kumar, R. $TiNb_2O_7$-Keratin derived carbon nanocomposites as novel anode materials for high-capacity lithium-ion batteries. *Open Ceram.* 6, 100131 (**2021**).

The following part reports on the development of a unique TNBO/carbon material system that uses inexpensive and sustainable keratin-derived biological carbon sources as reinforcement to fabricate porous nanocrystalline TNBO/carbon composites *via* a surfactant-assisted precursor route. The electrochemical performance of these nanocomposites has been comprehensively evaluated, and the potential of these materials for the development of anode materials for LIBs is explored.

Figure 45a shows the X-ray diffractograms of KC and TNBO/KC nanocomposites. The carbon derived from keratin at 800 ºC demonstrates a broad peak around 2θ = ~25.2° indicating the amorphous nature of KC. Interestingly, TBNO/KC nanocomposites show peaks corresponding to $TiNb_2O_7$ [monoclinic, C2/m (Figure 45c) phase along with new peaks corresponding to $(Ti_{0.712}Nb_{0.288})O_2$ [tetragonal, P 42/m, Fig. 3 (d), 2θ = 27.1° (110), 35.6° (011) and 53.7° (121)] phase, which were absent in pristine TNBO. The Rietveld refinement of TNBO/KC nanocomposites revealed 63% and 37% of $TiNb_2O_7$

and $(Ti_{0.712}Nb_{0.288})O_2$ phases, respectively (Figure 45b). The formation of new peaks is attributed to the carbothermal reduction of TNBO with carbon present in TNBO/KC, resulting in a reduced non-stoichiometric oxide phase having shared lattice sites of Ti and Nb atoms in the crystal structure of $(Ti_{0.712}Nb_{0.288})O_2$ (Figure 45d) concordant with Raman results. The O^{2-} vacancies in the crystal structure of the non-stoichiometric $(Ti_{0.712}Nb_{0.288})O_2$ phase impart electrical conductivity due to electronic disorder. Similar observations were also made by Chunfu Lin et al.,[34] where $TiNb_2O_7$/carbon nanotubes composite showed the formation of reduced non-stoichiometric oxide, $Ti_2Nb_{10}O_{29}$ phase due to carbothermal reduction of $TiNb_2O_7$ with carbon nanotubes.

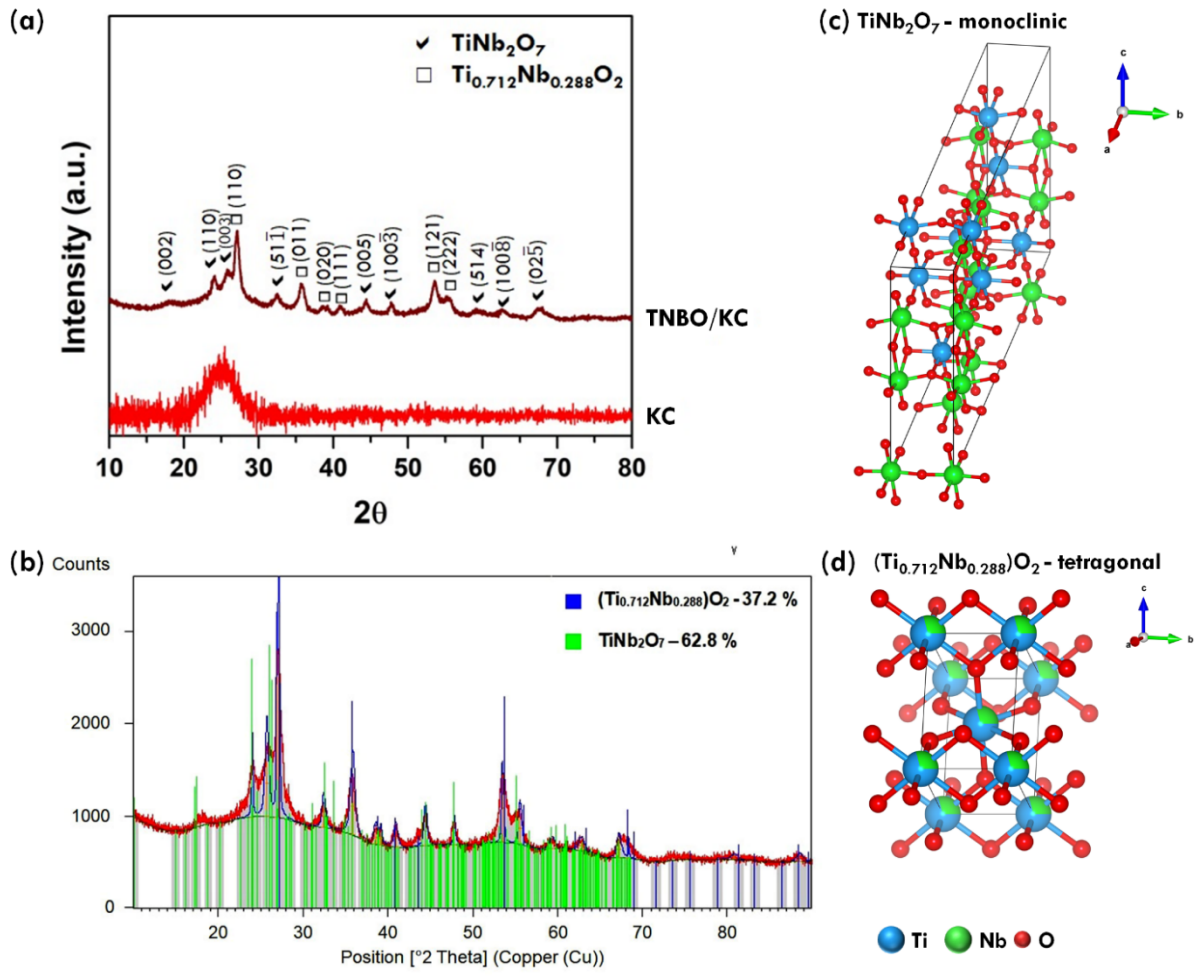

Figure 45: (a) X-ray diffractograms of KC and TNBO/KC nanocomposites. Crystal structures of (b) $TiNb_2O_7$ and (c) $(Ti_{0.712}Nb_{0.288})O_2$.

X-ray photoelectron spectroscopy (XPS) was further employed to analyze the chemical environment of Ti, Nb, C, and O elements in $TiNb_2O_7$ and $TiNb_2O_7$/KC. Survey scans of both samples reveal the existence of Ti, Nb, C, and O, as expected (Figure 46). Besides these signals, N and K were also observed, which belong to contaminations of the pyrolysis processes.

The presence of carbon (18.46 at.%) in $TiNb_2O_7$ can be attributed to adventitious carbon. In $TiNb_2O_7$/KC, the higher amount of carbon (58.44 at.%) appertains to the added carbon source. High-resolution investigations showed the presence of C=C (sp^2, 284.2 eV) bonds for the $TiNb_2O_7$/KC and C-C (sp^3, 285 eV) bonds for the pristine, which can be easily seen in the peak shift (dotted lines, Δ0.8 eV) and the asymmetric line shape in Figure 47a.[304] Moreover, for the pristine sample, signals of hydroxyl, carbonyl, and carboxyl groups at binding energies of 286.5, 288.0, and 289.0 eV were detected, whereas, for the sample with KC besides the C=C peak, a characteristic pi-pi* transition shake-up at 291 eV and a carboxyl peak at 289 eV was observed.[304,305]

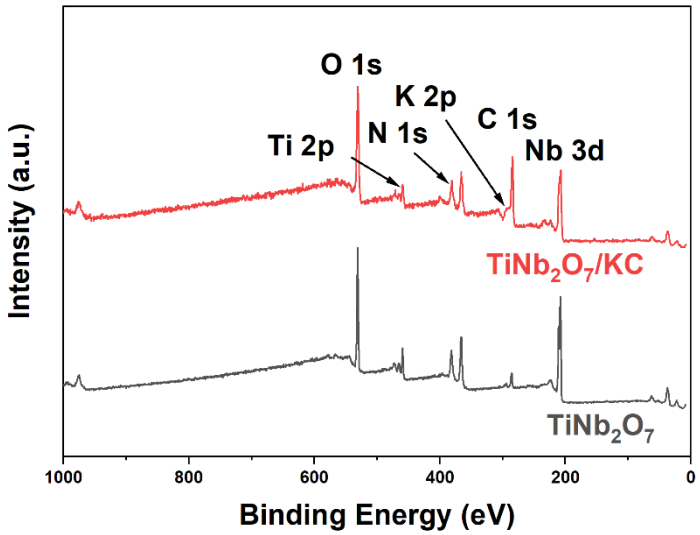

Figure 46: X-ray photoelectron survey spectra of $TiNb_2O_7$ and $TiNb_2O_7$/KC.

As expected, high-resolution analysis of the Nb 3d peak displays a doublet peak with an area ratio of 2:3 for Nb 3d 5/2 and Nb 3d 3/2, respectively. The binding energy of 207.2 eV for the Nb 3d 5/2 and a spin-orbit-splitting of Δ2.72 eV correspond to the pure pentavalent Nb in $TiNb_2O_7$ (Figure 47b).[306,307] In addition, HR spectra of Ti 2p pointed out that titanium is in the valence state +4 (Ti 2p 3/2: 458.61 eV, Ti 2p 1/2: 464.26 eV) (Figure 47c)[308] In comparison to the $TiNb_2O_7$/KC sample, titanium was also detected in the valence state 4+, whereas the HR spectra of Nb 3d displays beside the pentavalent Nb (207.2 eV) also the tetravalent Nb (206.0 eV) (Figure 47b).[306] This is in good agreement with the XRD measurements, that after the carbothermal reduction, niobium is present in valence states 4+ ($Ti_{0.712}Nb_{0.288}O_2$) and 5+ ($TiNb_2O_7$).

The main peak of the O 1s orbital was fitted to the metal-oxygen bonds (Ti-O, Nb-O) centered at 530.2 eV, while hydroxides and carbon oxides were fitted at 531.3 and 532.5 eV.[307] As already seen in the HR C 1s spectrum, only a small amount of oxygen

is bonded to carbon which is evident in the O 1s high-resolution spectra of $TiNb_2O_7$/KC (Figure 47d).

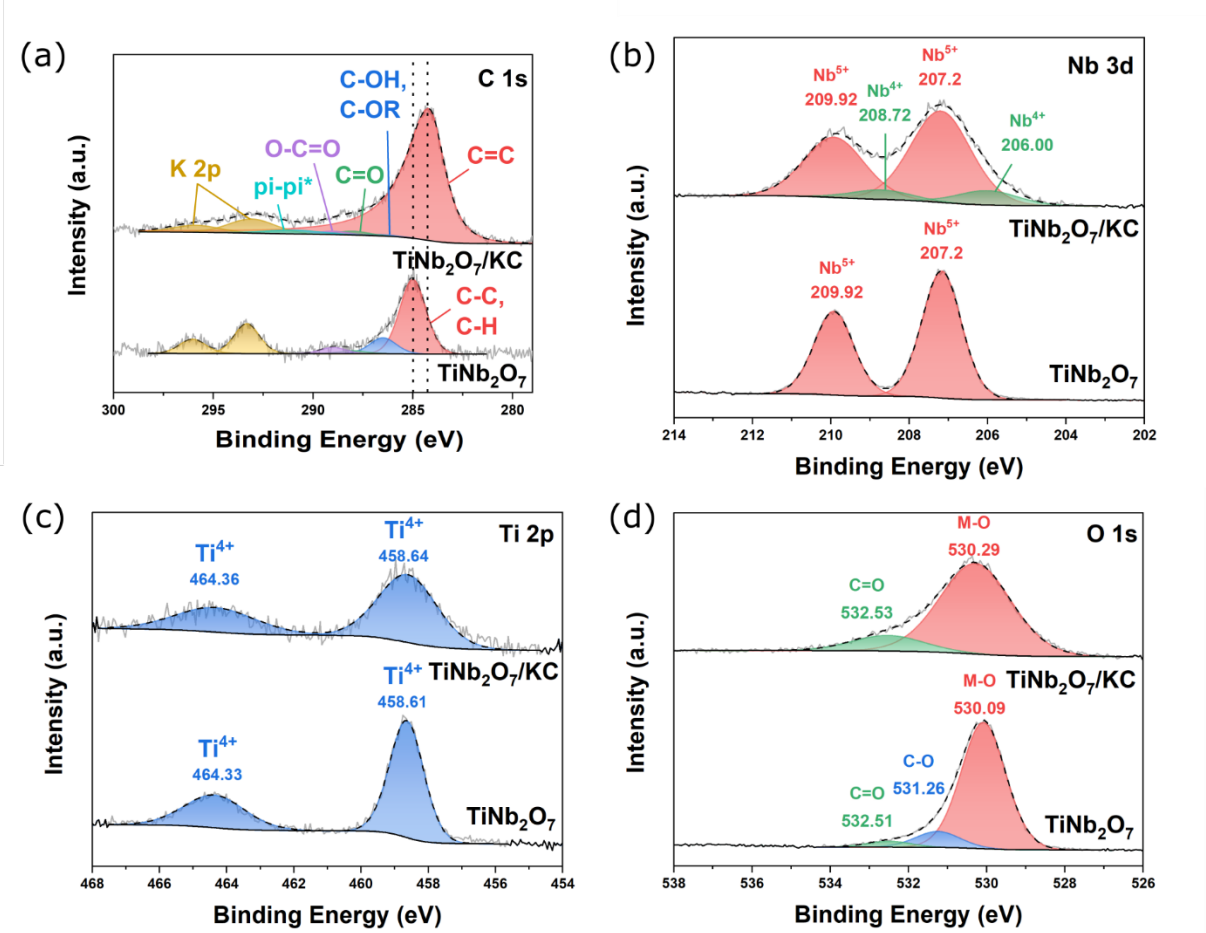

Figure 47: (a) X-ray photoelectron HR spectra C 1s/K2p, and (b) HR spectra Nb 3d, and (c) HR spectra Ti 2p, and (d) HR spectra O 1s of $TiNb_2O_7$ and $TiNb_2O_7$/KC.

The surface-active electrochemical phenomenon for TNBO‖Li and TNBO/KC‖Li cells were studied using cyclic voltammetry (CV). The CV experiments were conducted in half-cell configuration with respect to Li metal in the voltage range 0.8-3.0 V at the scan rate of 0.05 mV s^{-1} for 2 cycles. The corresponding voltammograms are presented in Figure 48a and b.

The single pair of prominent cathodic/anodic peaks at 1.50 V/1.67 V and 1.56 V/1.74 V for TNBO‖Li and TNBO/KC‖Li cells, respectively, are attributed to the redox couple of Nb^{5+}/Nb^{4+}. The shoulder peak at 1.80 V and 1.90 V in TNBO‖Li and TNBO/KC‖Li cells, respectively, is ascribed to Ti^{4+}/Ti^{3+} redox couples. The peaks at a low voltage of 1.24 V and 1.33 V in TNBO‖Li and TNBO/KC‖Li cells, respectively, are assigned to Nb^{4+}/Nb^{3+} redox couples. Nevertheless, TNBO/KC‖Li cell displayed symmetric redox couple and larger peak intensities revealing a good reversible cycling process and better electrochemical kinetics as compared to TNBO‖Li cell.

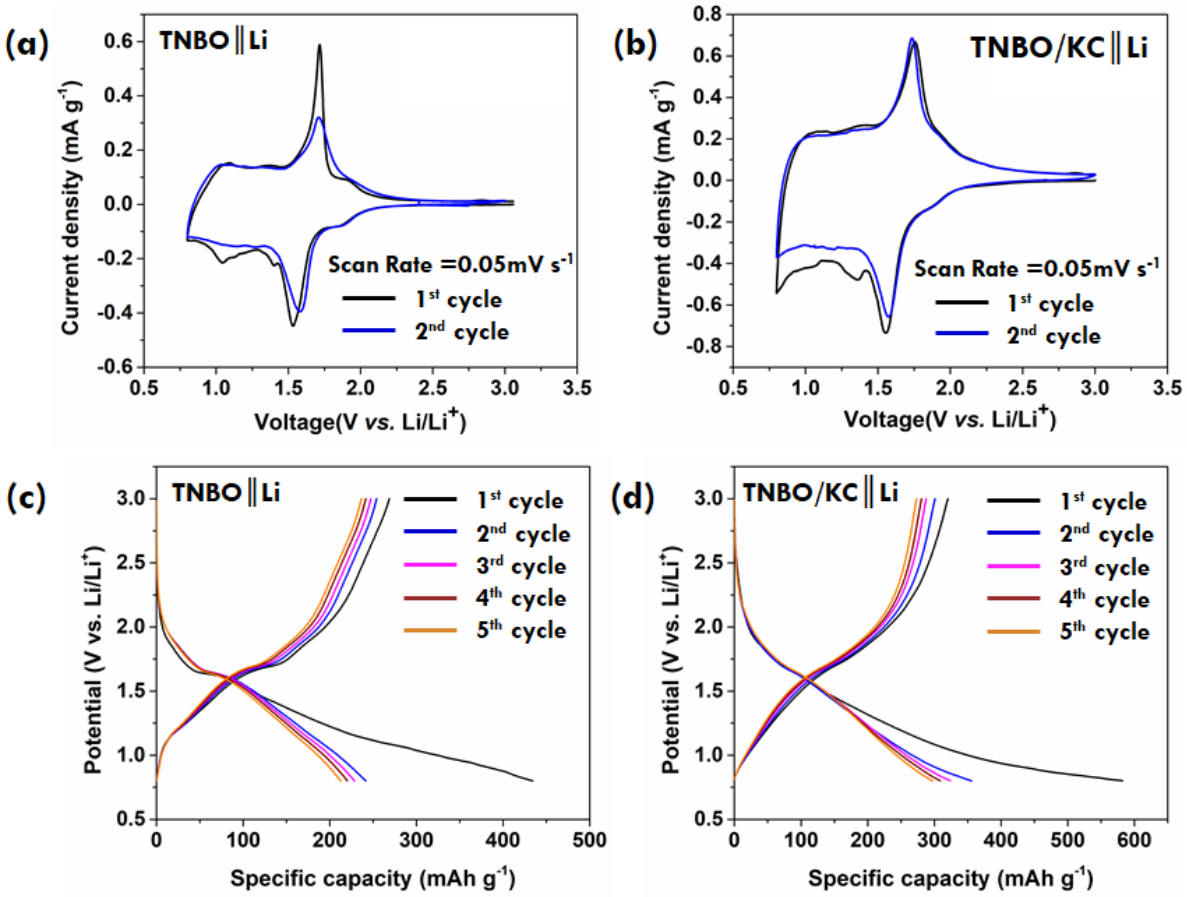

Figure 48: CV plots of (a) TNBO‖Li and (b) TNBO/KC‖Li cells, charge-discharge profiles of (c) TNBO‖Li and (d) TNBO/KC‖Li cells at 0.1 C (1 C=387 mAh g^{-1}).

The galvanostatic charge-discharge tests of the TNBO‖Li and TNBO/KC‖Li cells were conducted at different current rates (theoretical capacity at 1 C = 387 mAh g^{-1}) in the voltage range of 0.8-3.0 V. Figure 48c and d shows the charge-discharge profile of TNBO‖Li and TNBO/KC‖Li cells, respectively for the first five cycles at 0.1 C rate. It is noteworthy that the 1st cycle of both TNBO‖Li and TNBO/KC‖Li cells exhibited very high initial discharge capacity of 434 mAh g^{-1} and 582 mAh g^{-1} and low initial columbic efficiency of 62.0% and 55.0%, respectively. This is ascribed to the degradation of the electrolyte and SEI formation.[45] It is noteworthy that the reversible capacities obtained in TNBO/KC‖Li cells are much higher than so far reported in $TiNb_2O_7$ nanocomposites and twice the value of $Li_4Ti_5O_{12}$ (~170 mAh g^{-1}), indicating its practical applicability as anode material in LIBs.

The remarkable electrochemical performance of TNBO/KC‖Li is ascribed to the unique structure of the nanocomposites, as shown in the schematic. The interconnected porous scaffold-like structure of $TiNb_2O_7$ and $(Ti_{0.712}Nb_{0.288})O_2$ nanocrystals in TNBO/KC can effectively relieve the unexpected stress arising from continuous charge/discharging process of Li^+-ions, thereby facilitating the diffusion of Li^+-ions

between the electrode-electrolyte interface. Whereas the formation of reduced non-stoichiometric oxide phase having shared lattice sites of Ti and Nb atoms in the crystal structure of $(Ti_{0.712}Nb_{0.288})O_2$ (Figure 45d) creates O^{2-} vacancies in the crystal structure imparting electrical conductivity due to electronic disorder. As a result, reduced $(Ti_{0.712}Nb_{0.288})O_2$ nanocrystals can act as conducting bridge to build a good electrical contact between $TiNb_2O_7$ nano crystallites and the carbon matrix, which synergistically combines good electrochemical interaction with improved electronic and ionic conductivity leading to enhanced electrical conductivity, higher D_{Li} and lower charge transfer resistance in contrast to pristine TNBO.

4.1.2 Carbon-coated $TiNb_2O_7$ by PECVD as anode material for LIB

Inspired by the high performance of the $TiNb_2O_7$/KC material, an alternative route for adding carbon as a protective and supporting layer on $TiNb_2O_7$ was chosen. First, $TiNb_2O_7$ (TNO) was synthesized by sol-gel synthesis, and second, carbon was coated by PECVD using methane as the carbon source (Figure 49).

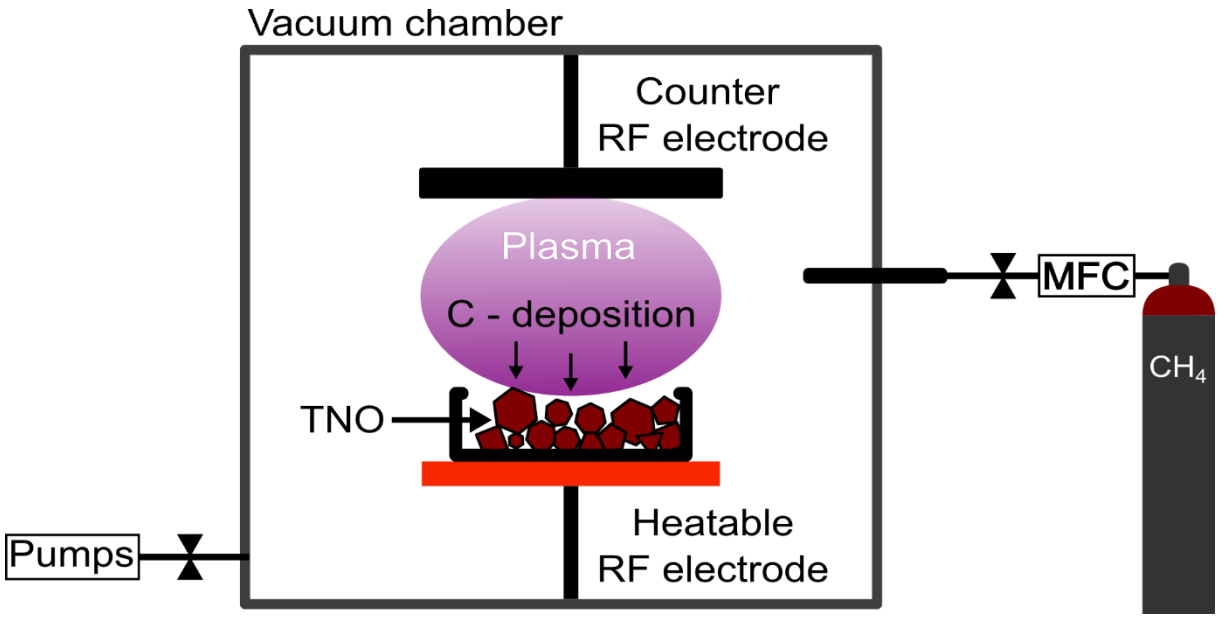

Figure 49: PECVD of TNO particles with methane as carbon source.

The benefit of the sol-gel process allows the obtainment of solid products by gelation rather than by crystallization or precipitation. During the sol-gel process, an oxide network is created by progressive polycondensation reactions of molecular precursors in a liquid medium and the final removal of the solvent, as illustrated in Figure 50. Typically, the sol-gel process is used for coatings where the gelation process occurs after the sol is cast, dip- or spray-coated on a substrate. However, the sol-gel route can be used for the synthesis of powders with nano-sized particles.[309]

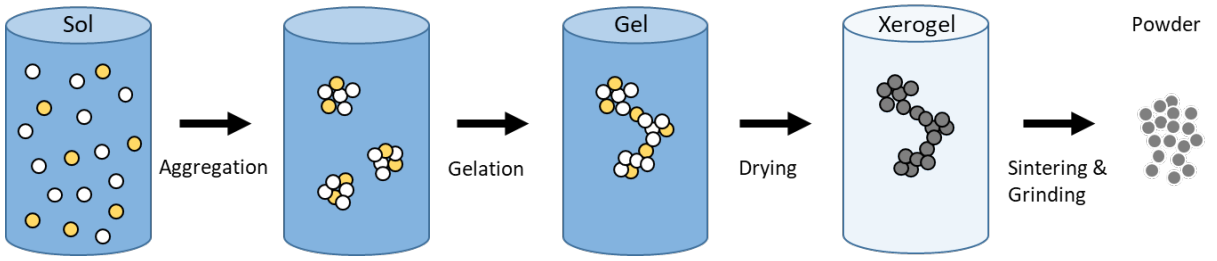

Figure 50: Schematic illustration of a Sol-Gel synthesis.

Figure 51a and b show the SEM images of the sol-gel-process synthesized TNO particles and the carbon-coated TNOC particles after the PECVD. In Figure 51c, a photograph of both powders is presented. As seen from SEM analysis, the as-synthesized particles (TNO) have an undefined shape but are uniformly distributed. The particle sizes range from 10 to 500 nm. The particles tend to form agglomerates forming bigger-sized microparticles. After the carbon-coating process, the particles did not change in morphology or size.

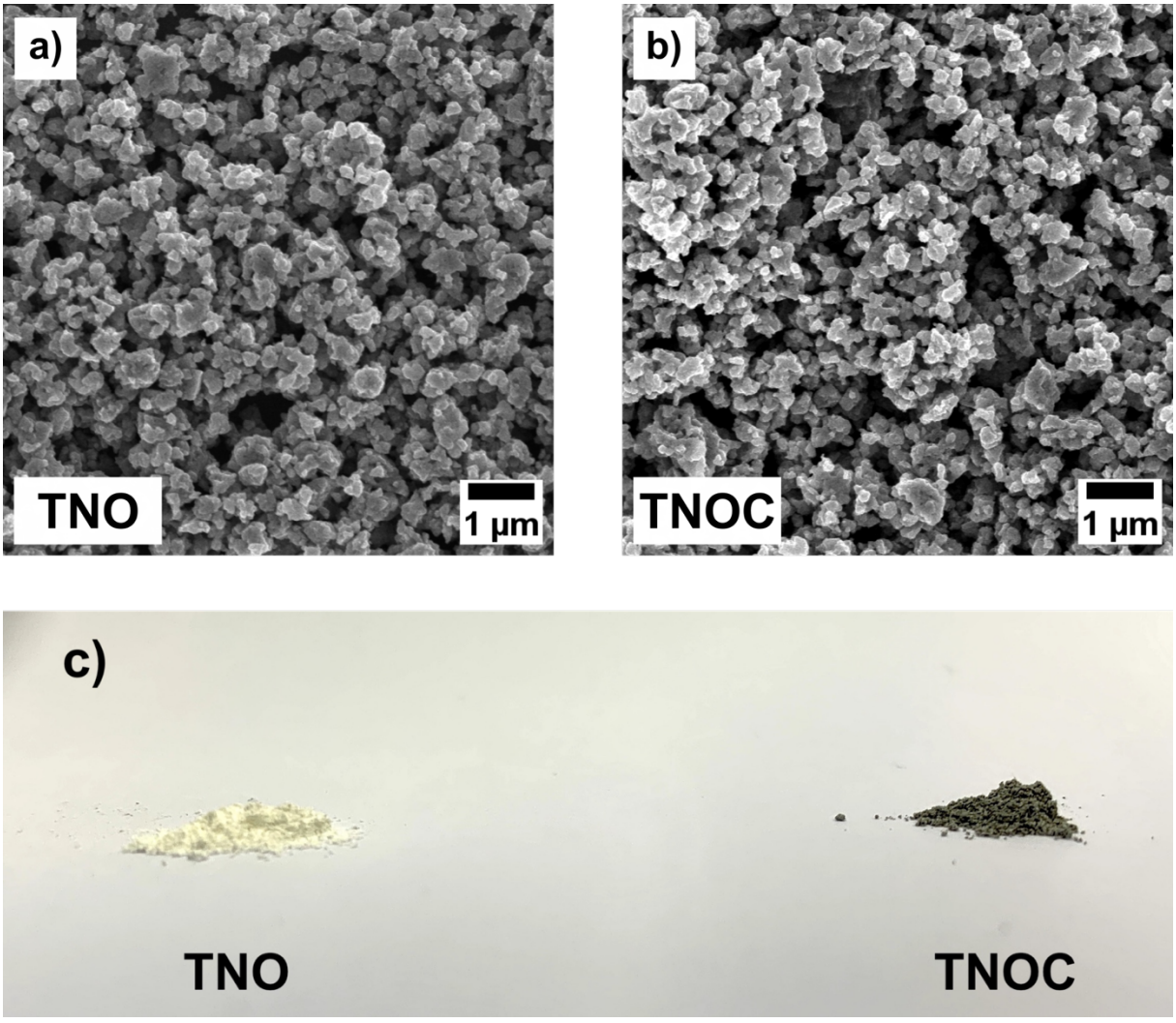

Figure 51: SEM image of a) TNO and b) TNOC. c) Photograph of TNO and TNOC.

The XRD pattern of the TNO and the TNOC is presented in Figure 52a. Before and after the plasma process, the peak positions nor the peak shapes were found to change. The characteristic peaks were assigned to the monoclinic $TiNb_7O_{10}$ (PDF# 39-1407). The peak positions are shifted slightly to higher 2 Theta values, and the peaks tend to broaden. These effects can be explained by limitations in measuring nanoparticles by XRD.[310]

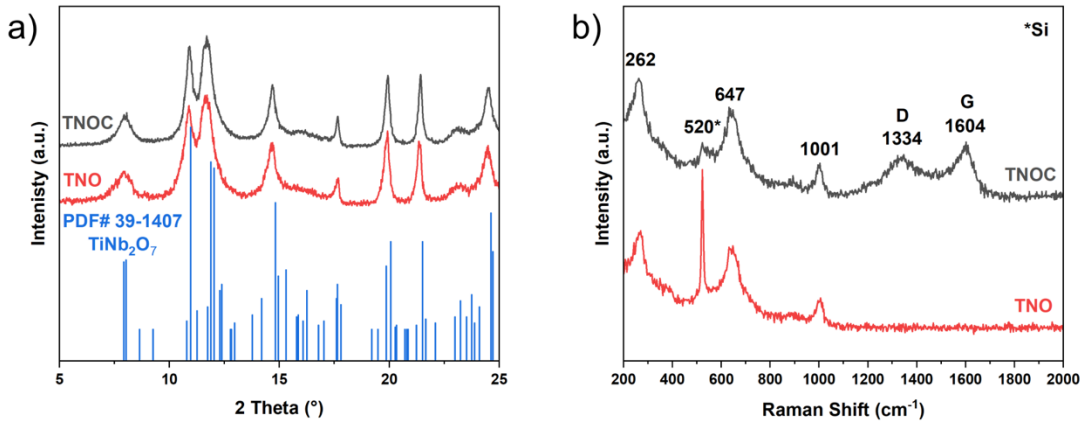

Figure 52: a) X-ray diffraction pattern of TNO and TNOC with the reference pattern of $TiNb_2O_7$ (PDF# 39-1407) and b) Raman spectra of TNO and TNOC.

Raman spectroscopic measurements were carried out to prove the origin of the TNO structures and the presence and nature of the carbon species. The Raman spectrum in Figure 52b shows the characteristic Raman shifts of 262, 647, and 1001 cm^{-1}. Both spectra additionally have a peak at 520 cm^{-1}, which is due to the used silicon substrate. The different intensities of the Si peak appear from the different measurement positions because the power, the integration time, and the accumulations were held the same for both samples. For the TNOC samples, two additional peaks at Raman shifts of 1334 and 1604 cm^{-1} could be measured. These peaks belong to the D and the G band of carbon structures. The broadness and the high intensity of the D band imply that most of the carbonous structures are of amorphous origin. However, the G band is a little bit sharper and has a more defined maximum peak position, which indicates the present of some sp^2 hybridized carbon atoms.

The origin of sp^2 carbon atoms could also be observed during XPS high-resolution measurements of the C 1s orbitals. First, from the XPS survey spectra, signals of niobium, carbon, titanium, and oxygen were measured in both samples (Figure 53). The element quantification of TNO showed a chemical composition ratio of Ti : Nb in 1 : 4, which is closer to the Ti : Nb_5 ratio in $Ti_2Nb_{10}O_{29}$ than the Ti : Nb_2 in $TiNb_2O_7$. This ratio did not change for the carbon-coated sample. The presence of carbon on the non-coated sample comes from adventitious carbon from the atmosphere and some unburned organic residiues.[304] After the PECVD process, the carbon content was increased by 6.3 at.%. This amount can be assigned to the carbon deposited by the PECVD (Figure 53).

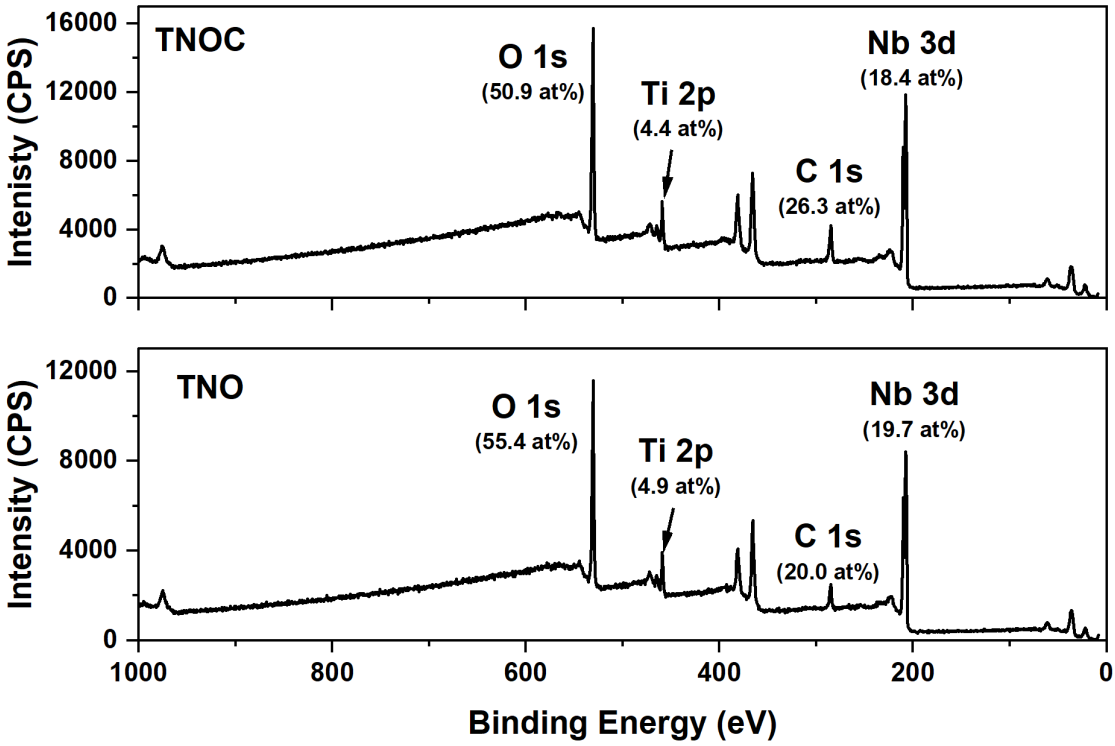

Figure 53: X-ray photoelectron spectra of TNO (bottom) and TNOC (top).

The deposition of a small amount of carbon could also be measured by EDX spectroscopy (Table 4). Moreover, the values in the table show that the ratio of Ti : Nb (1:2) is more in accordance with the $TiNb_2O_7$ measured by XRD as with the XPS results.

Table 4: EDX measured values of TNO and TNOC

	Titanium (at.%)	Niobium (at.%)	Oxygen (at.%)	Carbon (at.%)	Silicon (at.%)	Ratio (Ti:Nb)
TNO	6.1	11.8	39.0	16.1	27.0	1:1.9
TNOC	4.5	9.4	38.1	19.0	29.0	1:2.1

Since XPS is a surface-sensitive technique and only measures the composition of the first 10 nm of the sample, the electron beam for the EDX analysis penetrates the sample deeper and excites electrons deeper in the sample than 10 nm. By combining the results of XRD, XPS, and EDX, it seems that the core of TNO particles forms a $TiNb_2O_7$ structure, while the surface consists of $Ti_2Nb_{10}O_{29}$, as illustrated in Figure 54.

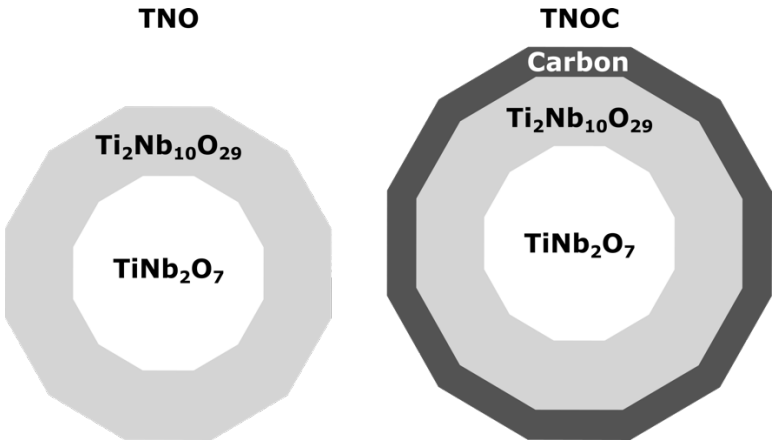

Figure 54: Schematic illustration of TNO and TNOC particles.

High-resolution analyses were performed on the one hand to analyze the chemical environment of the carbon atoms and on the other hand to investigate a possible reductive process of Ti or Nb by the plasma process since it is known that CH_x* radicals can have a reductive effect during the process (Figure 55). By comparing the C 1s HR spectra, it was analyzed that after the carbon-coating C=C binding could be found at binding energies of 284.5 eV.[311,312] Other bindings of C-C, C-OH, C=O, and O-C=O arise from the adventitious carbon.[304] By having a closer look at the HR spectra of Nb 3d and Ti 2p, the binding energies of 207.3 and 458.8 eV confirm the valence states of Nb^{5+} and Ti^{4+}. In comparison to the HRs of the TNOC, the binding energies shifted just slightly by 0.2 eV to higher binding energies, whereas no second species of possible Nb^{4+} nor Ti^{3+} were found. Finally, the HR of O 1s orbitals seems to be similar for the TNO and the TNOC sample, with the only difference of the 0.2 eV shift to the higher binding energy of the M-O peak.

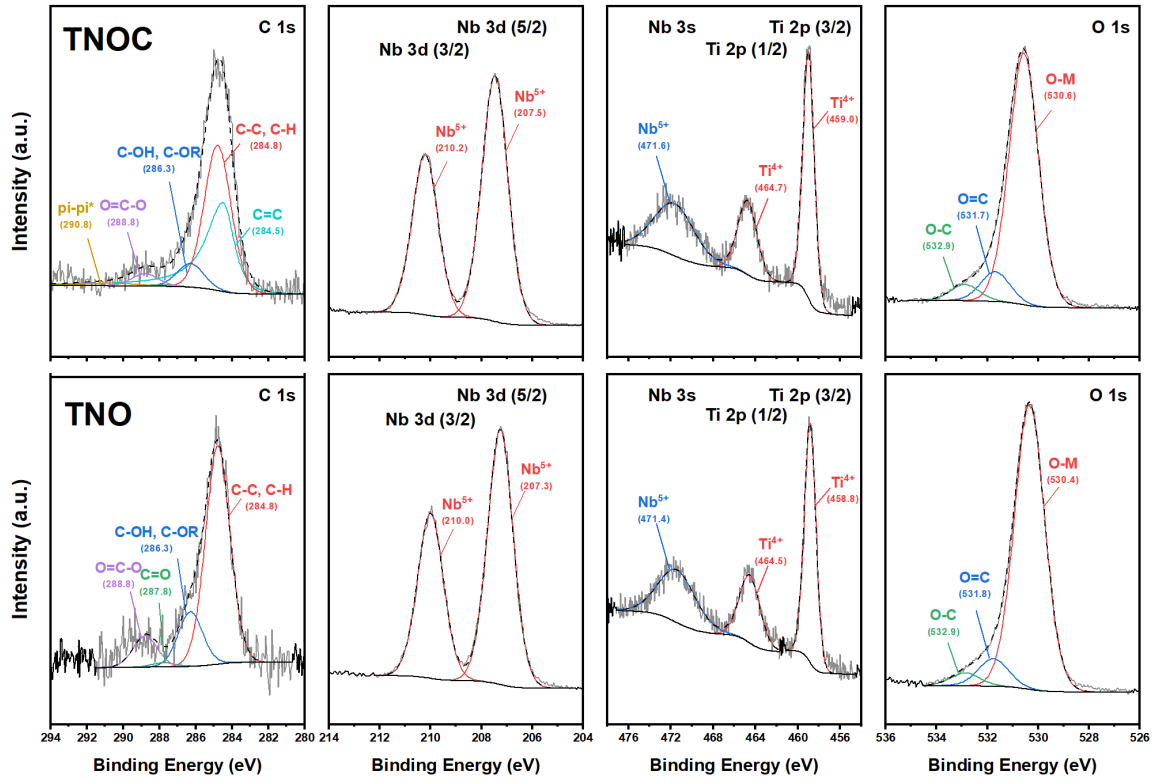

Figure 55: High-resolution X-ray photoelectron spectra of the C 1s, Nb 3d, Ti 2p/Nb 3s, and the O 1s orbitals for both TNO (bottom) and TNOC (top).

Cyclic voltammetry and galvanostatic charge-discharge rate measurements were performed to investigate the influence of the carbon-coating on the TNO particles. Figure 56a shows the cyclic voltammetry of the pristine TNO particles. The expected peaks at 1.50 V/1.67 V for TNO‖Li and TNO/C‖Li cells, respectively, are attributed to the redox couple of Nb^{5+}/Nb^{4+}. The shoulder peak at 1.80 V is ascribed to Ti^{4+}/Ti^{3+} redox couples. The peaks at a low voltage of 1.24 V, respectively, are assigned to Nb^{4+}/Nb^{3+} redox couples. As already seen by the TNBO/KC compositions, the TNOC cells displayed larger peak intensities revealing a good reversible cycling process and better electrochemical kinetics as compared to the TNO‖Li cell (Figure 56b).

TNO and TNOC were investigated under charge-discharge conditions for rate capability tests under different current rates between 50 mA g^{-1} and 1600 mA g^{-1} (1C = 387 mAh g^{-1}) (Figure 56c and d). TNO exhibits capacities of 280 mAh g^{-1} at a current density of 50 mA g^{-1} (C = ~0.1), which is lower compared to TNOC, with a specific capacity of 295 mAh g^{-1}. Moreover, TNOC cells retained higher reversible capacities of 150 mAh g^{-1} after 60 cycles at 1600 mA g^{-1} (C = ~4), along with high and constant coulombic efficiency (~99%). On the contrary, TNO cells showed poor performance

with a reversible capacity of 100 mAh g^{-1} after 60 cycles with an unstable coulombic efficiency (98-102%).

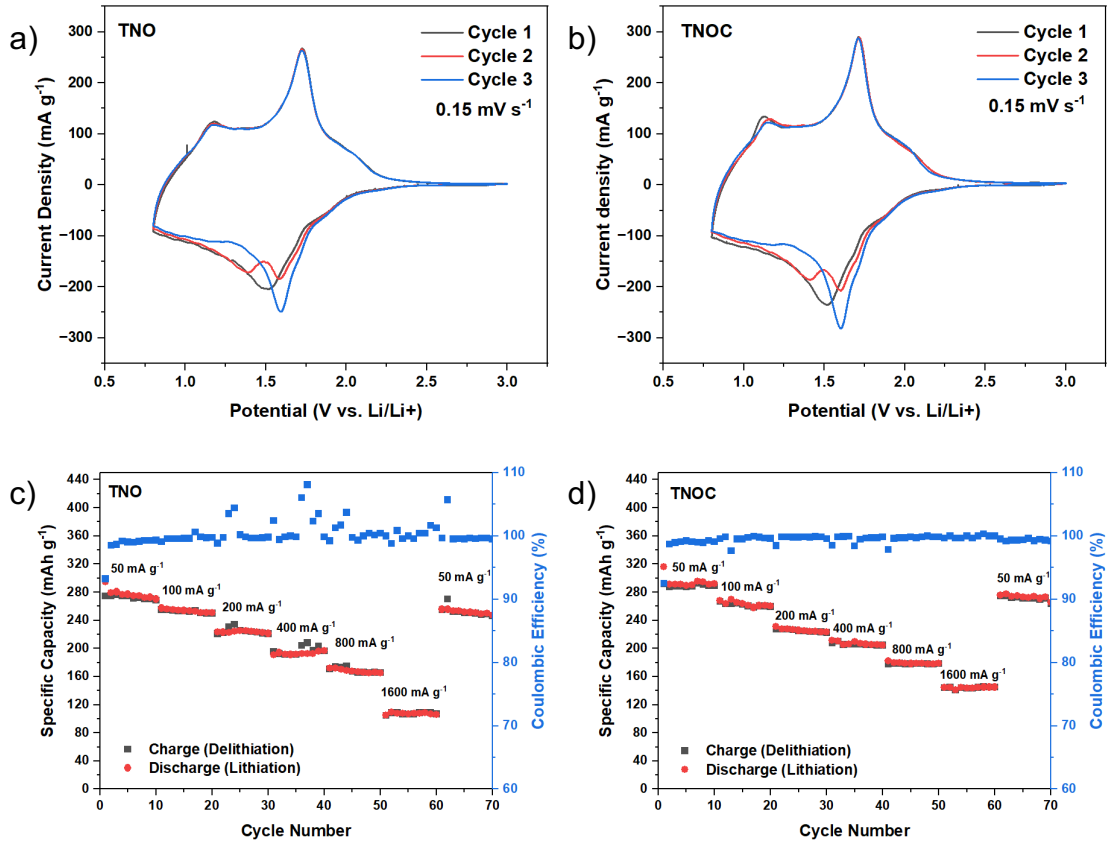

Figure 56: Cyclovoltammetry measurements of a) TNO and b) TNOC. Rate capability test of c) TNO and d) TNOC.

Moreover, TNOC cells showed remarkably higher capacity retention of 93% when cycled at 50 mA g^{-1}, whereas TNO showed lower capacity retention of 86% after 70 cycles. By comparing the coulombic efficiencies of the TNO and TNOC cells, a more stable efficiency close to 100% was measured for TNOC. However, TNO exhibits a very unstable efficiency between 97-108%. These results can be explained by the preservation of the carbon coating. Furthermore, the carbon coating supports the electron flow through a higher electrical conductivity measured by the increased amount of sp^2 carbons by XPS analysis. The effect of a higher electrical conductivity was already reported for the TNBO/KC composite material by retaining a higher reversible capacity and capacity retention for the TNBO/KC cell over the TNBO cell. It is noteworthy that the reversible capacities obtained in the TNO and TNOC cells are higher than in the TNBO and TNBO/KC cells.

4.2 Vanadium pentoxide (V_2O_5) as photoresponsive cathode

The following part of this section is published in the following peer-reviewed article with first author contribution, which includes the preparation of the manuscript, synthesis, graphics, and evaluation of the study. Post-mortem SEM measurements were conducted in collaboration with Prof. Yamada and Prof. Sekino SANKEN, Osaka university, Japan. Simulations of the band structures were done in collaboration with Prof. Hong, Fujian Normal University, Fuzhou, China. For the reproduction in the thesis/dissertation as an author, permission is not required [269]*:*

Wilhelm, M., Adam, R., Bhardwaj, A., Neumann, I., Cho, S. H., Yamada, Y., Sekino, T., Tao, J., Hong, Z., Fischer, T., & Mathur, S. Carbon-Coated Electrospun V_2O_5 Nanofibers as Photoresponsive Cathode for Lithium-Ion Batteries. *Adv. Eng. Mater.* 2200765 (**2022**).

The pristine and carbon-coated V_2O_5 nanofibers (VNFs) were analyzed by XRD for phase analysis that showed the formation of the orthorhombic phase Shcherbinaite of V_2O_5 (PDF no. 41-1426). Upon the carbon coating through plasma-enhanced chemical vapor deposition of CH_4, an additional peak was observed after 60 min at a 2 theta value of ~13°, which increased in intensity upon prolonged (120 min) treatment (Figure 57a). This peak indicated the formation of VO_2 as a result of the carbothermal reduction ($V^{5+} \rightarrow V^{4+}$) of the VNF under plasma conditions.[291] The decomposition of CH_4 during PECVD leads to the formation of hydrocarbon radicals with the following fragmentation sequence to carbon: $CH_3 \rightarrow CH_2 \rightarrow CH \rightarrow C$ (s) with concomitant formation of VO_2. [291,313] Through Rietveld refinement the amount of the VO_2 secondary phase could be identified for VNF-C-60 as V_2O_5(ortho):VO_2(tetra) = 95:05 and for VNF-C-120 as V_2O_5(ortho):VO_2(tetra) = 87:13.[314]

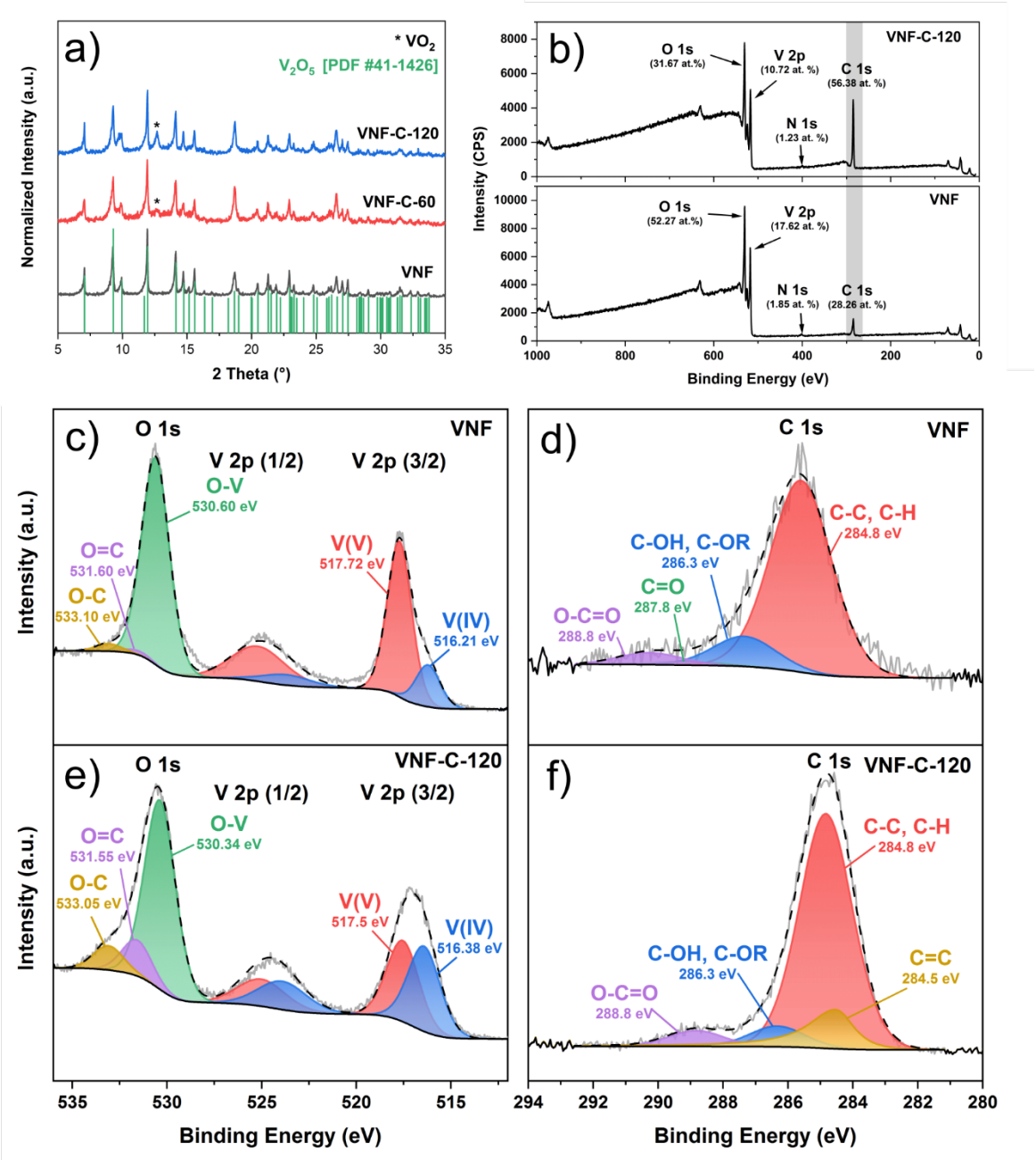

Figure 57: a) XRD pattern of VNF, VNF-C-60, and VNF-C-120, b) XPS survey spectra of VNF and VNF-C-120, c) O1s and V2p HR-spectra of VNF, d) C1s HR-spectra of VNF, e) O1s and V2p HR-spectra of VNF-C-120, f) C1s HR-spectra of VNF-C-120.

The survey X-ray photoelectron spectrum (XPS; Figure 57b) of pristine VNF (bottom) and VNF-C-120 (top) exhibited the expected signals of vanadium and oxygen. In addition, residual contents of carbon and nitrogen originating from methane and nitrogen plasma were observed. During the PECVD carbon-coating, the carbon content (C 1s) could be increased from 28.26 to 56.38 at.%, which is an increase in the C:V ratio from 1.6 to 5.3, respectively. A high-resolution XPS analysis of the C 1s signal (Figure 57f) showed a small amount of sp^2 hybridized carbon (284.5 eV) in the VNF-C-120 sample,

whereas this peak was absent in the pristine VNFs (Figure 57d).[315] The high-resolution XPS spectra of the V 2p peak (Figure 57c) of the VNF exhibited two peaks, which are separated by ~1.3 eV and can be assigned to V(IV) at ~516.3 eV and V(V) at ~517.6 eV. After the PECVD the amount of V(IV) is increased indicating the reducing effect of methane/nitrogen plasma that explains the near-surface reduction of overlayer leading VO_2// V_2O_5 shell-core structure, as evident in the XRD analysis (Figure 57e).[316–319]
The SEM image of the sintered green fibers (Figure 58a) showed nano-crystalline fiber structures with an average diameter of 100-200 nm. After the PECVD process, the fiber morphology was retained, showing that the PECVD treatment has no detrimental influence on the fibrous morphology (Figure 58b). TEM measurements of the VNF-C-120 fibers showed a carbon-coating of around 10 nm (Figure 58c, d, e). Besides some amorphous regions, a crystal lattice distance of d = ~ 0.33 nm could be measured by HR-TEM analysis, which is close to the distance of the hexagonal planes in graphitic carbon (Figure 58f).[320,321] These results are in accordance with the XPS measurements revealing the presence of sp^2 carbon.

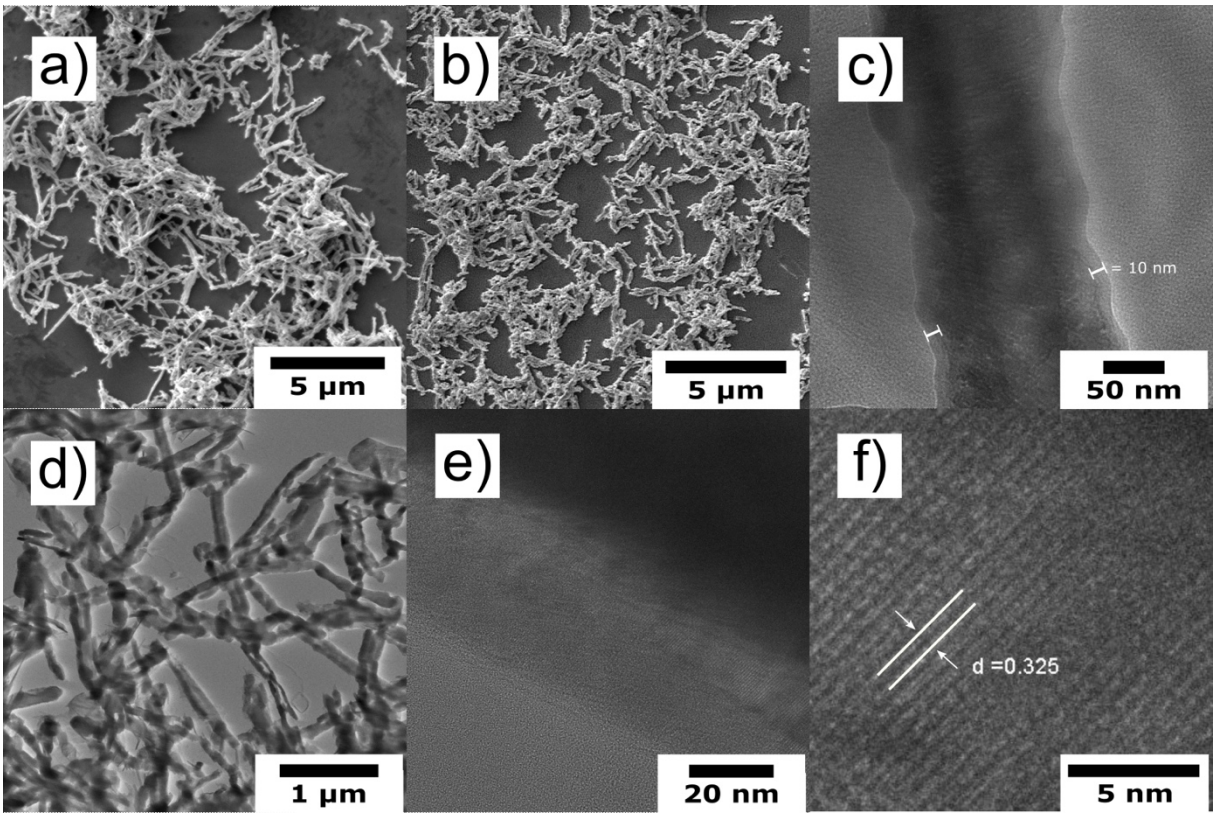

Figure 58: a) SEM image of VNF, b) SEM image of VNF-C-120, c) and d) TEM image of VNF-C-120, e) and f) HR-TEM images of VNF-C-120.

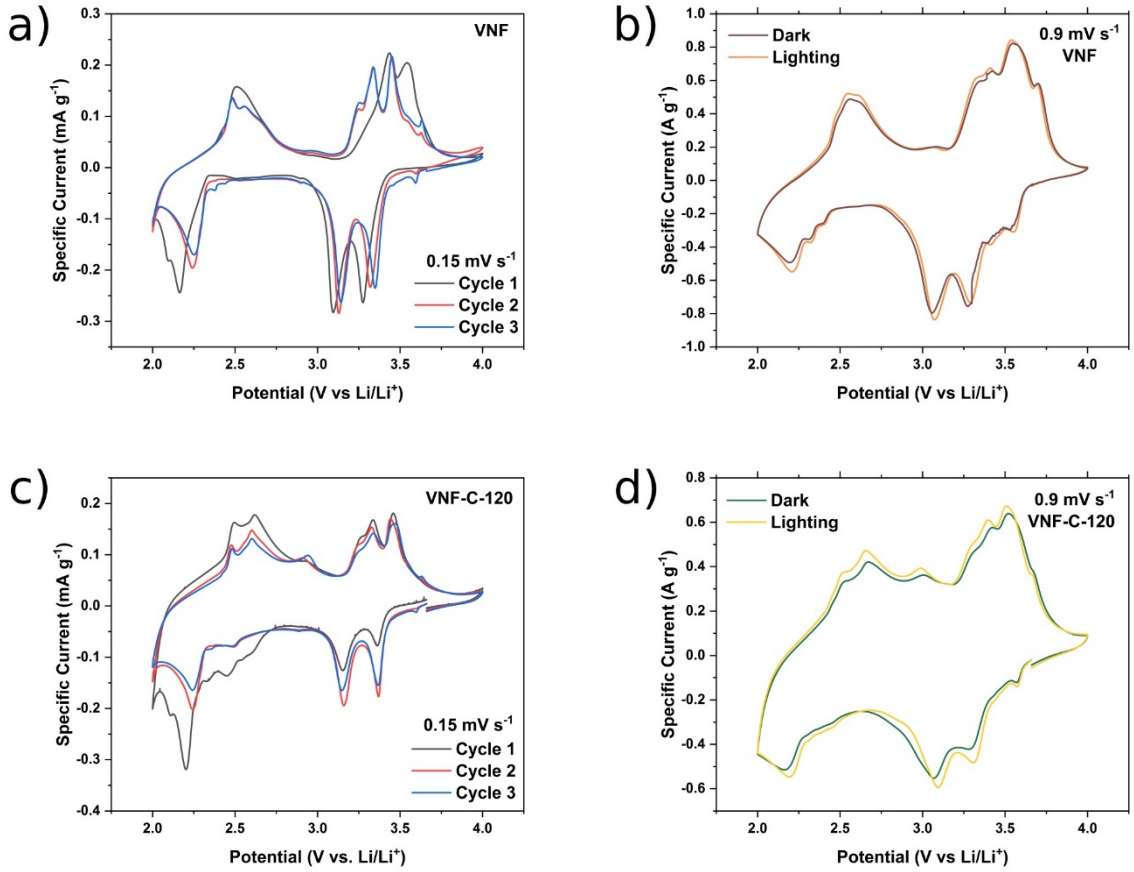

Figure 59: CVs of VNF cycles 1-3 at 0.15 mV s^{-1} in dark, b) CVs of VNF at a current density of 0.9 mV s^{-1} in dark and light (cycle 8 and 9), c) CVs of VNF cycles 1-3 at 0.15 mV s^{-1} in dark, d) CVs of VNF at a current density of 0.9 mV s^{-1} in dark and light (cycle 8 and 9).

The electrochemical performance of the photoelectrode containing the 1D electrospun V_2O_5 fibers was analyzed by potentiostatic and galvanostatic measurements. Figure 59a shows CV curves with applied potentials from 2 V to 4 V using a scan rate of 0.15 mV s^{-1} for the first three cycles. The cathodic peaks at 3.3 V, 3.1 V, and 2.2 V represent phase transitions of $Li_xV_2O_5$ induced by Li^+ intercalation. From 3.3 V to 3.1 V crystal phase changes from α-$Li_xV_2O_5$ to ε-$Li_xV_2O_5$, and from 3.1 V to 2.2 V, a transition to γ-$Li_xV_2O_5$ (2.2 V) corresponding to 2 intercalated Li^+ ions occurs.[283] The anodic peaks at 2.5 V, 3.3 V, and 3.5 V represent the deintercalation of Li^+ and oxidation of vanadium to the reversible formation of the α-$Li_xV_2O_5$ phase.[283,322] The phase transition peaks at the first cathodic cycle (black line) shifted towards the second (red) and third cycle (blue) to a more positive potential range for the pristine VNF. For the carbon-coated VNF, the redox peaks remained at the same positions (Figure 59c). The shift from the first to the second is caused by the formation of the solid electrolyte interphase (SEI) or rather cathode electrolyte interphase (CEI), which appeared because of the

reduction of the electrolyte.[323–326] Upon comparing both the CV curves, it is evident that the transitions between the redox peaks for the VNF-C-120 electrodes are much broader compared to the VNF. Moreover, different line shapes appeared in the voltage range of 2.7 V to 2.0 V. An additional redox peak during the cathodic reaction can be seen at around 2.5 V in the case of carbon-coated electrodes. This peak is also visible in the anodic reaction at around 2.9 V only for the carbon-coated sample, which could be related to the redox chemistry of the secondary VO_2 phases available in the associated material. VO_2 possessing vanadium in the 4+ valence state offers better accessibility of oxidation at relatively lower activation polarization.[319,327,328]

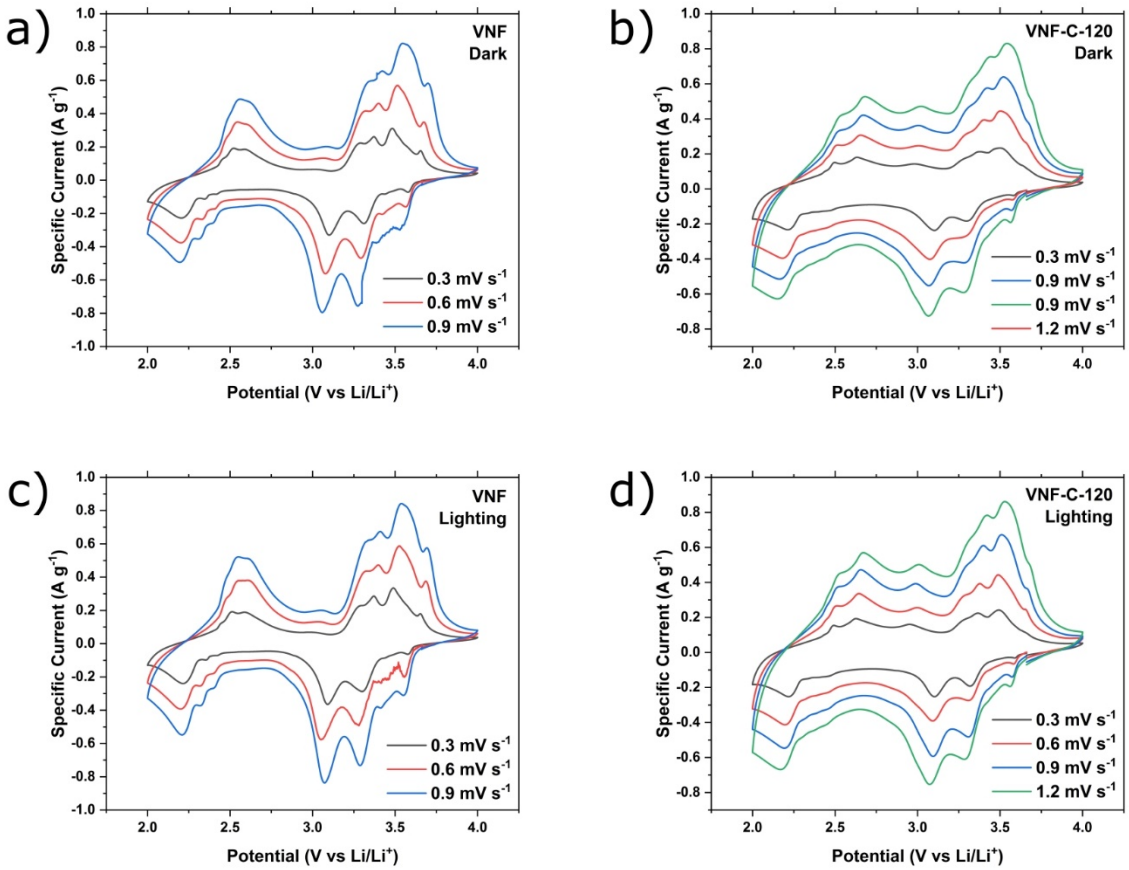

Figure 60: Cyclic voltammetry of VNF and VNF-C-120 in dark (a and b) and c) and d) under illumination at different current densities.

CV measurements at different scan rates (0.15 – 1.2 mV s^{-1}) of the photocathode were performed to investigate the influence of light (400 nm, 11 mW cm^{-2}) on the electrochemical processes in the voltage window of 2-4 V (Figure 60a-d). For the CV cycles, which were recorded under light illumination, the redox peak positions were retained, whereas the current density was found to increase indicating the photoresponsive nature of the electrode. Interestingly, similar observations were made for the carbon-

coated fibers. At higher current rates (0.9 mV s^{-1}), the redox peaks of the VNF appear to fade in current density and showed less stability compared to the VNF-C-120, indicating good reversibility of carbon-coated fibers during successive cycling (Figure 59b, d). Furthermore, by the direct comparison of the VNF and the VNF-C-120 at a scan rate of 0.9 mV s^{-1}, it was observed that the influence of photo illumination was higher for the carbon-coated fibers than for the non-carbon-coated fibers suggesting that the carbon-coating not only increases the structural integrity of V_2O_5 nanofibers through reduced surface reactions but also improves electrical conductivity.[329] Similar observations were made by Reddy et al. for V_2O_5-PEG nanobelt composites.[330] Moreover, a decomposition of the active material and a subsequent failure of the cell at higher current densities was seen at voltages around 3.5 V. Cycling at a current density of 1.2 mV s^{-1} was not possible to perform for the VNF cells due to degradation (Figure 60a, c). A similar failure of the cell at high C-rates (> 3C) was observed during charge-discharge cycling of uncoated VNFs whereas the carbon-coated VNF showed stable performances up to 6 C in the dark and illuminated state (Figure 62c, d). Interestingly, the impact of the illumination was much higher upon returning from a high C-rate (6 C) to a low C-rate (0.75C) of the VNF-C-120. Whereas in dark a specific discharge capacity of 72 mAh g^{-1} was measured, a specific capacity of 134 mAh g^{-1} could be measured after a light-stimulated charging (Figure 61).

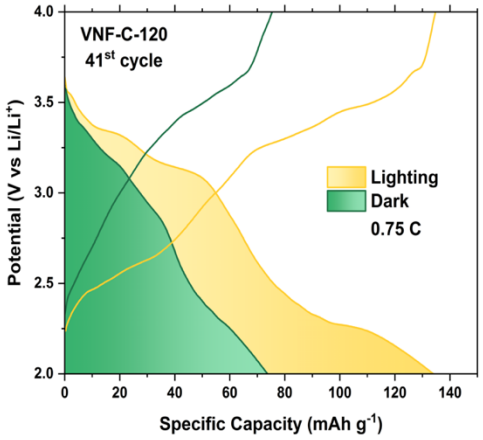

Figure 61: Galvanostatic discharge-charge curves at 0.75 C (= 221 mA g^{-1}) in dark and lighting conditions for the 41st cycle of VNF-C-120 after rate capability

Galvanostatic charging-discharging curves could be measured yielding a high discharge capacity of 164 mAh g^{-1}, which could be increased up to 179 mAh g^{-1} (C rate of 0.75) under light illumination (11 mW cm^{-2}, 11th cycle) for the VNF (Figure 62a).

Carbon-coated VNF delivered a discharge capacity of 146 mAh g^{-1} in dark, which was enhanced by 15 mAh g^{-1} (161 mAh g^{-1}, 11th cycle) under the illumination of light (Figure 62b).

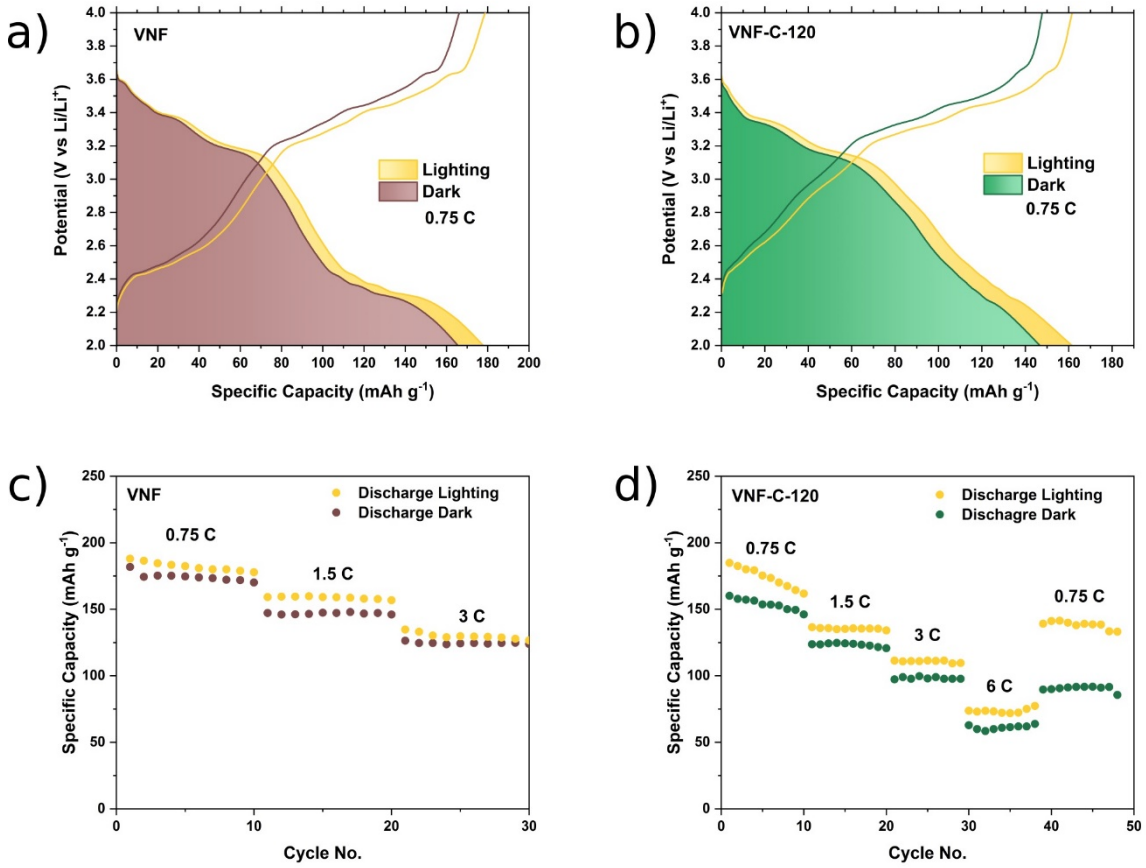

Figure 62: Galvanostatic discharge-charge curves at 0.75 C (= 221 mA g^{-1}) in dark and lighting conditions for VNF and VNF-C-120 (11th cycle). c) and d) presenting the rate performances of VNF and VNF-C-120 photo-batteries in dark and lighting.

Electrochemical impedance spectroscopy (EIS) was performed for the evaluation of numerous polarization processes and correlating their physical significance to the electrochemical device under study. The Nyquist plot in Figure 63a demonstrates a similar overall structure of EIS composed of a semicircular arc and diffusion-limited tail at the low frequencies. There is a significant reduction of impedance in carbon-coated VNF. The estimation from the equivalent circuit model (ECM, shown in Figure 63a) fitting suggested that both, the bulk resistance (R_b) and the charge-transfer resistance (R_{ct}) decreased from 13 to 9.2 Ω and 84.1 to 48.2 Ω, over the application of carbon coating, respectively verifying the conductive nature of carbon coating. This indicated that in addition to increasing the conductivity of vanadium oxide nanofibers, the carbon coating also helps in improving the kinetics of the charging and discharging process by facilitating an improved Li insertion/desertion reaction. To further study the polarization

properties of the VNF-C-120 cathode at different cell operation steps, impedance was measured at pristine, charged, discharged, and discharged under illumination conditions (7th cycle). In Figure 63b, the semicircular arc related to the charge-transfer resistance of the impedance is seen to be dramatically shrunk over the initially consecutive cycles. In addition, the additional tail related to diffusional processes was diminished. It is worth noting that the impedance of the charged cell has higher impedance in comparison to discharged due to a higher overpotential. Finally, the discharged cell under illumination shows the least impedance which was further quantified through ECM fitting. While the bulk resistance (R_b) reduced from 7.1 to 5.4 Ω upon 7 cycles, there is nearly no impact of charged or discharged conditions on it. Contrarily, the charge-transfer resistance (R_{ct}) related to the reaction between Li^+ and VNF gradually decreases at each step from 295.6 Ω at pristine, 77.1 Ω at the charged, 58.1 Ω at the discharged, and 36.1 Ω, least at the discharged under illumination condition.

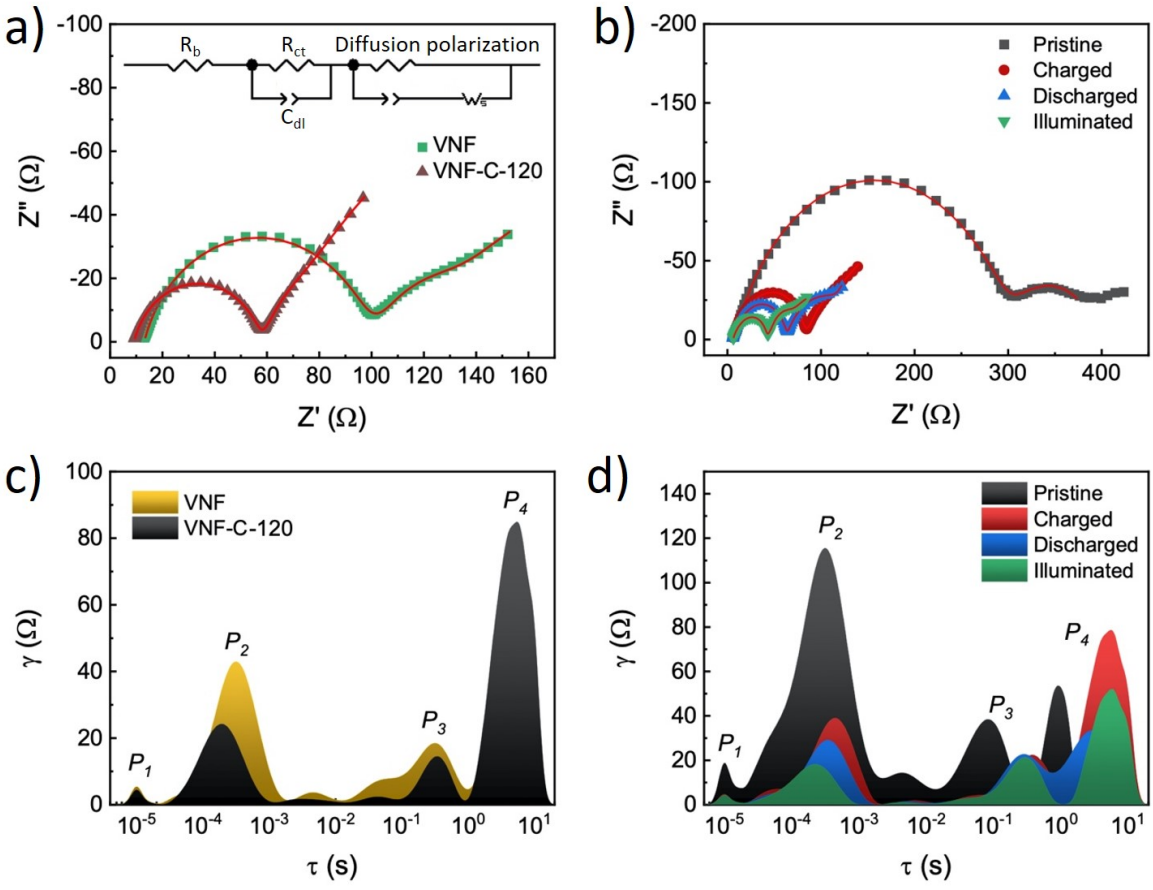

Figure 63: Nyquist plot and the DRT spectra of impedance for (a, c) VNF and VNF-C-120 cells, and (b, d) VNF-C-120 cell at pristine, charged, discharged and discharged under illumination condition.

The distribution of relaxation times (DRT) analysis of the impedance spectra could give a better picture of the polarization processes on a wider time constant scale. The DRT conducted with a regularization parameter of 10^{-3} on both the real and imaginary part

of impedance resulted in well classified numerous polarization peaks as illustrated in Figure 63c and d. Taking into account the major polarization processes, the observed spectra could be classified into four major peaks, **P_1**: assigned to the electronic and ionic conduction limited by ohmic resistance, **P_2**: Li^+–V_2O_5 reaction rate limited charge-transfer resistance, and **P_3**: interfacial resistance related to Li-ion motion at the VNF/electrolyte interface, and **P_4**: the solid-state Li-ion diffusion, respectively. As observed in Figure 63c, the carbon coating of VNF resulted in a significant reduction of P_1 to P_3, though an opposite observation for P_4 was also evident. In Figure 63d, the DRT spectra of impedance for VNF-C-120 as a function of cell condition is illustrated. Cycling the cell has a dramatic reduction in all the polarizations P_1 to P_4, but more importantly, the process classified as P_3 and P_4 has been shifted toward higher time constants. While the cell operation condition changes from charged to discharged and further subjected to illumination, P_2 related to the Li^+–V_2O_5 reaction diminishes gradually, indicating fast reaction kinetics especially enhanced under the light illumination. Meanwhile, P1 and P3 are not affected by these variations. P_4, at the charged state as well as under the charging process occurred due to the light illumination showed an increase due to the solid-state diffusion of Li-ion at the lithium metal counter electrode. Moreover, the DRT analysis indicated that although carbon coating of VNF minimizes the major polarization resistances such as indicated P_1 to P_3, the slower diffusion process of Li^+ migration points out further optimization of material characteristics for improving the performance of photo-driven LIBs.

The photograph in Figure 64a shows the charged (green-yellowish) and discharged (black) state of the VNF electrode in the coin cell. Long-term stability tests (300 cycles at 0.75 C in dark) showed that the carbon-coating can inhibit the structural instability of V_2O_5 representing a higher reserve of the capacity (98 mAh g^{-1}) upon cycling compared to the non-carbon-coated VNF (72 mAh g^{-1}). A capacity retention of 43.85% was achieved for VNF and 61.13% for VNF-C-120 after 300 cycles. Nevertheless, the pristine VNF electrode could not reach 400 cycles, due to the failure of the cell, which could be prevented by the carbon coating (Figure 64c). Photo charging tests were performed to calculate the photoconversion efficiency (PCE). Therefore, the coin cell was illuminated for three hours (400 nm, 11 mW cm^{-2}) without applying any external voltage. Afterward, the discharge capacity was measured at a current density of 10 mA g^{-1} in dark with a cut-off voltage of 2 V. In Figure 64d a photo charging up to 2.34 V for VNF and 2.43 V for VNF-C-120 could be measured. Discharge capacities

of 54.63 mAh g^{-1} (= 0.532 mWh) for VNF and 60.17 mAh g^{-1} (= 0.636 mWh) for VNF-C-120 could be reached. The calculation of the PCEs results in 4.24% (VNF) and 5.07% (VNF-C-120). The carbon-coated VNF electrode material showed a higher charging voltage, a higher discharge capacity, and a higher photoconversion efficiency compared to the non-carbon-coated VNF. Nevertheless, it was possible for both electrodes to power a blue LED (2V) by only light-charging the battery for 3 h (Figure 64b). The photo charging process of V_2O_5 electrodes mainly depends on the electronic cascade formed due to formation of VO_2 phase due to surficial reduction of V_2O_5 and conductive carbon coating.

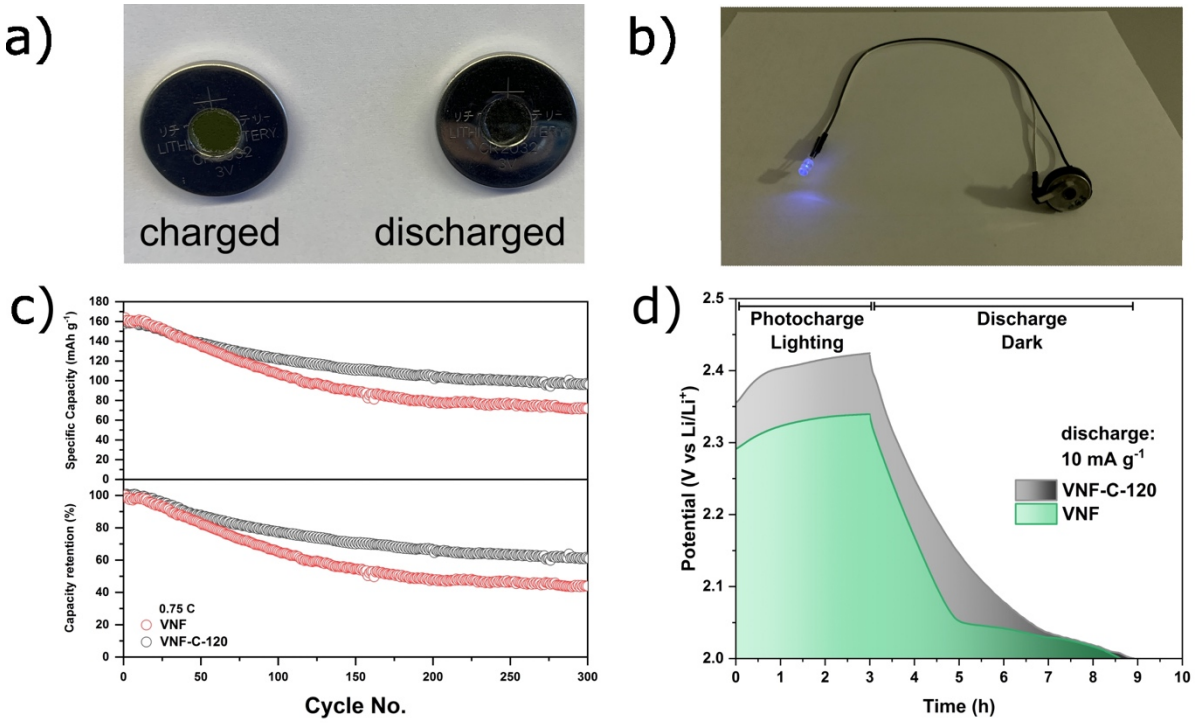

Figure 64: a) Photo-battery at de-lithiated charged (left) and the lithiated discharged (right) state, b) 2 V powered LED by photo charge only. c) Cycling stability and capacity retention tests at 0.75 C of VNF (red) and VNF-C-120 (gray). d) Photocharge under illumination without applying voltage and specific discharge in dark at a specific current of 10 mA g^{-1} of VNF (green) and VNF-C-120 (gray) of the photo-batteries.

The migration of photo-induced electrons and holes excited by the illuminated light could enhance the electronic and ionic conductivity of the electrode. According to the calculation results, the electronic conductivity of V_2O_5 under illuminated conditions is as high as $3.17 \times 10^{-3}\ S\ cm^{-1}$, and the Li^+ conductivity is $5.3 \times 10^{-4}\ S\ cm^{-1}$. According to the conditions (light intensity, window area, electrode porosity, etc.) adopted in our work, for the whole electrode, the photoexcited electron and Li^+ conductivity can be regarded as $6.04 \times 10^{-13}\ S\ cm^{-1}$ and $2.01 \times 10^{-13}\ S\ cm^{-1}$, respectively. The enhanced

ion transport capability under illuminated reduces the local polarization of the electrode under high current density, leading to the improved electrochemical performance, which is consistent with the results mentioned above. It is worth noting that these conductivities increase with increasing light intensity.

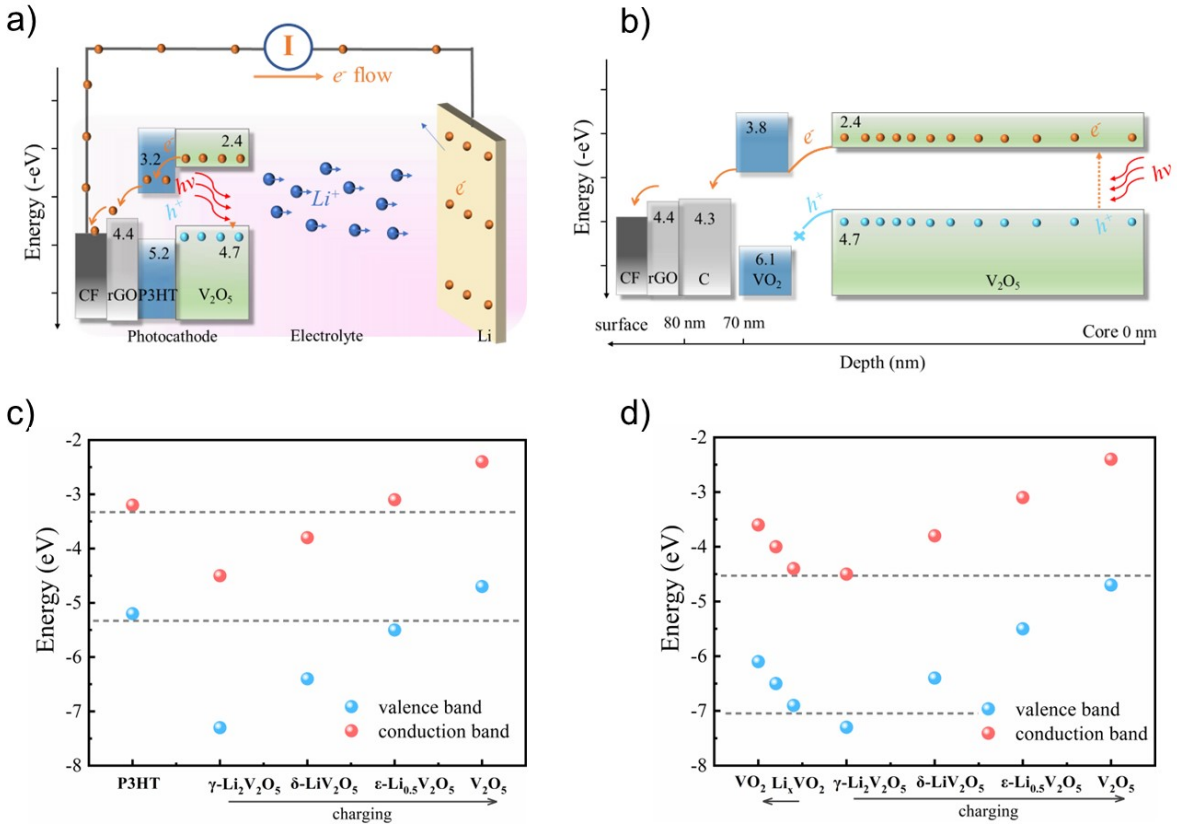

Figure 65: Schematic representing the photo charging mechanism of (a) VNF and (b) VNF-C-120. (c-d) the conduction band and valence band for the P3HT and the products after the insertion of Li^+ into V_2O_5 or VO_2.

The in-situ formation of VO_2 and carbon layer on the surface of V_2O_5, as displayed in Figure 65b, can effectively build a space charge layer which could move electrons but leave holes. This VO_2 layer formed via in-situ reduction, compared with the mechanically mixed P3HT, is undoubtedly better bonded and can further shorten the photoconduction channel, since the size of the V_2O_5 layer is reduced due to the formation of VO_2 overlayer, thus ensuring stable and high output of photocurrent density. Furthermore, as discussed in the Part II in Supplementary text and illustrated in Figure 65c, d, V_2O_5 and VO_2 have similar lithiation mechanisms and phenomena including the upward shift of Fermi level and the widen of bandgap, which could help build a dynamic self-adaptive interfacial band structure thus enabling photo chargeable behavior in the entire voltage range rather than a specific range. But it is impossible for V_2O_5 alone to achieve because the electronic structure and band gap of P3HT is fixed.

To elucidate the effect of carbon-coating on cycling stability, post-mortem SEM analysis of both pristine and carbon-coated VNF electrodes was carried out to investigate the structural deformation of the nanofibers upon electrochemical cycling (Figure 66). While the morphologies of the uncycled electrodes were quite similar, significant morphological differences were noticed in cycled electrodes. For the pristine VNF, it was observed that the fibers decomposed to smaller particles while losing the one-dimensional structure that was accompanied by the formation of nanosized needles corresponding to lithium dendrites (Figure 66c). On the other hand, the cycled carbon-coated VNF maintained the original fibrous morphology and a layered growth on the fibers is visible, which apparently prevents the dissolution of the active material in the electrolyte and leads to higher cyclic stability and better overall performance of the carbon-coated VNFs.[324,325]

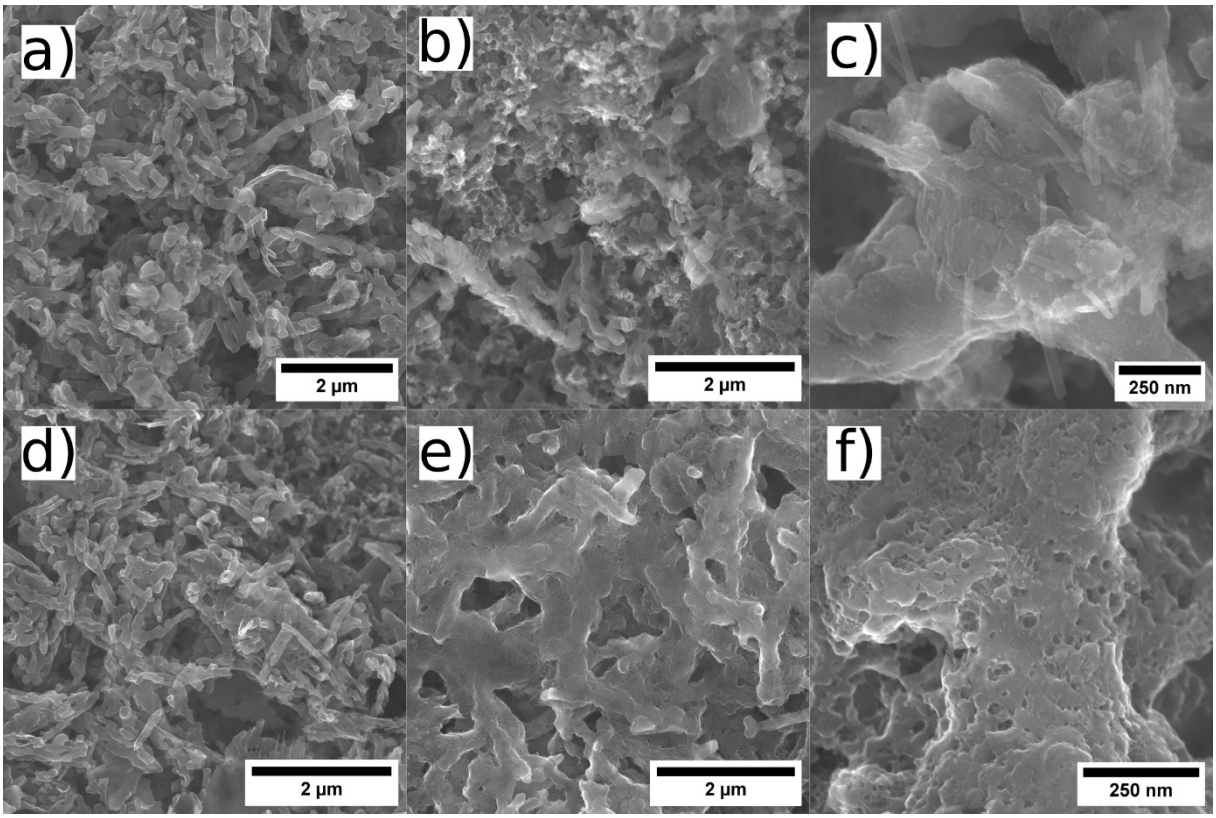

Figure 66: SEM images of photo electrodes at different states: a) VNF fresh prepared. b,c) VNF discharged (10th cycle). d) VNF-C-120 fresh prepared. e,f) VNF-C-120 discharged (10th cycle).

Table 5: Comparison with photocathode materials toward LIBs.

Photocathode material	Light wavelength/intensity/running time	Photo-conversion efficiencies (η)	Cycle performance: current density / cycle number/ capacity (mAh g^{-1}) /retention ratio	Ref.
VNF-C-120 (V_2O_5@VO_2@C)	400 nm/11 mW cm^{-2}/3 h	5.07%	0.221 A g^{-1}/300/98/ 61%	This work
VNF	400 nm/11 mW cm^{-2}/3 h	4.24%	0.221 A g^{-1}/200/72/ 44%	This work
V_2O_5	455 nm/12 mW cm^{-2}/5 h	2.6%	0.3 A g^{-1}/200/~75/ ~47%	[280]
LiV_2O_5	LED/33 mW cm^{-2}/5 min	9.1%	1 A g^{-1}/50/141/ ~70%	[331]
NT-COF	AM 1.5G/300W/0.5 h	-	0.02 A g^{-1}/100/100/ ~80%	[332]
N719 + $LiFePO_4$	1 sun	0.06%~0.08%	15 cycles	[333]

The overall photo-conversion efficiency was calculated based on the following equation:[266,280,334]

$$\eta_{overall} = \frac{E_{out}}{E_{in}} * 100\% = \frac{E_{discharge}}{P_{in} * t_{ph} * A_{ph}} * 100\%$$

Where, $E_{discharge}$ (E_{VNF} = 0.532 mWh – from BST8-MA battery analyzer, $E_{VNF\text{-}C\text{-}120}$ = 0.636 mWh) is the discharge energy at the specific current density of 10 mA g^{-1}, P_{in} (= 11 mW cm^{-2} for 400 nm illumination source) is the intensity of illuminated light, t_{ph} (= 3 h) represents the time of photo-charge, and A_{ph} (=0.38 cm^2) describes the illuminated surface area. The photoconversion efficiencies for VNF and VNF-C-120 are 4.24% and 5.07%.

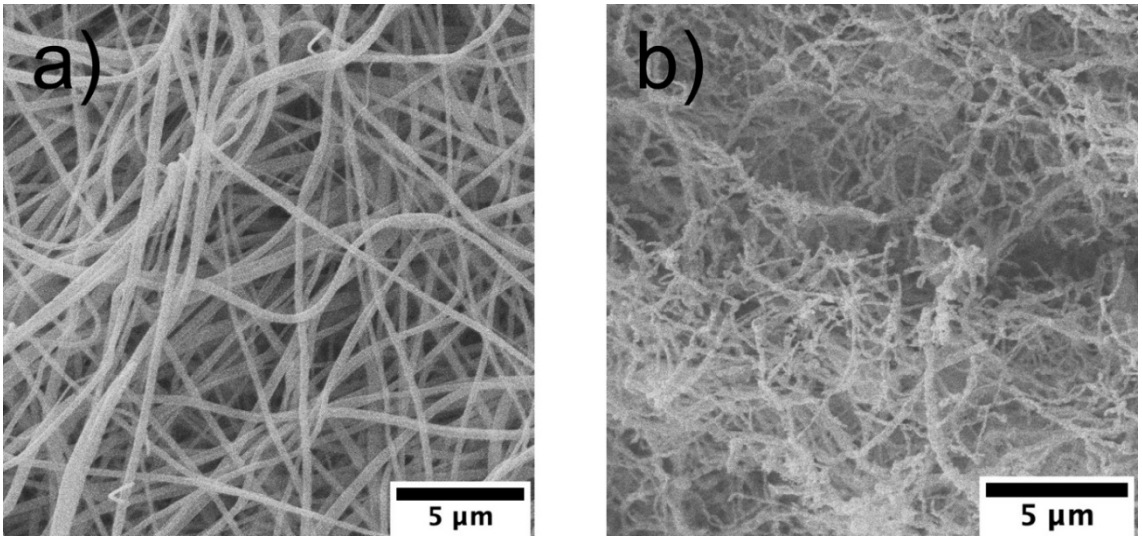

Figure 67: SEM images of a) electrospun green fibers of $VO(acac)_2$/PVP and b) calcinated V_2O_5 fibers at 450°C.

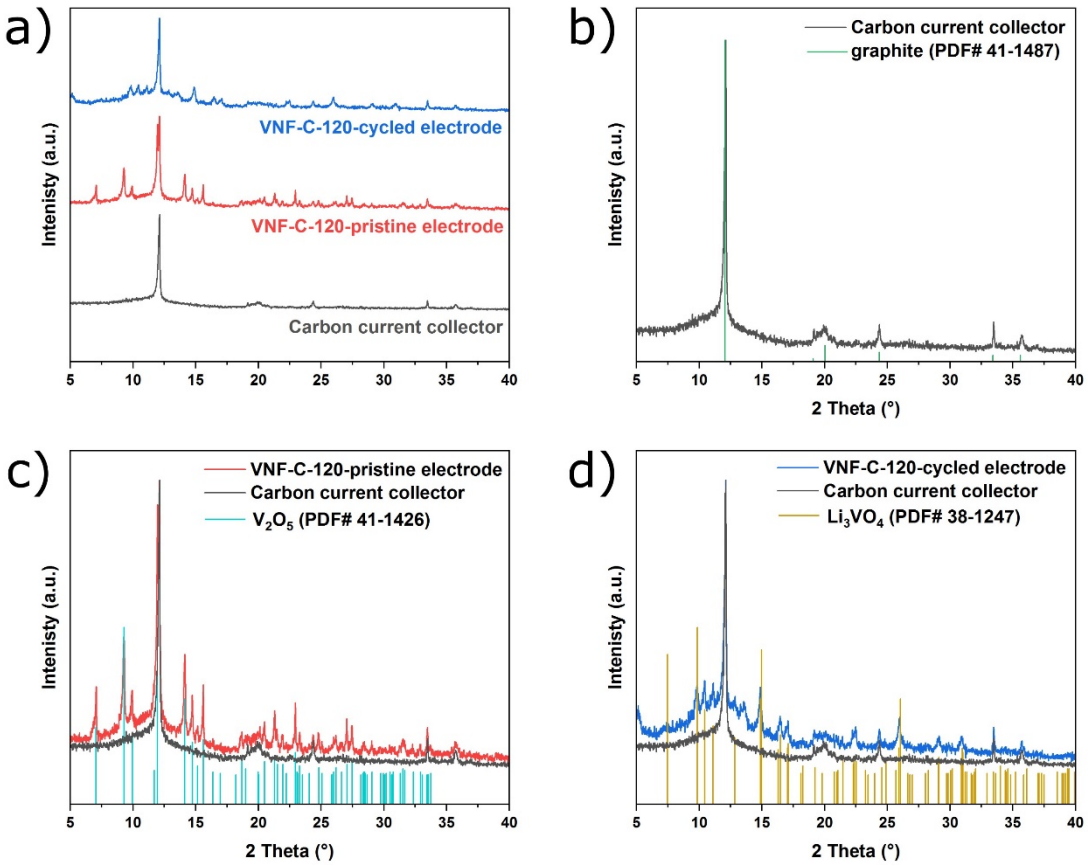

Figure 68: XRD pattern of VNF-C-120-cycled and pristine electrode vs. the current collector. b) Carbon current collector with the graphite reference. c) VNF-C-120-pristine electrode with the carbon current collector and the V_2O_5 reference pattern. d) VNF-C-120-cycled electrode with the carbon current collector and the Li_3VO_4 reference pattern.

Table 6: Estimated values of bulk and charge-transfer polarizations from the ECM fitting of impedance spectra.

Cell	R_b (Ω)	R_{ct} (Ω)
VNF	13	84.1
VNF-C	9.2	48.2
VNF-C pristine	7.1	295.6
VNF-C charged	5.4	77.1
VNF-C discharged	5.4	58.1
VNF-C discharged illuminated	5.9	36.1

Calculation for the Li^+ and electronic conductivity under illuminated:

The charging process of photo rechargeable Li-ion batteries using photocathodes, as shown in Figure 65a, has occurred in the following ways. Light excites the electrons on the valence band (VB) of $Li_xV_2O_5$, thus transferring them to the conduction band (CB) while leaving holes in the VB. The photo-excited electrons could migrate to the surface of P3HT particles by drift, diffusion or applied electric field, and then be guided

to the collector via the energy level gradient of P3HT and rGO to form photo-current for $Li^{+}+ze^{-}\rightarrow zLi$. Unpaired photo-induced holes are blocked by P3HT and accumulate in the photo-cathode to drive the charging process ($Li_xV_2O_5+yh^{+}\rightarrow yLi^{+}+Li_{x-y}V_2O_5$).
As the average size of V_2O_5 nanofibers prepared is at 140 nm, the maximum distance of diffusion for photo-excited electrons is 70 nm. The high LUMO level of electrolyte and the chemical potential difference of electrons between electrolyte and electrode could prevent electrons from entering the electrolyte. On the premise of ignoring the drift motion of photo-excited electrons and the conduction between P3HT and graphene, the number of surviving photo-excited electrons, the diffusion distance and diffusion rate determine the photogenerated current density.

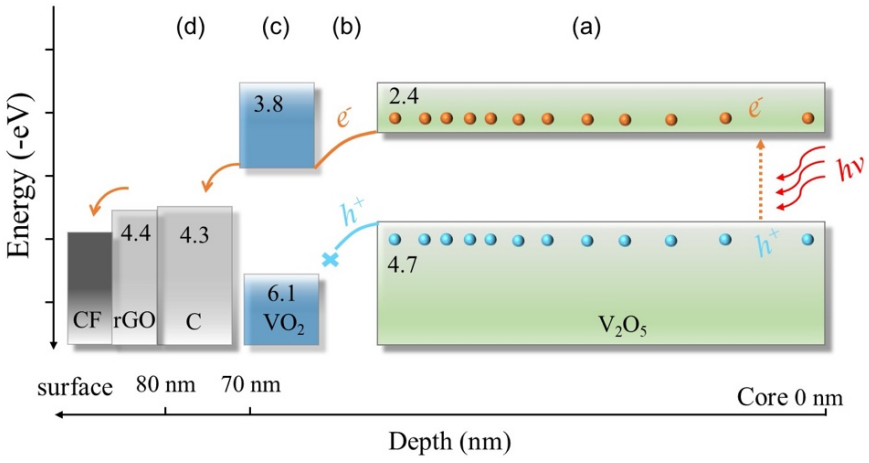

Figure 69: Structure of a V_2O_5@VO_2@C junction

V_2O_5@VO_2@C nanofibers, prepared in this work, have an average size of 160 nm including a 20 nm VO_2 and 20 nm carbon sandwich coatings. As displayed in Figure 69, the transport path of photo-excited electrons can be divided into the following sections: (a) the diffusion layer in the V_2O_5; (b) the drift layer in the space-charge layer between V_2O_5 and VO_2; (c) the diffusion layer in the VO_2; (d) the drift layer in VO_2/carbon interface and the flow layer in carbon.
Compared with the diffusion conduction of V_2O_5, the space charge layer between V_2O_5 and VO_2 accelerates the migration of photo-excited electrons and restricts the diffusion of photo-induced holes. On the other hand, the in-situ generated VO_2 is undoubtedly more favorable for conducting electrons than the P3HT which has a lower contact surface with V_2O_5 nanofibers. To discuss expediently, the photo-current density could be evaluated by the average conductivity of a single fiber.

The number of incident photons per unit time in our experiences (P_{in} = 11 mW cm^{-2}, $\lambda = 400\ nm$), can be given by,

$$A = \frac{P_{in}}{h\nu} = \frac{P_{in}\,\lambda}{hc} = 2.2 \times 10^{16}\ s^{-1}\ cm^{-2}$$

Based on the hypothesis that the incident light is sufficient to excite electron, the number of photoelectrons can be obtained via $n_{le} = \eta A$. Where η is the quantum yield defined as the ratio of the average number of photoelectrons produced per unit time to the number of incident photons at a particular wavelength. In most cases, its value is about 1% to 25%. Therefore, the value of photoelectrons in this work could be calculated as $n_{le} = 1.1 \times 10^{15}\ s^{-1}\ cm^{-2}$ when we fix η as 5%. Ignoring the problems of surface scattering and material transmittance, it is assumed that the probability of photoelectron generation per unit of V_2O_5 nanofiber as a whole is constant. For a single V_2O_5 cylindrical fiber in the illuminated region with a diameter of 150 nm, the relationship between the number of photoelectrons from the center to the surface and the radial distance is as follows,

$$n_e(r) = 2n_{le}\pi r dr \quad (0 \le r \le 75\ nm)$$

Theoretically speaking, the photogenerated electronic conductivity can be given by,

$$\sigma_e(r) = \frac{n_e(r) q \mu_{le}}{2\pi r dr} = 3.17 \times 10^{-3}\ S\ cm^{-1}$$

Where $q = 1.602 \times 10^{-19}\ C$, μ_{le} is the photogenerated electron mobility which is reported as 18 $cm^2\ V^{-1}\ s^{-1}$ for V_2O_5 [335].

As carbon is a conductive material, only the V_2O_5 and VO_2 layers need to be considered in V_2O_5@VO_2@C. The space charge layer in V_2O_5/VO_2 interface could accelerates the electrons, resulting in improved current density. This improved current density can be given by,

$$J = q v_{sc} L_{sc} \frac{d\sigma_e(r)}{dx} = q v_{sc} L_{sc} \frac{dn_e(r)}{dx} = q v_{sc} n_{le}$$

Where the $\frac{1}{2} m v_{sc}^2 = q(E_{V2O5}^{CB} - E_{VO2}^{CB})$. So, the electronic conductivity in the VO_2 region can be given by,

$$\sigma_e(VO_2) = J \frac{E_{V2O5}^{CB} - E_{VO2}^{CB}}{L_{sc}}$$

$$L_{sc} = \left[\frac{\varepsilon_0 \varepsilon k T}{q^2 n_e(r)}\right]^{1/2} \left[\frac{2q(E_{V2O5}^{CB} - E_{VO2}^{CB})}{KT}\right]^{1/2}$$

Therefore, the stoichiometric photogenerated electronic conductivity

$$\sigma_{le} = \frac{\int_0^{75nm} \sigma_e(r)dr}{\pi \times 75\ nm \times 75nm} > 3.18 \times 10^{-3}\ S\ cm^{-1}.$$

On the other hand, since the holes left on the VB can participate in the charging reaction ($Li_xV_2O_5+yh^+ \rightarrow yLi^+ + Li_{x-y}V_2O_5$), the conductivity of the holes can be considered as the conductivity of photogenerated Li^+ in a certain extent. Reference to the numerical relationship between electroconductivity and hole conductivity of lightly doped-silicon, we defined μ_{lh} (the photogenerated hole mobility) as 6 $cm^{-2}\ V^{-1}\ s^{-1}$. Therefore, the value of the photogenerated hole conductivity $\sigma_{lh} = 5.3 \times 10^{-4}\ S\ cm^{-1}$. For the electrolytes prepared (7 mm ($S_{lighted}$=~0.38 cm^2), a thickness (h) of 5 μm and 50% space ratio for the V_2O_5 nanofibers), the value of n_{le} is $5.5 \times 10^{14}\ s^{-1}\ cm^{-2}$ for all V_2O_5 nanofibers. If the mass load active materials in our works are set as L=1 mg cm^{-2}, the number of V_2O_5 unit cell in the lighted area can be calculated as $n_{V2O5} = N_A \times \frac{L \times 0.38\ cm^2}{M_w} = 2.77 \times 10^{18}$. As the far a smaller number of photons than V_2O_5, the average photogenerated electronic conductivity and hole conductivity can be regarded as $6.04 \times 10^{-13}\ S\ cm^{-1}$ and $2.01 \times 10^{-13}\ S\ cm^{-1}$, respectively.

Discussion of the dynamic self-adaptive interfacial band structure

According to the previous results [280,331,336,337], the working voltage vs. Li^+/Li, bandgap, CB and VB information are summarized in Table 7. The VB and VB of γ-$Li_xV_2O_5$ (x>1), are assigned to -7.3 eV and -4.5 eV, respectively. The VB and VB of VO_2, are assigned to -6.1 eV and -3.8 eV, respectively. The VB and VB of V_2O_5, are assigned to -4.7 eV and -2.4 eV, respectively. This means that the electron transport path will be quite different from the reported energy level diagram, and the space charge layer of P3HT will be unfavorable to the accumulation of photocurrent at least.

Table 7: The working voltage vs. Li^+/Li, bandgap, CB and VB information for all the products.

Phase	γ-$Li_2V_2O_5$	δ-LiV_2O_5	ε-$Li_{0.5}V_2O_5$	V_2O_5	VO_2
Voltage vs. Li^+/Li	2 V	2.5 V	3.1 V	3.3 V	2.7 V
Bandgap	2.8 eV	2.6 eV	2.4 eV	2.2 eV	2.3 eV
CB	-4.5 eV	-3.8 eV	-3.1 eV	-2.4 eV	-3.8 eV
VB	-7.3 eV	-6.4 eV	-5.5 eV	-4.7 eV	-6.1 eV
Ref.	331	337	337	280	336

4.3 Metal sulfides

4.3.1 Lithium-sulfur battery

The following chapter includes parts that are published in the following article, including the preparation of the various specific section related to synthetic work, formal analysis, and characterization of the Li_2S-loaded carbon fibers. Coin cell preparations and electrochemical measurements were done by co-authors from the Fuel Cell Research Center (ZBT) Duisburg. For the reproduction in the thesis/dissertation as an author, permission is not required [63]*:*

Brune, V., Bohr, C., Ludwig, T., Wilhelm, M., Hirt, S. D., Fischer, T., Wennig, S., Oberschachtsiek, B., Ichangi, A., & Mathur, S. A novel molecular synthesis route to Li_2S loaded carbon fibers for lithium-sulfur batteries. *J. Mater. Chem. A* 10, 9902–9910 (**2022**).

To overcome the current limitations in the synthesis of Li_2S electrospun fibers, a molecular approach of the stable synthesized precursor will be presented in the following, which, to the best of our knowledge, has not been reported before. This molecular precursor enables the electrospinning of lithium sulfide-based fibers at ambient conditions from a single precursor solution, which is not limited to only aqueous solutions, ensuring a simple preparation of Li_2S/C nanofibers.
Complexes of the tridentate ligand *N*-methyldiethanethiolamine (**I**) with lithium-delivered molecular precursors of formula $(LiSC_2H_4)_2NMe$ have been successfully synthesized and characterized. The *N*-methyldiethanethiolamine was synthesized according to a process described in literature before (Figure 70a) and isolated by distillation under reduced pressure as a colorless oil.[95,338,339] To deprotonate the thiol function of the isolated compound **I**, an acid-base reaction of *n*-butyllithium or lithium alcoholate was performed in *n*-heptane to produce the lithium derivative *N*-methyldiethanethiolatoamine-lithium $(LiSC_2H_4)_2NMe$ (**I-Li**) (Figure 70b) as colorless solid. The synthesized compound is air-stable and soluble in protic solvents like alcohols or water as well as in dimethylsulfoxide (DMSO). The appropriate solubility combined with good stability reveals that compound as an ideal precursor for a simple preparation of lithium sulfide material.[78,340,341] The comfortable handling at ambient conditions and high degrees of

freedom regarding the choice of solvents make this molecular compound an ideal precursor for material processing methods.

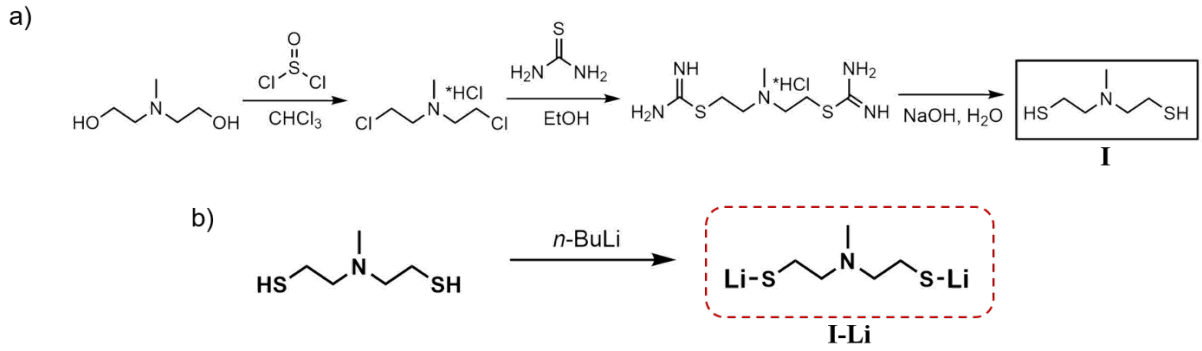

Figure 70: a) General synthesis route to N-methyldiethanethiolamine $(HSC_2H_4)_2NMe$ (**I**) modified from [95] and b) synthesis of N-methyldiethanethiolatoamine-lithium $(LiSC_2H_4)_2NMe$ (**I-Li**).

The new compound was analyzed by multi-nuclear magnetic resonance (NMR) spectroscopy using a combination of 1D and 2D NMR experiments (^1H, ^{13}C, $^1H^1H$ COSY, $^1H^{13}C$ HSQC, $^1H^{13}C$ HMBC). For **I**, three different proton signals were detected with an integrative ratio of 2 : 3 : 8 (Figure 71b) which is attributed to the symmetry of **I** along with the methyl function and the nitrogen, showing the possible free rotation around the CH_2 axis.

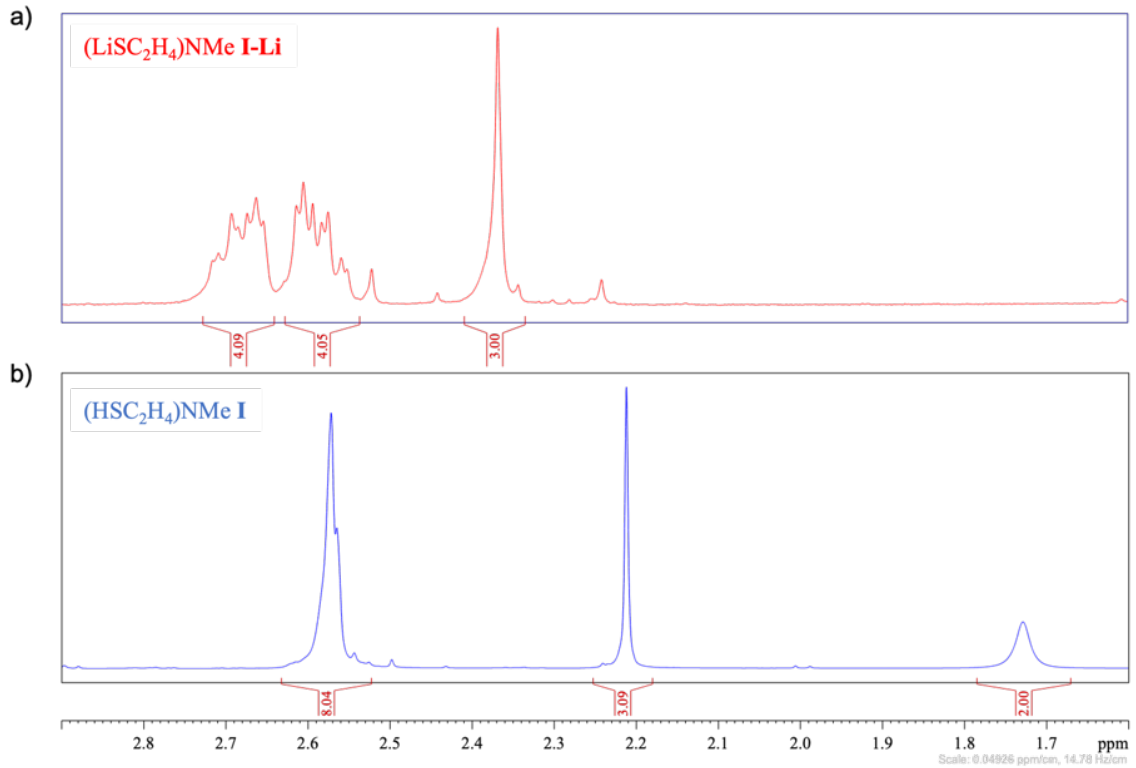

Figure 71: ^1H NMR of (a) $(LiSC_2H_4)_2NMe$ **I-Li** and (b) $(HSC_2H_4)_2NMe$ **I**.

The signals of both ethanethiol chains appear as one signal with an equal chemical shift located at 2.58 ppm. The two acidic thiol protons resulted in a broad signal at 1.74 ppm and the methyl group was found at 2.24 ppm. The NMR spectroscopic studies of compound **I** were in agreement with the literature[339] and corroborated the proposed structure of the ligand in solution (Figure 71b). The deprotonation of **I** by treatment with butyllithium resulted in the lithium derivative **I-Li** (Figure 71a) showing separated CH_2 protons for the ethanethiol chains in NMR analysis, resulting from the hindered rotation around the C–C-axis. In total 11 protons were detected, confirming the deprotonation of pre-synthesized ligand **I** and successful proton exchange by the desired alkali metal. To investigate the thermal decomposition behavior of **I-Li**, thermogravimetric measurements were performed under an inert atmosphere (Figure 72a). The multi-step decomposition showed a total weight loss of 72% at temperatures up to 800°C, resulting in the formation of crystalline residue of lithium sulfide (Li_2S). The decomposition of molecular precursor sets in at around 100°C and a nearly complete decomposition was observed at around 350°C. At this point, Li_2S was already formed in an amorphous phase, which was confirmed by XRD measurements.[342,343] At elevated temperatures, beginning at 650°C, conversion to the crystalline cubic phase of Li_2S takes place.

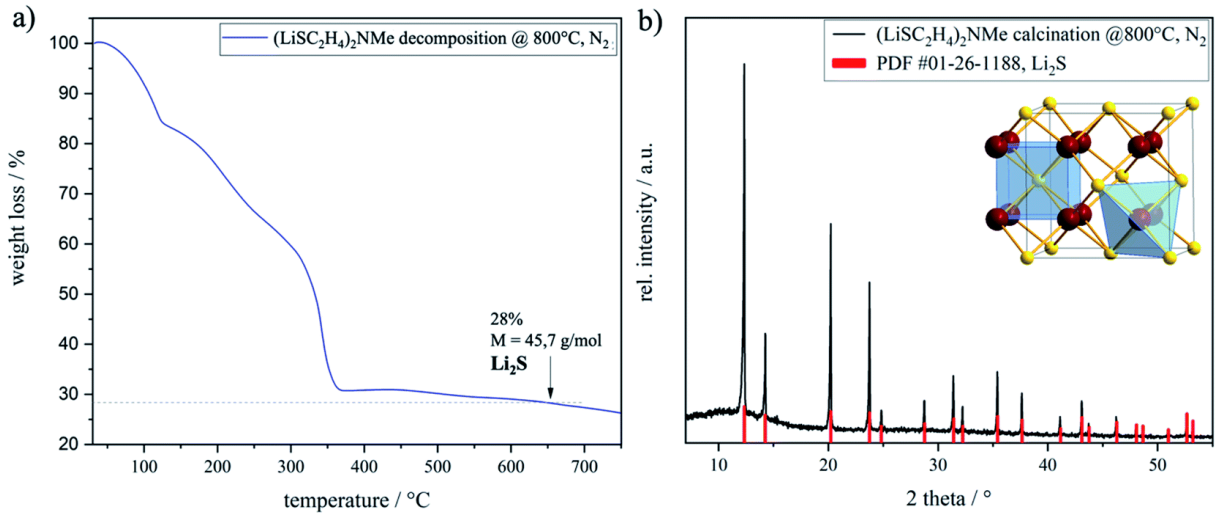

Figure 72: a) Thermogravimetric measurements of the synthesized precursor $(LiSC_2H_4)_2NMe$ **I-Li** up to 800°C under a nitrogen atmosphere; b) XRD pattern of the decomposed compound **I-Li** to the corresponding lithium sulfide Li_2S (ref. PDF #01-26-1188).

X-ray diffraction investigations of the decomposition residue obtained at 800°C under a nitrogen atmosphere confirmed the formation of the desired crystalline Li_2S phase (Figure 72b). The simple thermal decomposition to phase pure Li_2S in combination with the comfortable operation, good solubility in protic solutions and air stability

qualified the synthesized precursor **I-Li** as an efficient molecular source for the fabrication of Li_2S loaded carbon-based 1D materials.

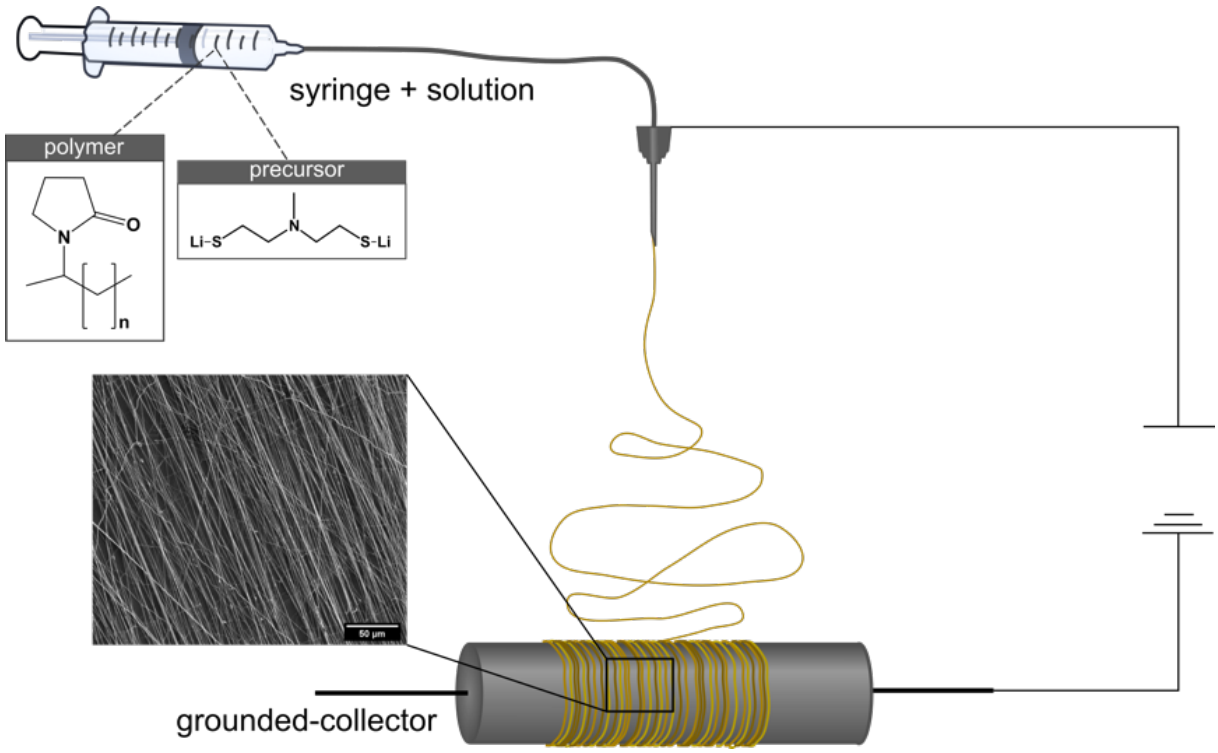

Figure 73: Electrospinning of **I-Li**/PVP solution with a drum collector.

Therefore, $(LiSC_2H_4)_2NMe$–PVP aligned fiber mats were produced from ethanolic solutions of **I-Li** with polyvinylpyrrolidone (PVP) by the electrospinning process (Figure 73).

Calcination of electrospun fibers was performed by applying a ramping of 2°C min^{-1} up to 280°C (holding time 2 h) under ambient conditions, to stabilize the fibrous structure by partly oxidizing,[344] followed by a temperature increase of 2°C min^{-1} up to 700°C (holding time 5 h) under a nitrogen atmosphere to finalize the carbonization process and to produce crystalline Li_2S/C-fiber mats (**I-Li**/C_45%, Figure 74a), respectively. The desired product formation was confirmed by XRD measurements of the calcined specimen (Figure 74b).

A precursor solution with an **I-Li** to PVP ratio of 1 : 1.5 was used to yield an appropriate viscosity for electrospinning which is mandatory to produce homogeneous fibers. A rotary drum collector was chosen since electrospinning onto a stationary collector led to low fiber adhesion towards the aluminum foil with bundling or aggregation effects. The aligned composite fiber (**I-Li**/PVP_58%) contained a $(LiSC_2H_4)_2NMe$ mass fraction of 58 wt%. After the calcination process, a lithium sulfide/conductive carbon composite

fiber mat with a total Li_2S fraction of 45 wt% (**I-Li**/C_45%) was obtained which was determined by thermogravimetric measurements.

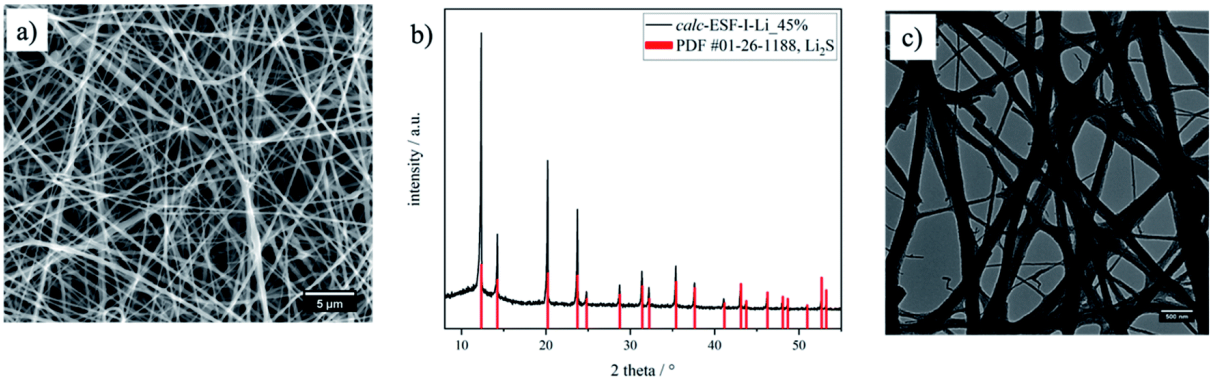

Figure 74: Electrospun **I-Li** fibers containing 45% Li_2S in their calcined form. a) SEM image of the electrospun green **I-Li** fibers (**I-Li**/PVP_58%), b) XRD of **I-Li**/C_45% (ref. PDF #01-26-1188) and c) TEM image of the calcined electrospun **I-Li** fibers (**I-Li**/C_45%).

TEM analysis of **I-Li**/C_45% displayed a 3D fiber network out of 1D electrospun fibers (Figure 74c).[344] The porosity of the fiber structure leads to a high surface-to-volume ratio and therefore to an intensive contact between the active material and electrolyte, which results in fast lithium-ion diffusion enabling higher charge and discharge rates.
Electrodes made from **I-Li**/C_45% fibers, PVP as the binder and carbon black as the conductive additive were characterized electrochemically.
Cyclic voltammetry (Figure 75a) was used to investigate the electrochemical behavior of **I-Li**/C_45% fibers. In the first cycle, two oxidation peaks located at 2740 mV *vs.* Li/Li^+ and at 3710 mV *vs.* Li/Li^+ were observed. In the literature, the first peak at 2751 mV *vs.* Li/Li^+ is attributed to side reactions or the formation of sulfur from Li_2S or polysulfides.[55,345] The broad peak between 3170 and 3900 mV *vs.* Li/Li^+ with a maximum at 3708 mV *vs.* Li/Li^+ is assigned to the oxidation of Li_2S to lithium polysulfides and sulfur, respectively. Usually, the oxidation of Li_2S to elemental sulfur is located between 2200 and 2600 mV *vs.* Li/Li^+ depending on particle size and active material loading.[346,347]
The size of the crystalline Li_2S material was calculated using Scherrer's equation at around 10 nm. However, for the activation of a fresh Li_2S cathode, a higher potential within the first cycle is required.[348] The overpotential was necessary for phase nucleation of polysulfides, the removal of surface passivation[348] and successive further oxidation to elemental sulfur.[347] This phenomenon has been reported for electrodes containing PVP, due to the interaction of lithium ions from Li_2S with the oxygen functions

of the PVP matrix.[349] A significant current flow was still observed between 3900 and 4000 mV *vs.* Li/Li$^+$, which can be assigned to side reactions such as electrolyte decomposition. For the oxidation reaction, a capacity of 1456 mA h g^{-1} was calculated from the CV. This capacity is 290 mA h g^{-1} higher than the theoretical capacity of Li_2S. Presumably, this can be explained by side reactions such as electrolyte decomposition and the shuttle mechanism, respectively. Three cathodic peaks located at 2355, 2111 and 2025 mV *vs.* Li/Li$^+$ were observed, which were assigned to the reduction of sulfur. At 2355 mV *vs.* Li/Li$^+$ the reaction of elemental sulfur (S_8 ring) with two lithium ions forming long-chain polysulfide Li_2S_8 has been observed.[346] The reduction peak at 2111 mV *vs.* Li/Li$^+$ is not characteristic for all Li_2S cathodes. However, it can be assigned to the further reduction of the long-chained Li_2S_8 to the shorter-chained polysulfide Li_2S_4.[350] The electrochemical conversion of Li_2S_4 to Li_2S_2 and Li_2S occurred at 2025 mV *vs.* Li/Li$^+$. The calculated capacity for the reduction was 863 mA h g^{-1} giving a coulombic efficiency of 59.2%. A low coulombic efficiency in the first cycle was already described in the literature and can be explained by the formation of passivation layers as well as by the dissolution of polysulfides in the electrolyte.[351] For the second cycle, the cut-off oxidation potential was set to 3000 mV *vs.* Li/Li$^+$. Two anodic peaks at 2307 and 2407 mV *vs.* Li/Li$^+$ were detected. The peak at 2307 mV *vs.* Li/Li$^+$ corresponded to the formation of short-chain polysulfides and the latter peak was assigned to the formation of long-chain polysulfides and sulfur, respectively.[352,353] The 1705 mV *vs.* Li/Li$^+$ lower oxidation potential of the second cycle was identified as a common phenomenon of Li_2S cathodes.[354] The polysulfides, which were formed in the first cycle, dissolved in the electrolyte and catalyzed the oxidation of Li_2S to S_8 leading to a lower oxidation potential.[355]

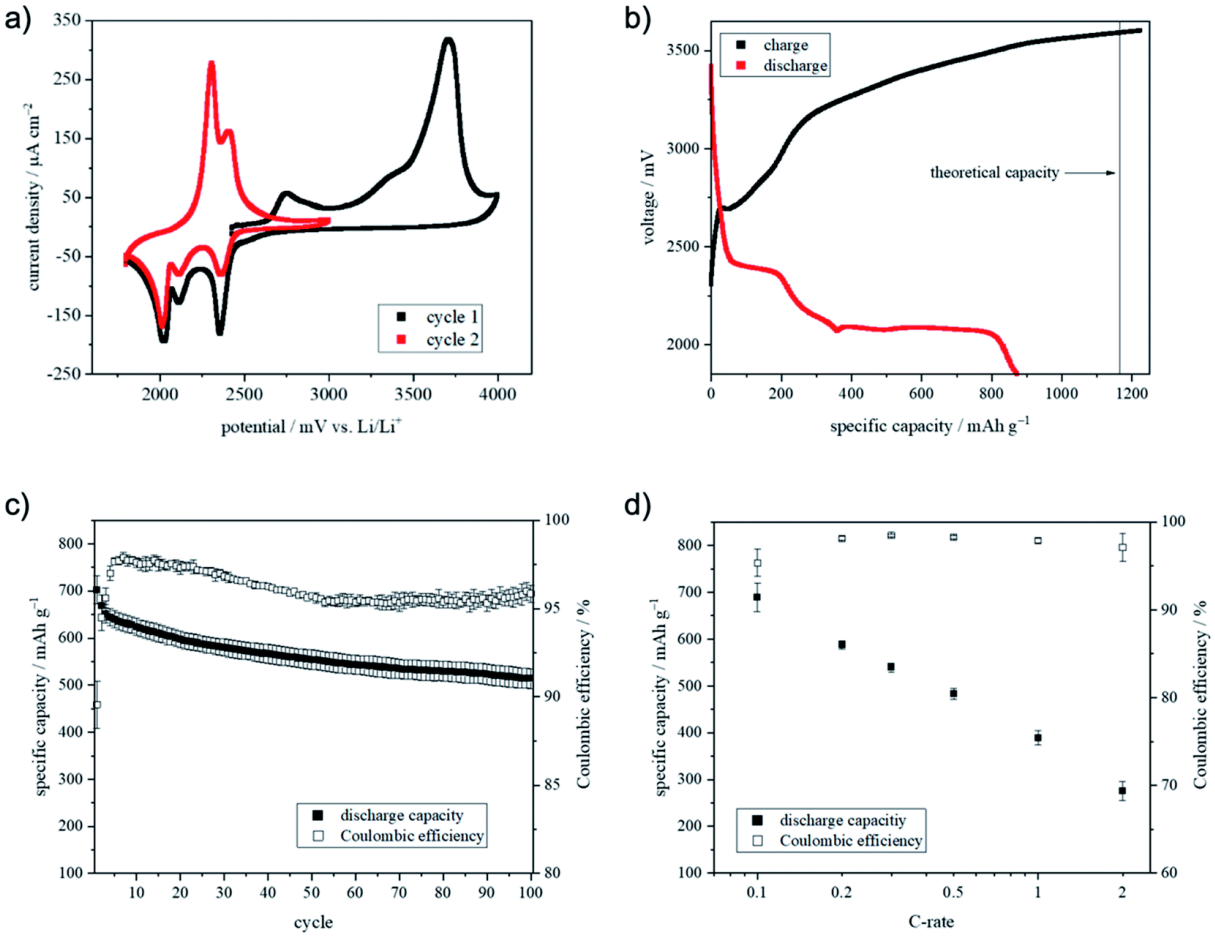

Figure 75: a) Cyclic voltammogram of **I-Li**/C_45%; b) voltage profile of the first cycle measured at C/20; c) specific capacity retention of **I-Li**/C_45% at C/10 when cycled between 2600 and 1850 mV and d) discharge capacities and coulombic efficiencies of **I-Li**/C_45% at different C-rates; each data point represents the mean value of five cycles at the specific current from three different cells.

The reductive peaks showed comparable potentials as identified in the first cycle, which was consistent with the literature.[55,129] Additionally, cycling experiments were performed to evaluate the capacity, capacity retention and high-rate capability (Figure 75b-d). The initial cycle was performed at C/20 and the voltage profile is shown in Figure 75b. During the charging process, a small plateau at 2696 mV was observed, which seemed to be corresponding to the peak at 2740 mV vs. Li/Li$^+$ in the first cycle of the CV. The voltage shift resulted from the cell setup (CV: three-electrode configurations, cycling: two-electrode configuration) as well as the different current flow. As seen in Fig. 6a the cell voltage rose after the plateau drastically. However, the voltage seemed to run into a plateau at about 3600 mV instead of reaching the set cut-off voltage of 3900 mV. This leads to the presumption that the polysulfide shuttle had a strong influence on cell voltage. The shuttle caused a constant voltage by generating polysulfides which were reduced and re-oxidized at the electrode.[356]

Additionally, electrolyte decomposition at a voltage higher than 3500 mV vs. Li/Li^+ was more and more likely. Hence, the charging process was stopped after 21 h. The further cycles were recorded at C/10 (Figure 75c).

A capacity of 702 mA h g^{-1} and capacity retention of 73% after 100 cycles were observed. The mean coulombic efficiency was 96%. The reason for the limited coulombic efficiency could be the side reactions caused by the polysulfide shuttle.[357] In comparison with the Li_2S–C–PVP material of Liu et al.[349] the material showed a slightly lower initial capacity. However, after 50 cycles the capacity of Liu's material reached 460 mA h g^{-1} instead of the 554 mA h g^{-1} for **I-Li**/C_45%.[349] Perhaps, this can be explained by the better structural integrity of our material.

Additionally, the high-rate capability was measured by applying different currents (Figure 75d). A reduced capacity at higher C-rates is a commonly known property of lithium-sulfur batteries[358] and can be explained by the slow kinetics of the polysulfide redox reaction and the very low electrical conductivity of the lithium-sulfur species.[359] The presented material showed at a rate of 1C at least 56% of the capacity at 0.1C. This promising result can be explained by the good electrical connection between the particles and of the particles with the current collector, respectively.

4.3.2 Copper sulfide as cathode material for rechargeable magnesium batteries

Figure 76a displays the SEM images of CuS particles achieved by simple precipitation reaction between $CuCl_2$ and $(NH_4)_2S$. The precipitated particles are not uniform in shape and size and tend to agglomerate. Figure 76b-f show the transition of the CuS particles to $Cu_{7.4}S_4$ particles by simple heat treatment at different temperatures under an inter (N_2) environment. Comparing the as synthesized (Figure 76a) and the 150°C (Figure 76b) samples, it can be observed that the particles display uniform shape and size throughout the entire sample. However, by increasing the temperature from 150°C to 450°C, the particles start to melt together to form a dense material leading to micrometer-sized particles at 450°C. By increasing the treatment temperature to 850°C, the sample loses the small particle size to form high-dense Cu_2S material with larger grains.

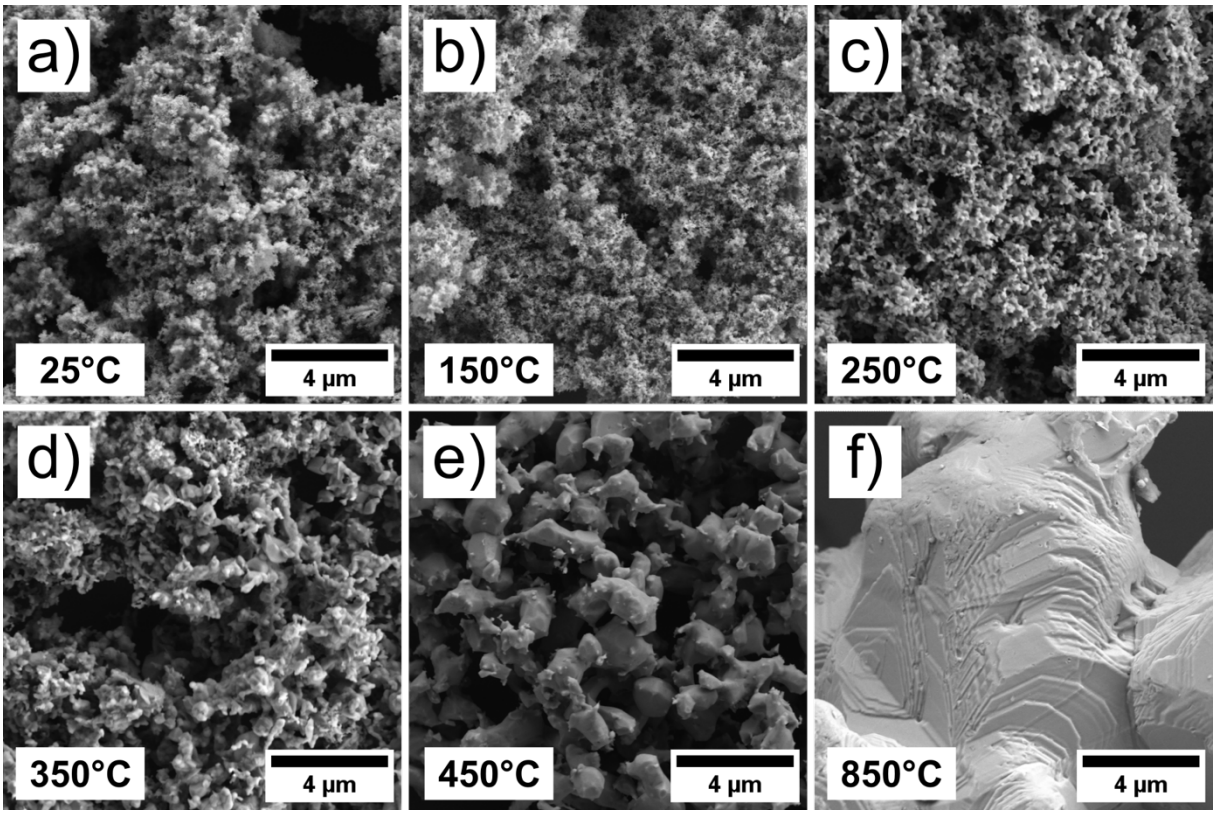

Figure 76: SEM images of CuS treated at different temperatures (25°C, 150°C, 250°C, 350°C, 450°C, 850°C).

XRD analysis was carried out to provide the crystal structures at the different temperature stages. Whereas the pristine material shows a hexagonal CuS (covellite) crystal structure, the signal measured with XRD improves upon heat treatment to 350°C (Figure 77b). As can be seen from the TG/DSC analysis (Figure 77a), the material shows,

until this point, an endothermic behavior mainly from the melting of the material. Between 350°C and 450°C, the material undergoes a phase change from hexagonal CuS to cubic $Cu_{7.4}S_4$. This phase transition is also visible in the DSC through an exothermic deflection in this temperature range, which is due to the crystallization process. Further, by increasing the temperature to 850°C, the material follows the exothermic reaction by changing the crystal structure to monoclinic Cu_2S (high-chalcocite) under the decomposition of sulfur, measured by XRD.

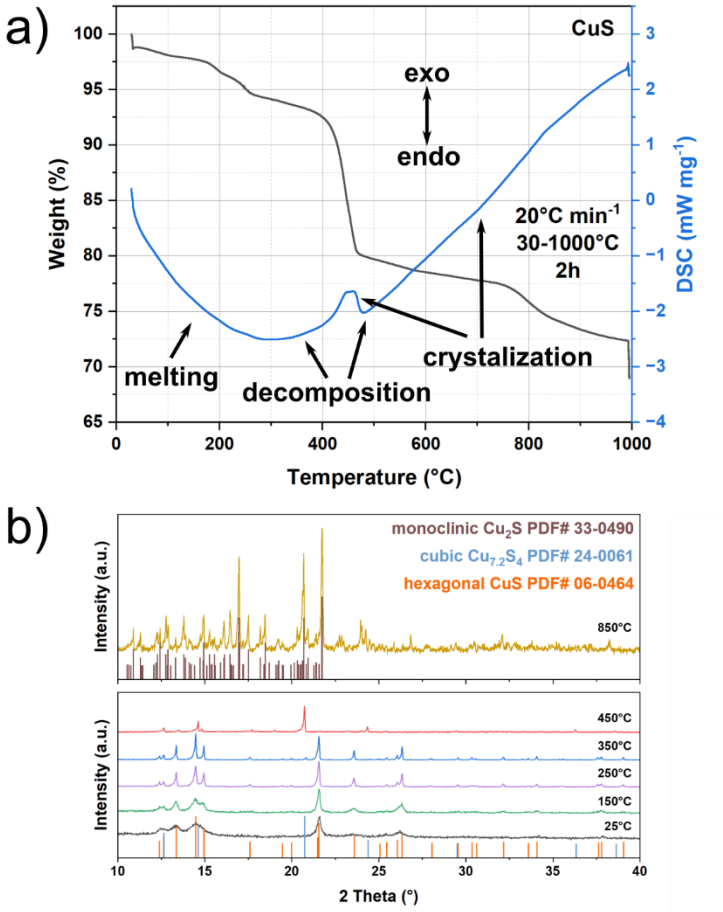

Figure 77: a) TG/DSC of pristine precipitated CuS at 25°C and b) XRD of CuS treated at different temperatures (25°C, 150°C, 250°C, 350°C, 450°C, 850°C).

XPS high-resolution spectra of the S 2p, Cu 2p, and Cu $L_3M_{4,5}M_{4,5}$ Auger peaks were recorded to investigate the chemical environment during the heat treatment and crystal structure changes. Figure 78 presents measurements of the S 2p and Cu 2p orbitals of CuS treated at different temperatures. In the S 2p orbital, three doublets can be measured for the pristine CuS corresponding to S^{2-}, S_2^{2-}, and S_n^{2-}.[228,229,360,361] However, these peaks maintain until a temperature of 350°C. By increasing the temperature to 450°C, the peaks of S_2^{2-} and S_n^{2-} disappeared while only the peaks of the S^{2-}

were maintained. The signal improves from 450°C to 850°C, suggesting the complete transition from $Cu_{7.2}S_4$ to Cu_2S. The changes in the Cu 2p peaks are in accordance with the trends seen from the S2p peaks. Whereas, in the low-temperature range (<450°C), the Cu 2p peak splits into two peaks, one for a Cu^{+I} and one for the Cu^{+II} peak, decreasing the Cu^{+II} peak upon an increase in temperature.

Therefore, the samples treated at 450°C and 850°C show only one peak for the Cu^{+I} species. Additionally, it can be observed that the peak position of the Cu^{+I} signal is shifting slightly to a higher binding energy for the $Cu_{2-n}S$ samples, which is literature known for the transition from CuS to Cu_2S.

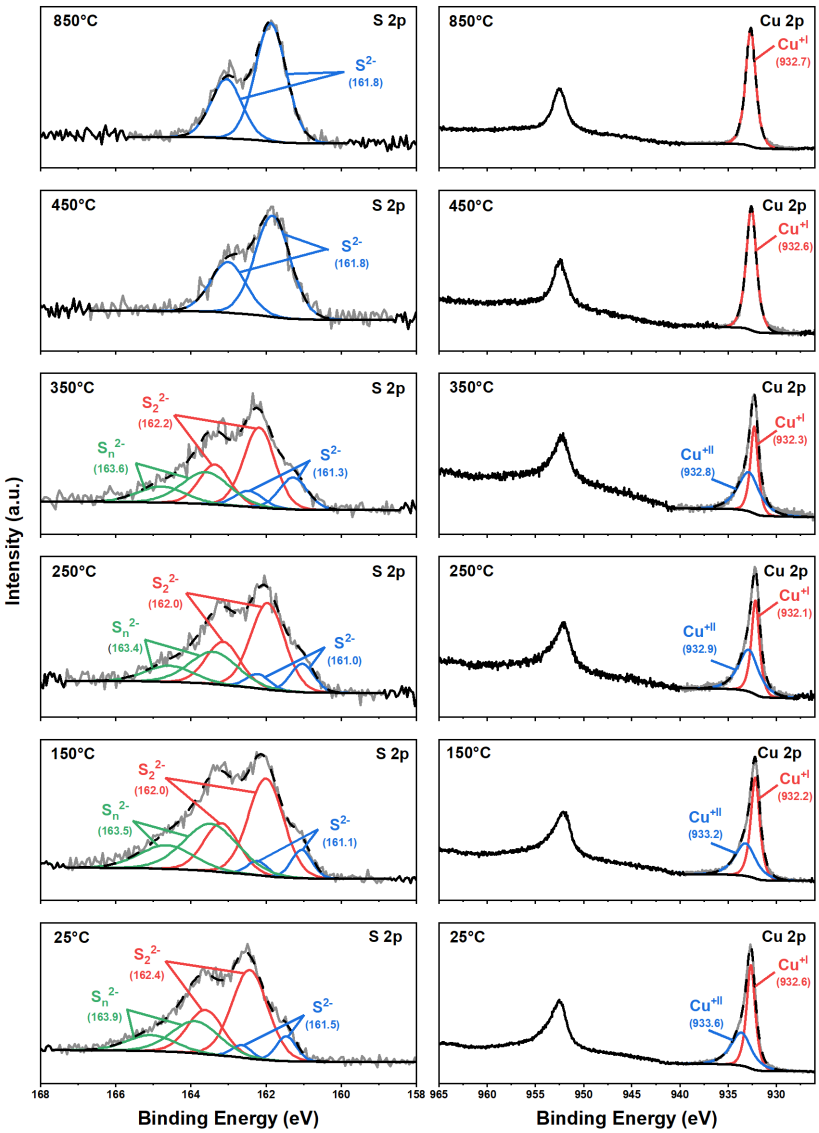

Figure 78: High-resolution X-ray photoelectron spectra of the S 2p and Cu 2p orbitals of CuS treated at different temperatures (25°C, 150°C, 250°C, 350°C, 450°C, 850°C).

For an advanced analysis of copper, the Cu $L_3M_{4,5}M_{4,5}$ peak can give more information. The peak shift of the Auger peak indicates the chemical environment of the copper

atom. As seen in Figure 79, the peak position shifts first to lower binding energies till 350°C before it shifts to higher binding energies for the samples treated at 450°C and 850°C, representing the reduction from Cu^{2+} to Cu^{+}. The peak shift to higher binding energies indicates the formation of Cu_2S at higher temperatures. However, interestingly the first peak shift to lower binding energy indicates a more defined formation of CuS when increasing the temperature from 25°C to 150°C.

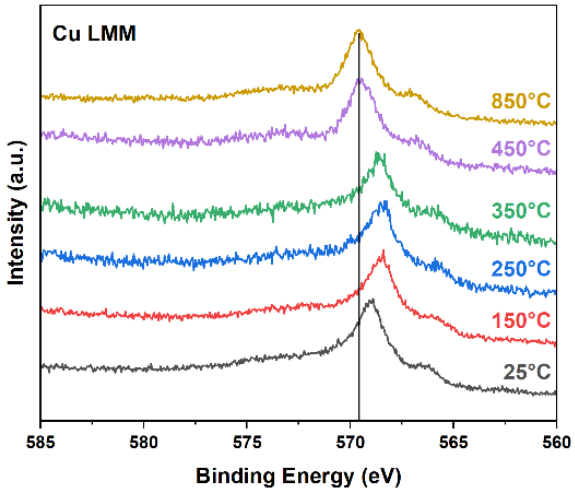

Figure 79: High-resolution XPS of the Cu LMM Auger peak of CuS treated at different temperatures.

Electrochemical investigations were done to investigate the influence of different treatment temperatures, and therefore crystallinity of the materials, on the redox behavior vs. Mg/Mg^{2+}. Cyclovoltammetric measurements of the four selected materials are presented in Figure 80, showing different redox behaviors. For the pristine CuS precipitated at 25°C (Figure 80a), a very intense peak at 0.8 V during the first discharge can be observed. Further, a broader shoulder peak is visible between 0.7-0.5 V. During the first charging, no reversible peak at lower potentials can be observed. At a potential of 2 V vs. Mg/Mg^{2+}, an increase in current can be seen, due to the oxidation of polysulfides.

In the second and third discharge cycles, the reduction peak shifts towards a higher potential of 1.0 V, which is much lower in intensity compared to the first discharge. However, the peak intensity increases in the third discharge compared to the second. The second discharge peak at 0.6 V gets less intense upon the second and third cycles. Two peaks at 1.8 V and 2 V are visible for the second charging cycle.

As discussed earlier in the introduction, two different reaction mechanisms are known for the displacement reaction between Mg and Cu. The following discussion is based on the fact that no oxidation peak was detected in the first charging process.
Since pristine CuS consists of Cu^{2+}, Cu^{+}, S_2^{2-}, and S^{2-}, the following reactions occur during the first and second cycles:

1st discharge:

$$S_2^{2-} + 2\ e^- \rightarrow 2\ S^{2-}\ (0.8\ V)$$

$$Cu^{2+} + e^- \rightarrow Cu^{+}\ (0.7\text{-}0.5\ V)$$

1st charge:

$$2\ S^{2-} \rightarrow S_2^{2-} + 2\ e^-\ (\text{Mg-polysulfides})\ (>2\ V)$$

2nd discharge:

$$Cu^{+} + e^- \rightarrow Cu\ (1\ V)$$

2nd charge:

$$Cu \rightarrow Cu^{+} + e^-\ (1.8\ V)$$

Overall reaction 1st cycle:

$$2\ CuS + Mg \rightarrow Cu_2S + MgS$$

Overall reaction ongoing cycles:

$$Cu_2S + Mg \rightarrow 2\ Cu + MgS$$

Only through the decomposition of the S-S bonds during the first discharge, Cu^{+} in the inner of the CuS structure is accessible for Mg^{2+} in the following cycles. Therefore, only the reversible redox reaction $Cu^{+} + e^- \rightleftharpoons Cu^0$ occurs from the second cycle on. This is in accordance with the differences seen in galvanostatic and cyclic voltammetry measurements with the increase in voltages at the beginning of the galvanostatic measurements.[151] Whereas in galvanostatic measurements, the voltage is not fixed (only the current), an increase in voltage can be explained that after breaking some S-S bonds at lower voltages, Cu^{+} from the structure is accessible, which is getting already reduced to Cu^0 at a higher potential during the first discharge simultaneously. This fact could explain the discrepancy in the literature regarding the mechanism that some studies report the detection of Cu^0 in the first cycle and some do not.
As seen from the third discharge cycle, more Cu^{+}-ions are reduced, causing an increase and peak shift of the first oxidation peak to 1.8 V. Depending on the electrolyte

and potential windows (>2 V), the oxidation of Cu^{+} to Cu^{2+} could be triggered, but in contrast this also the oxidation to polysulfides and dissolution in the electrolyte, causing the cells to fail.[163,362]

By comparing Figure 80a and b, it is visible that both materials follow similar electrochemistry. In the CuS sample teated at 150°C (Figure 80b), the reduction peaks during the first discharge appear much broader compared to the pristine CuS material. The broader and less intense peak can be explained by a slower diffusion rate of the Mg-ions into CuS. The higher density of the material slows the diffusion of the ions to the electrode broadening the peak of the reductive discharge and decreasing the current density. It can also be seen that the reduction peaks in the 2nd and 3rd discharge processes show multiple peaks between 1.0-0.7 V, which is due to the diffusion limitation during the first cycles.

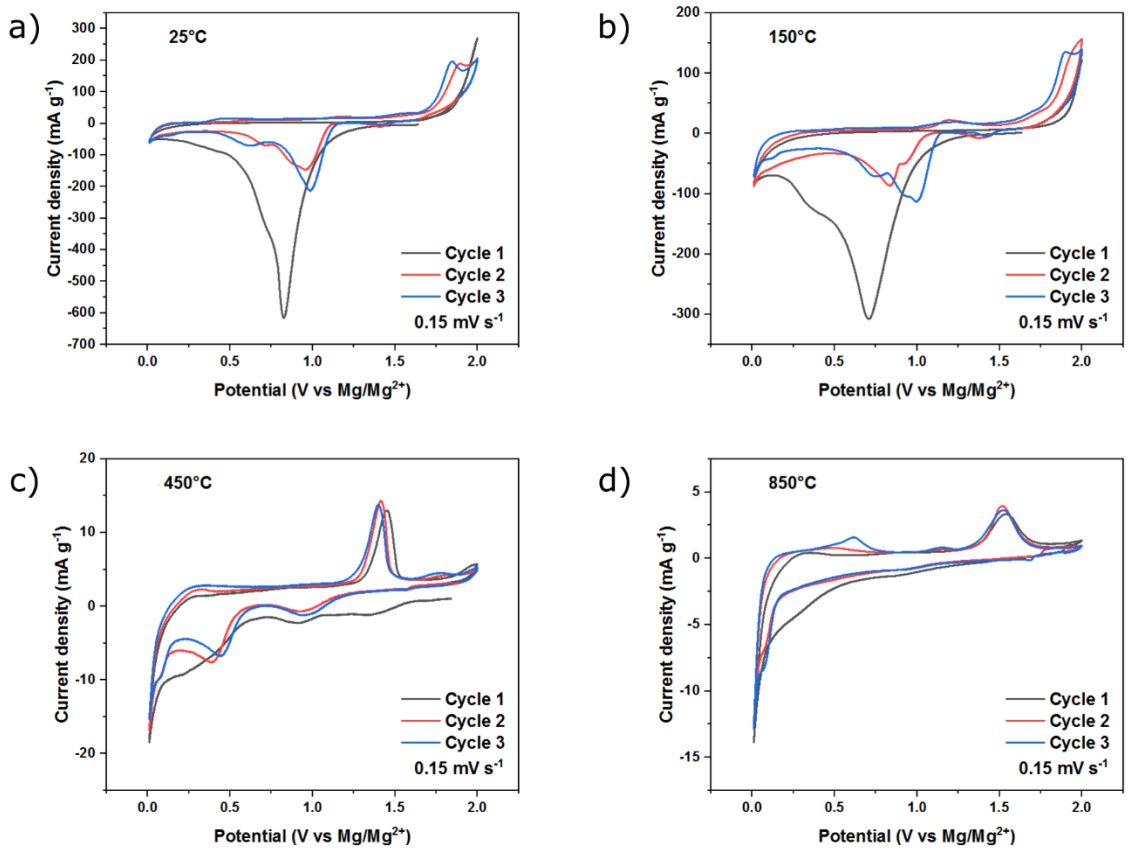

Figure 80: Cyclovoltammetries of CuS treated at different temperatures a) 25°C, b) 150°C, c) 450°C, and d) 850°C).

Since it was measured by TG/DSC and XRD, two changes in phase occur towards higher temperatures (450°C = $Cu_{7.4}S_4$, 850°C = Cu_2S), influencing the electrochemistry of the battery. The assumption could be made that the first cycle is irreversible and only Cu_2S is the reversible redox reaction vs. Mg/Mg^{2+}, as seen from CuS. The

samples treated at 450°C and 850°C follow the second and third redox behaviors immediately as seen from CuS treated at 25°C and 150°C.

First, the current densities are dramatically decreased compared to the CuS samples treated below temperatures of 450°C. This can be explained by the extreme morphology change described from the SEM measurements, losing the nano structuring effect as discussed previously in the literature.[151] However, much difference could be measured during CV analysis. Sample treated at 450°C undergoes multiple reductions at 1.4 V, 1.0 V, and 0.5-0.01 V during the first cycle, whereas in the second and third cycles, the peaks are more defined at 1.0 V, 0.5 V, and 0.01 V. The peak at 1.0 V was expected for the reduction of $Cu^{+} \rightarrow Cu^{0}$, which was observed previously in the other CuS samples after cycling. The reduction peak at 0.5 V was not expected but was assumed to correspond to the remaining CuS, which was not fully transformed to Cu_2S during the temperature treatment.

Interestingly, the peak at 0.01 V was not expected but correspond to the intercalation of Mg^{2+} into the carbon host framework of the electrode (current collector) without undergoing a conversion reaction as known from anode materials in lithium-ion batteries at similar low potentials as discussed previously. However, in all three charging cycles, a defined peak at 1.4 V can be measured. This peak is assigned to the deintercalation of the Mg^{2+} from the carbon framework. Additionally, minor oxidation happens at a higher potential of 1.8-1.9 V, which results from the oxidation of Cu^{0} to Cu^{+}.

In the 850°C cells, only the intercalation and deintercalation peaks of Mg^{2+} at low potentials during the cathodic peak and 1.5 V during the anodic peak can be observed. This is due to the high density of the active material and poor kinetics of Mg^{2+}, where no Mg^{2+} can transit into the structure of Cu_2S to undergo the conversion reaction.

According to the CV measurements, galvanostatic charge-discharge curves were recorded to measure the specific capacities and long-term stabilities of the described cells.

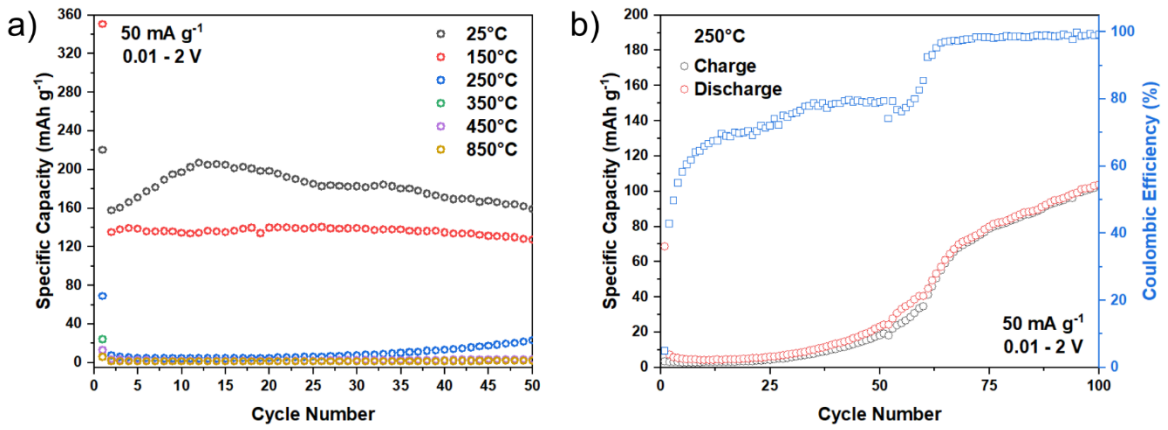

Figure 81: a) Galvanostatic charge-discharge measurements comparing the specific discharge capacities of CuS treated at different temperatures and b) more detailed galvanostatic charge-discharge curves of CuS treated at 250°C.

Figure 81a presents the specific discharge capacities of CuS treated at different temperatures. As synthesized CuS (25°C) exhibits the highest specific capacity of 50 cycles (160 mAh g^{-1}). However, for this material, an increase of capacity in the first ten cycles was measured before rapidly losing capacity towards 50 cycles.

CuS treated at 150°C revealed to have a high capacity of 139 mAh g^{-1} for the first cycles maintaining a high capacity of 130 mAh g^{-1} after 50 cycles. For the CuS heated to 250°C, an exciting behavior was observed (Figure 81b). During the first 25 cycles, the cell runs low on specific capacity (<10 mAh g^{-1}) before increasing in capacity slowly to the 50th cycle and dramatically increasing its capacity to ca. 100 mAh g^{-1} after 100 cycles. It is believed that while cycling some pores were formed due to the dissolution of polysulfide in the electrolyte, which supports the migration of Mg^{2+} into the CuS structure. The higher amount of magnesium penetrating the structure causes the rapid increase in capacity in each cycle. As seen from the curve in Figure 81b, the capacity tends to stabilize upon 100 cycles and beyond.

The electrochemical cell using CuS heated to 350°C did not perform well, exhibiting only a specific capacity below 5 mAh g^{-1} after 50 cycles. For the higher temperature treated (450°C and 850°C) CuS, which were proved to be Cu_2S by XRD analysis previously, capacities lower than 5 mAh g^{-1} were measured without any increase during more prolonged cycling. However, it could be measured that the specific capacities slightly increase during cycling for the cells using CuS treated at 350°C, 450°C, and 850°C, even when not exceeding 5 mAh g^{-1}.

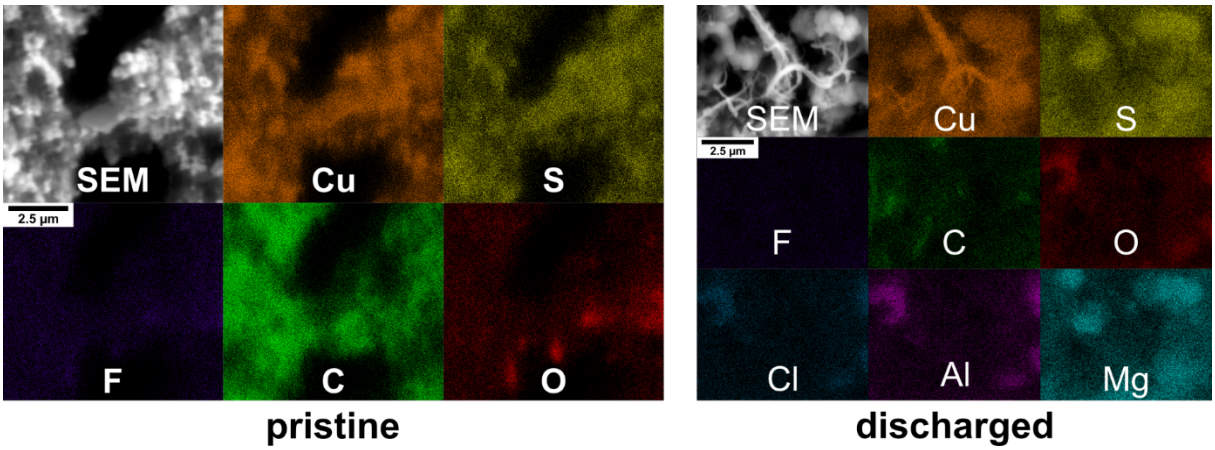

Figure 82: EDX analysis of the pristine and discharged (3rd cycle) electrode of the CuS material treated at 150°C.

Post-mortem analysis by EDX analysis of the pristine and the cycled (discharged) electrode of CuS material treated at 150°C electrode was done to investigate the material composition after the cycling (Figure 82). For the pristine electrode, the elements copper, sulfur, fluorine, carbon, and oxygen were detected. Copper and sulfur represent the active material, while the signal of carbon and fluorine occurs from the additives (PVDF binder and conductive carbon). The oxygen signal must come from some impurities, and it can be excluded to be from some CuO since the location of the oxygen and copper signals differ.

After cycling and discharging, additional signals of chlorine, aluminum, and magnesium were detected. Chlorine and aluminum can be assigned to some Mg(hexamethyldisilazane)$_2$*$AlCl_3$/DME electrolyte decompositions on the electrode. Moreover, oxygen is located in the same position as well as chlorine and aluminum, suggesting a formation of aluminum oxychloride. The signals of carbon and fluorine seem to be unchanged. More interestingly, already seen from the electron image, the formation of nanowires occurs for the discharged electrode. By comparing the electron image with the EDX images of the elements, especially copper and sulfur, it is visual that the formed nanowires consist of copper. However, the images of sulfur and magnesium fit well, suggesting the expected formation of MgS at the discharged state. The additional signal of copper at the MgS proves the reduction of copper as seen from CV measurements. These results show that less reversible redox behavior takes place when CuS is treated at higher temperatures as a result of losing the nanostructured size. The phase change from CuS to $Cu_{2-x}S$ can prevent energy loss during the first irreversible cycle (CuS + Mg → Cu_2S + MgS) in CuS samples. To counter the first irreversible reaction of CuS → Cu_2S, nanostructured Cu_2S synthesized at low temperatures could be a potential pathway for long-term rechargeable magnesium batteries.

Therefore, two different synthetic strategies were tested to synthesize Cu_2S on the nanoscale. In the first approach, Cu_2S was synthesized by precipitation from a Cu(I)-complex solution as a brownish powder (Cu_2S-PR). SEM images showed homogeneous agglomerated particles with a particle size of around 30-50 nm (Figure 83c). XRD analysis pointed out that the crystalline part is related to the covellite (CuS) structure. However, the XRD showed low signal and the presence of some amorphous Cu_2S formed incidentally cannot be ruled out.

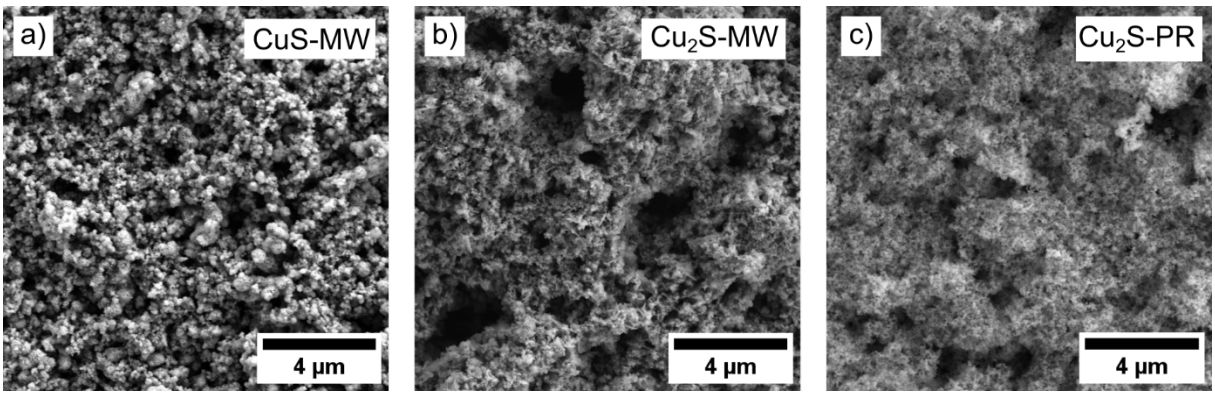

Figure 83: SEM images of CuS synthesized by microwave-assisted synthesis, Cu_2S synthesized by microwave-assisted synthesis, and precipitated Cu_2S.

The XPS analysis of the Cu LMM showed only a tiny shift towards higher binding energies, suggesting a mixture of CuS and Cu_2S (Figure 84a). HR XPS measurements of the Cu 2p and the S 2p orbitals fit more to a CuS rather than to Cu_2S due to the existence of Cu^{+I} and Cu^{+II} as well as disulfides and polysulfides in the S 2p spectra Figure 85a, b.

However, interestingly CV measurements of this material showed a slightly different behavior compared to the previously measured CuS materials (Figure 86). During the first discharge event, two prominent sharp peaks were measured at 1.05 V and 0.8 V, whereas the second peak has a broad shoulder towards lower potentials. According to the previous discussion, the first peak results from the reduction of Cu^+ to Cu^0, due to already accessible Cu^+.The second peak is from the reduction of CuS to Cu_2S and MgS. During the first charge, the oxidation peak starts from 1.75 to 2 V, indicating oxidation from Cu^0 to Cu^+ and the oxidation to polysulfides. Especially the peak for the oxidation of copper is much higher compared to previous discussed CuS material. From the second cycle on, the cell using Cu_2S-PR as active material reacts similar to copper sulfides as discussed before.

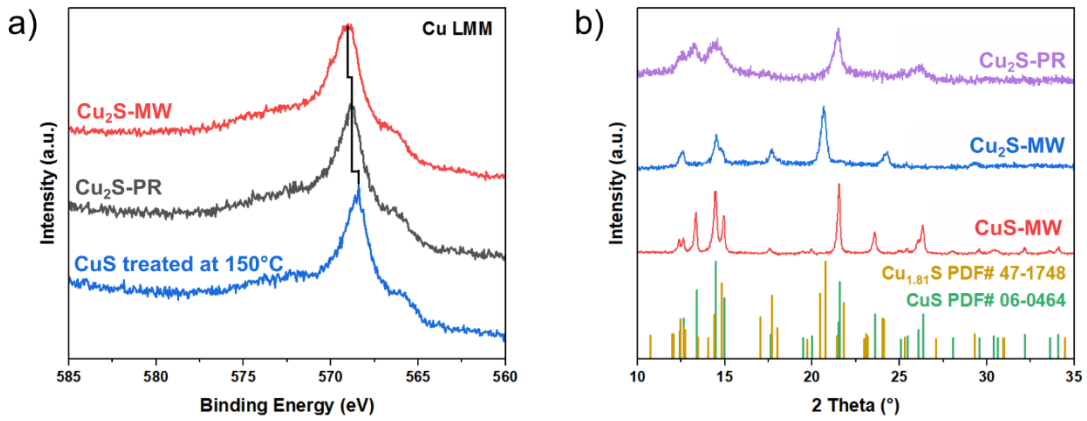

Figure 84: a) XPS high-resolution spectra of the LMM Auger peak of CuS treated at 150°C, Cu_2S precipitated at 25°C, and Cu_2S synthesized by microwave-assisted synthesis, and b) XRD of CuS synthesized by microwave-assisted synthesis, Cu_2S synthesized by microwave-assisted synthesis, and Cu_2S precipitated at 25°C.

In a second approach, Cu_2S was synthesized by microwave-assisted hydrothermal synthesis with a Cu : S ratio of 2 : 1 (Cu_2S-MW). As a control, CuS was synthesized following the same parameters except for higher access of sulfur during the synthesis (Cu:S = 1:2, CuS-MW). SEM images of the synthesized particles are presented in Figure 83a and b. The morphology of CuS microwaves is a non-uniform, mixed particle size, ranging from 50 nm to one micrometer. The SEM image of Cu_2S-MW particles shows two types of morphologies, dominant spherical particles and less dominant platelet structure. XRD characterizations revealed that $Cu_{1.81}S$ was formed during the microwave-assisted synthesis for a Cu:S ratio of 2:1. As expected, CuS was formed for the synthesis with a higher amount of sulfur used in synthesis. High-resolution XPS investigations of the Cu LMM peaks showed a shift towards higher binding energies for Cu_2S synthesized by microwave-assisted synthesis compared to CuS treated at 150°C. Moreover, HR XPS of the Cu 2p orbital revealed that copper is to be found in valence states +I and +II, as expected from the unstoichiometric compositions seen from XRD. However, measurements of the S 2p orbital result in S^{2-} as meaningful bonds. Only minor shares of S_2^{2-} and S_n^{2-} were measured (Figure 85c, d).

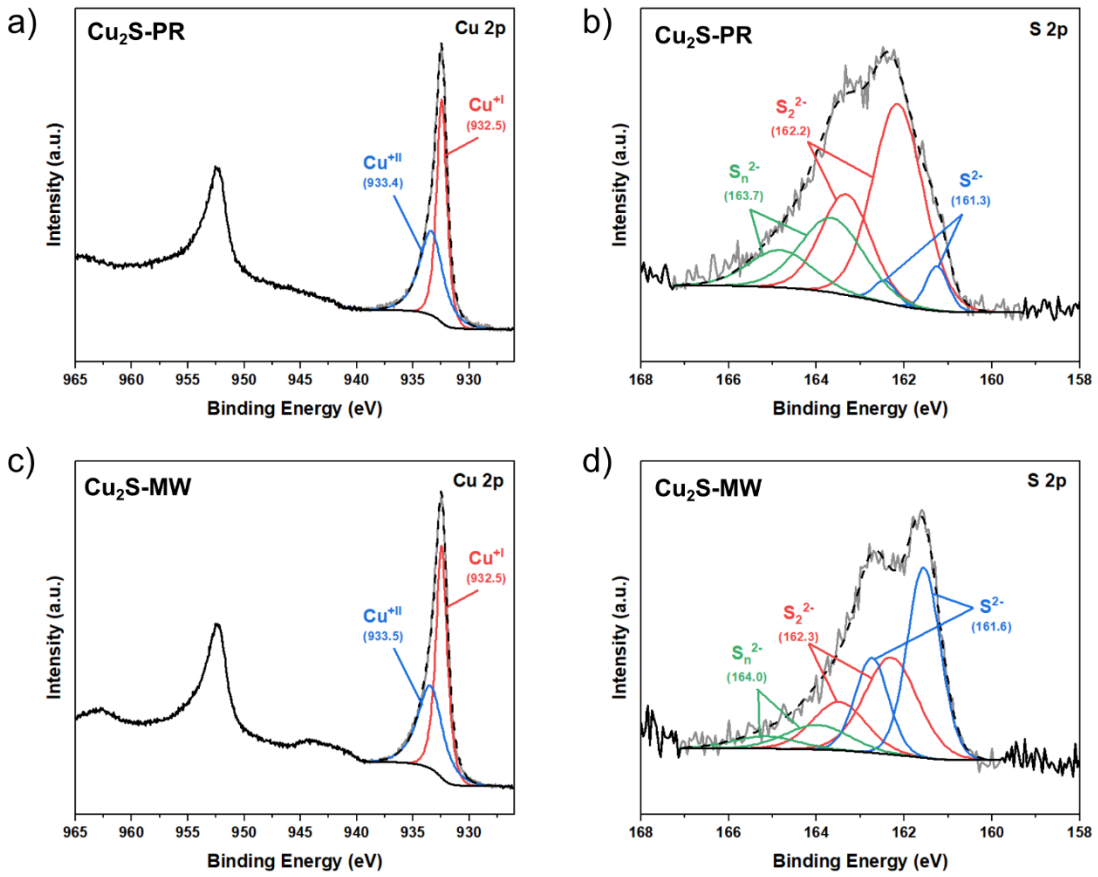

Figure 85: HR XPS spectra of a) Cu 2p of Cu_2S precipitated at 25°C, b) S 2p of Cu_2S precipitated at 25°C, c) Cu 2p of Cu_2S synthesized by microwave-assisted synthesis, and d) S 2p of Cu_2S synthesized by microwave-assisted synthesis.

Similar to precipitated Cu_2S, a sharp peak at higher potentials (1.3 V) during CV analysis has been measured, which is assigned to the reduction of Cu^+ to Cu^0 from Cu_2S formed during the synthesis. However, interestingly the second reduction peak looks similar to those of CuS synthesized by microwave. The difference between both peaks is the higher reduction potential of 0.75 V for the Cu_2S-MW compared to 0.6 V for the CuS-MW material. Similar to Cu_2S-PR is an oxidation peak at a potential of 1.75 V visible, which is almost missing in the CV of the CuS-MW cell. During the second and third cycles, a reversible cyclovoltammetry could be measured for Cu_2S with the redox pair at 1.0 V/1.8 V. For CuS-MW, similar behavior as seen from CuS can be observed during the second and third cycles (Figure 86a).

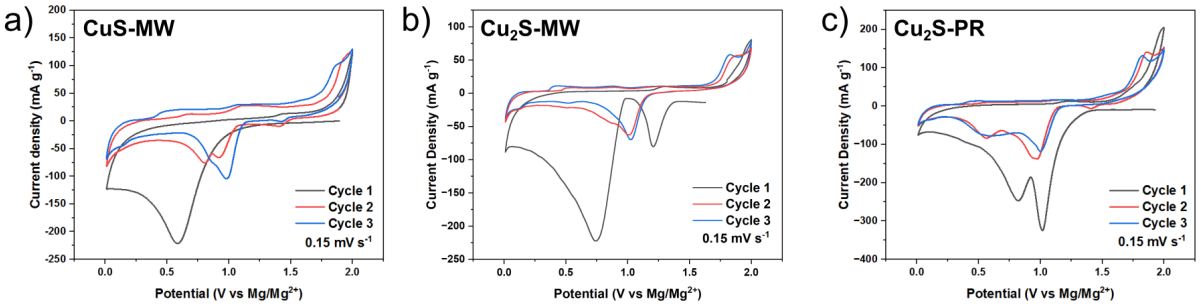

Figure 86: Cyclovoltammetry measurements of a) CuS synthesized by microwave-assisted synthesis, b) Cu_2S synthesized by microwave-assisted synthesis, and c) precipitated Cu_2S.

Comparing Cu_2S-MW and Cu_2S-PR under galvanostatic charge-discharge conditions, two plateaus in both materials were measured. However, the first plateau in the Cu_2S-MW cell is much shorter compared to the one in Cu_2S-PR Figure 87a and b. This can be explained by the higher amount of CuS in Cu_2S-PR as measured previously by XRD and XPS.

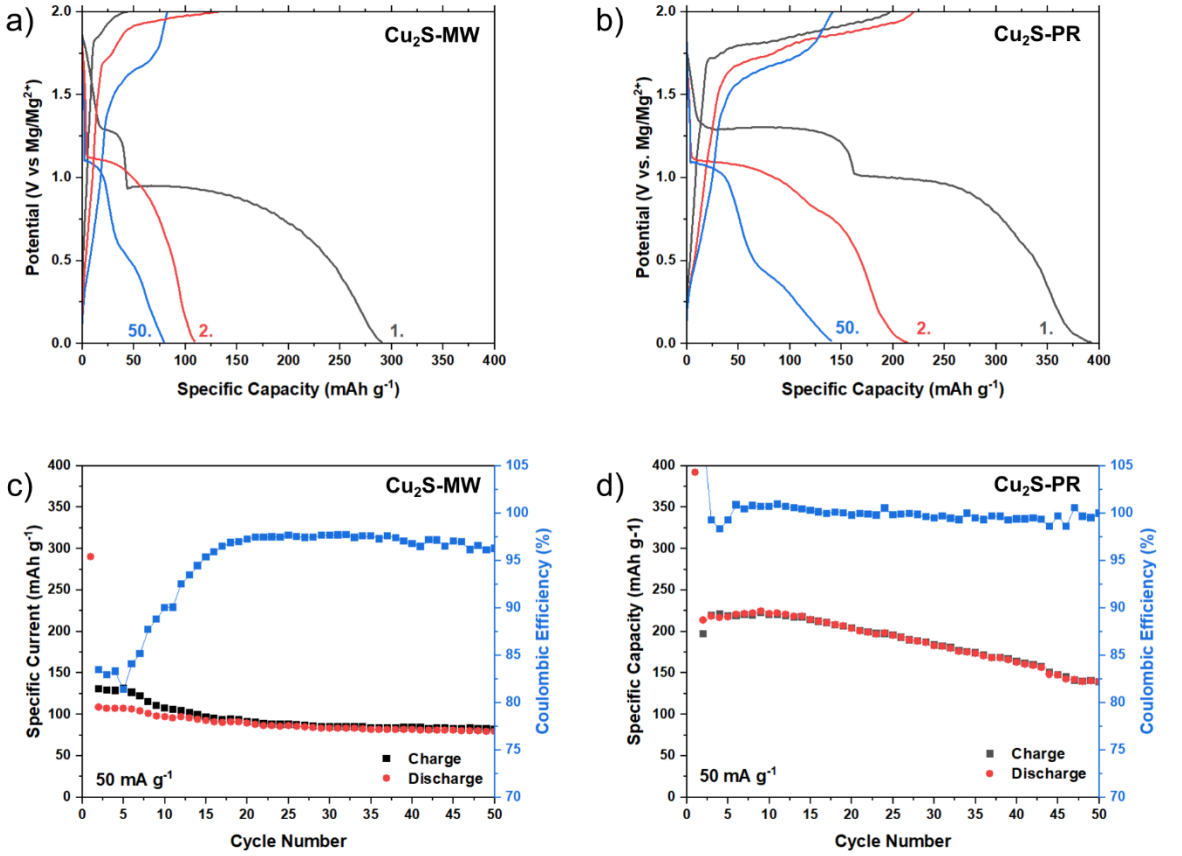

Figure 87: Galvanostatic charge-discharge measurements of the 1., 2., and 50. cycle of a) Cu_2S synthesized by microwave-assisted synthesis and b) precipitated Cu_2S at a current density of 50 mA g^{-1}. Stability tests of c) Cu_2S synthesized by microwave-assisted synthesis and d) precipitated Cu_2S

Stability test over 50 cycles at a current density of 50 mA g^{-1} measured capacities of 110 mAh g^{-1} in the second cycle and 77 mAh g^{-1} in the 50th cycle, which is a capacity retention of around 70%.

However, as discussed before, a higher specific capacity of 220 mAh g^{-1} in the second cycle and 140 mAh g^{-1} in the 50th cycle was measured, leading to a capacity retention of 64%. The coulombic efficiency of the Cu_2S-MW increased from around 80% to 96% after the first 20 cycles and retained this efficiency towards 50 cycles. In contrast, Cu_2S-PR achieves a coulombic efficiency of nearly 100% after 5 cycles. Moreover, it can be observed that Cu_2S-PR is constantly losing capacity each cycle, whereas Cu_2S-MW seems to be stabilized after 20 cycles maintaining the specific capacity of 80 mAh g^{-1}. This difference can be explained due to the higher amount of CuS in Cu_2S-PR compared to Cu_2S-MW (Figure 87c, d).

The results intend that using phase pure Cu_2S nanostructures compared to CuS nanostructures have fewer side reactions during the cell's first discharge, increasing the cell's lifetime. Furthermore, Cu_2S samples show lower overall specific capacity; however, compared to their theoretical values, Cu_2S outperformed CuS materials. The highest challenge is synthesizing phase pure Cu_2S as suitable nanostructures at low temperatures for long-term cell viability. Due to their high density, high-temperature modifications of CuS and Cu_2S seem not promising as suitable cathode materials for rechargeable magnesium batteries. Moreover, up to now, only a few *ex-situ* studies exist, reporting a discrepancy in the working mechanism. More investigations must be done with *in-situ* studies to understand the ongoing electrochemical processes fully. Although, all reports agree to the fact of the difference between the first and the ongoing discharges. Therefore, potential strategies of synthesizing nanostructure, phase pure, low-temperature Cu_2S should be the next steps to overcome the capacity loss during the first cycle. Here, the differences between hexagonal and cubic Cu_2S in combination with *in-situ* TEM analysis during the electrochemical reaction are of highest interest.

However, cycling retention is a second issue that also must be addressed in upcoming studies. The fact of dissolution of Cu^{2+} and polysulfides in the electrolyte can be addressed by testing copper sulfide as cathode material in all-solid-state-batteries, which is enabled through the existents of potential Mg^{2+} solid-state conductors with a conductivity of around 10^{-3} S cm^{-1} or by interface engineering to prevent the dissolution process.[363,364]

4.3.3 Fe_3S_4 thiospinel for rechargeable magnesium batteries and beyond

As iron is more available in the earth's crust compared to copper, iron sulfides can be potential candidates as cathode material for rechargeable magnesium batteries. Additionally, thiospinels can enable higher mobilities for the insertion of Mg^{2+} into the host material. Therefore, Fe_3S_4 was synthesized by autoclave-assisted hydrothermal synthesis.

Figure 88a shows an SEM image of the synthesized iron sulfide thiospinel structures grown as micrometer-size flower-like structures. XRD characterization (Figure 88b) was performed to investigate the crystallinity of the material. However, characteristic peaks of the Greigite (Fe_3S_4) structure were identified.

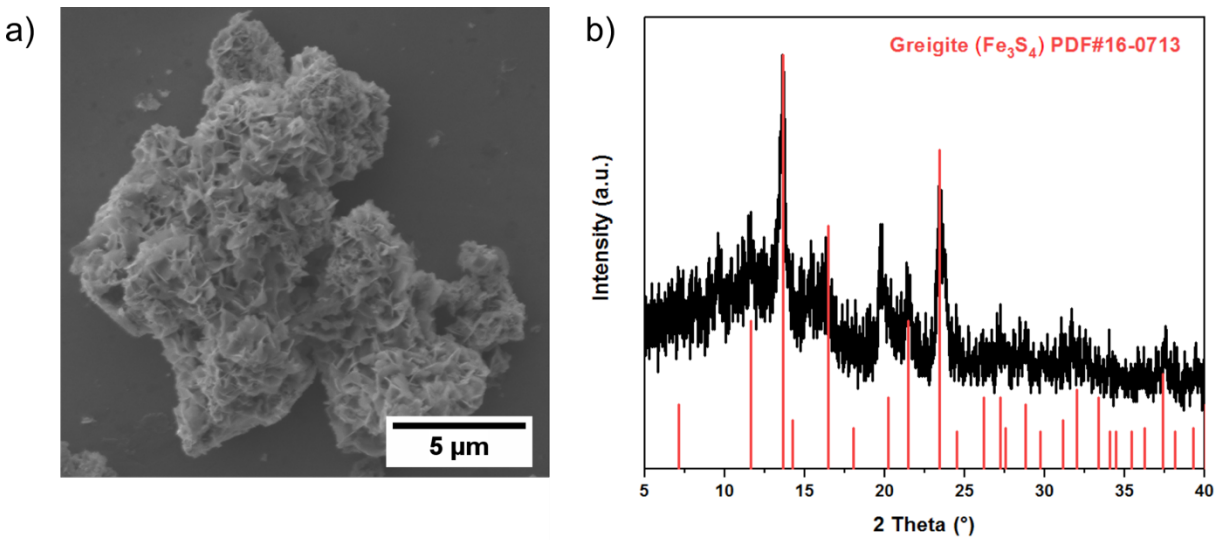

Figure 88: a) SEM image and b) XRD characterization of Fe_3S_4.

First, the material was tested in an electrochemical cell vs. Mg/Mg^{2+} on the redox potentials in the voltage window from 0.5-2.2 V for the first three cycles. For the discharging peak now clear reduction peak could be identified. However, a broad discharge plateau extends from 1.5-0.5 V. This broad peak is due to the simultaneous reductions from $Fe^{3+} \rightarrow Fe^{2+} \rightarrow Fe^0$. Differences between the first, second, and third cycles can be seen in decreasing current densities. This can be explained by irreversible losses upon cycling by the leaching of $Fe^{3+}/Fe2^+$ of the active material in the acetic electrolyte (Mg(hexamethyldisilazane)*2 $AlCl_3$/DME) or the dissolution of polysulfides through the oxidation of S as reported for other thiospinels.[211] During the charging cycles, two peaks could be identified at 1.7 V and 2.0 V. The peaks are assigned to the oxidation from $Fe^0 \rightarrow Fe^{2+}$ and later to the partial oxidation from $Fe^{2+} \rightarrow Fe^{3+}$. Higher potentials

then 2.0 V show an increase in current density, which corresponds to the decomposition of the electrolyte. The dramatic capacity loss was also observed during the galvanostatic charge-discharge stability test, as presented in Figure 89. The initial capacity for Fe_3S_4 vs. Mg/Mg^{2+} at a current density of 50 mA g^{-1} was 41 mAh g^{-1} which decreased quickly to 15 mAh g^{-1} after 50 cycles. However, the coulombic efficiency of the material improved upon cycling close to 97%.

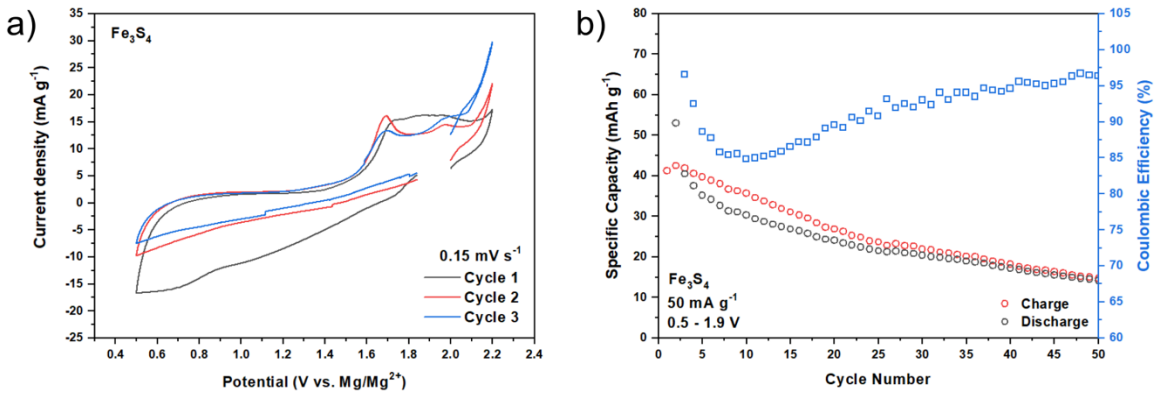

Figure 89: a) Cyclovoltammetry measurements and b) galvanostatic charge-discharge stability tests for the Fe_3S_4 electrode material vs. Mg/Mg^{2+}.

For an improved electrochemical reaction, the ionic conductivity within the electrolyte was increase by adding a small amount of LiCl (0.4 M) to the Mg-based electrolyte, and hybrid electrochemical cells were produced and tested vs. a magnesium metal anode. The addition of small amounts of lithium-ions into the system can achieve fast electrode kinetics and smooth anode deposition morphology. The improved redox reactions are presented in Figure 90a with the cyclovoltammetry analysis of the hybrid cell. In the first discharge cycle, two broad peaks at 1.2 V and 0.9 V, as well as a sharper peak at 0.6-0.5 V, were measured. The peak at 1.2 V is assigned to the reduction from $Fe^{3+} \rightarrow Fe^{2+}$, whereas the peak at 0.9 V is assigned to the reduction from $Fe^{2+} \rightarrow Fe^{0}$. The third peak at 0.6-0.5 V is due to the formation of a Li-solid electrolyte interface.

During the charging process in the first cycle, two overlapping peaks at 1.5 V and 1.7 V are observed. These peaks show the reversible redox reaction of $Fe^{0} \rightarrow Fe^{2+}$ and $Fe^{2+} \rightarrow Fe^{3+}$. In the second and third discharge cycles, the reduction peak at 1.2 V almost disappeared, indicating that less Fe^{3+} was oxidized during the first charging as it was in the pristine electrode. The reduction peak at 0.9 V appeared in the second and third cycles much sharper, affirming the assumption of less oxidation from $Fe^{2+} \rightarrow Fe^{3+}$ in the first charging cycle. The third peak at 0.6-0.5 V from the first discharge cycle

disappeared in the second and third cycles. During the second and third charging cycles, the first oxidation peak shifted from 1.5 V to 1.3 V and the second from 1.7 V to 1.6 V, showing improved electrochemical redox reactions. Galvanostatic charge-discharge analysis revealed an initial specific capacity of 440 mAh g^{-1} running at a low current density of 25 mA g^{-1}. For the second and third cycles, the specific capacity decreased to around 180 mAh g^{-1} at the same current density. After 40 cycles at a current density of 200 mAh g^{-1}, the electrochemical cell delivered a high capacity of 115 mAh g^{-1} (Figure 90b). Rate capability tests were performed to investigate the performance of the system at higher current densities (Figure 90c). Even at a high current density of 1600 mA g^{-1}, the cell was vital and delivered a specific capacity of 25 mAh g^{-1}. It can be seen by cycling at lower current densities that the cell runs unevenly. However, performing long-term measurements over 200 cycles at a current density of 200 mA g^{-1} show remarkable cycling stability with specific capacities of 100 mAh g^{-1} at a coulombic efficiency of around 100%. Towards 200 cycles, the cell improved in specific capacity to 120 mAh g^{-1} and a stabilized coulombic efficiency (Figure 90d), which is higher compared to Mg/Li-hybrid FeS_2 systems.[365]

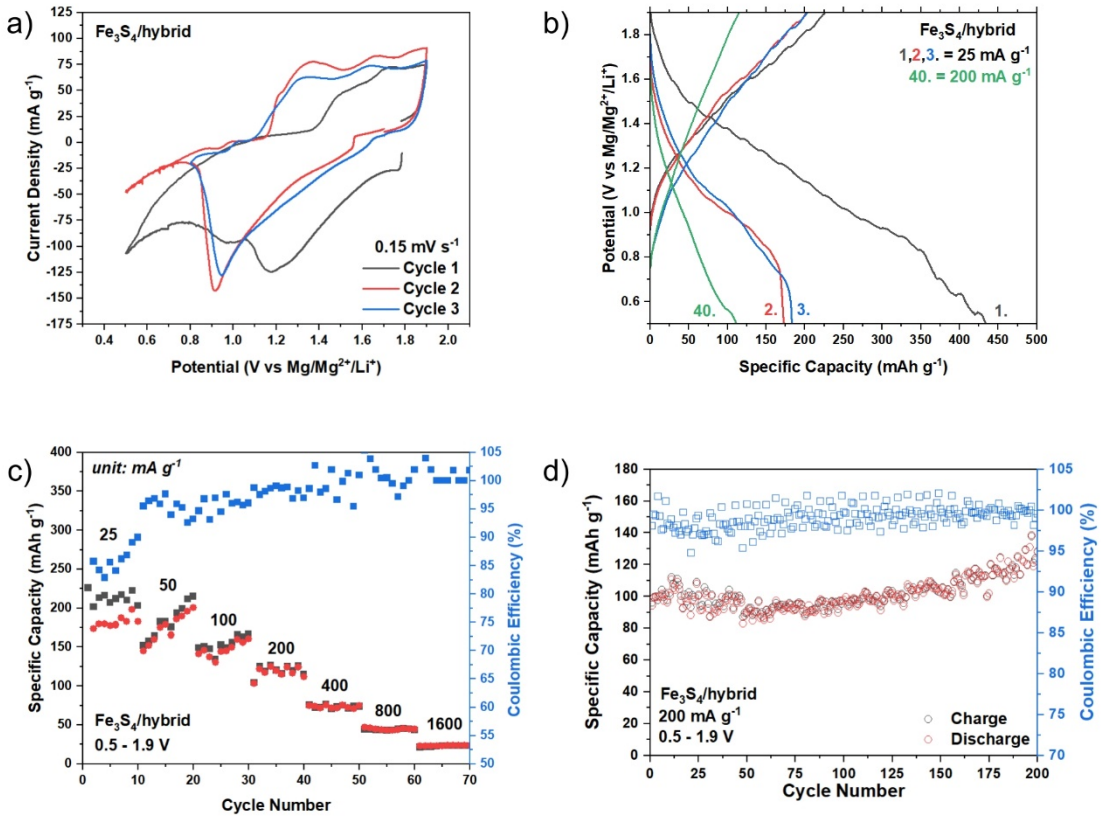

Figure 90: a) Cyclovoltammetry, b) galvanostatic charge-discharge curves of the 1., 2., 3., and 40. cycle, c) rate capability test at different current densities, and d) stability tests of Fe_3S_4 half-cell cycled vs. Mg-metal anode and a Mg/Li-hybrid electrolyte.

4.3.4 Copper iron sulfide as cathode material

It was shown in chapter 4.3.2, that copper is getting oxidized only to Cu^+ in the voltage range of up to 2 V. Even though iron can play a significant role in terms of availability, therefore, the binary $CuFeS_2$ might have an interest in electrochemical reaction behavior vs. magnesium since copper is found in oxidation state +1 and iron in +3, potentially following a redox conversion reaction like lithium batteries:

$$CuFeS_2 + 2\ Mg \rightarrow Cu + Fe + 2\ MgS$$

To investigate this hypothesis, $CuFeS_2$ was produced by hydrothermal synthesis using the precursor $CuCl_2$, $FeCl_2 * 4\ H_2O$, and L-cysteine as a sulfur source. During the synthesis, iron was oxidized while copper was reduced, ending in the chemical sum formula $Cu^{+I}Fe^{+III}S_2^{-II}$.

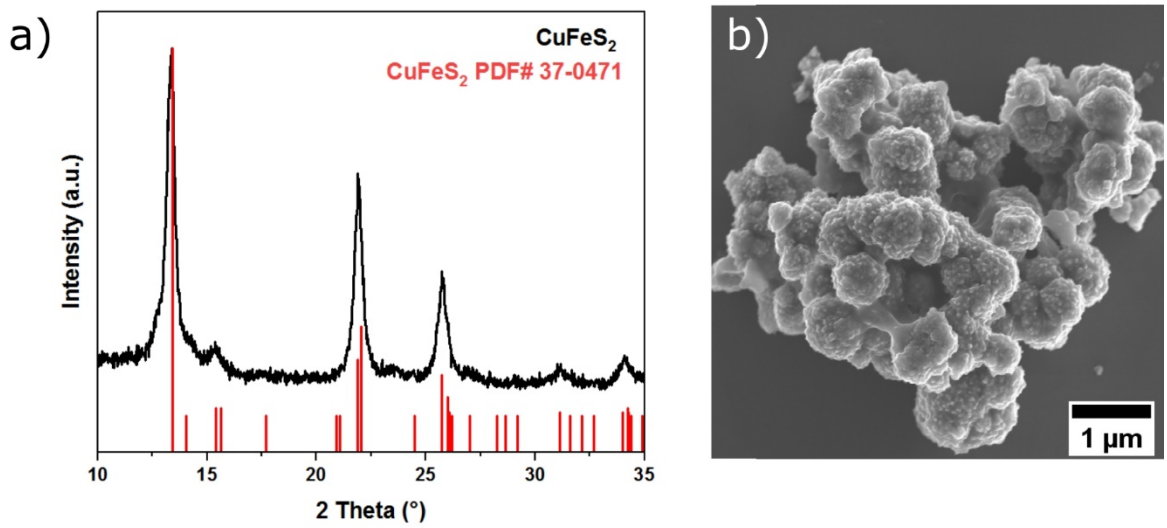

Figure 91: a) XRD of $CuFeS_2$ with the reference pattern #37-0471 and b) SEM image of $CuFeS_2$ micrometer particles.

The XRD pattern presented in Figure 91a proves the crystal structure of the synthesized material as chalcopyrite ($CuFeS_2$) fitting to the reference pattern PDF# 37-0471. The particles have micrometer size observed as agglomerated spherical particles in the SEM image in Figure 91b.

From EDX analysis, it was identified that the ratios of Cu : Fe : S are in accordance with the desired material. Beside high amount of Si resulting from the substrate, contaminations of carbon and oxygen were additionally detected during the measurement.

The relatively high amount of carbon can be explained by some remaining carbon residuals from the hydrothermal synthesis (Figure 92).

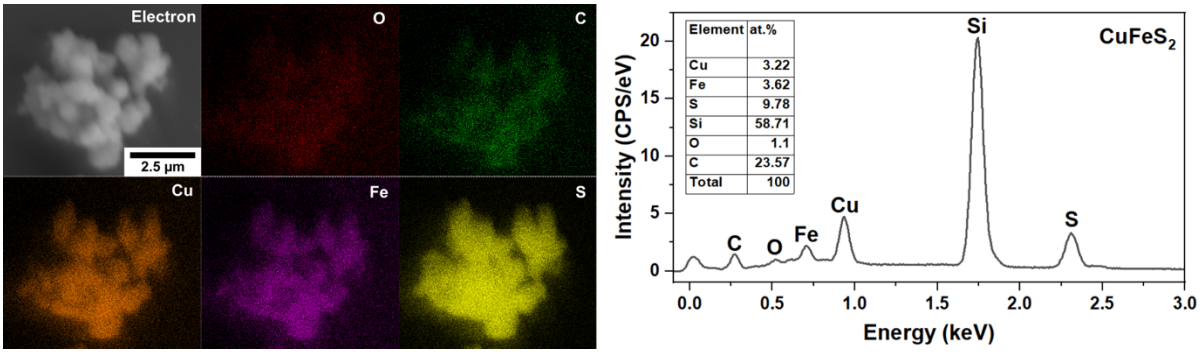

Figure 92: EDX analysis of $CuFeS_2$.

Cyclovoltammetry was performed in the $CuFeS_2$ material vs. a magnesium metal electrode in a Mg(hexamethyldisilazane)$_2$ * 2 $AlCl_3$/DME electrolyte, as displayed in Figure 93a. During the first discharge cycle, no clear reduction peak could be identified as it would be expected for the reduction of Cu^{+I} to Cu^{+II} and the multiple-step reduction from Fe^{+III} to Fe^{+II} and finally to Fe^0. Instead, a broad discharge plateau is visible in the voltage range from 1.8 V – 0.2 V, whereas the current density increases towards lower potentials, especially at 1.4 V and 0.75 V. This broad peak is assumed to originate from the overlapping reactions of the above mentioned reduction reactions in the crystal structure.

In the first charging, a minor oxidation peak at 1.4 V and around 2.0 V could be observed. From the first to the second to the third discharge cycle, a dramatic loss in current density was measured. In the second charge cycle, the first oxidation peak shifted from 1.4 V to 1.3 V and increased in intensity, which almost disappeared in the third cycle. These oxidation peaks are assumed to correspond to some intercalated Mg-ions, which intercalate at relatively low potentials into the carbon framework of the current collector as seen from lithium-ion batteries. The oxidation peaks at around 2 V remained in the second and third cycles, which corresponds to the oxidation of Cu to Cu^{+I}.

By comparing the results from the Fe_3S_4 half-cell measurements with these findings, the redox behavior of Fe_3S_4 and $CuFeS_2$ looks quite similar. However, it is believed that only Cu-S plays the dominant and active role when cycling $CuFeS_2$ vs. Mg/Mg^{2+}. Even when a stable performance at 80 mA g^{-1} over 200 cycles was measured, the specific capacity was found to be too low for practical applications (Figure 93b). Nevertheless, the investigated $CuFeS_2$ material is expected to increase the specific

capacity by nano-structuring chalcopyrite, enabling the practical application of re-chargeable magnesium batteries, as already seen for CuS cathode material.

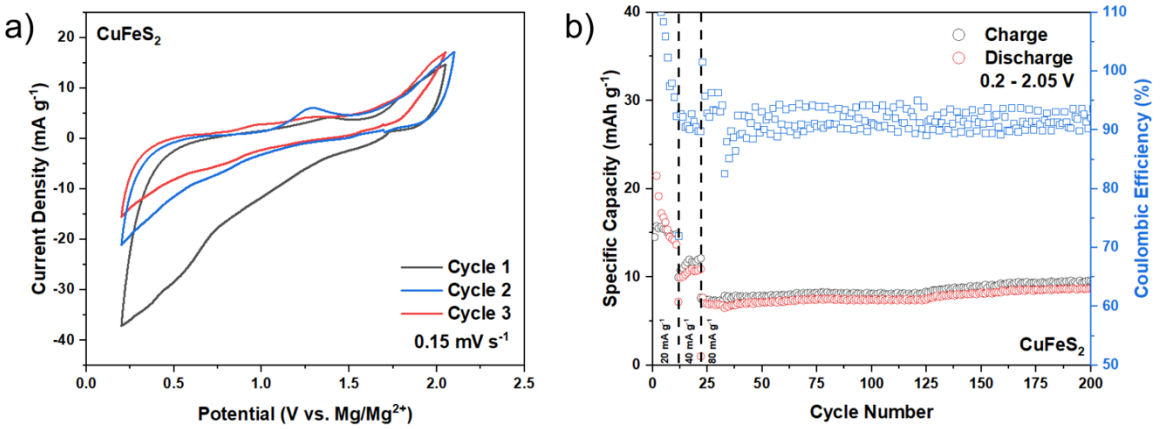

Figure 93: Cyclovoltammetry of $CuFeS_2$ and galvanostatic charge-discharge measurements of $CuFeS_2$.

The results present the high potential of iron and copper-iron sulfide as potential candidates as cathode materials for rechargeable magnesium batteries. Particularly, the addition of a small amount of lithium salts demonstrated the dramatic bottleneck of magnesium-based electrolytes so far. Even if some reports present more suitable Mg^{2+} liquid conductors, the development of the magnesium-based electrolytes is an ongoing and demanding research field.[145,366] That copper-iron sulfide has the potential to deliver very high capacities of over 500 mAh g^{-1} in other energy storage systems, such as sodium or lithium batteries, was already reported.[243,367,368] Similar capacities might be achievable in rechargeable magnesium batteries in combination with the right choice of electrolyte.

4.3.5 Copper iron sulfide / reduced graphene oxide (rGO) free-standing films for lithium-sulfur batteries

Light weight, sustainable resources, and high energy densities of the active materials are required to achieve a suitable energy storage system for the next generation of batteries. Therefore, electrode materials and cell design play an essential role. Finding solutions for omitting the current collector to reduce weight in the cell could be one advantage. Therefore, free-standing and flexible rGO films were developed as self-supported electrode materials and combined with a sustainable and high-energy density material consisting of $CuFeS_x$.[57] The rGO films were prepared by pressure-induced filtration of a GO dispersion. Two ways were used to incorporate copper iron sulfide particles into the free-standing electrode. In the first approach, $CuFeS_2$ particles were synthesized on the GO sheets before the pressure filtration. For second method, particles with high stability in aqueous solutions were synthesized. However, the first attempt by synthesizing particles on the GO sheets via microwave-assisted synthesis was successful, however it could not yield stable dispersions for the pressure filtration. Therefore, in the second attempt, copper iron sulfide particles with surface functional groups were synthesized with high stability in aqueous solutions (CFS-I). Furthermore, the idea was to run these composite films vs. Mg/Mg^{2+}, however no functional cell could be made. Therefore, the composite films were tested against Li/Li^+ to show their potential as free-standing, flexible, and high-energy-density electrodes.

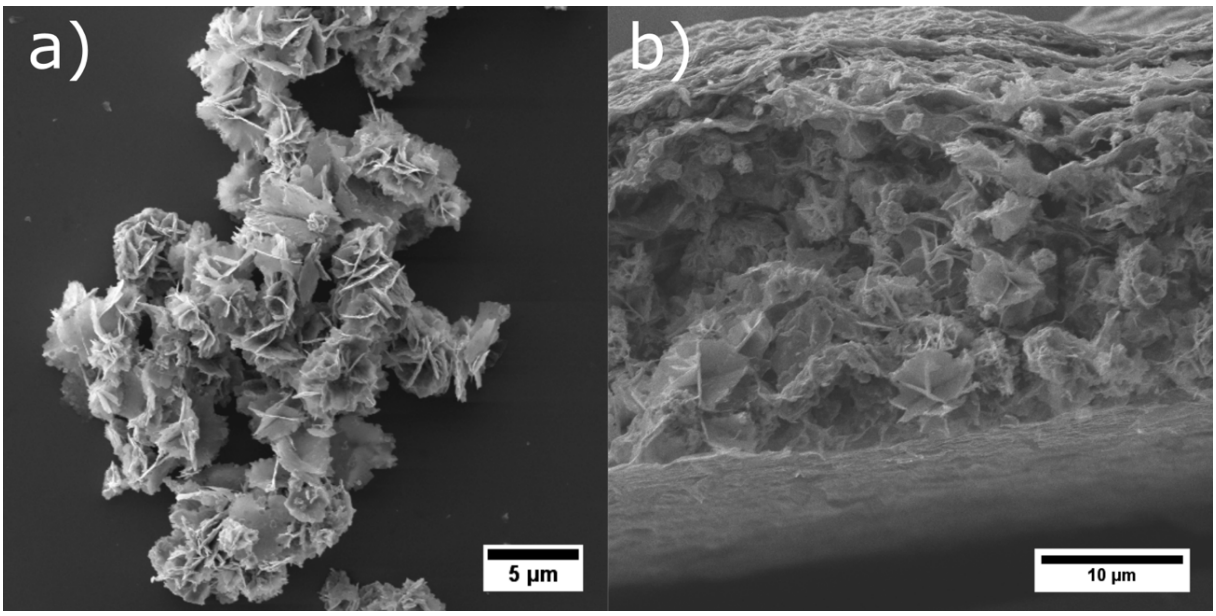

Figure 94: SEM images of a) as-synthesized CFS-I. And b) pressure-filtrated and reduced graphene oxide-CFS composite film.

The SEM image (Figure 94a) of the as-synthesized material revealed a flower-like structure with thin nanosheets. XRD characterization of the flower-like materials revealed a mixture of CuS and $CuFe_2S_3$ phases (Figure 97a). The CFS-I material turned into crystalline Bornite (Cu_5FeS_4) through simple heat treatment. After the pressure filtration of the GO/CFS-I mixture, a free-standing and flexible film was obtained. The cross-sectional SEM image (Figure 94b) showed the CFS-I material to be sandwiched between two GO layers. With a large spacing between the GO layers of 15 µm, high loading of the active material into the carbon framework could be visualized. Interestingly, the properties of free-standing and flexibility could be maintained even after the calcination of the GO/CFS-I to the rGO/CFS film (Figure 95b).

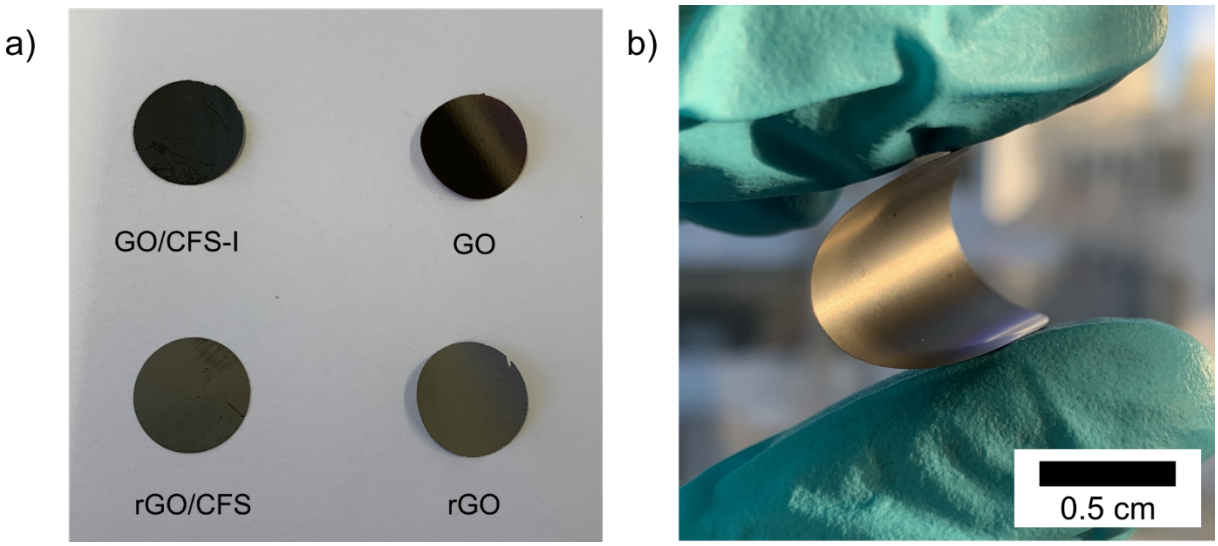

Figure 95: a) Photograph of the four different pressure-filtrated and temperature-treated film electrodes. b) Photograph of the freestanding and flexible rGO/CFS film electrode.

As can be seen in Figure 95a, GO film has a light brown color which changed after annealing to gray with a metallic shining. However, the color of the composite film (GO/CFS-I) is also brownish and changes to gray with a metallic shining after annealing, whereas the composite films appeared a bit darker. XRD analysis of the rGO/CFS free-standing film was investigated to see if the reduction of the carbon allotrope has an influence on the crystal structure of the CFS. The results showed (Figure 97a) that there was no influence on the crystal structure of the CFS by the reduction of GO to rGO under the heat treatment in Argon, even though the material maintained the morphology of flower-like organized nanosheets.

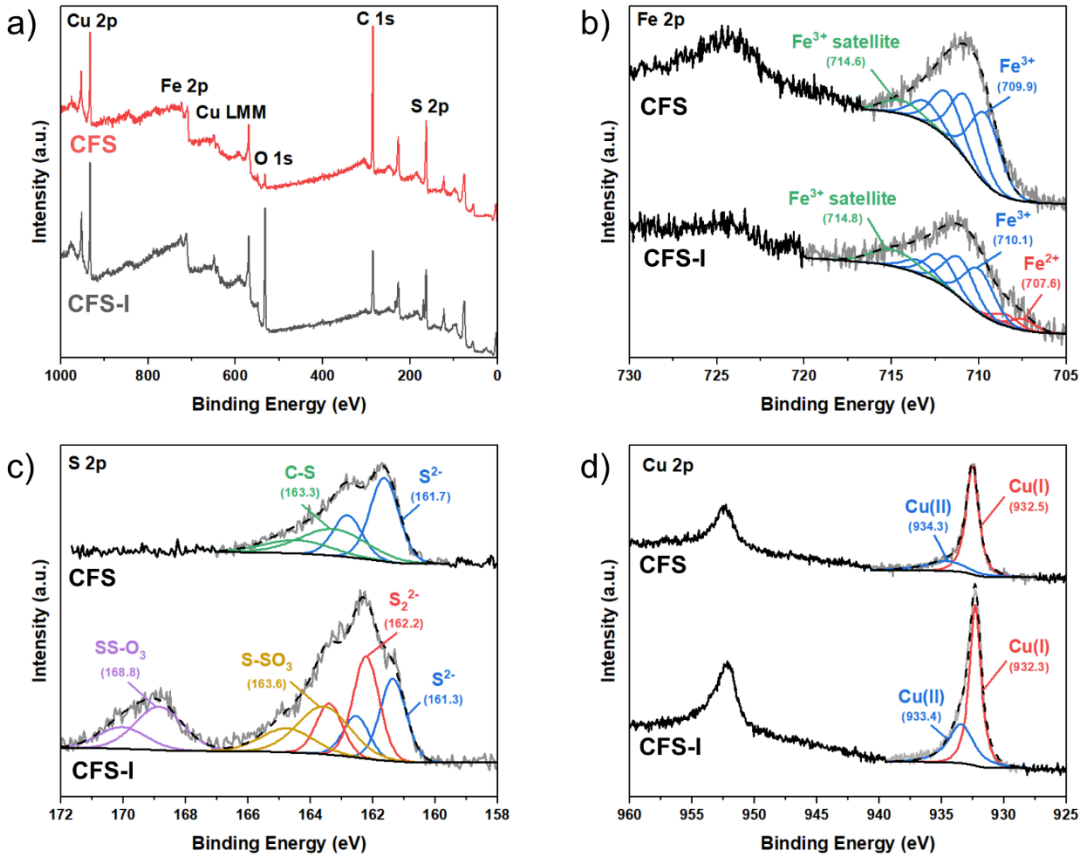

Figure 96: XPS a) survey spectra, b) HR Fe 2p, c) HR S 2p, and d) HR Cu 2p of CFS (top) vs. CFS-I (bottom).

XPS measurements of $CuFeS_2$ and CFS-I were compared to analyze surface groups to explain the high stability of CFS-I in aqueous solutions. XPS survey measurements (Figure 96a) could measure the contents of copper, iron, sulfur, carbon, and oxygen. However, by comparing the atomic ratios, dramatically higher oxygen content was measured for the CFS-I sample. High-resolution analyses were done to investigate the valence states of the elements in the compounds. For the $CuFeS_2$ specimen, only Fe^{3+} could be measured in the Fe 2p orbital, as expected from crystal structure analysis. The results revealed that, sulfur was mainly present in S^{2-} state and copper in the oxidation state +1. However, small amounts of C-S and Cu^{2+} were found as residuals in the sample. In contrast, the CFS-I exhibit beside Fe^{3+} also Fe^{2+}. Due to that, a higher amount of Cu^{2+} was measured compared to $CuFeS_2$. The HR S 2p orbital exhibit beside S^{2-} also S_2^{2-} dimers and some thiosulfates at higher binding energies. Considering previous XRD measurements (Figure 97a), the existence of Fe^{2+} can be explained by the $CuFe_2S_3$ structure, in which iron is found in oxidation states +2 and +3. The S_2^{2-} dimers result from the existence of CuS in the sample.

The formation of $S_2O_3^{2-}$ groups was unexpected but can be explained by redox reactions involving copper and iron with the support of thiourea as a complexing agent in the presence of water and oxygen.[369] These findings can explain the higher stability in aqueous solutions, due to dipolar interactions of the $S_2O_3^{2-}$-functional groups and the water molecules.

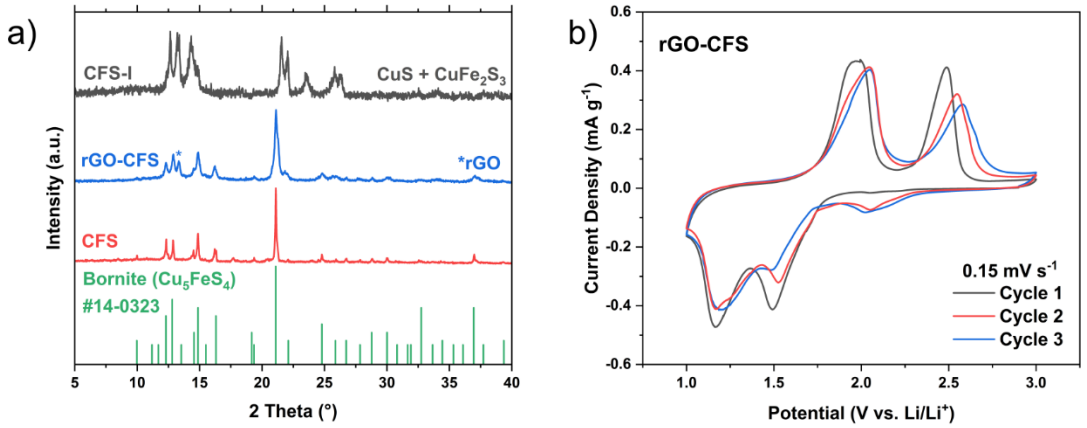

Figure 97: a) XRD patterns of CFS particles after heat treatment, rGO-CFS film electrode, and CFS-I. b) Cyclovoltammetry of CFS/rGO film electrode vs. Li/Li^+.

Cyclovoltammetry measurements were conducted to investigate the redox reactions during the cycling of the half-cell in the potential range of 3-1 V at a scan rate of 0.15 mV s^{-1} Figure 97b. For the cathodic scan, two peaks at 1.49 V and 1.17 V can be observed during the first scan, whereas for the following cycles, an additional third peak showed up at a potential of 2.05 V. The first peak at 1.49 V is assigned to the insertion of Li^+ into Cu_5FeS_4 while reducing iron from Fe^{3+} to Fe^{2+}, and the second peak is due to the reduction of Cu^+ to Cu. The reversible reaction could be demonstrated during the anodic scan with the oxidation of Cu^0 to Cu^+ and the extraction of Li^+ from remaining Li_xFeS. The oxidation from Fe^{2+} to Fe^{3+} occurred at potentials of 1.99 V and 2.49 V in the first cycle. An additional peak at 2.7 V for the second and the third cycle was measured. During the second and third cycle all peaks slightly shifted towards higher potentials. Due to the formation of a carbonate layer on the electrodes surface from the carbonate-based electrolyte, the reduction peak at 1.49 V and the as-mentioned oxidation peak are decreasing in intensity.

Post-mortem EDX analysis of the cycled electrode was done to investigate the electrochemical reactions on a morphological level (Figure 98). For the pristine electrode, the contents of copper, iron, sulfur, carbon, and oxygen were determined. After three cycles of the electrode, additional fluorine was detected. For the pristine electrode, the

amount of carbon and oxygen originate from the self-supported rGO layers. After cycling (charged state, 3rd cycle), the amount of carbon and the amount of oxygen dramatically increased, suggesting the formation of carbonates on the surface of the electrode. The amount of fluorine is assigned to other CEI formed from the fluorine-containing electrolyte [$LiPF_6$ in ethylene carbonate, ethyl methyl carbonate, diethyl carbonate].

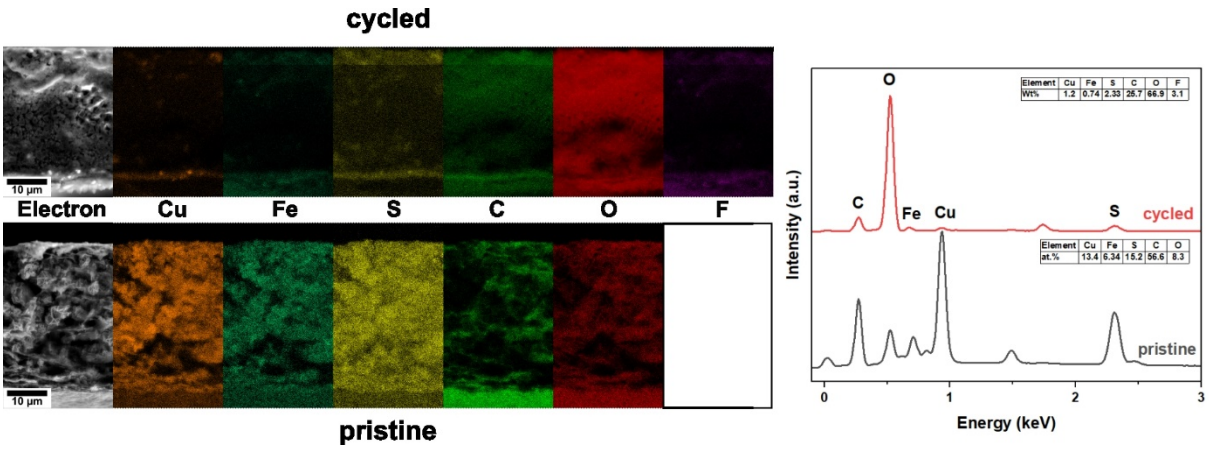

Figure 98: EDX cross-section analysis of the free-standing and flexible CFS-rGO films of the pristine and cycled state (3rd cycle charged).

The formation of carbonates at the surface of the electrode can be explained by choice of electrolyte. Since a carbonate-based electrolyte was used for the electrochemical measurements, the formation of carbonates occurs, which has a higher impact on the electrochemical performance compared to ether-based electrolytes.[370]

The formation of a carbonate-based surface coating inhibits the insertion of Li^+ into the CFS structure, decreasing the current density.[370] Similar effect has been reported upon changing the shape of the CFS particles.[371]

These redox behaviors could also be observed during galvanostatic investigations seen as large plateaus at the mentioned redox potentials (Figure 99a). At galvanostatic rate tests, high capacities of 400 mAh g^{-1} at 50 mA g^{-1} and 300 mAh g^{-1} at 100 mA g^{-1} have been measured (Figure 99b). A higher capacity loss is expected for longer cycling periods due to further decomposition of the electrolyte on the surface of the electrode, hindering Li^+ from entering the CFS structure, as seen from cyclovoltammetry measurements.

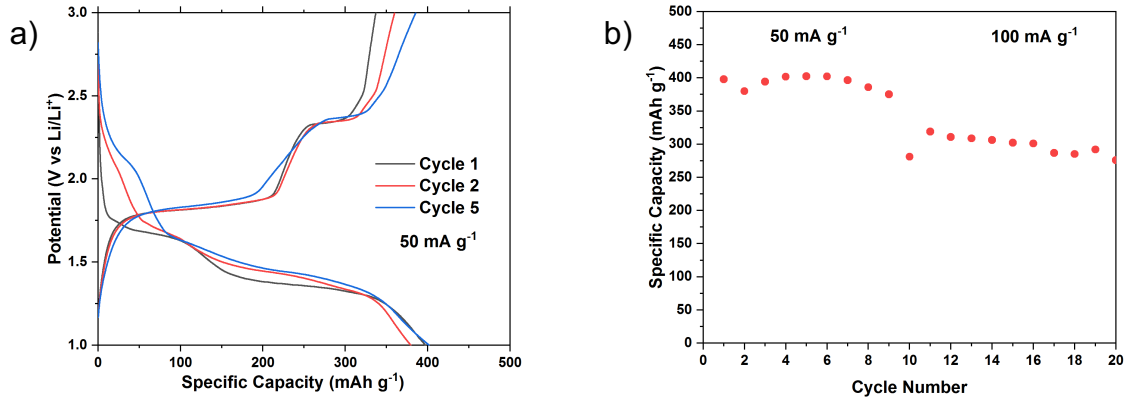

Figure 99: a) Galvanostatic charge-discharge curves of rGO/CFS free-standing films of the 1st, 2nd, and 5th cycles at a current density of 50 mA g^{-1} and b) rate capability test of rGO/CFS freestanding films at 50 mA g^{-1} and 100 mA g^{-1}.

However, the results show that rGO/CFS free-standing films can deliver a high capacity at suitable cell voltages.

The presented outcome of this study can be used to develop solutions for magnesium or magnesium-lithium hybrid systems. With its high practical performance and utilizing sustainable materials, rGO/CFS free-standing films can be a potential candidate for the next generation of batteries. Furthermore, recent reports presented the use of self-supported graphene oxide encapsulated chalcopyrite electrodes for high-performance Li-ion capacitors. The utilization of the here presented rGO/CFS free-standing films could have also the potential for such an application to reach a large energy density of ca. 200 Wh kg^{-1}.[368]

5 Summary

The development of electrode materials for the next generation of batteries considering the demands of high power and energy density, safety, enhanced charging ability, and sustainable resources, are still following goals for building better batteries (Figure 100). This research work investigated several materials and synthetic pathways for developing efficient electrode materials and their advanced materials and electrochemical characterization.

Figure 100: Target of batteries for the next generation.

I. New Electrode materials: Oxides vs. Sulfides

Role of Chemical Engineering: Pristine vs. Carbon composites

In this context, two different preparation ways of $TiNb_2O_7$ – carbon composites were tested to investigate their influence on the charging performance and cyclic stability of the electrode materials for lithium-ion batteries.

Porous and conductive TNBO/KC nanocomposite anode material for LIBs was synthesized from a surfactant-assisted precursor route followed by heat treatment under an N_2 atmosphere. Compared to pristine $TiNb_2O_7$, TNBO/KC yielded reduced crystalline $(Ti_{0.712}Nb_{0.288})O_2$ phase and $TiNb_2O_7$ phase with higher specific surface area. The synergistic effect of the reduced crystal size and connection to the electrically conductive carbon matrix obtained from biowaste resulted in better electrochemical performances of TNBO/KC as compared to pristine TNBO. At 0.1 C, TNBO/KC showed a high initial discharge capacity of 356 mAh g^{-1} compared to 269 mAh g^{-1} for TNBO. Moreover,

TNBO/KC retained higher reversible capacity at 1 C (175 mAh g^{-1} vs. 89 mAh g^{-1} over 50 cycles) along with higher capacity retention (85% vs. 60%) as compared to pristine TNBO. At an ultra-higher C rate of 32 C, TNBO/KC demonstrated remarkable stability with a capacity of ~26 mAh g^{-1}. In comparison, a capacity of only 9 mAh g^{-1} was obtained for pristine TNBO at 2 C. This exemplifies the potential of TNBO/KC nanocomposites as promising, economical, and environment-friendly alternative anode materials for commercializing LIBs technology.

In a second approach, $Tb_2Nb_{10}O_{29}$:$TiNb_2O_7$ was synthesized first by a simple and saleable sol-gel method. The electrochemical reactions and stability of the cells could be improved by a thin carbon layer coated on the surface of TNO by plasma-enhanced chemical vapor deposition from methane. Improved electrochemical behavior for the carbon-coated TNO compared to the uncoated TNO was demonstrated (Figure 101). Primarily, high cycling stability at high current rates was found for TNOC over TNO. Moreover, TNOC cells showed higher capacity retention of 93% when cycled at 50 mA g^{-1}, whereas TNO showed lower capacity retention of 86% after 70 cycles.

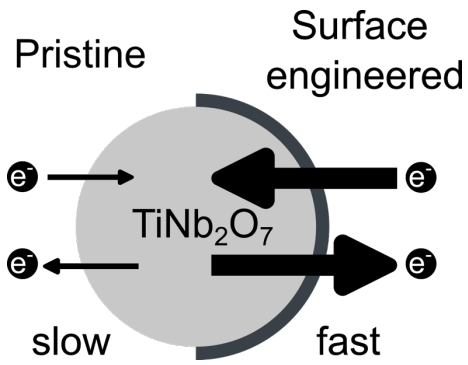

Figure 101: Carbon-based surface engineering of titanium niobium oxide enables faster charging rates and an overall enhanced electrochemical performance.

Therefore, the optimization of active material by surface engineering and additive manufacturing of the electrode materials could achieve improved electrochemical performances. However, the engineering of the interfaces of the active material and the additives in the electrode itself, such as a binder or conductive carbon, and the electrolyte are remaining goals for future research. This study could prove that $TiNb_2O_7$ is a very suitable anode material in Li-ion batteries and surface and interface engineering has enough space for improvement.

Lithium-Sulfur Batteries

Furthermore, metal-sulfur systems for lithium-sulfur and magnesium-sulfur batteries were investigated to meet the demand for high energy density for application in the electric vehicle sector. A new synthetic approach of a novel molecular approach to lithium sulfide for battery application to improve material production was presented for Li-S systems. Characterizing the synthesized molecular precursor $(LiSC_2H_4)_2NCH_3$ provides great control of the desired material formation. Through the already performed Li-S bonds on a molecular level, the controlled synthesis of well-defined Li_2S is enabled.

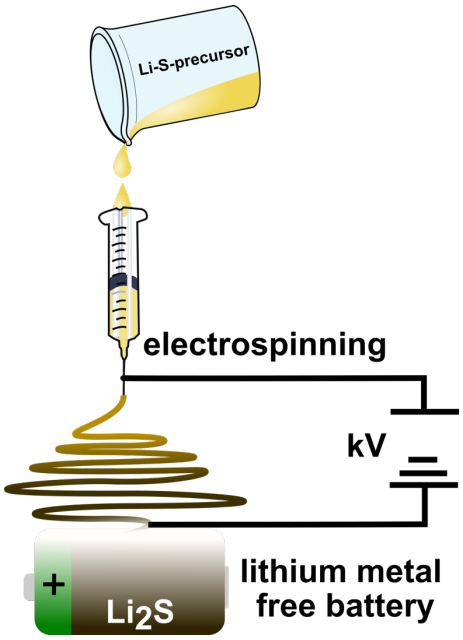

Figure 102: Synthesis of hierarchically 1D nanostructures loaded with a Li-S precursor by electrospinning for a Li_2S-lithium metal-free anode battery.

Good solubility in various solvents enables simple handling and an innovative preoperational fabrication carbon embedded Li_2S. Ethanolic solution of both compounds, polymer, and precursor, united in the same spinning solution makes preparing a suitable electrospinning system possible, resulting in homogeneous Li_2S/C-based fiber mats (Figure 102). Calcination of the electrospun fibers provides Li_2S-loaded fiber mats, which in the case of Li_2S/C show a capacity retention of 73% over 100 cycles and a capacity of about 400 mA h g^{-1} at 1C. For further application of electrospun Li_2S-loaded carbon fibers, PVP with lower molecular weight will allow higher Li_2S loading through optimized PVP/I-Li ratios in the spinning solution. This will influence the electrochemical performance of battery cells. The use of the as-prepared molecular precursor and the obtained Li_2S/C as the cathode material enable lithium metal-free lithium-sulfur

batteries with a higher safety level. Throughout this molecular approach, the development of improved battery manufacturing through a controlled material synthesis was presented. The remaining challenges are improving the capacity retention of 73% towards current values (96%) for Li-ion batteries using NMC as cathode material. Strategies to achieve this goal are chemical interface engineering, e.g., through this surface coatings of carbon, metal oxides, or metal sulfides to prevent the dissolution of polysulfides in the electrolyte. However, by applying heavier alkali metals to the pristine molecular precursor $(MSC_2H_4)_2NCH_3$ (M = Na, K), the corresponding Na_2S and K_2S materials can be prepared and tested in Na-S and K-S battery systems.

II. New Battery Technology Concepts

Dual-Functional Electrode Materials

The innovative materials approach for improved photo-chargeable lithium-ion batteries based on electrospun photoresponsive V_2O_5 nanofibers allowed the construction of a photo battery with V_2O_5 serving as a dual-function electrode responsible for photogenerated electrons and holes as well as serving as host for lithium-ions were presented (Figure 103). Therefore, optimization by surface engineering of vanadium pentoxide as photoresponsive cathode material in lithium-ion batteries was studied in this work. The limited cycling stability of V_2O_5 nanofibers was evident in capacity fading due to structural disintegration (post-mortem analysis) that was counteracted by coating the V_2O_5 nanofibers with a conductive overlayer of sp^2 carbon that enhanced both charge transport and electrical conductivity. Light conversion efficiencies of 4.24% and 5.07% for pristine and carbon-coated electrospun V_2O_5 nanofibers, respectively, validated the concept of photo enhancement and a self-charged and solar-assisted battery that can power a 2 V blue LED.

The light-illuminated samples showed an increased capacity for both carbon-coated (146 mAh g^{-1} to 161 mAh g^{-1}, 11^{th} cycle) and uncoated (164 mAh g^{-1} to 179 mAh g^{-1}, 11^{th} cycle) samples. Improved cyclic stability, after 300 cycles, could be measured for the carbon-coated VNFs with higher capacity retention (61.13%) compared to the uncoated VNF (43.85%).

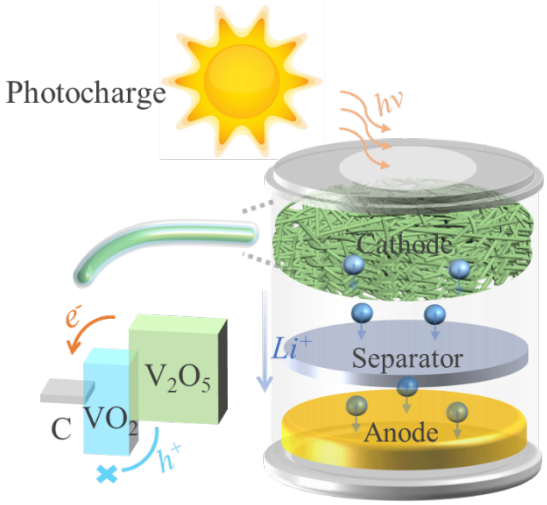

Figure 103: Concept of a photo-responsible electrode material consisting of carbon-coated electrospun V_2O_5 : VO_2 nanofibers.

These results reflect the benefit of dual-functional materials in Li-ion batteries. The synergetic effect of harvesting and storing energy with the same material provide future pathways for new concepts of future electrode materials. However, low light conversion efficiencies compared to current solar cells (~45%) is the most important challenge. Surface and interface chemical engineering are possible strategies for improving this efficiency and the overall performance of the dual-functional material. However, other dual-functional materials must be screened as potential future candidates. In this case, a balance of high light conversion efficiency and high energy storage capacity must be found.

Li^+ vs. Mg^{2+}: A New Age of Battery Technology

To employ sustainable and safe electrode materials, research beyond lithium-ion batteries was done in this work. In this context, suitable cathode materials based on transition metal sulfides, mainly copper sulfides, iron sulfides, and copper-iron-sulfides, were studied for researchable magnesium batteries due to their high theoretical capacities and high abundance in the earth's crust. The influence of their crystal structures and morphologies and nano-sized effects were investigated to elucidate and further understand the electrochemical behavior in interaction with Mg^{2+} as the active ion. For all three different systems, it was found that only nano-sized materials are viable to cycle stable at high capacities vs. magnesium metal anode. Especially for the Cu-S configuration, the influences of the density of the material and the crystal structure have a high impact on the cycling performance. However, inducing a small amount of Li-containing salts into the magnesium electrolyte, forming a hybrid electrolyte, has

excellent potential to improve the electrochemical behavior. Therefore, it was demonstrated in this thesis that Fe_3S_4 cycled vs. a $Mg/Mg^{2+}/Li^+$ hybrid system exhibits capacities of over 100 mAh g^{-1} cycled at a current density of 200 mA g^{-1}. These findings enable the potential to improve the system further to exploit its high theoretical capacity fully.

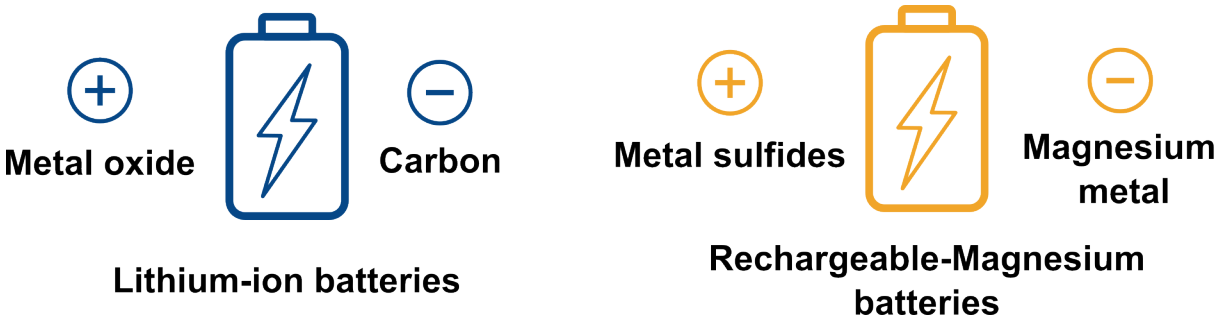

Figure 104: Current state-of-the-art lithium-ion batteries and potential next generation magnesium-sulfur batteries.

Further, it was shown that $CuFeS_2$ is a promising material for use as active material in rechargeable magnesium batteries due to its high cyclic stability. However, nano-sized engineering is required to improve its capacity for practical application. Changing the sulfur precursor in the synthesis yielded a material that showed high stability in aqueous solutions, making it suitable for pressure-filtrating rGO-CFS free-standing, flexible, and binder-free composite materials. For the rGO-CFS films, reversible redox reactions could be demonstrated for lithium-sulfur batteries.

Moreover, galvanostatic charging-discharging measurements revealed high capacities but low-capacity retention. This loss in capacity could be explained by post-mortem EDX analysis. The formation of lithium-carbonates can be prevented by choice of electrolyte (carbonate-free), e.g., the use of LiTFSI in DOL/DME, to increase the cycling stability and overall electrochemical performance of the rGO-CFS electrodes.

These rGO-CFS free-standing, flexible, and binder-free composite materials overdue some heavy current collectors and can save space and additional weight in the cell design while enabling the potential for usage in flexible batteries. Due to the high surface area of graphene oxide and reduced graphene oxide and the high expected surface area from the CFS nanoflowers, rGO-CFS composites could be potentially investigated as self-supported reduced graphene oxide encapsulated chalcopyrite electrode for high-performance Li-ion capacitor (192.33 Wh/kg, 14,280 W/kg, and cyclic stability of >90 % for 10,000 cycles).[368]

Changing the working ion from Li^+ to Mg^{2+} starts a new age of battery technology (Figure 104). A rethinking of concepts and electrochemistry in the cell enables the use of

conversion type active materials compared to the currently used intercalation types. Higher capacities and lower material costs are the main advantages of these concepts. However, sluggish kinetics in liquid electrolytes and dissolution of the active materials in the electrolyte are still challenges to overcome. Possible strategies to address these issues are solid-state-electrolytes. However, low ion diffusion in solid states are parameters that needs to be improved. Mid-term solutions might be hybrid systems with the combination of two working ions such as Li^+/Mg^{2+} or Li^+/Na^+.

In summary, the results obtained in this work demonstrate the synergetic effect of chemical surface engineering and nanotechnology for the development of new electrode materials for the next generation of batteries considering the requirements of high power and energy density, safety, enhanced charging ability, and sustainable resources.

6 Outlook

“Building better batteries” is and will continue to be the major motivation in the energy storage sector. The economic, social, and environmental requirements of modern society place high demands on the further development of battery technology, true to the Olympic motto, *“Citius, altius, fortius.”* (=lat. faster, higher, stronger). Especially considering electric cars covering longer distances or the electrification of the aviation sector. Therefore, the chemical engineering of well-known battery materials and the development of new materials and concepts, e.g., beyond Li-ion, will drive the next decades of research in the field of battery technology (Figure 105).

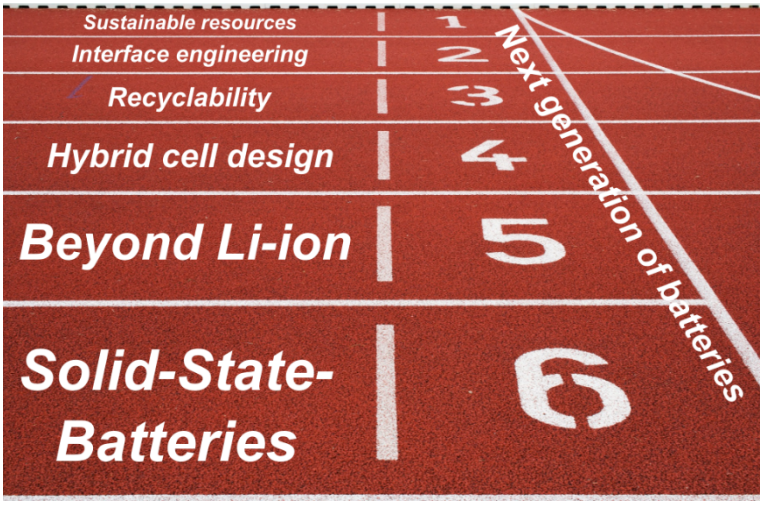

Figure 105: Future perspective of battery research for the next generation of batteries.

The search for new electrode materials for lithium batteries with high theoretical capacities (>1700 mAh g^{-1}) and high abundance in the earth’s crust (>350 ppm) has currently saturated. Sulfur has been reported multiple times as the most promising cathode material for the next generation of lithium batteries. Various researchers have studied the well-known issues of soluble polysulfide, volume expansion, high sulfur loading, and low electrical conductivity of the electrode with carbon composites. Current values for Li-S systems of 2 mg cm^{-2} sulfur loading, 800 mAh g^{-1} initial capacity, and 80-90 % capacity retentions after 1000 cycles must be increased. In this regard, chemical engineering of the surfaces and interfaces will play a significant role in future research. This will not only affect lithium-sulfur systems but also Li-O, Na-, K-, Al-, or Mg-batteries, especially all-solid-state batteries.

However, *in-situ* advanced electrochemical and material characterizations need to be represented and are highly required for future research. The influence of interfacial and surface engineering, e.g., with the surface decoration of catalysis to boost the reaction kinetics of conversion of polysulfides, is a potential field of research. Regarding Li-S systems, Chen et al. proposed a surface catalyst (CoZn-S) with both sulfur vacancies and heterogeneous interfaces that could alleviate the problem of a sluggish multielectron conversion reaction in Li-S batteries. The Li−S batteries based on CoZn-S as the sulfur cathode achieved a high discharge capacity, an excellent rate performance (764 mAh g^{-1} at 3 C), and an extremely long cycle life (over 1800 cycles at 1 C with a low-capacity decay of 0.04% per cycle). Even with a sulfur loading of 9.2 mg cm^{-2} and a harsh electrolyte/sulfur ratio of 3 µL mg^{-1}, CoZn-S delivered a high areal capacity of 8.7 mAh cm^{-2} and stable 45 cycles.[372] This approach shows the potential of surface and interface engineering on known electrode materials (sulfur, metal oxides, metal sulfides) to boost their performance, narrowing the gap between their experimental (S = 800 mAh g^{-1}) and theoretical (S = 1,675 mAh g^{-1}) capacities.

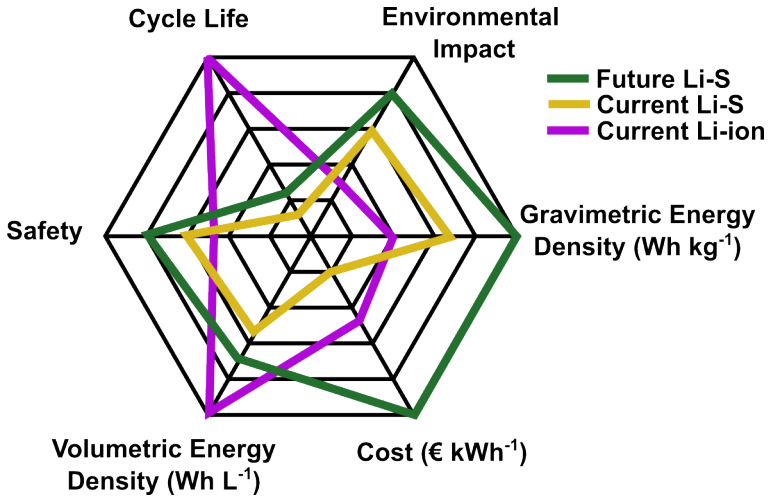

Figure 106: Future of Lithium batteries

All-solid-state lithium-sulfur batteries are under investigation with different solid electrolytes ($0.7Li_3PS_4$*0.3LiI, $Li_{10}GeP_2S_{12}$, and $Li_7P_3S_{11}$) presenting high and reversible capacity of 830 mAh g^{-1} at 1.0 C for 750 cycles. However, elevated temperatures of >60°C are necessary for such an achievement.[373,374] Improved interfaces of thin films (<60 µm) between sulfur and the solid electrolyte can lower the internal resistance of the cell, yielding in higher ion mobility in the cell ($2.4*10^{-4}$ S cm^{-1}). Defined coatings of lithium conductors show great potential in this field.[375]

However, strategies for new electrode materials (oxides, sulfides, etc.) can benefit from developing the interplay of amorphous and crystalline phases considering their interfaces. Data mining and machine learning can support the search for optimal combinations of materials and interfaces to increase the overall efficiency under the consideration of availability while keeping the cell costs low.[376]

Rechargeable magnesium batteries are still potential candidates for the generation of the next battery technologies. However, the application fields for rechargeable magnesium batteries, such as stationary storage or energy storage in space, have specific requirements for average power consumption. Commercialization of this new battery technology is a long way from the present. The integration of this system will benefit from and depend significantly on the individual advances in Mg-based electrolyte engineering, both liquid (~10^{-3} S cm^{-1}) and solid-state (~10^{-4} S cm^{-1} for $MgSc_2Se_4$).[377,378] The initial focus should target medium-power applications whereby compactness and minimum packaging requirements have more merit. Copper sulfide and copper iron sulfide have been presented as possible new electrode materials for rechargeable magnesium batteries. However, they have not been tested with solid-state electrolytes for rechargeable magnesium batteries so far.[379–381]

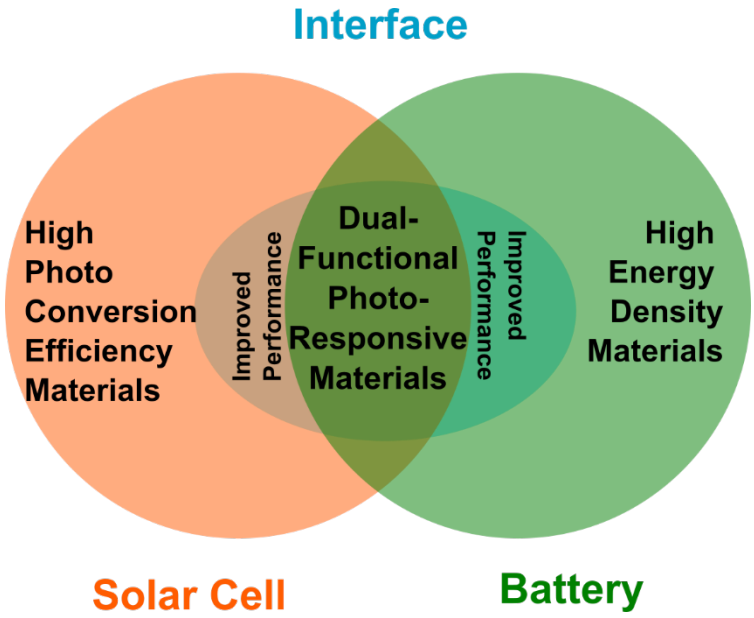

Figure 107: Synergetic effect of high efficient solar cells and high energy dense battery materials through the support of a chemical engineered interface.

The integrated photovoltaic-battery system approach is still in early research and development. Further directions need to focus on the feasibility of innovative materials development and new device designs that meet the requirements by incorporating high-capacity, efficient and stable materials. The use of bifunctional materials, e.g.,

organic photochromic materials, with energy harvesting and storage properties, must meet the properties of the existing single functional materials, operating simultaneously. Besides this, material development efforts should target on highly specific capacity storage materials, use of lithium-ion capacitors, electrochemical compatibilities between electrodes and electrolytes, new redox species with tunable redox potential, and excellent redox kinetics (Figure 107).[282]

Exploring real-world applications with low-power requirements, such as wearables, self-powered sensor networks, and electronics, should be the aim of further efforts.[382]

Beneficial for the prediction of suitable novel materials would be the use of simulation or modeling studies. Some modeling approaches in solar cells and energy storage systems can help better identify the limiting factors for the bifunctional material and optimally guide experimental conditions concerning the state of lithiation without significantly affecting the photovoltaic performance of the energy harvesting part and the electrochemical cycling performance of the energy storage part.

The journey of exploring new electrode materials for the next generation batteries, e.g., metal-sulfur-batteries or all-solid-state-batteries, will be guided by data-driven modeling research. While contemplating future challenges, the importance of obtaining high-quality extensive datasets for enhancing battery research will be key for building better batteries.[383]

7 Experimental

7.1 Data handling

Most of the presented data are published in peer-reviewed journal articles, as mentioned in the thesis. Necessary copyright permissions were requested and approved. Wherever copyright permission is needed, a statement is added in the thesis. Data obtained at the University of Cologne are stored on the server of the research group of Prof. Dr. Dr. *(h.c.)* Sanjay Mathur respecting the guidelines of easy findability and reusability. Protocols to experiments were documented in an online lab journal which is copied as a PDF on the server as well. Data obtained from collaborations are stored in the related data repositories of the cooperation partners.

7.2 Chemicals and materials

Compound	Formula	Purity	Supplier
1,2-Dimethoxyethane (DME)	$C_4H_{10}O_2$	99.5%	Sigma-Aldrich
1,3-Dioxolane (DOL)	$C_3H_6O_2$	99.8%	Sigma-Aldrich
Aluminum (III) chloride	$AlCl_3$	Sublimed for synthesis	Merck KGaA
Ammonium chloride	NH_4Cl	99.5%	Wilhelm Schnitzler GmbH
Bis(trifluoromethane)sulfonimide lithium salt (LiTFSI)	$LiC_2NO_4F_6S_2$	99.99%	Sigma-Aldrich
Bis(trimethylsilyl)amine or hexamethyldisilazane (HMDS)	$C_6H_{19}NSi_2$	98%	Carbolution
Copper (I) chloride	CuCl	99%	Sigma-Aldrich
Copper(II)chloride	$CuCl_2$	99%	Sigma-Aldrich
Ethanol absolute	C_2H_6O	>99.8%	Fisher Scientific
Glacial acetic acid	CH_3COOH	≥99.7%	Fisher Chemical
Graphite	C		Sigma-Aldrich

Hydrochloric acid	HCl	37%	Fischer Chemicals
Hydrogen peroxide	H_2O_2	33%	Sigma-Aldrich
Iron(II)chloride tetrahydrate	$FeCl_2 * 4H_2O$	98%	Alfa Aesar
L-cysteine	$C_3H_7NO_2S$	97%	Sigma-Aldrich
Lithium foil	Li	99.9%	Alfa Aesar
Lithium hexafluorophosphate in EC, EMC, DEC	$LiPF_6$	1 M solution 37:46:17	BASF, Germany
Lithium nitrate	$LiNO_3$	99.999%	Alfa Aesar
Magnesium ribbon	Mg	(≥99.5% Mg basis)	Sigma-Aldrich
Methane	CH_4		Air products
Mg powder	Mg	≥99%	Sigma-Aldrich
***n*-Butyl lithium**	C_4H_9Li	2.5 M in *n*-hexane solution	Acros Organics
N-Methyl-2-pyrrolidone (NMP)	C_5H_9NO	99+%	Alfa Aesar
N-methyl-diethanolamine	$CH_3N(C_2H_4OH)_2$	98+%	Alfa Aesar
Niobium pentachloride	$NbCl_5$	99%	Alfa Aesar
Nitric acid	HNO_3	70%	Fischer Chemicals
Phosphoric acid	H_3PO_4	85%	Fischer Chemicals
Poly(3-hexylthiophen-2,5-diyl) (P3HT)	$(C_{10}H_{14}S)_n$		Sigma-Aldrich
Polyvinylidene fluoride av. MW 534,000	$(C_2H_2F_2)_n$		Sigma-Aldrich
Polyvinylpyrrolidone av. MW 1,300,000	$(C_6H_9NO)_n$		Alfa Aesar
Polyvinylpyrrolidone av. MW 90,000	$(C_6H_9NO)_n$	K90	Sigma-Aldrich

Potassium permanganate	$KMnO_4$	98%	Acros Organics
Pyridine	C_5H_5N	≥99%	Fisher Scientific
Tin(II) chloride	$SnCl_2$	98%	Sigma-Aldrich
Sodium hydroxide	NaOH	98%	Fischer Chemicals
Sulfuric acid	H_2SO_4	99%	Fischer Chemicals
Super P	C	C65	Timcal
Thionyl chloride	$SOCl_2$	99.5+%	Acros Organics
Thiourea	$(NH_2)_2CS$	99+% for analysis	Acros Organics
Titanium (IV) isopropoxide	$C_{12}H_{28}O_4Ti$	99%	Acros Organics
Vanadyl acetylacetonate	$VO(acac)_2$	98%	ABCR GmbH

7.3 Characterization techniques

X-ray diffractometry

Powder X-ray diffraction analysis was used to perform the phase characterization in electrode materials and to correlate the volume-averaged grain size and crystallinity with other complementary techniques. The co-existence of different phases was analyzed by Rietveld analysis.

X-ray diffraction patterns were recorded at a STOE STADI MP using a Mo Kα excitation source (λ = 0.7093 Å) equipped with a Mythen 1K detector (Figure 108). The powder samples were measured in 0.5 mm glass capillaries.

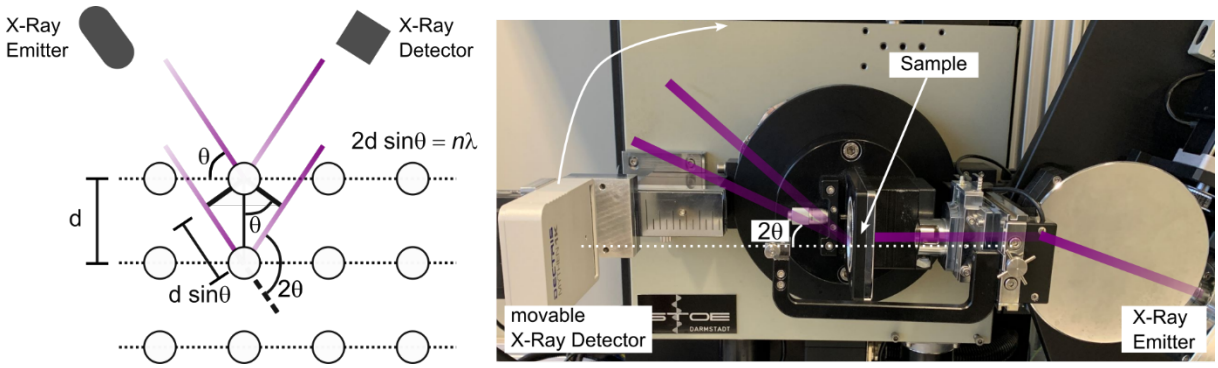

Figure 108: Principle and photograph of X-ray diffractometry.

X-Ray photoelectron spectroscopy

X-ray photoelectron spectroscopy is a surface-sensitive quantitative spectroscopic technique, which was performed to quantify the chemical composition of the synthesized materials and chemical environment on the elements of surfaces (1-10 nm). Monochromatic X-rays (photons) irritate the surface and eject photoelectrons from the orbitals of the elements. The kinetic energies (KE) of these photoelectrons will be measured through the magnetic controlled detector, which are specific for the valance state of the atoms. The binding energy (BE) can be calculated afterwards by the following formula: $E_{BE} = E_{KE} - h\nu - \phi$; where $h\nu$ = photon energy, ϕ = work function.

X-ray photoelectron spectra were recorded using an ESCA M-Probe from Surface Science Instruments equipped with a monochromatic Al Kα X-ray source (1486.6 eV, λ = 8.33 Å) in a range of 0-1000 eV in ultra-high vacuum of 10^{-10}-10^{-9} mbar (Figure 109). Survey spectra were recorded with a detector pass energy of 158.3 eV (0.5 eV step size, 125 ms dwell time, averaged over seven scans) and high-resolution spectra with 55.2 eV (0.05 eV, step size, 175 ms dwell time, averaged over 25 scans). Spectral

calibration was determined by referencing the main C 1s component to the adventitious carbon signal at 284.8 eV. For data processing, CasaXPS software from Casa Software Ltd. was used for the quantification of the signals by using the integrated peak areas and the corresponding Scofield relative sensitivity factors. The backgrounds were corrected with a Shirley line shape. For peak fitting of the C=C bonds, an asymmetric line shape (LA(1,2,0)) was used, whereas all other peaks were fitted with a symmetric GL(30) line shape.

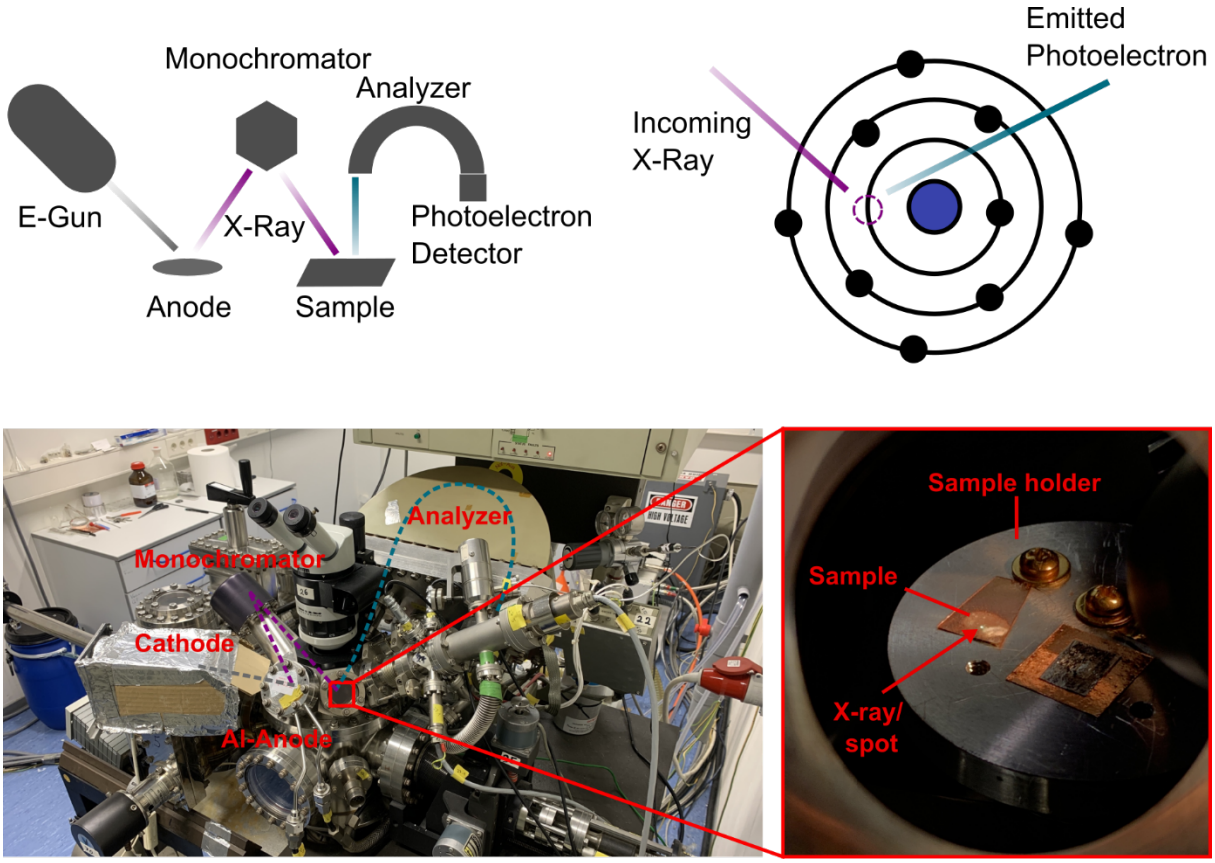

Figure 109: Principle of X-ray photoelectron spectroscopy (top) and the ESCA M-Probe spectrometer.

Cyclic voltammetry

Cyclic voltammetry measurements were performed to investigate the electrochemical oxidation and reduction potentials of the electrode materials. During the measurement, the working electrode potential is ramped up linearly vs. time to a limit before it is ramped in the opposite direction to the initial potential, while the current is measured. The cyclic voltammogram is plotted by the current of the working electrode vs. the applied voltage (Figure 110).

Cyclic voltammetry measurements were carried out with an Autolab PGSTAT101 (from Metrohm) in defined voltage windows versus the corresponding metals in half-cell

configurations. Standard measurements were performed with a scan rate of 0.15 mV s^{-1}, whereas faster scan rates were tested for advanced analytics.

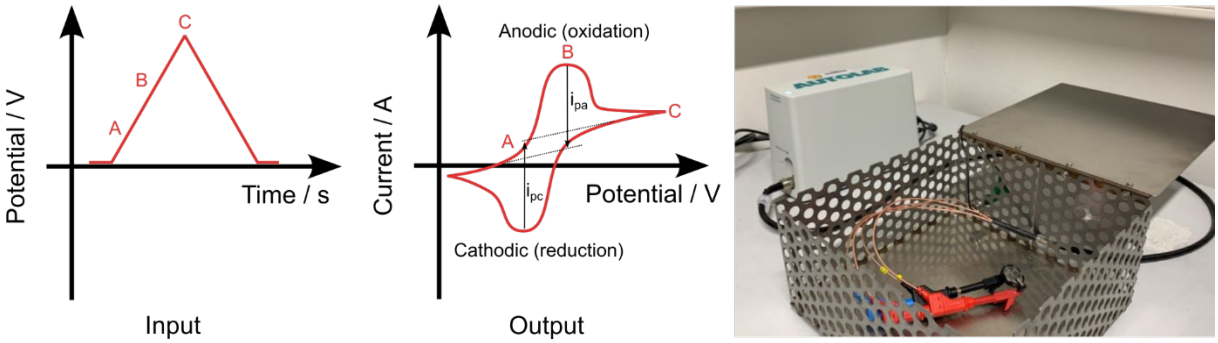

Figure 110: Principle of cyclic voltammetry and photograph of the potentiostat Autolab PGSTAT 101.

Galvanostatic charge-discharge measurements

Galvanostatic charge-discharge measurements were performed to investigate the charge/discharge capacities, coulombic efficiencies, and cycle stabilities of the electrochemical cells at different C-rates (1C = theoretical capacity per hour). Therefore, a constant current for charging and discharging is applied to the cell, while the potentials over time are measured (Figure 111).

Galvanostatic charge-discharge curves were recorded in different voltage windows *vs.* the corresponding metals in half-cell configurations. The measurements were carried out by applying different C-rates using a BST8-MA battery analyzer (MTI Corporation) using Neware software.

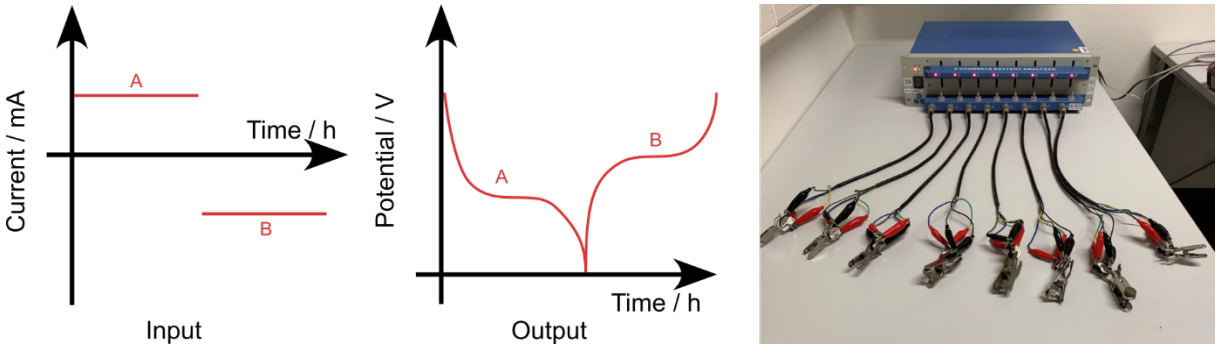

Figure 111: Principle of galvanostatic charge-discharge measurements and photograph 8-channel battery analyzer from MTI for galvanostatic charge-discharge measurements

Raman spectroscopy

Raman spectroscopy was performed to investigate the appearance of carbon coating on the active material through their vibrational modes. The Raman effect correlates with polarizability of the electrons in a material or molecule, which is a form of inelastic light scattering. Monochromatic light, mostly phonons from lasers, interacts with

molecular vibrations, phonons or other excitations in the material, leading to an energy shift (Stokes or Anti-Stokes) of the laser, which gives information about the vibrational modes (Figure 112).

Raman spectroscopy (Lab Ram HR 800 Raman spectrometer) was carried out by using a 514.5 nm green line of Ar^+ ion laser to study the crystallinity and disorder of the vanadium pentoxide materials.

Raman spectroscopic measurements of $TiNb_2O_7$ and $TiNb_2O_7$/C were carried out at a RISE system using a UHTS 300 SMFC VIS-NIR spectrometer (532 nm laser, 80 mW max.) from WITec attached to a SEM Sigma 300 VP from Zeiss (Carl Zeiss Microscopy Deutschland GmbH, Germany) (Figure 114).

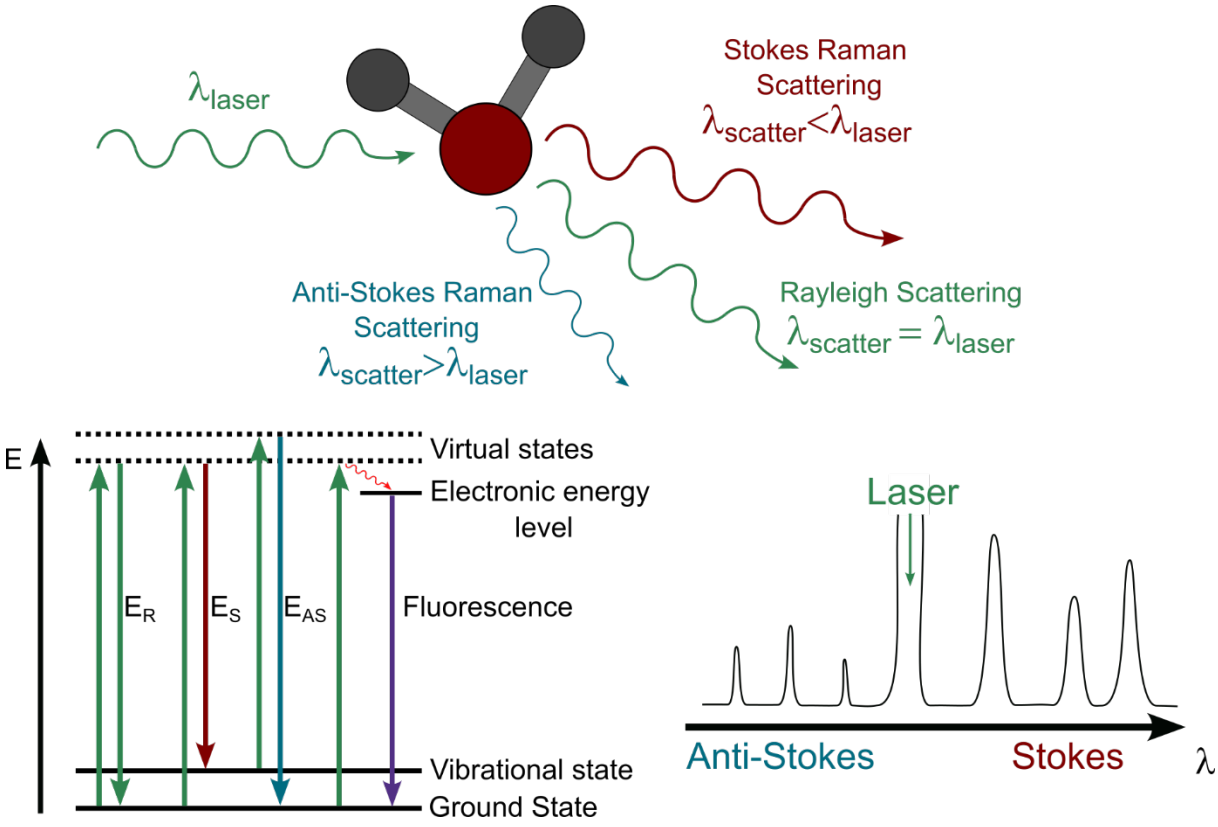

Figure 112: Principle of Raman spectroscopy.

Electrochemical impedance spectroscopy

Electrochemical impedance measurements were done to investigate the interfacial properties related to electrochemical events occurring at the electrode surface.

The electrochemical impedance measurements were conducted on a Versastat 4 potentiostat with the potentiostat mode at the OCV conditions. A sinusoidal signal with a perturbation potential of 10 mV was applied to record the impedance spectra over a frequency range of 100 kHz to 0.1 Hz. The recorded impedance was verified to be of

high quality (less than 2% error) by Kramers–Kronig (KK) relation prior to the ECM and DRT analysis via ZView 4 software (Scribners) and DRTTools (Matlab code).[384]

Scanning electron microscopy

Scanning electron microscopy is a powerful technique to produce images of samples in the micrometer and nanometer sized region. Images are recorded by simply scanning the surface with a focused electron beam. The interaction of the electrons and the atoms produce various signals that contain information about the surface topography and composition of the sample. Mostly secondary electrons are detected for the imaging. Sometimes back-scattered electrons delivering additional information of the specimen. Ejected X-rays from these interactions can be measured by energy-dispersive X-ray spectroscopy (Figure 113).

The morphology and size of nanoparticles were evaluated using a Nova Nano SEM 430 field emission scanning electron microscope with an acceleration voltage of 20 kV. For electron tomography, the samples were dispersed in ethanol or water and drop-casted on a silicon wafer mounted on a graphite tape holder.

The SEM measurements regarding the vanadium pentoxide nanofibers were recorded with a FEI Strata 235 Dual Beam and a field-emission scanning electron microscopy (FE-SEM) (SU9000, Hitachi High-Technologies Corporation, Tokyo, Japan).

SEM measurements of TNO, TNOC, and all copper and iron sulfide materials, as well as post-mortem analysis, were carried out at a Sigma 300 VP from Zeiss (Carl Zeiss Microscopy Deutschland GmbH, Germany).

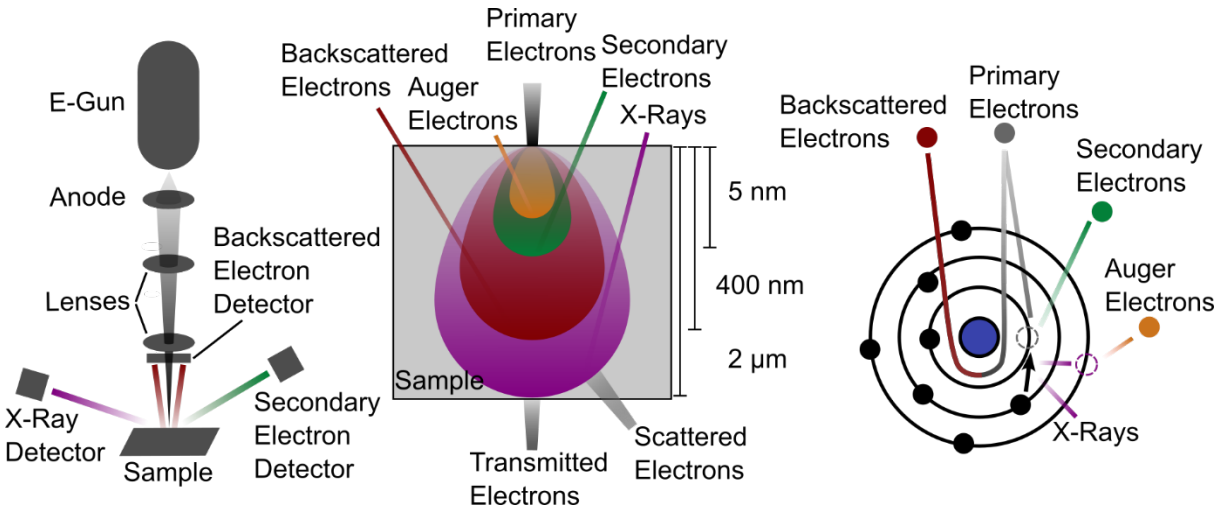

Figure 113: Principle of scanning electron microscopy.

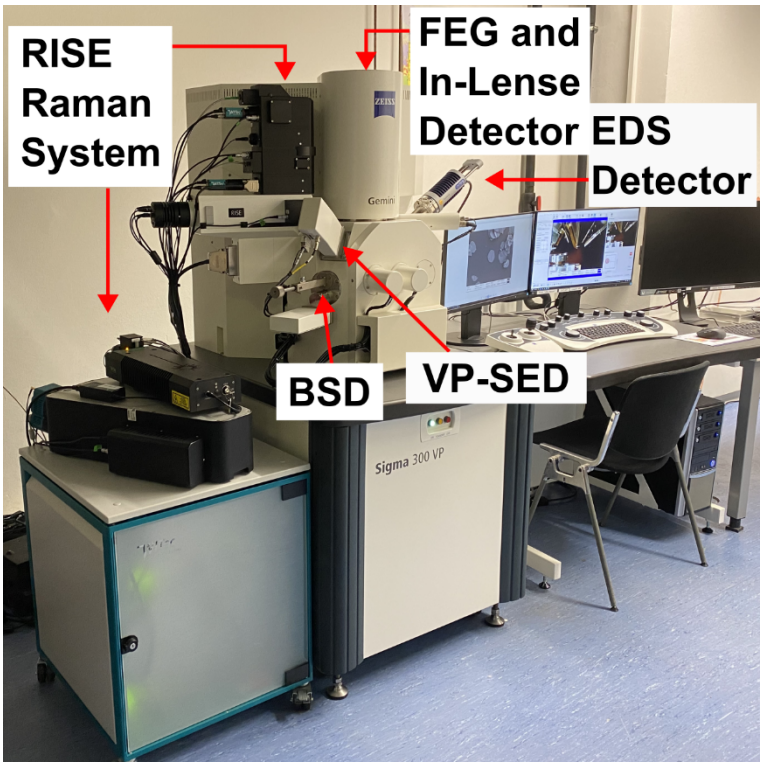

Figure 114: Photograph of the used Sigma 300 VP SEM from Zeiss equipped with an Oxford energy-dispersive X-ray spectroscopy detector (EDS), a variable pressure secondary electron detector (VP-SED), a back-scattered detector (BSD), and a RISE Raman system from WITec.

Energy-dispersive X-ray spectroscopy

Energy-dispersive X-ray spectroscopy is the detection of X-rays generated by the interaction with a focused electron beam and a sample. The emitted X-rays, which can be measured by an energy-dispersive spectrometer, are characteristic for different types of atoms and can deliver information of the chemical composition of the sample. Energy-dispersive X-ray spectroscopy measurements were performed at a SEM Sigma 300 VP from Zeiss (Carl Zeiss Microscopy Deutschland GmbH, Germany) equipped with a 30 Xplore EDS detector from Oxford instruments (Figure 114).

High-resolution transmission electron microscopy

Transmission electron microscopy was used to measure the thickness of the carbon layer on the vanadium pentoxide nanofibers by using a JEOL JEM-2200 FS. Samples were prepared by drop coating the particles from diluted ethanolic dispersions of the powders on a carbon-free TEM grid. The solvent was evaporated under air before the measurement. Images were analyzed using the software ImageJ.

Thermogravimetric analysis

Thermogravimetric analysis and differential scanning calorimetry of CuS were performed using a PerkinElmer STA 6000 with defined scan rates under desired environments (N_2) with a flow-rate of 19.8 ml min^{-1}.

Thermal analysis was performed on a TGA/DSC (Mettler-Toledo GmbH, Germany) in a nitrogen atmosphere (25 mL/min) at a rate of 10°C/min from 30 to 800°C (Figure 115). For the determination of the Li_2S amount in the final product, synthetic air was used at a rate of 10°C/min from 30 to 800°C. This temperature was held for 5 h. The sample weight was in the range of 5−20 mg.

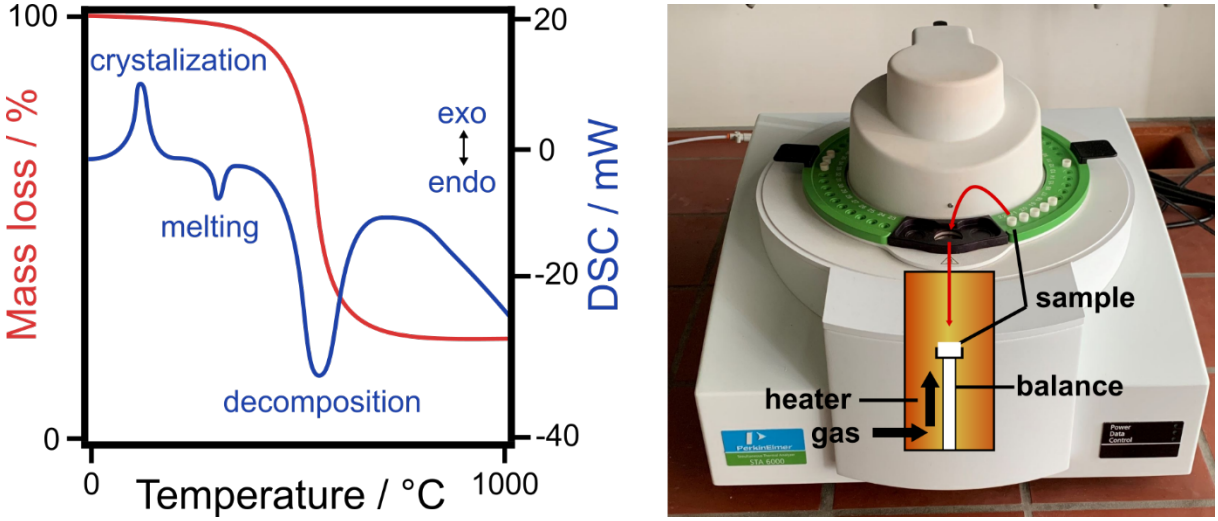

Figure 115: Principle and photograph of thermogravimetric analysis and differential scanning colorimetry.

Power/Photo-conversion efficiency

The overall photo-conversion efficiency was calculated based on the following equation:[266,280,334]

$$\eta_{overall} = \frac{E_{out}}{E_{in}} * 100\% = \frac{E_{discharge}}{P_{in} * t_{ph} * A_{ph}} * 100\%$$

where $E_{discharge}$ (E_{VNF} = 0.532 mWh – from BST8-MA battery analyzer, $E_{VNF\text{-}C\text{-}120}$ = 0.636 mWh) is the discharge energy at the specific current density of 10 mA g^{-1}, P_{in} (= 11 mW cm^{-2} for 400 nm illumination source) is the intensity of illuminated light, t_{ph} (= 3 h) represents the time of photo-charge, and A_{ph} (= 0.38 cm^2) describes the illuminated surface area. The photo-conversion efficiencies for VNF and VNF-C-120 are 4.24% and 5.07%.

Nuclear magnetic resonance spectroscopy

Nuclear magnetic resonance (NMR) spectroscopy is a spectroscopic method for studying the electronic environment of individual atoms and the interactions with neighboring atoms. This enables the structure and dynamics of molecules to be elucidated and concentration determinations to be made. The method is based on nuclear magnetic resonance. A resonant interacts between the magnetic moment of the atomic nuclei of the sample, which is in a strong static magnetic field, and a high-frequency alternating magnetic field (Figure 116).

NMR spectra were recorded on a Bruker Avance II 300 spectrometer; chemical shifts are quoted in parts per million relative to tetramethyl silane (^{1}H and ^{13}C).

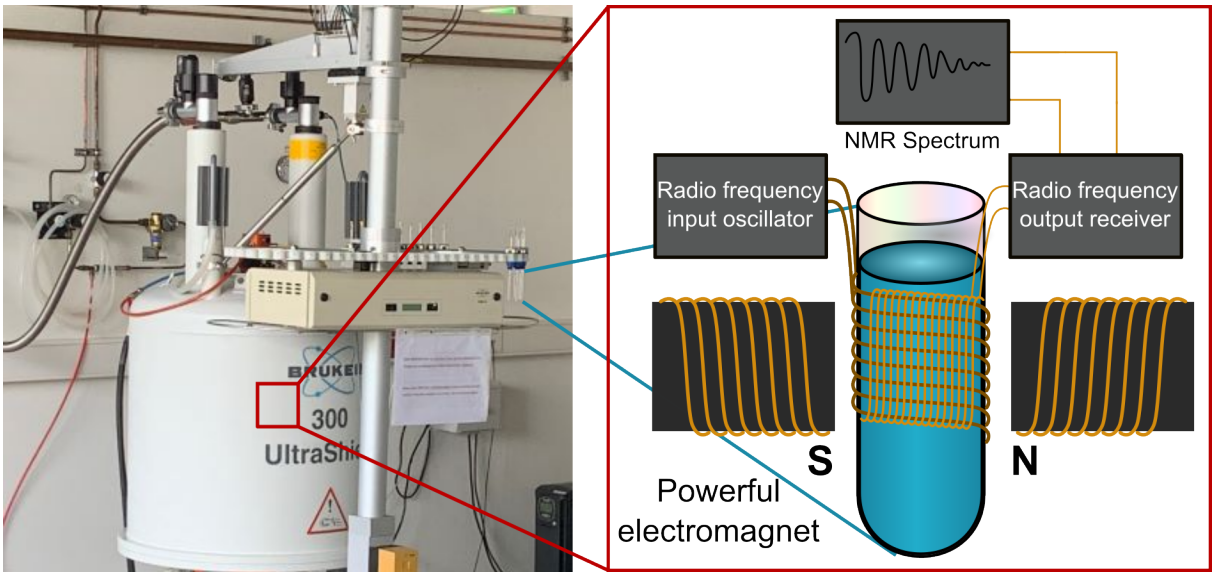

Figure 116: Photograph of nuclear magnetic resonance spectrometer and principle of NMR.

7.4 Methods

Parts of the synthesis protocols are published in the associated publications mentioned in the chapters. For the reproductions in the thesis/dissertation as an author, permissions are not required.

7.4.1 Coin cell preparation

Battery slurries were in general mixed in N-methyl-2-pyrrolidone with a weight ratio of 80:10:10 or 70:15:15 of active material, polyvinylidene fluoride, and Super P, and were doctor blade coated on carbon felt (SGL AA 29, 300 µm), copper or aluminum disks (14 mm diameter). Minor changes were applied for the V_2O_5 fibers with a ratio of 80:8:8:2:2 weight ratios of active material (VNF or VNF-C-120), PVDF, Super P, reduced graphene oxide, and poly(3-hexylthiophen-2,5-diyl) in NMP.

For the Li_2S-fibers, the ratio of active material, carbon black, and PVP was set to 80:5:15. The corresponding slurry was cast on a non-woven carbon (Sigracet 28AA, SGL Carbon SE) by a doctor blade. Subsequently, the electrodes were dried at 90°C under vacuum for 16 hours. Finally, the electrodes with a diameter of 13 mm (coin cells) and 12 mm (Swagelok® T-cells) were punched out. The loading of Li_2S was about 0.5 mg cm^{-2}.

Lithium foil (12 mm diameter) or magnesium ribbon was used as counter and reference electrodes. The electrode performances were tested in a half-cell configuration using a standard two-electrode coin cell (CR2032) assembly. As an electrode separator, a Celgard 2400 separator (18 mm diameter) was soaked with 65 µl of a 1 M solution of $LiPF_6$ in a 37:46:17 with a weight ratio of EC, EMC, DEC as electrolyte for Lithium-ion batteries (Figure 117). For magnesium-ion batteries a 0.35 M Mg(hexamethyldisilazane)$_2$ * 2 $AlCl_3$ in DME electrolyte and for Li-S systems a 1 M Lithium-bis(trifluoromethane)sulfonimide with 2 wt% lithium nitrate in 1,3-dioxolane and 1,2-dimethoxyethane (1:1, v:v) was used. For the V_2O_5 photobatteries, 75 µl of 1 M Lithium-bis(trifluoromethane)sulfonimide and 2 wt% lithium nitrate in 1,3-dioxolane and 1,2-dimethoxyethane (1:1, v:v) was used. The coin cell assembly process was carried out in an Argon-filled glove box (MBraun, H_2O>0.1 ppm, O_2>0.1 ppm).

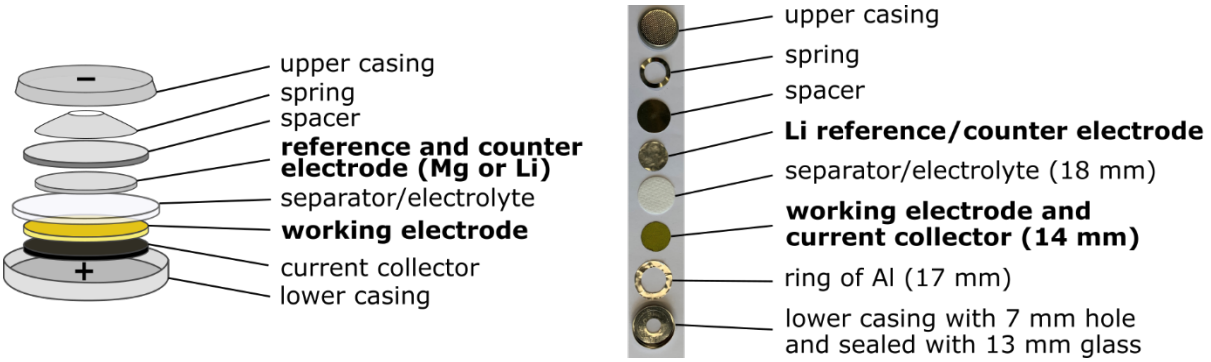

Figure 117: Assembly of a CR2032 coin cell in half-cell configuration.

7.4.2 Photoresponsive tests

Photoresponsive measurements were carried out in a modified CR2032 by punching a 7 mm hole (diameter) on the coin cell case and sealing it with a transparent glass window using EPOXY (EVO-STICK) Figure 117 (right). For the electronic conductivity between the casing and the photoelectrode, a ring of aluminum foil was placed in between. As a light source for illumination, a Diyeeni 9W USB UV lamp (λ = 400 nm, distance = ~15 cm) was used. With the reference cell (RR-1001 Shunted Si from Rera Solutions) a light intensity of ~11 mW cm^{-2} was measured (Figure 118).

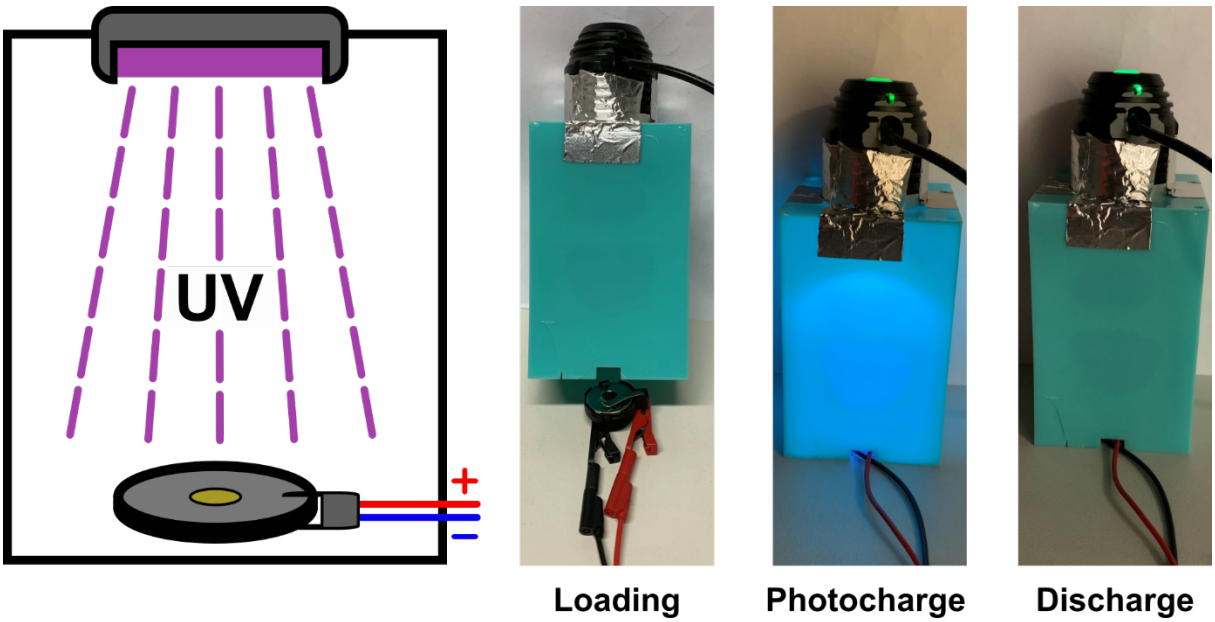

Figure 118: Photo charge set-up with UV lamp and casing.

7.4.3 Electrospinning

Electrospinning is a production method that uses electric forces to draw (nano)fibers from polymeric solutions. A liquid droplet is injected through a metallic needle towards a grounded metallic collector. A sufficiently high voltage is applied to the needle, while

the droplet becomes charged and electrostatic repulsion counteracts the surface tension so that the droplet is stretched. At a critical point a stream of liquid erupts from the surface (Taylor cone) and dries during the flight to the collector (Figure 119). The success and the control of the nanofibers is affected by many parameters (solution parameters: viscosity, polymer concentration, molecular weight, conductivity, surface tension; processing parameters: voltage, tip to collector distance, feed rate; ambient parameters: humidity, temperature). If the polymeric solution contains additional additives, such as precursors or solids, the polymer can be pyrolyzed or converted into a carbon matrix when heat treated under the exclusion of air.

A FuG electronics GmbH high voltage power supplier and a Landgraf Laborsysteme LA-100 syringe pump have been used for electrospinning. As spinnerets, 21G (inner diameter 0.5 mm) blunt needles were applied.

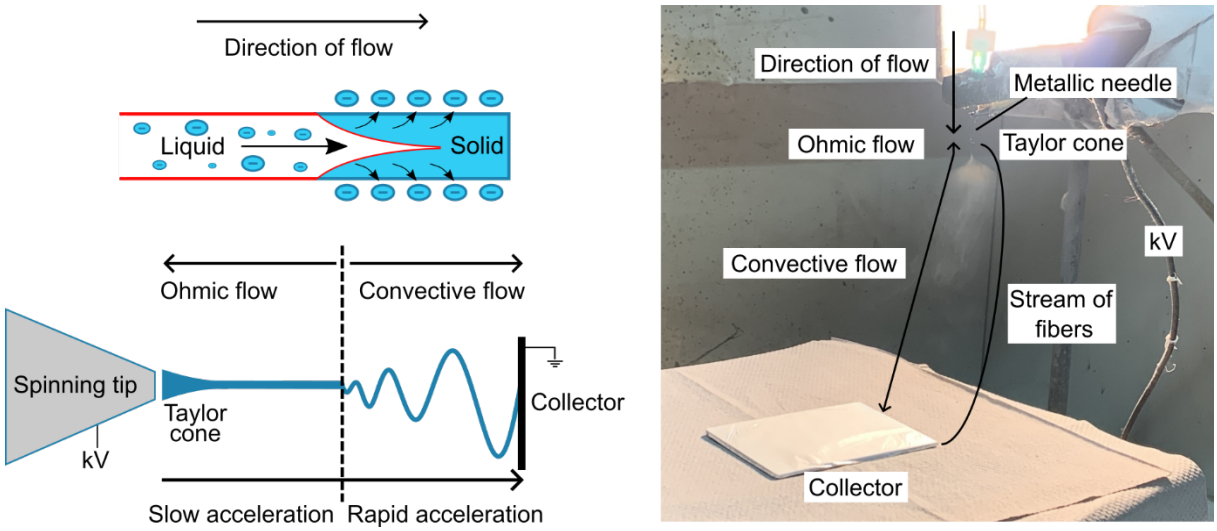

Figure 119: Principle of electrospun nanofibers.

7.4.4 Autoclave-assisted synthesis

Autoclave-assisted synthesis is a specific synthetic pathway in the group of solvothermal synthesis. In an autoclave a solvent containing educts is set under high pressure and temperature for a period. The solubility of some products increases in the solvent compared to ambient conditions, enabling reactions which would normally not occur. By controlling the parameters of pressure, temperature, time, solvent, surfactant, and educt concentration the control of the crystal size and shape is possible.

Hydrothermal synthesis were carried out in a Berghof BLH 600 autoclave. Solutions of max. 20 ml were transferred in a Teflon tube (max. capacity 40 mL), which was placed in a stainless-steal Autoclave.

7.4.5 Microwave-assisted hydrothermal synthesis

Microwave-assisted synthesis is a specific synthetic pathway in the group of solvothermal synthesis. Compared to the autoclave synthesis the purpose is not to set the sample under high pressure, instead fast heating and the induction of microwave radiation is triggered. The working principle is based on aligning dipoles of the material in an external field via the excitation produced by microwave electromagnetic radiations. The synthesis of nanomaterials is enabled through the combination of speed and homogeneous heating of the precursor materials. Polar solvents are heated, whereby their component molecules are forced to rotate with the field and lose energy in collisions (Figure 120).

Microwave-assisted synthesis were carried out in a Discover-S (CEM, Matthews, NC)(Figure 121). In a typical synthesis, a reaction volume of 5 ml was used in a max. 10 ml capacity-sized microwave glass tube.

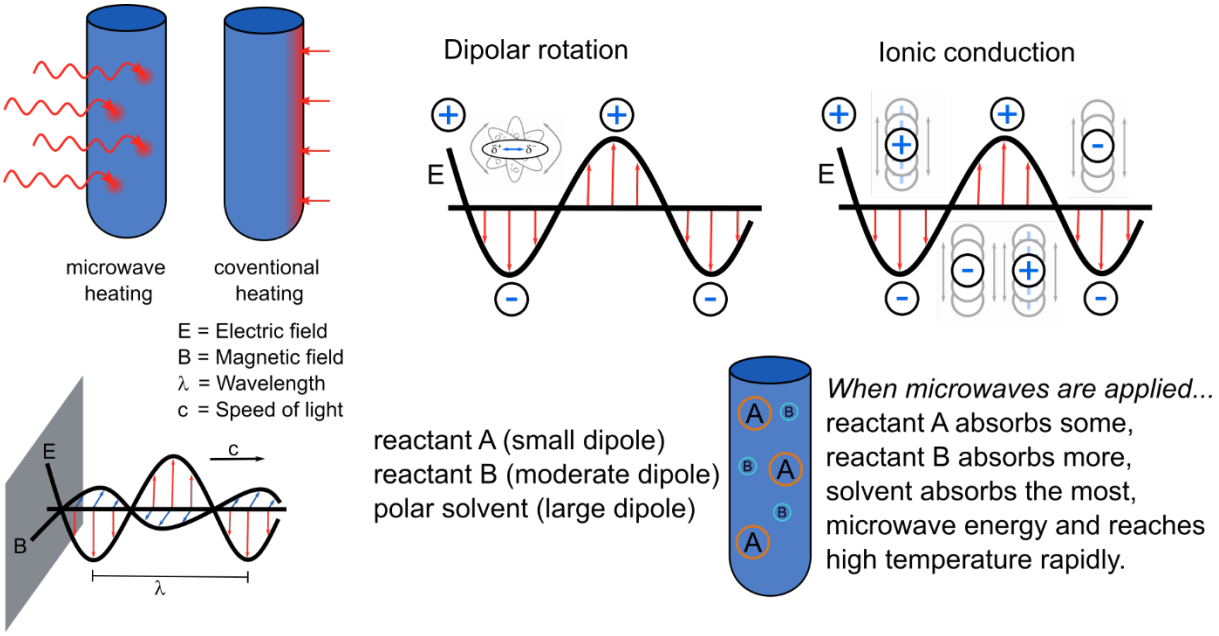

Figure 120: Principle of solvothermal microwave-assisted synthesis.

Figure 121: Photograph of the Discover-S microwave.

7.4.6 Plasma-enhanced chemical vapor deposition

Plasma-enhanced chemical vapor deposition is a chemical vapor deposition process used to deposit thin films from a gas state to a solid state on a substrate. Compared to a CVD the dissociation of the molecules is additionally to the temperature triggered by the plasma. A plasma is a mixture of charged particles in any combination of ions and free electrons as well as neutral atoms and molecules.

Plasma-enhanced chemical vapor deposition was used for carbon-coating using a commercial vacuum system from Plasma Electronics (CVD-PECVD DOMINO), working with a radio-frequency excitation (13.56 MHz). A defined flow rate in sccm of CH_4 was introduced into the reaction chamber through a mass flow controller (MKS MFC 1179) controlled by a software interface during the reaction, and the reactor pressure was maintained at 3.5 Pa. The materials were placed in a ceramic boat on the heatable RF electrode to decompose the CH_4 on the surface of the materials (Figure 122).

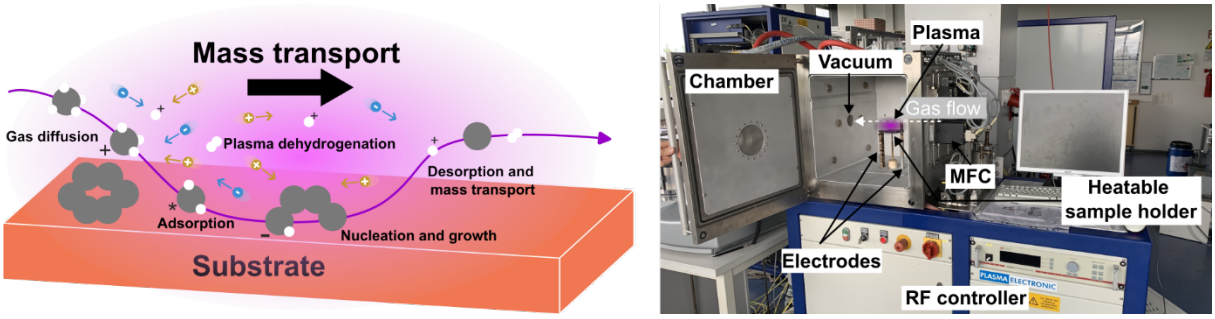

Figure 122: Principle of plasma-enhanced chemical vapor deposition and photograph of the CVD-PECVD DOMINO.

7.5 Synthesis

Parts of the synthesis protocols are published in the associated publications mentioned in the chapters. For the reproductions in the thesis/dissertation as an author, permissions are not required.

7.5.1 $TiNb_2O_7$ – sol-gel synthesis

Nanoparticulate $TiNb_2O_7$ (TNO) was synthesized via a sol-gel process using as precursors niobium pentachloride ($NbCl_5$) and titanium (IV) isopropoxide (TTIP). First, SOL 1 was prepared by dissolving 10 mmol of $NbCl_5$ in 150 mmol glacial acetic acid under an inert environment. Second, SOL 1 and 5 mmol of TTIP were added at the same time to 5 mmol of pure water and 75 mmol of conc. HNO_3. This reaction mixture was kept at 35°C for 60 h at 700 rpm. Afterward, the temperature was increased to 100°C to remove the remaining solvents. The powder was ground and calcinated in a tubular furnace with a ramping rate of 10°C/min until 800°C in air. The temperature was held for 3 h. A white powder with a yield of 1.291 g was achieved.

7.5.2 Carbon-coating on $TiNb_2O_7$ by plasma-enhanced chemical vapor deposition

The pristine $TiNb_2O_7$ particles were carbon-coated by plasma-enhanced chemical vapor deposition using methane (CH_4) gas as a carbon precursor. The coating process was performed using a commercial vacuum system from Plasma Electronics (CVD-PECVD DOMINO), working with a radio-frequency excitation (13.56 MHz). 40 sccm of CH_4 were introduced into the reaction chamber through a mass flow controller (MKS MFC 1179) controlled by a software interface during the reaction, and the reactor pressure was maintained at 3.5 Pa. The 0.2 g of TNO was placed in a ceramic boat on the heatable RF electrode to decompose the CH_4 on the surface of the TNO. The temperature was set to 500°C and the plasma power to 20 W (resulting in a bias of 180-200 V) for 1 h to achieve a thin carbon coating on TNO (TNOC).

7.5.3 Synthesis Li_2S – fibers

All manipulations of air- and moisture-sensitive materials were carried out under a nitrogen atmosphere using Stock-type all-glass assemblies. All solvents and reactants were used without further purification except otherwise mentioned.

The synthesis of $(HSC_2H_4)_2NMe$ I has been described before.[95]

For the synthesis of *N*-methyl-diethanethiolamine-lithium ($LiSCH_4)_2NMe$ (I-Li), 12.60 ml (31.20 mmol) of 2.5 M *n*-butyl lithium in *n*-hexane was added to a liquid nitrogen-cooled solution of *N*-methyl-diethanethiolamine (2.39 g, 15.60 mmol) in 10 ml heptane and stirred for 30 min at room temperature. The resulting colorless powder was washed several times with *n*-heptane. Afterward, the solvent was removed under reduced pressure. The product was isolated as a colorless solid with a yield of 94% (2.39 g, 14.60 mmol).

^{1}H NMR (D_2O, 300 MHz, RT, ppm): 2.37 (s, 3H, -NCH_3), 2.61 (m, 4H, - NCH_2CH_2S -), 2.66 (m, 4H, -SCH_2CH_2N-).

^{13}C NMR (D_2O, 75 MHz, RT, ppm): 20.4 (-SCH_2CH_2N-), 40.4 (-NCH_3), 62.4 (-SCH_2CH_2N-).

Preparation of composite metal sulfide/conductive carbon fiber mats:

In a typical electrospinning process, the corresponding spinning solution (Precursor Concentration [mol/L] = 0.46, PVP Concentration [mol/L] = $4.29 \cdot 10^{-5}$) was fed with a feed rate of 10 µL/min. The distance between the needle and rotary drum collector was kept constant at 15 cm, and a high voltage of 15 kV was applied. The process was conducted at room temperature with relative humidity below 35%.

The obtained green fibers have been calcined in a tubular furnace with a temperature program of 1°C/min up to 280°C (holding for 2 h) under ambient conditions, followed by a temperature increase of 1°C/min up to 700°C (holding for 3 h) under nitrogen atmosphere. All handling after calcination was performed under strictly inert conditions.

7.5.4 CuS precipitation

CuS was precipitated from an aqueous copper chloric solution. First, 1 mmol of $CuCl_2$ was dissolved in 20 ml of dest. H_2O (blue solution) in a 100 ml beaker. Second, in a second beaker (50 ml), 1 mmol of Na_2S and 2 mmol of NH_4Cl were dissolved in 20 ml of dest. H_2O to form $(NH_4)_2S$ (aq) and NaCl (aq). Afterward, the solution was transferred into a dropping funnel. CuS was precipitated by introducing dropwise the second solution to the first solution while a dark blue solid product was formed. After complete mixing, the reaction mixture was steered for 30 min at 25°C. The product was washed by filtration several times with water and ethanol. Finally, the product dried for 12 h at ambient conditions.

CuS (150°C, 250°C, 350°C, 450°C, and 850°C) were synthesized by taking 200 mg in a ceramic boat treated at the desired temperature for 2 h in a tube furnace under inert (N_2) conditions. The ramping time was set to 10°C/min.

7.5.5 Cu_2S precipitation (Cu_2S-PR)

For the precipitation of Cu_2S, 2 mmol of CuCl was dissolved in 20 ml of pyridine (green solution) in a 100 ml beaker. In a second beaker (50 ml), 1 mmol of Na_2S and 2 mmol of NH_4Cl were dissolved in 20 ml of dest. H_2O to form $(NH_4)_2S$ (aq) and NaCl (aq). Afterward, the solution was transferred into a dropping funnel. Cu_2S was precipitated by introducing dropwise the second solution to the first solution while a solid brown product was formed. After complete mixing, the reaction mixture was steered for 30 min at 25°C. The product was washed by filtration several times with water and ethanol. Finally, the product dried for 12 h at ambient conditions.

7.5.6 Synthesis of copper (II) sulfide by microwave (CuS-MW)

Copper (II) sulfide particles were synthesized by a microwave-assisted hydrothermal route. In a 10 ml microwave vessel, $CuCl_2$ (1 mmol) and L-cysteine (2 mmol) were dissolved in 5 ml dest. H_2O. Afterward, the solution was transferred into the microwave and decomposed for 5 minutes under a dynamic program with the parameters set to 55 W, 13 bar, and 160°C. After the solution cooled down to room temperature, the mixture was washed several times with H_2O and ethanol using a centrifuge until the pH value was above 3. The wet powder was dried at 120°C for 6 hours under vacuum.

7.5.7 Synthesis of copper (I) sulfide by microwave (Cu_2S-MW)

Copper (I) sulfide particles were synthesized by a microwave-assisted hydrothermal route. In a 10 ml microwave vessel, $CuCl_2$ (1 mmol) and L-cysteine (0.5 mmol) were dissolved in 5 ml dest. H_2O. Afterward, the solution was transferred into the microwave and decomposed for 5 minutes under a dynamic program with the parameters set to 55 W, 13 bar, and 160°C. After the solution cooled down to room temperature, the mixture was washed several times with H_2O and ethanol using a centrifuge until the pH value was above 3. The wet powder was dried at 120°C for 6 hours under vacuum.

7.5.8 Synthesis of Geigerite

Geigerite (Fe_3S_4) particles were synthesized by a microwave-assisted hydrothermal route. In a 10 ml microwave vessel, $FeCl_2$ (1 mmol) and L-cysteine (2 mmol) were dissolved in 5 ml dest. H_2O. Afterward, the solution was transferred into the microwave and decomposed for 5 minutes under a dynamic program with the parameters set to 55 W, 13 bar, and 160°C. After the solution cooled down to room temperature, the mixture was washed several times with H_2O and ethanol using a centrifuge until the pH value was above 3. The wet powder was dried at 120°C for 6 hours under vacuum.

7.5.9 Synthesis of $CuFeS_2$ (CFS)

Copper iron sulfide ($CuFeS_2$) particles were synthesized by a hydrothermal synthesis route. $CuCl_2$ (0.5 mmol), $FeCl_2$ * 4 H_2O (0.5 mmol), and L-cysteine (2 mmol) were dissolved in 20 ml of DI water and transferred to a Teflon tube. The reaction as carried out in a stainless-steal Autoclave for 12 h at 160°C. After the reaction cooled down to room temperature, the reaction mixture was washed several times with DI water and ethanol until a pH value of >3. The final product was vacuum dried for 6 h at 80°C.

7.5.10 Synthesis graphene oxide

A 9:1 mixture of concentrated H_2SO_4/H_3PO_4 (360:40 mL) was added to 3 g of graphite flakes. Following this, 18 g of $KMnO_4$ was added to the mixture. The reaction was heated to 50°C and stirred for 12 h with a magnetic stirring bar. The reaction mixture was cooled to room temperature and poured onto ice (ca. 400 cm^{-3}). A 33% solution of hydrogen peroxide was added to the mixture until the color changed to yellow, and no more gas evolution was observed. The product was washed in succession with 200 ml of distilled water, 200 ml of 30% concentrated hydrochloric acid, 200 ml of

distilled water, and 200 ml of ethanol. The resulting solid was vacuum-dried overnight at room temperature.

7.5.11 Reduction of graphene oxide

Reduced graphene oxide was obtained from the thermal decomposition of GO powder. The thermal reduction was performed in a porcelain boat using a tube furnace at 800°C for 3 h in an Ar/H_2 atmosphere (95/5) with a ramping rate of 10°C/min. The obtained rGO flakes have a lateral size of 0.5-1.5 µm and a layer number of 11-13.

7.5.12 Preparation of rGO-films and CFS-rGO films

For the free-standing GO and GO-CFS composite films, a GO-dispersion was prepared first by mixing 1 mg mL^{-1} in DI water and ultrasonicated with a sonicate probe for 1 h with 80% power and 8 cycles. The dispersion was centrifugated at 4000 rpm for 10 min, and the supernatant was collected. For GO/CFS films, 50 ml of the GO dispersion was used, and 25 mg of the CFS-I was added. The mixture was sonicated again for 30 min. For native GO films, only 50 ml was used for the GO dispersion. The dispersions were filtered through the Whatman Anodisc 0.2 µm filter membrane to receive freestanding GO films. These films were then calcined in an Ar atmosphere at 700°C for 3h with a ramping and cooling time of 2°C min^{-1} to obtain reduced rGO or rGO-CFS films, respectively.

7.5.13 Synthesis of copper iron sulfide precursor (CFS-I)

$CuCl_2$ (1 mmol), $FeCl_2 * 4\ H_2O$ (1 mmol), and thiourea (4 mmol) were dissolved in 20 ml of DI water and transferred to a Teflon tube. The reaction as carried out in a stainless-steal Autoclave for 12 h at 160°C. After the reaction cooled down to room temperature, the reaction mixture was washed several times with DI water and ethanol until a pH value of >3. The final product was vacuum dried for 6 h at 80°C.

7.5.14 Synthesis of Mg(hexamethyldisilazane)$_2$

For the magnesium-based electrolyte, first, Mg(hexamethyldisilazane)$_2$ was synthesized at a Stock line by a transmetallation route of Sn(hexamethyldisilazane)$_2$ and Mg powder.

In an inert flask 7.13 ml HDMS (5.56 g, 34.5 mmol) was placed and cooled down to -196°C with liquid nitrogen. 13.7 ml n-Butyllithium (2.5 M, 34.3 mmol) was added

under nitrogen counterflow and the solution was allowed to warm up to room temperature and was stirred for 30 min. $SnCl_2$ (3.32 g, 17.5 mmol) was solved in 10 ml dry THF in another flask.
Both solutions were put together at 0°C and the resulting orange solution was stirred for 1 d at room temperature. The solvent was removed under reduced pressure and the residue was distilled in a vacuum. The product was received at about 75°C head temperature as an orange oil.
In an inert flask, 231 mg $Sn(HDMS)_2$ (0.526 mmol) was placed. 20 ml dry THF and ten spatula tips of elemental magnesium powder were added under nitrogen counterflow. The mixture was allowed to stir for one week. For purification, Mg(hexamethyldisilazane)$_2$ (aq) was first separated from Sn and the solvent was removed under reduced vacuum. Secondly, Mg(hexamethyldisilazane)$_2$ was sublimed in vacuum at a temperature of 100°C. A white powder was obtained.

7.5.15 Synthesis of Mg(hexamethyldisilazane)$_2$ / $AlCl_3$ * DME electrolyte

The as-synthesized Mg(hexamethyldisilazane)$_2$ was used in a ratio of 1:2 to anhydrous $AlCl_3$ to prepare the 0.35 M electrolyte. To receive 10 ml of the electrolyte, 1.208 g of Mg(hexamethyldisilazane)2 was added to 3.6 ml of dry DME. In a second round flask, 0.934 g of $AlCl_3$ was slowly added to 6.2 ml of dried DME. Once the $AlCl_3$ was fully dissolved, the $AlCl_3$ solution was slowly added to the Mg(hexamethyldisilazane)$_2$ solution while stirring. The overnight stirring allowed the salts in the complex electrolyte solution to equilibrate.

7.5.16 Synthesis of V_2O_5 electrospun (green)fibers and carbon coating

The vanadium oxide nanofibers (VNF) were synthesized by simple electrospinning of $VO(acac)_2$ in a polymeric solution. Poly(vinylpyrrolidone) (PVP, 0.08 mg ml^{-1}) of molecular weight 1,300,000 and 0.08 g ml^{-1} vanadyl acetylacetonate ($VO(acac)_2$) were dissolved in a mixture (1:4, v:v) of acetic acid and ethanol absolute by stirring for 12 h to obtain a homogenous solution. The precursor solution was loaded into a 5 ml syringe with a ~ 0.514 mm diameter needle made of stainless steel and ejected with a flow rate of 2 ml h^{-1}. A positive potential of 14 kV was applied between the needle tip and an aluminum foil collector at a distance of 10 cm. In the electric field, the ejected polymer jet was accelerated toward the collector, and fibers were formed on the aluminum

foil after solvent evaporation. These electrospun fiber mats were heat-treated at 450°C for 75 min with a heating and cooling rate of 2°C min^{-1} under an air atmosphere.
After calcination, the VNF were carbon-coated by plasma-enhanced chemical vapor deposition using methane gas as a carbon precursor. The coating process was performed using a commercial vacuum system from Plasma Electronics (CVD-PECVD DOMINO), working with a radio-frequency excitation (13.56 MHz). 20 sccm of CH_4 were introduced into the reaction chamber through a mass flow controller (MKS MFC 1179) controlled by a software interface during the reaction, and the reactor pressure was maintained at 3.5 Pa. The 0.02 g of VNF was placed in a ceramic boat on the heatable RF electrode to decompose the CH_4 on the surface of the VNF. The temperature was set to 450°C and the plasma power to 15 W (resulting in a bias of 250 V). The duration of the treatment was set to 60 (VNF-C-60) and 120 min (VNF-C-120).

7.5.17 Guide to understanding battery specifications

C-rate

The C-rate is often used to express the discharge current. It normalizes the battery capacity, which varies from different compositions and types of batteries. The C-rate describes the specific current with which the battery is discharged relative to its maximum capacity. As an example, if a battery has a capacity of 300 Ah and the applied rate is 1C, this means that the battery can is discharged with 300 A for one hour. By increasing the C-rate, the capacity decreases. The *specific current* is a description of the C-rate per unit mass (Ah kg^{-1}).

Terminal voltage

The terminal voltage describes the different potential between the electrodes with an applied load, which varies depending on the state of charge of the battery.

Open-circuit voltage

The open-circuit voltage measures the potential between the electrodes without an applied load.

Internal resistance

The internal resistance varies depending on the charging and discharging processes as well as on the battery's state of charge. In principle, factors of size, state of charge, chemical properties, age, temperature, and the discharge current have an influence on the internal resistance of a battery.

Impedance

Impedance is an alternating electrical resistance describing the relationship of the voltage and amperage in a two-pole setup.

Nominal voltage

The reported or reference voltage of the battery.

Cut-off Voltage

The minimum allowable voltage. In general, this voltage defines the 'empty' state of the battery. Beyond this voltage, the further discharge could cause harm to the battery. Modern electronic devices will automatically power off when the cut-off voltage has been reached. In contrast, the *charge voltage* is the voltage limit when the battery is fully charged.

Capacity

The capacity describes the maximally available amperes per hour when the battery is discharged fully discharged to the cut-off voltage at a certain discharge current (C-rate). The *specific capacity* expresses the total capacity per unit mass (Ah kg^{-1}).

Energy

The energy of the batteries is an expression of the total watts per hour when the battery is discharged fully discharged to the cut-off voltage at a specific discharge current (C-rate). The energy is calculated by multiplying Amps by the terminal Voltage and the discharge time. The *specific energy* (or gravimetric energy density) expresses the total energy per unit mass (Wh kg^{-1}), while the *energy density* (volumetric energy density) is the nominal energy per unit volume.

Cycle Life

The cycle life provides the number of discharge-charge cycles before the battery fails to meet specific performance criteria. Cycle life measurements are mainly performed at specific charge and discharge conditions as well as constant environmental conditions such as temperature and humidity.

8 Abbreviations

°	degree
°C	degree Celsius
A	Ampere
Å	Angstrom, 1 Å = 10^{-10} m
a.u.	Arbitrary unit
acac	Acetylacetone
at.%	Atomic concentration
BE	Binding energy
CB	Conduction band
ccp	Cubic closest packing
CEI	Cathode electrolyte interface
CFS	$CuFeS_2$
CIGS	Copper indium gallium selenide thin-film cells
CNF	Carbon nanofibers
CPS	Counts per second
CV	Cyclic voltammetry
CVD	Chemical vapor deposition
DEC	Diethyl carbonate
DFT	Density Functional Theory
DME	Dimethoxyethane
DOL	Dioxolane
DSC	Thermogravimetric analysis
DSSC	Dye-sensitized solar cells
EC	Ethylene carbonate
EDX	Energy-dispersive X-ray spectroscopy
EIS	Electrochemical impedance spectroscopy
EMC	Ethyl methyl carbonate
ETL	Electron transport layer
eV	Electron volt
fcc	Face-centered cubic
FIB-SEM	Focus ion beam scanning electron microscope
GO	Graphene oxide

h	Hours
hcp	Hexagonal closest packing
HMDS	Hexamethyldisilazane
HR-SEM	High-resolution scanning electron microscopy
HR-TEM	High-resolution transmission electron microscopy
HTL	Hole transport layer
JCPDS	Joint committee on powder diffraction standards
KE	Kinetic energy
kV	Kilo volt
LCP	Lowest energy charged polymorph
LDP	Lowest energy discharged polymorph
LFP	Lithium-Iron-Phosphate
LIB	Lithium-ion battery
LiTFSI	Bis(trifluoromethane)sulfonimide lithium salt
LMO	Lithium Manganese Oxide ($LiMn_2O_4$)
LTO	Lithium Titanate
mA	Milliampere
mbar	Millibar
MHz	Megahertz
min	Minutes
NCA	Nickel-Cobalt-Aluminium
Nm	Nano meter
NMC	Nickel-Manganese-Cobalt
NMP	N-Methyl-2-pyrrolidone
OCV	Open-circuit voltage
OPV	Organic photovoltaic
P3HT	Poly(3-hexylthiophene)
Pa	Pascal
PCE	Power/Photo conversion efficiency
PECVD	Plasma-enhanced chemical vapor deposition
ppm	Part per million
PSC	Perovskite solar cell
PV	Photovoltaic
PVDF	Polyvinylidene difluoride

PVP	Polyvinylpyrrolidone
RF	Radiofrequency
rGO	reduced graphene oxide
RMB	Rechargeable magnesium battery
sccm	Standard cubic centimeters per minute
SEI	Solid electrolyte interface
SEM	Scanning electron microscopy
TCO	Transparent conductive oxide
TEM	Transmission electron microscopy
TGA	Differential scanning calorimetry
THF	Tetrahydrofuran
TMS	Transition metal sulfide
TNBO	$TiNb_2O_7$
TNBO/KC	$TiNb_2O_7$ keratin carbon
TNO	$TiNb_2O_7$
TNO/C	$TiNb_2O_7$ carbon-coated
TTIP	Titanium (IV) isopropoxide
V	Volt
v	Volume
VB	Valence band
VNF	Vanadium pentoxide nanofibers
VNF -C-120	Vanadium pentoxide nanofibers 120 minutes carbon-coated
VNF-C-60	Vanadium pentoxide nanofibers 60 minutes carbon-coated
W	Watt
wt.%	Weight percent
XPS	X-ray photoelectron spectroscopy
XRD	X-ray diffractometry
µm	Micrometer

9 References

1. Armand, M., & Tarascon, J.-M. Building better batteries. *Nature* 451, 652–657 (**2008**).
2. Martin, G., Rentsch, L., Höck, M., & Bertau, M. Lithium market research – global supply, future demand and price development. *Energy Storage Mater.* 6, 171–179 (**2017**).
3. Whittingham, M. S. Lithium Batteries: 50 Years of Advances to Address the Next 20 Years of Climate Issues. *Nano Lett.* 20, 8435–8437 (**2020**).
4. Vopava, J., Koczwara, C., Traupmann, A., & Kienberger, T. Investigating the impact of e-mobility on the electrical power grid using a simplified grid modelling approach. *Energies* 13, 39 (**2019**).
5. Airbus Innovation. Airbus' high-voltage battery technology prepares for EcoPulse flight test and beyond. (**2022**) https://www.airbus.com/en/newsroom/news/2022-03-airbus-high-voltage-battery-technology-prepares-for-ecopulse-flight-test (accessed 9 December 2022).
6. Schwab, A., Thomas, A., Bennett, J., Robertson, E., & Cary, S. *Electrification of Aircraft: Challenges, Barriers, and Potential Impacts*. (**2021**) https://www.osti.gov/biblio/1827628 doi:10.2172/1827628.
7. CUSTOMCELLS. High Voltage in the Clouds. *Master of Batteries* (**2022**) https://medium.com/master-of-batteries/high-voltage-in-the-clouds-5f0633183615 (accessed 29 November 2022).
8. Vaalma, C., Buchholz, D., Weil, M., & Passerini, S. A cost and resource analysis of sodium-ion batteries. *Nat. Rev. Mater.* 3, 18013 (**2018**).
9. Grey, C. P., & Tarascon, J. M. Sustainability and in situ monitoring in battery development. *Nat. Mater.* 16, 45–56 (**2017**).
10. Larcher, D., & Tarascon, J.-M. Towards greener and more sustainable batteries for electrical energy storage. *Nat. Chem.* 7, 19–29 (**2015**).
11. Van Noorden, R. The rechargeable revolution: A better battery. *Nature* 507, 26–28 (**2014**).
12. Olabi, A. G., Onumaegbu, C., Wilberforce, T., Ramadan, M., Abdelkareem, M. A., & Al – Alami, A. H. Critical review of energy storage systems. *Energy* 214, 118987 (**2021**).

13. Hong, Z., Maleki, H., Ludwig, T., Zhen, Y., Wilhelm, M., Lee, D., Kim, K.-H., & Mathur, S. New insights into carbon-based and MXene anodes for Na and K-ion storage: A review. *J. Energy Chem.* 62, 660–691 (**2021**).
14. Mei, J., Liao, T., Kou, L., & Sun, Z. Two-Dimensional Metal Oxide Nanomaterials for Next-Generation Rechargeable Batteries. *Adv. Mater.* 29, 1700176 (**2017**).
15. EUROBAT. Benefits of batteries. (**2022**) https://www.eurobat.org/about-secondary-batteries/batteries-101/benefits-of-batteries/ (accessed 29 November 2022).
16. Daniell, J. F. *An introduction to the study of chemical philosophy: being a preparatory view of the forces which concur to the production of chemical phenomena*. (JW Parker, **1839**).
17. Whittingham, M. S. Electrical energy storage and intercalation chemistry. *Science (80).* 192, 1126–1127 (**1976**).
18. Whittingham, M. S. Chemistry of intercalation compounds: Metal guests in chalcogenide hosts. *Prog. Solid State Chem.* 12, 41–99 (**1978**).
19. Whittingham, M. S. The Nobel Prize in Chemistry 2019. *Facts* Nobel Prize Outreach AB 2022 (**2019**) https://www.nobelprize.org/prizes/chemistry/2019/whittingham/facts/ (accessed 1 September 2022).
20. Yang, Y., Hoang, M. T., Bhardwaj, A., Wilhelm, M., Mathur, S., & Wang, H. Perovskite solar cells based self-charging power packs: Fundamentals, applications and challenges. *Nano Energy* 94, 106910 (**2022**).
21. Yuan, L.-X., Wang, Z.-H., Zhang, W.-X., Hu, X.-L., Chen, J.-T., Huang, Y.-H., & Goodenough, J. B. Development and challenges of $LiFePO_4$ cathode material for lithium-ion batteries. *Energy Environ. Sci.* 4, 269–284 (**2011**).
22. Whittingham, M. S. Lithium Batteries and Cathode Materials. *Chem. Rev.* 104, 4271–4302 (**2004**).
23. Goodenough, J. B. Evolution of Strategies for Modern Rechargeable Batteries. *Acc. Chem. Res.* 46, 1053–1061 (**2013**).
24. Gamble, F. R., Osiecki, J. H., Cais, M., Plsharody, R., DiSalvo, F. J., & Geballe, T. H. Intercalation complexes of lewis bases and layered sulfides: A large class of new superconductors. *Science (80).* 174, 493–497 (**1971**).
25. Xie, J., & Lu, Y.-C. A retrospective on lithium-ion batteries. *Nat. Commun.* 11, 2499 (**2020**).

26. Li, J., Hwang, S., Guo, F., Li, S., Chen, Z., Kou, R., Sun, K., Sun, C.-J., Gan, H., Yu, A., Stach, E. A., Zhou, H., & Su, D. Phase evolution of conversion-type electrode for lithium ion batteries. *Nat. Commun.* 10, 2224 (**2019**).
27. Li, T., Qin, A., Wang, H., Wu, M., Zhang, Y., Zhang, Y., Zhang, D., & Xu, F. A high-performance hybrid Mg^{2+}/Li^{+} battery based on hierarchical copper sulfide microflowers conversion cathode. *Electrochim. Acta* 263, 168–175 (**2018**).
28. Zhang, Z., Dong, S., Cui, Z., Du, A., Li, G., & Cui, G. Rechargeable Magnesium Batteries using Conversion-Type Cathodes: A Perspective and Minireview. *Small Methods* 2, 1800020 (**2018**).
29. Yu, S.-H., Feng, X., Zhang, N., Seok, J., & Abruña, H. D. Understanding Conversion-Type Electrodes for Lithium Rechargeable Batteries. *Acc. Chem. Res.* 51, 273–281 (**2018**).
30. Wu, F., & Yushin, G. Conversion cathodes for rechargeable lithium and lithium-ion batteries. *Energy Environ. Sci.* 10, 435–459 (**2017**).
31. Thiyagarajan, G. B., Shanmugam, V., Wilhelm, M., Mathur, S., Moodakare, S. B., & Kumar, R. $TiNb_2O_7$-Keratin derived carbon nanocomposites as novel anode materials for high-capacity lithium-ion batteries. *Open Ceram.* 6, 100131 (**2021**).
32. Han, X., Lu, L., Zheng, Y., Feng, X., Li, Z., Li, J., & Ouyang, M. A review on the key issues of the lithium ion battery degradation among the whole life cycle. *eTransportation* 1, 100005 (**2019**).
33. Inada, R., Mori, T., Kumasaka, R., Ito, R., Tojo, T., & Sakurai, Y. Characterization of vacuum-annealed $TiNb_2O_7$ as high potential anode material for lithium-ion battery. *Int. J. Appl. Ceram. Technol.* 16, 264–272 (**2019**).
34. Lin, C., Hu, L., Cheng, C., Sun, K., Guo, X., Shao, Q., Li, J., Wang, N., & Guo, Z. Nano-$TiNb_2O_7$/carbon nanotubes composite anode for enhanced lithium-ion storage. *Electrochim. Acta* 260, 65–72 (**2018**).
35. Liu, G., Zhao, L., Sun, R., Chen, W., Hu, M., Liu, M., Duan, X., & Zhang, T. Mesoporous $TiNb_2O_7$ microspheres as high performance anode materials for lithium-ion batteries with high-rate capability and long cycle-life. *Electrochim. Acta* 259, 20–27 (**2018**).
36. Liu, M., Dong, H., Zhang, S., Chen, X., Sun, Y., Gao, S., Xu, J., Wu, X., Yuan, A., & Lu, W. Three-Dimensional Porous $TiNb_2O_7$/CNT-KB Composite Microspheres as Lithium-Ion Battery Anode Material. *ChemElectroChem* 6,

3959–3965 (**2019**).

37. Zhu, G., Li, Q., Zhao, Y., & Che, R. Nanoporous $TiNb_2O_7$/C Composite Microspheres with Three-Dimensional Conductive Network for Long-Cycle-Life and High-Rate-Capability Anode Materials for Lithium-Ion Batteries. *ACS Appl. Mater. Interfaces* 9, 41258–41264 (**2017**).
38. Griffith, K. J., Seymour, I. D., Hope, M. A., Butala, M. M., Lamontagne, L. K., Preefer, M. B., Koçer, C. P., Henkelman, G., Morris, A. J., Cliffe, M. J., Dutton, S. E., & Grey, C. P. Ionic and Electronic Conduction in $TiNb_2O_7$. *J. Am. Chem. Soc.* 141, 16706–16725 (**2019**).
39. Lou, S., Cheng, X., Zhao, Y., Lushington, A., Gao, J., Li, Q., Zuo, P., Wang, B., Gao, Y., Ma, Y., Du, C., Yin, G., & Sun, X. Superior performance of ordered macroporous $TiNb_2O_7$ anodes for lithium ion batteries: Understanding from the structural and pseudocapacitive insights on achieving high rate capability. *Nano Energy* 34, 15–25 (**2017**).
40. Fei, L., Xu, Y., Wu, X., Li, Y., Xie, P., Deng, S., Smirnov, S., & Luo, H. SBA-15 confined synthesis of $TiNb_2O_7$ nanoparticles for lithium-ion batteries. *Nanoscale* 5, 11102–11107 (**2013**).
41. Lou, S., Ma, Y., Cheng, X., Gao, J., Gao, Y., Zuo, P., Du, C., & Yin, G. Facile synthesis of nanostructured $TiNb_2O_7$ anode materials with superior performance for high-rate lithium ion batteries. *Chem. Commun.* 51, 17293–17296 (**2015**).
42. Tang, K., Mu, X., van Aken, P. A., Yu, Y., & Maier, J. “Nano-Pearl-String” TiNb2O7 as Anodes for Rechargeable Lithium Batteries. *Adv. Energy Mater.* 3, 49–53 (**2013**).
43. Song, H., & Kim, Y.-T. A Mo-doped $TiNb_2O_7$ anode for lithium-ion batteries with high rate capability due to charge redistribution. *Chem. Commun.* 51, 9849–9852 (**2015**).
44. Wen, X., Ma, C., Du, C., Liu, J., Zhang, X., Qu, D., & Tang, Z. Enhanced electrochemical properties of vanadium-doped titanium niobate as a new anode material for lithium-ion batteries. *Electrochim. Acta* 186, 58–63 (**2015**).
45. Li, S., Cao, X., Schmidt, C. N., Xu, Q., Uchaker, E., Pei, Y., & Cao, G. TiNb2O7/graphene composites as high-rate anode materials for lithium/sodium ion batteries. *J. Mater. Chem. A* 4, 4242–4251 (**2016**).
46. Ashish, A. G., Arunkumar, P., Babu, B., Manikandan, P., Sarang, S., & Shaijumon, M. M. $TiNb_2O_7$/Graphene hybrid material as high performance anode

for lithium-ion batteries. *Electrochim. Acta* 176, 285–292 (**2015**).

47. Fu, K. K., Cheng, J., Li, T., & Hu, L. Flexible Batteries: From Mechanics to Devices. *ACS Energy Lett.* 1, 1065–1079 (**2016**).
48. Wan, J., Xie, J., Kong, X., Liu, Z., Liu, K., Shi, F., Pei, A., Chen, H., Chen, W., Chen, J., Zhang, X., Zong, L., Wang, J., Chen, L.-Q., Qin, J., & Cui, Y. Ultrathin, flexible, solid polymer composite electrolyte enabled with aligned nanoporous host for lithium batteries. *Nat. Nanotechnol.* 14, 705–711 (**2019**).
49. Chi, X., Li, M., Di, J., Bai, P., Song, L., Wang, X., Li, F., Liang, S., Xu, J., & Yu, J. A highly stable and flexible zeolite electrolyte solid-state Li–air battery. *Nature* 592, 551–557 (**2021**).
50. Mo, R., Rooney, D., Sun, K., & Yang, H. Y. 3D nitrogen-doped graphene foam with encapsulated germanium/nitrogen-doped graphene yolk-shell nanoarchitecture for high-performance flexible Li-ion battery. *Nat. Commun.* 8, 13949 (**2017**).
51. Long, H., Shi, T., Hu, H., Jiang, S., Xi, S., & Tang, Z. Growth of Hierarchal Mesoporous NiO Nanosheets on Carbon Cloth as Binder-free Anodes for High-performance Flexible Lithium-ion Batteries. *Sci. Rep.* 4, 7413 (**2014**).
52. Chang, J., Shang, J., Sun, Y., Ono, L. K., Wang, D., Ma, Z., Huang, Q., Chen, D., Liu, G., Cui, Y., Qi, Y., & Zheng, Z. Flexible and stable high-energy lithium-sulfur full batteries with only 100% oversized lithium. *Nat. Commun.* 9, 4480 (**2018**).
53. Liu, Q.-C., Xu, J.-J., Xu, D., & Zhang, X.-B. Flexible lithium–oxygen battery based on a recoverable cathode. *Nat. Commun.* 6, 7892 (**2015**).
54. Chang, C. H., Chung, S. H., & Manthiram, A. Highly flexible, freestanding tandem sulfur cathodes for foldable Li-S batteries with a high areal capacity. *Mater. Horizons* 4, 249–258 (**2017**).
55. Yu, M., Wang, Z., Wang, Y., Dong, Y., & Qiu, J. Freestanding Flexible Li_2S Paper Electrode with High Mass and Capacity Loading for High-Energy Li–S Batteries. *Adv. Energy Mater.* 7, 1700018 (**2017**).
56. Kong, L., Tang, C., Peng, H.-J., Huang, J.-Q., & Zhang, Q. Advanced energy materials for flexible batteries in energy storage: A review. *SmartMat* 1, (**2020**).
57. Ludwig, T., Je, M., Choi, H., Fischer, T., Roitsch, S., Müller, R., Mane, R. S., Kim, K. H., & Mathur, S. Boosting nitrogen-doping and controlling interlayer spacing in pre-reduced graphene oxides. *Nano Energy* 78, 105286 (**2020**).

58. Deng, X., Xie, K., Li, L., Zhou, W., Sunarso, J., & Shao, Z. Scalable synthesis of self-standing sulfur-doped flexible graphene films as recyclable anode materials for low-cost sodium-ion batteries. *Carbon N. Y.* 107, 67–73 (**2016**).
59. Hu, T., Sun, X., Sun, H., Yu, M., Lu, F., Liu, C., & Lian, J. Flexible free-standing graphene–TiO_2 hybrid paper for use as lithium ion battery anode materials. *Carbon N. Y.* 51, 322–326 (**2013**).
60. Liang, J., Zhao, Y., Guo, L., & Li, L. Flexible Free-Standing Graphene/SnO2 Nanocomposites Paper for Li-Ion Battery. *ACS Appl. Mater. Interfaces* 4, 5742–5748 (**2012**).
61. Wu, C., Fu, L., Maier, J., & Yu, Y. Free-standing graphene-based porous carbon films with three-dimensional hierarchical architecture for advanced flexible Li–sulfur batteries. *J. Mater. Chem. A* 3, 9438–9445 (**2015**).
62. He, D., Sun, M., Cao, D., Ding, Y., Chen, H., & He, G. Flexible Free-Standing Fe2O3 Nanoparticle/Carbon Shells/Graphene Films for Advanced Lithium-Ion Batteries. *ACS Appl. Nano Mater.* 5, 5017–5024 (**2022**).
63. Brune, V., Bohr, C., Ludwig, T., Wilhelm, M., Hirt, S. D., Fischer, T., Wennig, S., Oberschachtsiek, B., Ichangi, A., & Mathur, S. A novel molecular synthesis route to Li_2S loaded carbon fibers for lithium–sulfur batteries. *J. Mater. Chem. A* 10, 9902–9910 (**2022**).
64. Fan, X., Yue, J., Han, F., Chen, J., Deng, T., Zhou, X., Hou, S., & Wang, C. High-Performance All-Solid-State Na-S Battery Enabled by Casting-Annealing Technology. *ACS Nano* 12, 3360–3368 (**2018**).
65. Dunn, B., Kamath, H., & Tarascon, J. M. Electrical energy storage for the grid: A battery of choices. *Science (80-.).* 334, 928–935 (**2011**).
66. Longo, R. C., Camacho-Forero, L. E., & Balbuena, P. B. Li_2S growth on graphene: Impact on the electrochemical performance of Li-S batteries. *J. Chem. Phys.* 152, 014701 (**2020**).
67. Bruce, P. G., Freunberger, S. A., Hardwick, L. J., & Tarascon, J. M. Li-O_2 and Li-S batteries with high energy storage. *Nat. Mater.* 11, 19–29 (**2012**).
68. Xiao, Y., Lee, S. H., & Sun, Y. K. The Application of Metal Sulfides in Sodium Ion Batteries. *Adv. Energy Mater.* 7, 1601329 (**2017**).
69. Pham, C. Van, Liu, L., Britton, B., Walter, M., Holdcroft, S., & Thiele, S. Stabilization of Li-S batteries with a lean electrolyte: Via ion-exchange trapping of lithium polysulfides using a cationic, polybenzimidazolium binder. *Sustain.*

Energy Fuels 4, 1180–1190 (**2020**).

70. Yan, J., Li, W., Wang, R., Feng, P., Jiang, M., Han, J., Cao, S., Zhang, Z., Wang, K., & Jiang, K. An in Situ Prepared Covalent Sulfur–Carbon Composite Electrode for High-Performance Room-Temperature Sodium–Sulfur Batteries. *ACS Energy Lett.* 5, 1307–1315 (**2020**).
71. Huo, J., & Wang, Y. High performance lithium-sulfur batteries obtained by employing spiked carbon nanofibers as host materials. *Int. J. Electrochem. Sci.* 15, 1529–1538 (**2020**).
72. Fang, X., & Peng, H. A Revolution in Electrodes: Recent Progress in Rechargeable Lithium-Sulfur Batteries. *Small* 11, 1488–1511 (**2015**).
73. Ng, S. F., Lau, M. Y. L., & Ong, W. J. Lithium–Sulfur Battery Cathode Design: Tailoring Metal-Based Nanostructures for Robust Polysulfide Adsorption and Catalytic Conversion. *Adv. Mater.* 2008654, 1–54 (**2021**).
74. Ho, Y. C., & Chung, S. H. A design of the cathode substrate for high-loading polysulfide cathodes in lean-electrolyte lithium-sulfur cells. *Chem. Eng. J.* 422, 130363 (**2021**).
75. Manthiram, A., Fu, Y., Chung, S. H., Zu, C., & Su, Y. S. Rechargeable lithium-sulfur batteries. *Chem. Rev.* 114, 11751–11787 (**2014**).
76. Feng, Z., Kim, C., Vijh, A., Armand, M., Bevan, K. H., & Zaghib, K. Unravelling the role of Li_2S_2 in lithium–sulfur batteries: A first principles study of its energetic and electronic properties. *J. Power Sources* 272, 518–521 (**2014**).
77. Sun, Z., Xiao, M., Wang, S., Han, D., & Song, S. interpenetrating network structure as a novel lithium – sulfur cathode. *J. Mater. Chem. A* 2, 9280–9286 (**2014**).
78. Zhang, X., Xie, H., Kim, C. S., Zaghib, K., Mauger, A., & Julien, C. M. Advances in lithium—sulfur batteries. *Mater. Sci. Eng. R Rep.* 121, 1–29 (**2017**).
79. Su, D., Zhou, D., Wang, C., & Wang, G. Toward High Performance Lithium–Sulfur Batteries Based on Li_2S Cathodes and Beyond: Status, Challenges, and Perspectives. *Adv. Funct. Mater.* 28, 1–23 (**2018**).
80. Liu, J., Li, Z., Jia, B., Zhu, J., Zhu, W., Li, J., Pan, H., Zheng, B., Chen, L., Pezzotti, G., & Zhu, J. A freestanding hierarchically structured cathode enables high sulfur loading and energy density of flexible Li–S batteries. *J. Mater. Chem. A* 8, 6303–6310 (**2020**).
81. Tong, Z., Huang, L., Lei, W., Zhang, H., & Zhang, S. Carbon-containing

electrospun nanofibers for lithium–sulfur battery: Current status and future directions. *J. Energy Chem.* 54, 254–273 (**2021**).

82. Ge, X., Liu, S., Qiao, M., Du, Y., Li, Y., Bao, J., & Zhou, X. Enabling Superior Electrochemical Properties for Highly Efficient Potassium Storage by Impregnating Ultrafine Sb Nanocrystals within Nanochannel-Containing Carbon Nanofibers. *Angew. Chemie - Int. Ed.* 58, 14578–14583 (**2019**).
83. Pakki, T., Mohan, E. H., Hebalkar, N. Y., Adduru, J., Bulusu, S. V., Srinivasan, A., Mantravadi, K. M., & Tata, N. R. Flexible and free-standing carbon nanofiber matt derived from electrospun polyimide as an effective interlayer for high-performance lithium–sulfur batteries. *J. Mater. Sci.* 54, 9075–9087 (**2019**).
84. Cavaliere, S., Subianto, S., Savych, I., Jones, D. J., & Rozière, J. Electrospinning: Designed architectures for energy conversion and storage devices. *Energy Environ. Sci.* 4, 4761–4785 (**2011**).
85. Sun, G., Sun, L., Xie, H., & Liu, J. Electrospinning of nanofibers for energy applications. *Nanomaterials* 6, 1–30 (**2016**).
86. Strubel, P., Thieme, S., Biemelt, T., Helmer, A., Oschatz, M., Brückner, J., Althues, H., & Kaskel, S. ZnO hard templating for synthesis of hierarchical porous carbons with tailored porosity and high performance in lithium-sulfur battery. *Adv. Funct. Mater.* 25, 287–297 (**2015**).
87. Ren, W., Ma, W., Jin, X., Zhang, S., & Tang, B. Polysulfide Trapping in Carbon Nanofiber Cloth/S Cathode with a Bifunctional Separator for High-Performance Li–S Batteries. *ChemSusChem* 12, 2447–2456 (**2019**).
88. Cheng, Q., Xu, W., Qin, S., Das, S., Jin, T., Li, A., Li, A. C., Qie, B., Yao, P., Zhai, H., Shi, C., Yong, X., & Yang, Y. Full Dissolution of the Whole Lithium Sulfide Family (Li_2S_8 to Li_2S) in a Safe Eutectic Solvent for Rechargeable Lithium–Sulfur Batteries. *Angew. Chemie - Int. Ed.* 58, 5557–5561 (**2019**).
89. Liu, D., Zhang, C., Zhou, G., Lv, W., Ling, G., Zhi, L., & Yang, Q. H. Catalytic Effects in Lithium–Sulfur Batteries: Promoted Sulfur Transformation and Reduced Shuttle Effect. *Adv. Sci.* 5, 1700270 (**2018**).
90. Liu, M., Deng, N., Ju, J., Fan, L., Wang, L., Li, Z., Zhao, H., Yang, G., Kang, W., Yan, J., & Cheng, B. A Review: Electrospun Nanofiber Materials for Lithium-Sulfur Batteries. *Adv. Funct. Mater.* 29, 1–34 (**2019**).
91. Han, K., Shen, J., Hayner, C. M., Ye, H., Kung, M. C., & Kung, H. H. Li_2S-reduced graphene oxide nanocomposites as cathode material for lithium sulfur batteries.

J. Power Sources 251, 331–337 (**2014**).

92. Li, Z., Zhang, S., Zhang, C., Ueno, K., Yasuda, T., Tatara, R., Dokko, K., & Watanabe, M. One-pot pyrolysis of lithium sulfate and graphene nanoplatelet aggregates: In situ formed Li2S/graphene composite for lithium-sulfur batteries. *Nanoscale* 7, 14385–14392 (**2015**).
93. Ye, F., Hou, Y., Liu, M., Li, W., Yang, X., Qiu, Y., Zhou, L., Li, H., Xu, Y., & Zhang, Y. Fabrication of mesoporous Li_2S–C nanofibers for high performance Li/Li2S cell cathodes. *Nanoscale* 7, 9472–9476 (**2015**).
94. Brune, V., Hegemann, C., Wilhelm, M., Ates, N., & Mathur, S. Molecular Precursors to Group IV Dichalcogenides MS_2 (M=Ti, Zr, Hf). *Zeitschrift für Anorg. und Allg. Chemie* 648, e202200049 (**2022**).
95. Brune, V., Hegemann, C., & Mathur, S. Molecular Routes to Two Dimensional Metal Dichalcogenides MX_2 (M = Mo, W; X = S, Se). *Inorg. Chem.* 58, 9922–9934 (**2019**).
96. Wasalathilake, K. C., Li, H., Xu, L., & Yan, C. Recent advances in graphene based materials as anode materials in sodium-ion batteries. *J. Energy Chem.* 42, 91–107 (**2020**).
97. Peng, L., Zhu, Y., Chen, D., Ruoff, R. S., & Yu, G. Two-Dimensional Materials for Beyond-Lithium-Ion Batteries. *Adv. Energy Mater.* 6, 1600025 (**2016**).
98. Hou, H., Qiu, X., Wei, W., Zhang, Y., & Ji, X. Carbon Anode Materials for Advanced Sodium-Ion Batteries. *Adv. Energy Mater.* 7, 1602898 (**2017**).
99. Cao, Y., Xiao, L., Sushko, M. L., Wang, W., Schwenzer, B., Xiao, J., Nie, Z., Saraf, L. V, Yang, Z., & Liu, J. Sodium Ion Insertion in Hollow Carbon Nanowires for Battery Applications. *Nano Lett.* 12, 3783–3787 (**2012**).
100. Qiu, S., Xiao, L., Sushko, M. L., Han, K. S., Shao, Y., Yan, M., Liang, X., Mai, L., Feng, J., Cao, Y., Ai, X., Yang, H., & Liu, J. Manipulating Adsorption–Insertion Mechanisms in Nanostructured Carbon Materials for High-Efficiency Sodium Ion Storage. *Adv. Energy Mater.* 7, 1700403 (**2017**).
101. Ding, J., Wang, H., Li, Z., Kohandehghan, A., Cui, K., Xu, Z., Zahiri, B., Tan, X., Lotfabad, E. M., Olsen, B. C., & Mitlin, D. Carbon Nanosheet Frameworks Derived from Peat Moss as High Performance Sodium Ion Battery Anodes. *ACS Nano* 7, 11004–11015 (**2013**).
102. Li, S., Qiu, J., Lai, C., Ling, M., Zhao, H., & Zhang, S. Surface capacitive contributions: Towards high rate anode materials for sodium ion batteries. *Nano*

Energy 12, 224–230 (**2015**).

103. Wang, Z., Selbach, S. M., & Grande, T. Van der Waals density functional study of the energetics of alkali metal intercalation in graphite. *RSC Adv.* 4, 4069–4079 (**2014**).
104. Ge, P., & Fouletier, M. Electrochemical intercalation of sodium in graphite. *Solid State Ionics* 28–30, 1172–1175 (**1988**).
105. Slater, M. D., Kim, D., Lee, E., & Johnson, C. S. Sodium-Ion Batteries. *Adv. Funct. Mater.* 23, 947–958 (**2013**).
106. Wenzel, S., Hara, T., Janek, J., & Adelhelm, P. Room-temperature sodium-ion batteries: Improving the rate capability of carbon anode materials by templating strategies. *Energy Environ. Sci.* 4, 3342–3345 (**2011**).
107. Sun, Y., Guo, S., & Zhou, H. Exploration of Advanced Electrode Materials for Rechargeable Sodium-Ion Batteries. *Adv. Energy Mater.* 9, 1800212 (**2019**).
108. Stevens, D. A., & Dahn, J. R. An In Situ Small-Angle X-Ray Scattering Study of Sodium Insertion into a Nanoporous Carbon Anode Material within an Operating Electrochemical Cell. *J. Electrochem. Soc.* 147, 4428 (**2000**).
109. Datta, D., Li, J., & Shenoy, V. B. Defective Graphene as a High-Capacity Anode Material for Na- and Ca-Ion Batteries. *ACS Appl. Mater. Interfaces* 6, 1788–1795 (**2014**).
110. Hwang, J. Y., Myung, S. T., & Sun, Y. K. Sodium-ion batteries: Present and future. *Chemical Society Reviews* vol. 46 3529–3614 (**2017**).
111. Raccichini, R., Varzi, A., Passerini, S., & Scrosati, B. The role of graphene for electrochemical energy storage. *Nat. Mater.* 14, 271–279 (**2015**).
112. Wang, Y.-X., Chou, S.-L., Liu, H.-K., & Dou, S.-X. Reduced graphene oxide with superior cycling stability and rate capability for sodium storage. *Carbon N. Y.* 57, 202–208 (**2013**).
113. Kang, Y.-J., Jung, S. C., Choi, J. W., & Han, Y.-K. Important Role of Functional Groups for Sodium Ion Intercalation in Expanded Graphite. *Chem. Mater.* 27, 5402–5406 (**2015**).
114. Paraknowitsch, J. P., & Thomas, A. Doping carbons beyond nitrogen: an overview of advanced heteroatom doped carbons with boron, sulphur and phosphorus for energy applications. *Energy Environ. Sci.* 6, 2839–2855 (**2013**).
115. Su, F., Poh, C. K., Chen, J. S., Xu, G., Wang, D., Li, Q., Lin, J., & Lou, X. W. Nitrogen-containing microporous carbon nanospheres with improved capacitive

properties. *Energy Environ. Sci.* 4, 717–724 (**2011**).

116. Dobrota, A. S., Pašti, I. A., Mentus, S. V, Johansson, B., & Skorodumova, N. V. Functionalized graphene for sodium battery applications: the DFT insights. *Electrochim. Acta* 250, 185–195 (**2017**).
117. Lao, M., Zhang, Y., Luo, W., Yan, Q., Sun, W., & Dou, S. X. Alloy-Based Anode Materials toward Advanced Sodium-Ion Batteries. *Adv. Mater.* 29, 1700622 (**2017**).
118. Nijamudheen, A., Sarbapalli, D., Hui, J., Rodríguez-López, J., & Mendoza-Cortes, J. L. Impact of Surface Modification on the Lithium, Sodium, and Potassium Intercalation Efficiency and Capacity of Few-Layer Graphene Electrodes. *ACS Appl. Mater. Interfaces* 12, 19393–19401 (**2020**).
119. Panchakarla, L. S., Subrahmanyam, K. S., Saha, S. K., Govindaraj, A., Krishnamurthy, H. R., Waghmare, U. V, & Rao, C. N. R. Synthesis, Structure, and Properties of Boron- and Nitrogen-Doped Graphene. *Adv. Mater.* 21, 4726–4730 (**2009**).
120. Van Khai, T., Na, H. G., Kwak, D. S., Kwon, Y. J., Ham, H., Shim, K. B., & Kim, H. W. Significant enhancement of blue emission and electrical conductivity of N-doped graphene. *J. Mater. Chem.* 22, 17992–18003 (**2012**).
121. Gong, K., Du, F., Xia, Z., Durstock, M., & Dai, L. Nitrogen-Doped Carbon Nanotube Arrays with High Electrocatalytic Activity for Oxygen Reduction. *Science (80).* 323, 760–764 (**2009**).
122. Zhang, C., Wang, X., Liang, Q., Liu, X., Weng, Q., Liu, J., Yang, Y., Dai, Z., Ding, K., Bando, Y., Tang, J., & Golberg, D. Amorphous Phosphorus/Nitrogen-Doped Graphene Paper for Ultrastable Sodium-Ion Batteries. *Nano Lett.* 16, 2054–2060 (**2016**).
123. Xu, X., Zeng, H., Han, D., Qiao, K., Xing, W., Rood, M. J., & Yan, Z. Nitrogen and Sulfur Co-Doped Graphene Nanosheets to Improve Anode Materials for Sodium-Ion Batteries. *ACS Appl. Mater. Interfaces* 10, 37172–37180 (**2018**).
124. Wang, H., Wu, Z., Meng, F., Ma, D., Huang, X., Wang, L., & Zhang, X. Nitrogen-Doped Porous Carbon Nanosheets as Low-Cost, High-Performance Anode Material for Sodium-Ion Batteries. *ChemSusChem* 6, 56–60 (**2013**).
125. Huang, H., Xu, R., Feng, Y., Zeng, S., Jiang, Y., Wang, H., Luo, W., & Yu, Y. Sodium/Potassium-Ion Batteries: Boosting the Rate Capability and Cycle Life by Combining Morphology, Defect and Structure Engineering. *Adv. Mater.* 32,

1904320 (**2020**).

126. Yang, Y., Tang, D. M., Zhang, C., Zhang, Y., Liang, Q., Chen, S., Weng, Q., Zhou, M., Xue, Y., Liu, J., Wu, J., Cui, Q. H., Lian, C., Hou, G., Yuan, F., Bando, Y., Golberg, D., & Wang, X. 'Protrusions' or 'holes' in graphene: Which is the better choice for sodium ion storage? *Energy Environ. Sci.* 10, 979–986 (**2017**).
127. Quan, B., Jin, A., Yu, S.-H., Kang, S. M., Jeong, J., Abruña, H. D., Jin, L., Piao, Y., & Sung, Y.-E. Solvothermal-Derived S-Doped Graphene as an Anode Material for Sodium-Ion Batteries. *Adv. Sci.* 5, 1700880 (**2018**).
128. Wang, X., Li, G., Hassan, F. M., Li, J., Fan, X., Batmaz, R., Xiao, X., & Chen, Z. Sulfur covalently bonded graphene with large capacity and high rate for high-performance sodium-ion batteries anodes. *Nano Energy* 15, 746–754 (**2015**).
129. Hou, H., Shao, L., Zhang, Y., Zou, G., Chen, J., & Ji, X. Large-Area Carbon Nanosheets Doped with Phosphorus: A High-Performance Anode Material for Sodium-Ion Batteries. *Adv. Sci.* 4, 1600243 (**2017**).
130. Ma, G., Xiang, Z., Huang, K., Ju, Z., Zhuang, Q., & Cui, Y. Graphene-Based Phosphorus-Doped Carbon as Anode Material for High-Performance Sodium-Ion Batteries. *Part. Part. Syst. Charact.* 34, 1600315 (**2017**).
131. Ma, Y., Guo, Q., Yang, M., Wang, Y., Chen, T., Chen, Q., Zhu, X., Xia, Q., Li, S., & Xia, H. Highly doped graphene with multi-dopants for high-capacity and ultrastable sodium-ion batteries. *Energy Storage Mater.* 13, 134–141 (**2018**).
132. Yue, X., Huang, N., Jiang, Z., Tian, X., Wang, Z., Hao, X., & Jiang, Z.-J. Nitrogen-rich graphene hollow microspheres as anode materials for sodium-ion batteries with super-high cycling and rate performance. *Carbon N. Y.* 130, 574–583 (**2018**).
133. Yang, J., Zhou, X., Wu, D., Zhao, X., & Zhou, Z. S-Doped N-Rich Carbon Nanosheets with Expanded Interlayer Distance as Anode Materials for Sodium-Ion Batteries. *Adv. Mater.* 29, 1604108 (**2017**).
134. Adams, R. A., Varma, A., & Pol, V. G. Carbon Anodes for Nonaqueous Alkali Metal-Ion Batteries and Their Thermal Safety Aspects. *Adv. Energy Mater.* 9, 1900550 (**2019**).
135. Fu, N., Liu, Y., Liu, R., Wang, X., & Yang, Z. Metal Cation-Assisted Synthesis of Amorphous B, N Co-Doped Carbon Nanotubes for Superior Sodium Storage. *Small* 16, 2001607 (**2020**).
136. Wu, Z.-S., Winter, A., Chen, L., Sun, Y., Turchanin, A., Feng, X., & Müllen, K.

Three-Dimensional Nitrogen and Boron Co-doped Graphene for High-Performance All-Solid-State Supercapacitors. *Adv. Mater.* 24, 5130–5135 (**2012**).

137. Diklić, N. P., Dobrota, A. S., Pašti, I. A., Mentus, S. V, Johansson, B., & Skorodumova, N. V. Sodium storage via single epoxy group on graphene – The role of surface doping. *Electrochim. Acta* 297, 523–528 (**2019**).
138. Ling, C., & Mizuno, F. Boron-doped graphene as a promising anode for Na-ion batteries. *Phys. Chem. Chem. Phys.* 16, 10419–10424 (**2014**).
139. Aurbach, D., Lu, Z., Schechter, A., Gofer, Y., Gizbar, H., Turgeman, R., Cohen, Y., Moshkovich, M., & Levi, E. Prototype systems for rechargeable magnesium batteries. *Nature* 407, 724–727 (**2000**).
140. Mao, M., Gao, T., Hou, S., & Wang, C. A critical review of cathodes for rechargeable Mg batteries. *Chem. Soc. Rev.* 47, 8804–8841 (**2018**).
141. Zhao-Karger, Z., & Fichtner, M. Magnesium-sulfur battery: Its beginning and recent progress. *MRS Communications* vol. 7 770–784 (**2017**).
142. Rashad, M., Asif, M., Wang, Y., He, Z., & Ahmed, I. Recent advances in electrolytes and cathode materials for magnesium and hybrid-ion batteries. *Energy Storage Mater.* 25, 342–375 (**2020**).
143. Muñoz-Torrero, D., Palma, J., Marcilla, R., & Ventosa, E. A critical perspective on rechargeable Al-ion battery technology. *Dalt. Trans.* 48, 9906–9911 (**2019**).
144. Ponrouch, A., Bitenc, J., Dominko, R., Lindahl, N., Johansson, P., & Palacin, M. R. Multivalent rechargeable batteries. *Energy Storage Mater.* 20, 253–262 (**2019**).
145. Mohtadi, R., Tutusaus, O., Arthur, T. S., Zhao-Karger, Z., & Fichtner, M. The metamorphosis of rechargeable magnesium batteries. *Joule* 5, 581–617 (**2021**).
146. Ma, Z., MacFarlane, D. R., & Kar, M. Mg Cathode Materials and Electrolytes for Rechargeable Mg Batteries: A Review. *Batter. Supercaps* 2, 115–127 (**2019**).
147. Vinayan, B. P., Zhao-Karger, Z., Diemant, T., Chakravadhanula, V. S. K., Schwarzburger, N. I., Cambaz, M. A., Behm, R. J., Kübel, C., & Fichtner, M. Performance study of magnesium–sulfur battery using a graphene based sulfur composite cathode electrode and a non-nucleophilic Mg electrolyte. *Nanoscale* 8, 3296–3306 (**2016**).
148. Regulacio, M. D., Nguyen, D.-T., Horia, R., & Seh, Z. W. Designing Nanostructured Metal Chalcogenides as Cathode Materials for Rechargeable

Magnesium Batteries. *Small* 17, 2007683 (**2021**).

149. Zhao, Y., Wang, D., Yang, D., Wei, L., Liu, B., Wang, X., Chen, G., & Wei, Y. Superior Mg^{2+} storage properties of VS_2 nanosheets by using an APC-PP14Cl/THF electrolyte. *Energy Storage Mater.* 23, 749–756 (**2019**).
150. Liu, M., Rong, Z., Malik, R., Canepa, P., Jain, A., Ceder, G., & Persson, K. A. Spinel compounds as multivalent battery cathodes: a systematic evaluation based on ab initio calculations. *Energy Environ. Sci.* 8, 964–974 (**2015**).
151. Kravchyk, K. V, Widmer, R., Erni, R., Dubey, R. J.-C., Krumeich, F., Kovalenko, M. V, & Bodnarchuk, M. I. Copper sulfide nanoparticles as high-performance cathode materials for Mg-ion batteries. *Sci. Rep.* 9, 7988 (**2019**).
152. Zhao-Karger, Z., & Fichtner, M. Beyond Intercalation Chemistry for Rechargeable Mg Batteries: A Short Review and Perspective. *Front. Chem.* 6, 656 (**2019**).
153. Le, L. T., Truong, D. Q., Ung, T. T. D., Nguyen, L. H., Vu, L. D., & Tran, P. D. Cu_2MoS_4 Nanotubes as a Cathode Material for Rechargeable Magnesium-ion Battery. *ChemistrySelect* 5, 280–283 (**2020**).
154. He, P., Ford, H. O., Merrill, L. C., & Schaefer, J. L. Investigation of the Effects of Copper Nanoparticles on Magnesium–Sulfur Battery Performance: How Practical Is Metallic Copper Addition? *ACS Appl. Energy Mater.* 2, 6800–6807 (**2019**).
155. Montenegro, C. T., Peters, J. F., Baumann, M., Zhao-Karger, Z., Wolter, C., & Weil, M. Environmental assessment of a new generation battery: The magnesium-sulfur system. *J. Energy Storage* 35, 102053 (**2021**).
156. Kong, L., Yan, C., Huang, J.-Q., Zhao, M.-Q., Titirici, M.-M., Xiang, R., & Zhang, Q. A Review of Advanced Energy Materials for Magnesium–Sulfur Batteries. *ENERGY Environ. Mater.* 1, 100–112 (**2018**).
157. Razaq, R., Li, P., Dong, Y., Li, Y., Mao, Y., & Bo, S.-H. Practical energy densities, cost, and technical challenges for magnesium-sulfur batteries. *EcoMat* 2, e12056 (**2020**).
158. Amir, N., Vestfrid, Y., Chusid, O., Gofer, Y., & Aurbach, D. Progress in nonaqueous magnesium electrochemistry. *J. Power Sources* 174, 1234–1240 (**2007**).
159. Zhou, X., Tian, J., Hu, J., & Li, C. High Rate Magnesium–Sulfur Battery with Improved Cyclability Based on Metal–Organic Framework Derivative Carbon

Host. *Adv. Mater.* 30, 1704166 (**2018**).

160. Lu, Y., Wang, C., Liu, Q., Li, X., Zhao, X., & Guo, Z. Progress and Perspective on Rechargeable Magnesium–Sulfur Batteries. *Small Methods* 5, 2001303 (**2021**).
161. Zhao-Karger, Z., Liu, R., Dai, W., Li, Z., Diemant, T., Vinayan, B. P., Bonatto Minella, C., Yu, X., Manthiram, A., Behm, R. J., Ruben, M., & Fichtner, M. Toward Highly Reversible Magnesium–Sulfur Batteries with Efficient and Practical Mg[B(hfip)4]2 Electrolyte. *ACS Energy Lett.* 3, 2005–2013 (**2018**).
162. Kim, H. S., Arthur, T. S., Allred, G. D., Zajicek, J., Newman, J. G., Rodnyansky, A. E., Oliver, A. G., Boggess, W. C., & Muldoon, J. Structure and compatibility of a magnesium electrolyte with a sulphur cathode. *Nat. Commun.* 2, 427 (**2011**).
163. Robba, A., Vizintin, A., Bitenc, J., Mali, G., Arčon, I., Kavčič, M., Žitnik, M., Bučar, K., Aquilanti, G., Martineau-Corcos, C., Randon-Vitanova, A., & Dominko, R. Mechanistic Study of Magnesium–Sulfur Batteries. *Chem. Mater.* 29, 9555–9564 (**2017**).
164. Vinayan, B. P., Euchner, H., Zhao-Karger, Z., Cambaz, M. A., Li, Z., Diemant, T., Behm, R. J., Gross, A., & Fichtner, M. Insights into the electrochemical processes of rechargeable magnesium–sulfur batteries with a new cathode design. *J. Mater. Chem. A* 7, 25490–25502 (**2019**).
165. Nakayama, Y., Matsumoto, R., Kumagae, K., Mori, D., Mizuno, Y., Hosoi, S., Kamiguchi, K., Koshitani, N., Inaba, Y., Kudo, Y., Kawasaki, H., Miller, E. C., Weker, J. N., & Toney, M. F. Zinc Blende Magnesium Sulfide in Rechargeable Magnesium-Sulfur Batteries. *Chem. Mater.* 30, 6318–6324 (**2018**).
166. Zhao-Karger, Z., Zhao, X., Wang, D., Diemant, T., Behm, R. J., & Fichtner, M. Performance Improvement of Magnesium Sulfur Batteries with Modified Non-Nucleophilic Electrolytes. *Adv. Energy Mater.* 5, 1401155 (**2015**).
167. Zou, Q., Sun, Y., Liang, Z., Wang, W., & Lu, Y.-C. Achieving Efficient Magnesium–Sulfur Battery Chemistry via Polysulfide Mediation. *Adv. Energy Mater.* 11, 2101552 (**2021**).
168. Xu, Y., Ye, Y., Zhao, S., Feng, J., Li, J., Chen, H., Yang, A., Shi, F., Jia, L., Wu, Y., Yu, X., Glans-Suzuki, P.-A., Cui, Y., Guo, J., & Zhang, Y. In Situ X-ray Absorption Spectroscopic Investigation of the Capacity Degradation Mechanism in Mg/S Batteries. *Nano Lett.* 19, 2928–2934 (**2019**).
169. Richter, R., Häcker, J., Zhao-Karger, Z., Danner, T., Wagner, N., Fichtner, M.,

Friedrich, K. A., & Latz, A. Insights into Self-Discharge of Lithium– and Magnesium–Sulfur Batteries. *ACS Appl. Energy Mater.* 3, 8457–8474 (**2020**).

170. Gariano, G., Lesnyak, V., Brescia, R., Bertoni, G., Dang, Z., Gaspari, R., De Trizio, L., & Manna, L. Role of the Crystal Structure in Cation Exchange Reactions Involving Colloidal Cu_2Se Nanocrystals. *J. Am. Chem. Soc.* 139, 9583–9590 (**2017**).
171. Li, C.-S., Sun, Y., Gebert, F., & Chou, S.-L. Current Progress on Rechargeable Magnesium–Air Battery. *Adv. Energy Mater.* 7, 1700869 (**2017**).
172. Masquelier, C., & Croguennec, L. Polyanionic (Phosphates, Silicates, Sulfates) Frameworks as Electrode Materials for Rechargeable Li (or Na) Batteries. *Chem. Rev.* 113, 6552–6591 (**2013**).
173. Okamoto, S., Ichitsubo, T., Kawaguchi, T., Kumagai, Y., Oba, F., Yagi, S., Shimokawa, K., Goto, N., Doi, T., & Matsubara, E. Intercalation and Push-Out Process with Spinel-to-Rocksalt Transition on Mg Insertion into Spinel Oxides in Magnesium Batteries. *Adv. Sci.* 2, 1500072 (**2015**).
174. Tian, H., Gao, T., Li, X., Wang, X., Luo, C., Fan, X., Yang, C., Suo, L., Ma, Z., Han, W., & Wang, C. High power rechargeable magnesium/iodine battery chemistry. *Nat. Commun.* 8, 14083 (**2017**).
175. Rao, C. N. R., & Pisharody, K. P. R. Transition metal sulfides. *Prog. Solid State Chem.* 10, 207–270 (**1976**).
176. Brune, V., Grosch, M., Weißing, R., Hartl, F., Frank, M., Mishra, S., & Mathur, S. Influence of the choice of precursors on the synthesis of two-dimensional transition metal dichalcogenides. *Dalt. Trans.* 50, 12365–12385 (**2021**).
177. Wang, M., Zhang, L., He, Y., & Zhu, H. Recent advances in transition-metal-sulfide-based bifunctional electrocatalysts for overall water splitting. *J. Mater. Chem. A* 9, 5320–5363 (**2021**).
178. Yazdani, S., Yarali, M., & Cha, J. J. Recent progress on in situ characterizations of electrochemically intercalated transition metal dichalcogenides. *Nano Res.* 12, 2126–2139 (**2019**).
179. Chhowalla, M., Shin, H. S., Eda, G., Li, L. J., Loh, K. P., & Zhang, H. The chemistry of two-dimensional layered transition metal dichalcogenide nanosheets. *Nature Chemistry* vol. 5 263–275 (**2013**).
180. Xia, J., Wang, J., Chao, D., Chen, Z., Liu, Z., Kuo, J. L., Yan, J., & Shen, Z. X. Phase evolution of lithium intercalation dynamics in 2H-MoS2. *Nanoscale* 9,

7533–7540 (**2017**).

181. Li, Z., Mu, X., Zhao-Karger, Z., Diemant, T., Behm, R. J., Kübel, C., & Fichtner, M. Fast kinetics of multivalent intercalation chemistry enabled by solvated magnesium-ions into self-established metallic layered materials. *Nat. Commun.* 9, 5115 (**2018**).
182. Castro Neto, A. H. Charge Density Wave, Superconductivity, and Anomalous Metallic Behavior in 2D Transition Metal Dichalcogenides. *Phys. Rev. Lett.* 86, 4382–4385 (**2001**).
183. Kan, M., Wang, J. Y., Li, X. W., Zhang, S. H., Li, Y. W., Kawazoe, Y., Sun, Q., & Jena, P. Structures and phase transition of a MoS_2 monolayer. *J. Phys. Chem. C* 118, 1515–1522 (**2014**).
184. Canepa, P., Sai Gautam, G., Hannah, D. C., Malik, R., Liu, M., Gallagher, K. G., Persson, K. A., & Ceder, G. Odyssey of Multivalent Cathode Materials: Open Questions and Future Challenges. *Chem. Rev.* 117, 4287–4341 (**2017**).
185. Yang, S., Li, D., Zhang, T., Tao, Z., & Chen, J. First-Principles Study of Zigzag MoS 2 Nanoribbon As a Promising Cathode Material for Rechargeable Mg Batteries. *J. Phys. Chem. C* 116, 1307–1312 (**2012**).
186. Liang, Y., Feng, R., Yang, S., Ma, H., Liang, J., & Chen, J. Rechargeable Mg Batteries with Graphene-like MoS2 Cathode and Ultrasmall Mg Nanoparticle Anode. *Adv. Mater.* 23, 640–643 (**2011**).
187. Liu, Y., Jiao, L., Wu, Q., Du, J., Zhao, Y., Si, Y., Wang, Y., & Yuan, H. Sandwich-structured graphene-like MoS2/C microspheres for rechargeable Mg batteries. *J. Mater. Chem. A* 1, 5822–5826 (**2013**).
188. Wu, C., Zhao, G., Gong, S., Zhang, N., & Sun, K. PVP incorporated MoS2 as a Mg ion host with enhanced capacity and durability. *J. Mater. Chem. A* 7, 4426–4430 (**2019**).
189. Sun, X., Bonnick, P., & Nazar, L. F. Layered TiS_2 Positive Electrode for Mg Batteries. *ACS Energy Lett.* 1, 297–301 (**2016**).
190. Tao, Z. L., Xu, L. N., Gou, X. L., Chen, J., & Yuan, H. T. TiS2 nanotubes as the cathode materials of Mg-ion batteries. *Chem. Commun.* 2080–2081 (**2004**).
191. Yoo, H. D., Liang, Y., Dong, H., Lin, J., Wang, H., Liu, Y., Ma, L., Wu, T., Li, Y., Ru, Q., Jing, Y., An, Q., Zhou, W., Guo, J., Lu, J., Pantelides, S. T., Qian, X., & Yao, Y. Fast kinetics of magnesium monochloride cations in interlayer-expanded titanium disulfide for magnesium rechargeable batteries. *Nat. Commun.* 8, 339

(**2017**).

192. Xue, X., Chen, R., Yan, C., Zhao, P., Hu, Y., Kong, W., Lin, H., Wang, L., & Jin, Z. One-Step Synthesis of 2-Ethylhexylamine Pillared Vanadium Disulfide Nanoflowers with Ultralarge Interlayer Spacing for High-Performance Magnesium Storage. *Adv. Energy Mater.* 9, 1900145 (**2019**).
193. Jing, P., Lu, H., Yang, W., & Cao, Y. Interlayer-expanded and binder-free VS_2 nanosheets assemblies for enhanced Mg^{2+} and Li^+/Mg^{2+} hybrid ion storage. *Electrochim. Acta* 330, 135263 (**2020**).
194. Wang, Y., Liu, Z., Wang, C., Yi, X., Chen, R., Ma, L., Hu, Y., Zhu, G., Chen, T., Tie, Z., Ma, J., Liu, J., & Jin, Z. Highly Branched VS_4 Nanodendrites with 1D Atomic-Chain Structure as a Promising Cathode Material for Long-Cycling Magnesium Batteries. *Adv. Mater.* 30, 1802563 (**2018**).
195. Li, Z., Ding, S., Yin, J., Zhang, M., Sun, C., & Meng, A. Morphology-dependent electrochemical performance of VS_4 for rechargeable magnesium battery and its magnesiation/demagnesiation mechanism. *J. Power Sources* 451, 227815 (**2020**).
196. Gregory, T. D., Hoffman, R. J., & Winterton, R. C. Nonaqueous Electrochemistry of Magnesium: Applications to Energy Storage. *J. Electrochem. Soc.* 137, 775–780 (**1990**).
197. Kim, S., Kim, Y. J., & Ryu, W.-H. Zirconium disulfides as an electrode material alternative for Li-ion batteries. *Appl. Surf. Sci.* 547, 149029 (**2021**).
198. Latha, M., Biswas, S., & Rani, J. V. Application of WS_2-G composite as cathode for rechargeable magnesium batteries. *Ionics (Kiel).* 26, 3395–3404 (**2020**).
199. Vakili-Nezhaad, G. R., Gujarathi, A. M., Al Rawahi, N., & Mohammadi, M. Performance of WS_2 monolayers as a new family of anode materials for metal-ion (Mg, Al and Ca) batteries. *Mater. Chem. Phys.* 230, 114–121 (**2019**).
200. Pereira, A. O., & Miranda, C. R. First-Principles Investigation of Transition Metal Dichalcogenide Nanotubes for Li and Mg Ion Battery Applications. *J. Phys. Chem. C* 119, 4302–4311 (**2015**).
201. Liu, M., Jain, A., Rong, Z., Qu, X., Canepa, P., Malik, R., Ceder, G., & Persson, K. A. Evaluation of sulfur spinel compounds for multivalent battery cathode applications. *Energy Environ. Sci* 9, 3201 (**2016**).
202. Mathur, S., Veith, M., Ruegamer, T., Hemmer, E., & Shen, H. Chemical Vapor Deposition of $MgAl_2O_4$ Thin Films Using Different Mg-Al Alkoxides: Role of

Precursor Chemistry. *Chem. Mater.* 16, 1304–1312 (**2004**).

203. Lightfoot, P., Krok, F., Nowinski, J. L., & Bruce, P. G. Structure of the cubic intercalate $MgTiS_2$. *J. Mater. Chem.* 2, 139–140 (**1992**).
204. Bruce, P. G., Krok, F., Lightfoot, P., Nowinski, J. L., & Gibson, V. C. Multivalent cation intercalation. *Solid State Ionics* 53–56, 351–355 (**1992**).
205. Bruce, P. G., Krok, F., Nowinski, J., Gibson, V. C., & Tavakkoli, K. Chemical intercalation of magnesium into solid hosts. *J. Mater. Chem.* 1, 705–706 (**1991**).
206. Vaughan, D. J., & Craig, J. R. The crystal chemistry of iron-nickel thiospinels. *Am. Mineral.* 70, 1036–1043 (**1985**).
207. Ozel, F., Kılıc, H. S., Coskun, H., Deveci, I., Sarılmaz, A., Balıkcıoglu, A., Gundogdu, Y., Aljabour, A., Ozen, A., Gezgin, S. Y., Houimi, A., Yar, A., Kus, M., & Ersoz, M. A general review on the thiospinels and their energy applications. *Mater. Today Energy* 21, 100822 (**2021**).
208. Wyżga, P., Veremchuk, I., Bobnar, M., Hennig, C., Leithe-Jasper, A., & Gumeniuk, R. Ternary MIn_2S_4 (M = Mn, Fe, Co, Ni) Thiospinels – Crystal Structure and Thermoelectric Properties. *Zeitschrift für Anorg. und Allg. Chemie* 646, 1091–1098 (**2020**).
209. Hannah, D. C., Sai Gautam, G., Canepa, P., & Ceder, G. On the Balance of Intercalation and Conversion Reactions in Battery Cathodes. *Adv. Energy Mater.* 8, 1800379 (**2018**).
210. Wustrow, A., Key, B., Phillips, P. J., Sa, N., Lipton, A. S., Klie, R. F., Vaughey, J. T., & Poeppelmeier, K. R. Synthesis and Characterization of $MgCr_2S_4$ Thiospinel as a Potential Magnesium Cathode. *Inorg. Chem.* 57, 8634–8638 (**2018**).
211. Blanc, L., Bartel, C. J., Kim, H., Tian, Y., Kim, H., Miura, A., Ceder, G., & Nazar, L. F. Toward the Development of a High-Voltage Mg Cathode Using a Chromium Sulfide Host. *ACS Mater. Lett.* 3, 1213–1220 (**2021**).
212. Guo, S.-P., Li, J.-C., Xiao, J.-R., & Xue, H.-G. Fe3S4 Nanoparticles Wrapped in an rGO Matrix for Promising Energy Storage: Outstanding Cyclic and Rate Performance. *ACS Appl. Mater. Interfaces* 9, 37694–37701 (**2017**).
213. Canepa, P., Sai Gautam, G., Broberg, D., Bo, S.-H., & Ceder, G. Role of Point Defects in Spinel Mg Chalcogenide Conductors. *Chem. Mater.* 29, 9657–9667 (**2017**).
214. Saeed, M., Noor, Z., Laref, A., Althib, H., Flemban, T. H., & Murtaza, G. Insights

into the structural, electronic and optical properties of MgA_2B_4(A = Sc, Y; B = S, Se) spinel compounds: Direct energy band gap materials. *Mater. Sci. Semicond. Process.* 127, 105736 (**2021**).

215. Szopa, K., Krzykawski, T., Banasik, K., Król, P., Skreczko, S., Mounteanou, S. A., & Koziarska, M. EMPA, XRD, and Raman Characterization of Ag-Bearing Djurleite from the Lubin Mine, Lower Silesia, Poland. *Minerals* vol. 11 (**2021**).
216. Shen, J., Zhang, Y., Chen, D., Li, X., Chen, Z., Cao, S., Li, T., & Xu, F. A hollow CuS nanocube cathode for rechargeable Mg batteries: effect of the structure on the performance. *J. Mater. Chem. A* 7, 21410–21420 (**2019**).
217. Xiong, F., Fan, Y., Tan, S., Zhou, L., Xu, Y., Pei, C., An, Q., & Mai, L. Magnesium storage performance and mechanism of CuS cathode. *Nano Energy* 47, 210–216 (**2018**).
218. Ren, W., Xiong, F., Fan, Y., Xiong, Y., & Jian, Z. Hierarchical Copper Sulfide Porous Nanocages for Rechargeable Multivalent-Ion Batteries. *ACS Appl. Mater. Interfaces* 12, 10471–10478 (**2020**).
219. Rui, X., Tan, H., & Yan, Q. Nanostructured metal sulfides for energy storage. *Nanoscale* 6, 9889–9924 (**2014**).
220. Wang, Z., Zhu, Y., Peng, H., Du, C., Ma, X., & Cao, C. Microwave-induced phase engineering of copper sulfide nanosheets for rechargeable magnesium batteries. *Electrochim. Acta* 374, 137965 (**2021**).
221. Wu, M., Zhang, Y., Li, T., Chen, Z., Cao, S.-A., & Xu, F. Copper sulfide nanoparticles as high-performance cathode materials for magnesium secondary batteries. *Nanoscale* 10, 12526 (**2018**).
222. Shen, Y., Wang, Y., Miao, Y., Yang, M., Zhao, X., & Shen, X. High-Energy Interlayer-Expanded Copper Sulfide Cathode Material in Non-Corrosive Electrolyte for Rechargeable Magnesium Batteries. *Adv. Mater.* 32, 1905524 (**2020**).
223. Du, C., Zhu, Y., Wang, Z., Wang, L., Younas, W., Ma, X., & Cao, C. Cuprous Self-Doping Regulated Mesoporous CuS Nanotube Cathode Materials for Rechargeable Magnesium Batteries. *ACS Appl. Mater. Interfaces* 12, 35035–35042 (**2020**).
224. Tashiro, Y., Taniguchi, K., & Miyasaka, H. The Effect of Anion-sublattice Structure on the Displacement Reaction in Copper Sulfide Cathodes of Rechargeable Magnesium Batteries. *Chem. Lett.* 46, 1240–1242 (**2017**).

225. Li, M., Liu, Y., Zhang, Y., Han, X., Zhang, T., Zuo, Y., Xie, C., Xiao, K., Arbiol, J., Llorca, J., Ibáñez, M., Liu, J., & Cabot, A. Effect of the Annealing Atmosphere on Crystal Phase and Thermoelectric Properties of Copper Sulfide. *ACS Nano* 15, 4967–4978 (**2021**).
226. Evans, H. T. The crystal structures of low chalcocite and djurleite. 150, 299–320 (**1979**).
227. Khalid, S., Khan, Y., Ahmed, E., Nawaz, S., Khalid, N. R., & Ahmed, W. Chapter 16 - Transition metal sulfides for supercapacitors. in *Micro and Nano Technologies* 407–445 (**2021**).
228. Pattrick, R. A. D., Mosselmans, J. F. W., Charnock, J. M., England, K. E. R., Helz, G. R., Garner, C. D., & Vaughan, D. J. The structure of amorphous copper sulfide precipitates: An X-ray absorption study. *Geochim. Cosmochim. Acta* 61, 2023–2036 (**1997**).
229. Nesbitt, H. W., & Muir, I. J. X-ray photoelectron spectroscopic study of a pristine pyrite surface reacted with water vapour and air. *Geochim. Cosmochim. Acta* 58, 4667–4679 (**1994**).
230. Wu, M., Zhang, Y., Li, T., Chen, Z., Cao, S., & Xu, F. Copper sulfide nanoparticles as high-performance cathode materials for magnesium secondary batteries. *Nanoscale* 10, 12526–12534 (**2018**).
231. Mao, M., Gao, T., Hou, S., Wang, F., Chen, J., Wei, Z., Fan, X., Ji, X., Ma, J., & Wang, C. High-Energy-Density Rechargeable Mg Battery Enabled by a Displacement Reaction. *Nano Lett.* 19, 6665–6672 (**2019**).
232. Li, Y., Guan, S., Huo, H., Ma, Y., Gao, Y., Zuo, P., & Yin, G. A Review of Magnesium Aluminum Chloride Complex Electrolytes for Mg Batteries. *Adv. Funct. Mater.* 31, 2100650 (**2021**).
233. Hua, X., Robert, R., Du, L.-S., Wiaderek, K. M., Leskes, M., Chapman, K. W., Chupas, P. J., & Grey, C. P. Comprehensive Study of the CuF2 Conversion Reaction Mechanism in a Lithium Ion Battery. *J. Phys. Chem. C* 118, 15169–15184 (**2014**).
234. Shea, D., & Helz, G. R. The solubility of copper in sulfidic waters: Sulfide and polysulfide complexes in equilibrium with covellite. *Geochim. Cosmochim. Acta* 52, 1815–1825 (**1988**).
235. Ha, J. H., Lee, B., Kim, J. H., Cho, B. W., Kim, S.-O., & Oh, S. H. Silver chalcogenides (Ag_2X, X=S, Se) nanoparticles embedded in carbon matrix for

facile magnesium storage via conversion chemistry. *Energy Storage Mater.* 27, 459–465 (**2020**).

236. Zhang, Y., Li, X., Shen, J., Chen, Z., Cao, S., Li, T., & Xu, F. Rechargeable Mg batteries based on a Ag_2S conversion cathode with fast solid-state Mg^{2+} diffusion kinetics. *Dalt. Trans.* 48, 14390–14397 (**2019**).
237. Chen, Z., Zhang, Z., Du, A., Zhang, Y., Men, M., Li, G., & Cui, G. Fast magnesiation kinetics in α-Ag_2S nanostructures enabled by an in situ generated silver matrix. *Chem. Commun.* 55, 4431–4434 (**2019**).
238. He, D., Wu, D., Gao, J., Wu, X., Zeng, X., & Ding, W. Flower-like CoS with nanostructures as a new cathode-active material for rechargeable magnesium batteries. *J. Power Sources* 294, 643–649 (**2015**).
239. Pan, M., Zou, J., Laine, R., Khan, D., Guo, R., Zeng, X., & Ding, W. Using CoS cathode materials with 3D hierarchical porosity and an ionic liquid (IL) as an electrolyte additive for high capacity rechargeable magnesium batteries. *J. Mater. Chem. A* 7, 18880–18888 (**2019**).
240. Wu, X., Markir, A., Xu, Y., Hu, E. C., Dai, K. T., Zhang, C., Shin, W., Leonard, D. P., Kim, K., & Ji, X. Rechargeable Iron–Sulfur Battery without Polysulfide Shuttling. *Adv. Energy Mater.* 9, 1902422 (**2019**).
241. Chen, X., Wang, S., & Wang, H. High performance hybrid Mg-Li ion batteries with conversion cathodes for low cost energy storage. *Electrochim. Acta* 265, 175–183 (**2018**).
242. Ding, W., Wang, X., Peng, H., & Hu, L. Electrochemical performance of the chalcopyrite $CuFeS_2$ as cathode for lithium ion battery. *Mater. Chem. Phys.* 137, 872–876 (**2013**).
243. Guo, P., Song, H., Liu, Y., & Wang, C. $CuFeS_2$ Quantum Dots Anchored in Carbon Frame: Superior Lithium Storage Performance and the Study of Electrochemical Mechanism. *ACS Appl. Mater. Interfaces* 9, 31752–31762 (**2017**).
244. Jiang, F., Zhao, W., Zhang, L., Tian, Y., Gao, X., Ge, P., Sun, W., Chang, X., & Ji, X. Unraveling the Mechanism of Chalcopyrite's Superior Performance for Lithium Storage. *ACS Appl. Energy Mater.* 4, 5086–5093 (**2021**).
245. Zhang, Y., Zhao, G., Lv, X., Tian, Y., Yang, L., Zou, G., Hou, H., Zhao, H., & Ji, X. Exploration and Size Engineering from Natural Chalcopyrite to High-Performance Electrode Materials for Lithium-Ion Batteries. *ACS Appl. Mater.*

Interfaces 11, 6154–6165 (**2019**).

246. Mongo, M., Belaïd, F., & Ramdani, B. The effects of environmental innovations on CO_2 emissions: Empirical evidence from Europe. *Environ. Sci. Policy* 118, 1–9 (**2021**).
247. Lashof, D. A., & Ahuja, D. R. Relative contributions of greenhouse gas emissions to global warming. *Nature* 344, 529–531 (**1990**).
248. Sai, H., Kanamori, Y., Arafune, K., Ohshita, Y., & Yamaguchi, M. Light trapping effect of submicron surface textures in crystalline Si solar cells. *Prog. Photovoltaics Res. Appl.* 15, 415–423 (**2007**).
249. Schubert, G., Huster, F., & Fath, P. Physical understanding of printed thick-film front contacts of crystalline Si solar cells—Review of existing models and recent developments. *Sol. Energy Mater. Sol. Cells* 90, 3399–3406 (**2006**).
250. Kaelin, M., Rudmann, D., & Tiwari, A. N. Low cost processing of CIGS thin film solar cells. *Sol. Energy* 77, 749–756 (**2004**).
251. Lundberg, O., Edoff, M., & Stolt, L. The effect of Ga-grading in CIGS thin film solar cells. *Thin Solid Films* 480–481, 520–525 (**2005**).
252. Wöhrle, D., & Meissner, D. Organic Solar Cells. *Adv. Mater.* 3, 129–138 (**1991**).
253. Günes, S., Neugebauer, H., & Sariciftci, N. S. Conjugated Polymer-Based Organic Solar Cells. *Chem. Rev.* 107, 1324–1338 (**2007**).
254. Chiba, Y., Islam, A., Watanabe, Y., Komiya, R., Koide, N., & Han, L. Dye-Sensitized Solar Cells with Conversion Efficiency of 11.1%. *Jpn. J. Appl. Phys.* 45, L638–L640 (**2006**).
255. Grätzel, M. Dye-sensitized solar cells. *J. Photochem. Photobiol. C Photochem. Rev.* 4, 145–153 (**2003**).
256. Yang, Y., Hoang, M. T., Yao, D., Pham, N. D., Tiong, V. T., Wang, X., Sun, W., & Wang, H. High performance carbon-based planar perovskite solar cells by hot-pressing approach. *Sol. Energy Mater. Sol. Cells* 210, 110517 (**2020**).
257. Yang, Y., Pham, N. D., Yao, D., Fan, L., Hoang, M. T., Tiong, V. T., Wang, Z., Zhu, H., & Wang, H. Interface Engineering to Eliminate Hysteresis of Carbon-Based Planar Heterojunction Perovskite Solar Cells via CuSCN Incorporation. *ACS Appl. Mater. Interfaces* 11, 28431–28441 (**2019**).
258. Wang, H., Guerrero, A., Bou, A., Al-Mayouf, A. M., & Bisquert, J. Kinetic and material properties of interfaces governing slow response and long timescale phenomena in perovskite solar cells. *Energy Environ. Sci.* 12, 2054–2079

(**2019**).

259. Yang, Y., Hoang, M. T., Yao, D., Pham, N. D., Tiong, V. T., Wang, X., & Wang, H. Spiro-OMeTAD or CuSCN as a preferable hole transport material for carbon-based planar perovskite solar cells. *J. Mater. Chem. A* 8, 12723–12734 (**2020**).
260. Jung, M., Kim, Y. C., Jeon, N. J., Yang, W. S., Seo, J., Noh, J. H., & Il Seok, S. Thermal Stability of CuSCN Hole Conductor-Based Perovskite Solar Cells. *ChemSusChem* 9, 2592–2596 (**2016**).
261. Park, N.-G. Perovskite solar cells: an emerging photovoltaic technology. *Mater. Today* 18, 65–72 (**2015**).
262. Li, Z., Yang, M., Park, J.-S., Wei, S.-H., Berry, J. J., & Zhu, K. Stabilizing Perovskite Structures by Tuning Tolerance Factor: Formation of Formamidinium and Cesium Lead Iodide Solid-State Alloys. *Chem. Mater.* 28, 284–292 (**2016**).
263. Kojima, A., Teshima, K., Shirai, Y., & Miyasaka, T. Organometal Halide Perovskites as Visible-Light Sensitizers for Photovoltaic Cells. *J. Am. Chem. Soc.* 131, 6050–6051 (**2009**).
264. Wu, T., Qin, Z., Wang, Y., Wu, Y., Chen, W., Zhang, S., Cai, M., Dai, S., Zhang, J., Liu, J., Zhou, Z., Liu, X., Segawa, H., Tan, H., Tang, Q., Fang, J., Li, Y., … Han, L. The Main Progress of Perovskite Solar Cells in 2020–2021. *Nano-Micro Lett.* 13, 152 (**2021**).
265. Ansari, M. I. H., Qurashi, A., & Nazeeruddin, M. K. Frontiers, opportunities, and challenges in perovskite solar cells: A critical review. *J. Photochem. Photobiol. C Photochem. Rev.* 35, 1–24 (**2018**).
266. Xu, J., Chen, Y., & Dai, L. Efficiently photo-charging lithium-ion battery by perovskite solar cell. *Nat. Commun.* 6, 8103 (**2015**).
267. Hu, Y., Bai, Y., Luo, B., Wang, S., Hu, H., Chen, P., Lyu, M., Shapter, J., Rowan, A., & Wang, L. A Portable and Efficient Solar-Rechargeable Battery with Ultrafast Photo-Charge/Discharge Rate. *Adv. Energy Mater.* 9, 1900872 (**2019**).
268. Ahmad, S., George, C., Beesley, D. J., Baumberg, J. J., & De Volder, M. Photo-Rechargeable Organo-Halide Perovskite Batteries. *Nano Lett.* 18, 1856–1862 (**2018**).
269. Wilhelm, M., Adam, R., Bhardwaj, A., Neumann, I., Cho, S. H., Yamada, Y., Sekino, T., Tao, J., Hong, Z., Fischer, T., & Mathur, S. Carbon-Coated Electrospun V_2O_5 Nanofibers as Photoresponsive Cathode for Lithium-Ion Batteries. *Adv. Eng. Mater.* 2200765, (**2022**).

270. Banerjee, T., Podjaski, F., Kröger, J., Biswal, B. P., & Lotsch, B. V. Polymer photocatalysts for solar-to-chemical energy conversion. *Nat. Rev. Mater.* 6, 168–190 (**2021**).
271. Chen, S., Deng, Y., Xiao, X., Xu, S., Rudd, P. N., & Huang, J. Preventing lead leakage with built-in resin layers for sustainable perovskite solar cells. *Nat. Sustain.* 4, 636–643 (**2021**).
272. Ballif, C., Haug, F. J., Boccard, M., Verlinden, P. J., & Hahn, G. Status and perspectives of crystalline silicon photovoltaics in research and industry. *Nat. Rev. Mater.* 7, 597–616 (**2022**).
273. Zhu, X., Meng, F., Zhang, Q., Xue, L., Zhu, H., Lan, S., Liu, Q., Zhao, J., Zhuang, Y., Guo, Q., Liu, B., Gu, L., Lu, X., Ren, Y., & Xia, H. $LiMnO_2$ cathode stabilized by interfacial orbital ordering for sustainable lithium-ion batteries. *Nat. Sustain.* 4, 392–401 (**2021**).
274. Yang, Y., Okonkwo, E. G., Huang, G., Xu, S., Sun, W., & He, Y. On the sustainability of lithium ion battery industry – A review and perspective. *Energy Storage Mater.* 36, 186–212 (**2021**).
275. Xin, F., Zhou, H., Zong, Y., Zuba, M., Chen, Y., Chernova, N. A., Bai, J., Pei, B., Goel, A., Rana, J., Wang, F., An, K., Piper, L. F. J., Zhou, G., & Whittingham, M. S. What is the Role of Nb in Nickel-Rich Layered Oxide Cathodes for Lithium-Ion Batteries? *ACS Energy Lett.* 6, 1377–1382 (**2021**).
276. Niu, C., Liu, D., Lochala, J. A., Anderson, C. S., Cao, X., Gross, M. E., Xu, W., Zhang, J.-G., Whittingham, M. S., Xiao, J., & Liu, J. Balancing interfacial reactions to achieve long cycle life in high-energy lithium metal batteries. *Nat. Energy* 6, 723–732 (**2021**).
277. Zhang, H., Liu, H., Piper, L. F. J., Whittingham, M. S., & Zhou, G. Oxygen Loss in Layered Oxide Cathodes for Li-Ion Batteries: Mechanisms, Effects, and Mitigation. *Chem. Rev.* 122, 5641–5681 (**2022**).
278. Lee, A., Vörös, M., Dose, W. M., Niklas, J., Poluektov, O., Schaller, R. D., Iddir, H., Maroni, V. A., Lee, E., Ingram, B., Curtiss, L. A., & Johnson, C. S. Photo-accelerated fast charging of lithium-ion batteries. *Nat. Commun.* 10, 4946 (**2019**).
279. Boruah, B. D., Mathieson, A., Wen, B., Feldmann, S., Dose, W. M., & De Volder, M. Photo-rechargeable zinc-ion batteries. *Energy Environ. Sci.* 13, 2414–2421 (**2020**).

280. Boruah, B. D., Wen, B., & De Volder, M. Light Rechargeable Lithium-Ion Batteries Using V_2O_5 Cathodes. *Nano Lett.* 21, 3527–3532 (**2021**).
281. Kato, K., Puthirath, A. B., Mojibpour, A., Miroshnikov, M., Satapathy, S., Thangavel, N. K., Mahankali, K., Dong, L., Arava, L. M. R., John, G., Bharadwaj, P., Babu, G., & Ajayan, P. M. Light-Assisted Rechargeable Lithium Batteries: Organic Molecules for Simultaneous Energy Harvesting and Storage. *Nano Lett.* 21, 907–913 (**2021**).
282. Zhang, X., Su, K., Mohamed, A. G. A., Liu, C., Sun, Q., Yuan, D., Wang, Y., Xue, W., & Wang, Y. Photo-assisted charge/discharge Li-organic battery with a charge-separated and redox-active C60@porous organic cage cathode. *Energy Environ. Sci.* 15, 780–785 (**2022**).
283. Yue, Y., & Liang, H. Micro- and Nano-Structured Vanadium Pentoxide (V_2O_5) for Electrodes of Lithium-Ion Batteries. *Adv. Energy Mater.* 7, 1602545 (**2017**).
284. Whittingham, M. S. The Role of Ternary Phases in Cathode Reactions. *J. Electrochem. Soc.* 123, 315–320 (**1976**).
285. Pang, Q., He, W., Yu, X., Yang, S., Zhao, H., Fu, Y., Xing, M., Tian, Y., Luo, X., & Wei, Y. Aluminium pre-intercalated orthorhombic V_2O_5 as high-performance cathode material for aqueous zinc-ion batteries. *Appl. Surf. Sci.* 538, 148043 (**2021**).
286. Chen, X., Wang, L., Li, H., Cheng, F., & Chen, J. Porous V_2O_5 nanofibers as cathode materials for rechargeable aqueous zinc-ion batteries. *J. Energy Chem.* 38, 20–25 (**2019**).
287. Hu, Y.-S., Liu, X., Müller, J.-O., Schlögl, R., Maier, J., & Su, D. S. Synthesis and Electrode Performance of Nanostructured V_2O_5 by Using a Carbon Tube-in-Tube as a Nanoreactor and an Efficient Mixed-Conducting Network. *Angew. Chemie Int. Ed.* 48, 210–214 (**2009**).
288. Mai, L., Xu, L., Han, C., Xu, X., Luo, Y., Zhao, S., & Zhao, Y. Electrospun Ultralong Hierarchical Vanadium Oxide Nanowires with High Performance for Lithium Ion Batteries. *Nano Lett.* 10, 4750–4755 (**2010**).
289. Cao, A.-M., Hu, J.-S., Liang, H.-P., & Wan, L.-J. Self-Assembled Vanadium Pentoxide (V2O5) Hollow Microspheres from Nanorods and Their Application in Lithium-Ion Batteries. *Angew. Chemie Int. Ed.* 44, 4391–4395 (**2005**).
290. Pan, A., Zhu, T., Wu, H. Bin, & Lou, X. W. (David). Template-Free Synthesis of Hierarchical Vanadium-Glycolate Hollow Microspheres and Their Conversion to

V_2O_5 with Improved Lithium Storage Capability. *Chem. – A Eur. J.* 19, 494–500 (**2013**).

291. Cheah, Y. L., von Hagen, R., Aravindan, V., Fiz, R., Mathur, S., & Madhavi, S. High-rate and elevated temperature performance of electrospun V_2O_5 nanofibers carbon-coated by plasma enhanced chemical vapour deposition. *Nano Energy* 2, 57–64 (**2013**).
292. Yi, G., Fan, C., Hu, Z., Zhang, W., Han, S., & Liu, J. Construction of high performance N-doped $Na_3V_2(PO_4)_2F_3$/C cathode assisting by plasma enhanced chemical vapor deposition for sodium-ion batteries. *Electrochim. Acta* 383, 138370 (**2021**).
293. Yao, S., Ma, Y., Xu, T., Wang, Z., Lv, P., Zheng, J., Ma, C., Yu, K., Wei, W., & Ostrikov, K. (Ken). Ti–C bonds reinforced TiO_2@C nanocomposite Na-ion battery electrodes by fluidized-bed plasma-enhanced chemical vapor deposition. *Carbon N. Y.* 171, 524–531 (**2021**).
294. Sun, P., Zhao, X., Chen, R., Chen, T., Ma, L., Fan, Q., Lu, H., Hu, Y., Tie, Z., Jin, Z., Xu, Q., & Liu, J. $Li_3V_2(PO_4)_3$ encapsulated flexible free-standing nanofabric cathodes for fast charging and long life-cycle lithium-ion batteries. *Nanoscale* 8, 7408–7415 (**2016**).
295. Aravindan, V., Sundaramurthy, J., Kumar, E. N., Kumar, P. S., Ling, W. C., von Hagen, R., Mathur, S., Ramakrishna, S., & Madhavi, S. Does carbon coating really improves the electrochemical performance of electrospun SnO_2 anodes? *Electrochim. Acta* 121, 109–115 (**2014**).
296. Li, H., & Zhou, H. Enhancing the performances of Li-ion batteries by carbon-coating: present and future. *Chem. Commun.* 48, 1201–1217 (**2012**).
297. Kim, M., Park, T., Wang, C., Tang, J., Lim, H., Hossain, M. S. A., Konarova, M., Yi, J. W., Na, J., Kim, J., & Yamauchi, Y. Tailored Nanoarchitecturing of Microporous ZIF-8 to Hierarchically Porous Double-Shell Carbons and Their Intrinsic Electrochemical Property. *ACS Appl. Mater. Interfaces* 12, 34065–34073 (**2020**).
298. Kim, M., Xu, X., Xin, R., Earnshaw, J., Ashok, A., Kim, J., Park, T., Nanjundan, A. K., El-Said, W. A., Yi, J. W., Na, J., & Yamauchi, Y. KOH-Activated Hollow ZIF-8 Derived Porous Carbon: Nanoarchitectured Control for Upgraded Capacitive Deionization and Supercapacitor. *ACS Appl. Mater. Interfaces* 13, 52034–52043 (**2021**).

299. Kim, M., Fernando, J. F. S., Wang, J., Nanjundan, A. K., Na, J., Hossain, M. S. A., Nara, H., Martin, D., Sugahara, Y., Golberg, D., & Yamauchi, Y. Efficient lithium-ion storage using a heterostructured porous carbon framework and its in situ transmission electron microscopy study. *Chem. Commun.* 58, 863–866 (**2022**).
300. Kim, M., Fernando, J. F. S., Li, Z., Alowasheeir, A., Ashok, A., Xin, R., Martin, D., Kumar Nanjundan, A., Golberg, D. V, Yamauchi, Y., Amiralian, N., & Li, J. Ultra-stable sodium ion storage of biomass porous carbon derived from sugarcane. *Chem. Eng. J.* 445, 136344 (**2022**).
301. Zhu, H., Wei, J., Wang, K., & Wu, D. Applications of carbon materials in photovoltaic solar cells. *Sol. Energy Mater. Sol. Cells* 93, 1461–1470 (**2009**).
302. Liu, J., Durstock, M., & Dai, L. Graphene oxide derivatives as hole- and electron-extraction layers for high-performance polymer solar cells. *Energy Environ. Sci.* 7, 1297–1306 (**2014**).
303. Tune, D. D., & Shapter, J. G. The potential sunlight harvesting efficiency of carbon nanotube solar cells. *Energy Environ. Sci.* 6, 2572–2577 (**2013**).
304. Barr, T. L., & Seal, S. Nature of the use of adventitious carbon as a binding energy standard. *J. Vac. Sci. Technol. A Vacuum, Surfaces, Film.* 13, 1239–1246 (**1995**).
305. Greczynski, G., & Hultman, L. X-ray photoelectron spectroscopy: Towards reliable binding energy referencing. *Prog. Mater. Sci.* 107, 100591 (**2020**).
306. Bahl, M. K. ESCA studies of some niobium compounds. *J. Phys. Chem. Solids* 36, 485–491 (**1975**).
307. Gomes, M. A. B., Bulhões, L. O. de S., de Castro, S. C., & Damião, A. J. The Electrochromic Process at Nb_2O_5 Electrodes Prepared by Thermal Oxidation of Niobium. *J. Electrochem. Soc.* 137, 3067–3070 (**1990**).
308. Biesinger, M. C., Lau, L. W. M., Gerson, A. R., & Smart, R. S. C. Resolving surface chemical states in XPS analysis of first row transition metals, oxides and hydroxides: Sc, Ti, V, Cu and Zn. *Appl. Surf. Sci.* 257, 887–898 (**2010**).
309. Hench, L. L., & West, J. K. The sol-gel process. *Chem. Rev.* 90, 33–72 (**1990**).
310. Holder, C. F., & Schaak, R. E. Tutorial on Powder X-ray Diffraction for Characterizing Nanoscale Materials. *ACS Nano* 13, 7359–7365 (**2019**).
311. Estrade-Szwarckopf, H. XPS photoemission in carbonaceous materials: A ‘defect’ peak beside the graphitic asymmetric peak. *Carbon N. Y.* 42, 1713–1721

(**2004**).

312. Lesiak, B., Kövér, L., Tóth, J., Zemek, J., Jiricek, P., Kromka, A., & Rangam, N. C sp^2 /sp^3 hybridisations in carbon nanomaterials – XPS and (X)AES study. *Appl. Surf. Sci.* 452, 223–231 (**2018**).
313. Kheirollahivash, M., Rashidi, F., & Moshrefi, M. M. Hydrogen Production from Methane Decomposition Using a Mobile and Elongating Arc Plasma Reactor. *Plasma Chem. Plasma Process.* 39, 445–459 (**2019**).
314. Chung, F. H. Quantitative interpretation of X-ray diffraction patterns of mixtures. I. Matrix-flushing method for quantitative multicomponent analysis. *J. Appl. Crystallogr.* 7, 519–525 (**1974**).
315. Wilhelm, M., Ludwig, T., Fischer, T., Yu, W., Singh, D., & Mathur, S. Functionalized few-layered graphene nanoplatelets for superior thermal management in heat transfer nanofluids. *Int. J. Appl. Ceram. Technol.* n/a, (**2021**).
316. Lee, M., Balasingam, S. K., Jeong, H. Y., Hong, W. G., Lee, H.-B.-R., Kim, B. H., & Jun, Y. One-step hydrothermal synthesis of graphene decorated V_2O_5 nanobelts for enhanced electrochemical energy storage. *Sci. Rep.* 5, 8151 (**2015**).
317. Sathiya, M., Prakash, A. S., Ramesha, K., Tarascon, J., & Shukla, A. K. V_2O_5-Anchored Carbon Nanotubes for Enhanced Electrochemical Energy Storage. *J. Am. Chem. Soc.* 133, 16291–16299 (**2011**).
318. Li, Y., Huang, Z., Kalambate, P. K., Zhong, Y., Huang, Z., Xie, M., Shen, Y., & Huang, Y. V2O5 nanopaper as a cathode material with high capacity and long cycle life for rechargeable aqueous zinc-ion battery. *Nano Energy* 60, 752–759 (**2019**).
319. Mattelaer, F., Geryl, K., Rampelberg, G., Dobbelaere, T., Dendooven, J., & Detavernier, C. Atomic layer deposition of vanadium oxides for thin-film lithium-ion battery applications. *RSC Adv.* 6, 114658–114665 (**2016**).
320. Kharissova, O. V, & Kharisov, B. I. Variations of interlayer spacing in carbon nanotubes. *RSC Adv.* 4, 30807–30815 (**2014**).
321. Chao, D., Xia, X., Liu, J., Fan, Z., Ng, C. F., Lin, J., Zhang, H., Shen, Z. X., & Fan, H. J. A V2O5/Conductive-Polymer Core/Shell Nanobelt Array on Three-Dimensional Graphite Foam: A High-Rate, Ultrastable, and Freestanding Cathode for Lithium-Ion Batteries. *Adv. Mater.* 26, 5794–5800 (**2014**).

322. Tan, H., Yu, X. Z., Huang, K., Zhong, J., & Lu, B. Large-scale carambola-like V_2O_5 nanoflowers arrays on microporous reed carbon as improved electrochemical performances lithium-ion batteries cathode. *J. Energy Chem.* 51, 388–395 (**2020**).
323. Chou, S.-L., Wang, J.-Z., Sun, J.-Z., Wexler, D., Forsyth, M., Liu, H.-K., MacFarlane, D. R., & Dou, S.-X. High Capacity, Safety, and Enhanced Cyclability of Lithium Metal Battery Using a V_2O_5 Nanomaterial Cathode and Room Temperature Ionic Liquid Electrolyte. *Chem. Mater.* 20, 7044–7051 (**2008**).
324. Liu, D.-S., Zhang, Y., Liu, S., Wei, L., You, S., Chen, D., Ye, M., Yang, Y., Rui, X., Qin, Y., & Li, C. C. Regulating the Electrolyte Solvation Structure Enables Ultralong Lifespan Vanadium-Based Cathodes with Excellent Low-Temperature Performance. *Adv. Funct. Mater.* n/a, 2111714 (**2022**).
325. Zhang, L., Zhang, B., Hu, J., Liu, J., Miao, L., & Jiang, J. An In Situ Artificial Cathode Electrolyte Interphase Strategy for Suppressing Cathode Dissolution in Aqueous Zinc Ion Batteries. *Small Methods* 5, 2100094 (**2021**).
326. Liu, X., Zarrabeitia, M., Qin, B., Elia, G. A., & Passerini, S. Cathode–Electrolyte Interphase in a LiTFSI/Tetraglyme Electrolyte Promoting the Cyclability of V2O5. *ACS Appl. Mater. Interfaces* 12, 54782–54790 (**2020**).
327. Kulish, V. V, & Manzhos, S. Comparison of Li-, Na-, Mg- and Al-ion insertion in vanadium pentoxides and vanadium dioxides. *RSC Adv.* 7, 18643–18649 (**2017**).
328. Park, S. K., Dose, W. M., Boruah, B. D., & De Volder, M. In Situ and Operando Analyses of Reaction Mechanisms in Vanadium Oxides for Li-, Na-, Zn-, and Mg-Ions Batteries. *Adv. Mater. Technol.* 7, 2100799 (**2022**).
329. Zhang, X.-F., Wang, K.-X., Wei, X., & Chen, J.-S. Carbon-Coated V_2O_5 Nanocrystals as High Performance Cathode Material for Lithium Ion Batteries. *Chem. Mater.* 23, 5290–5292 (**2011**).
330. Reddy, C. V. S., Wei, J., Quan-Yao, Z., Zhi-Rong, D., Wen, C., Mho, S., & Kalluru, R. R. Cathodic performance of (V_2O_5+PEG) nanobelts for Li ion rechargeable battery. *J. Power Sources* 166, 244–249 (**2007**).
331. Wang, J., Wang, Y., Zhu, C., & Liu, B. Photoinduced Rechargeable Lithium-Ion Battery. *ACS Appl. Mater. Interfaces* 14, 4071–4078 (**2022**).
332. Lv, J., Tan, Y.-X., Xie, J., Yang, R., Yu, M., Sun, S., Li, M.-D., Yuan, D., & Wang,

Y. Direct Solar-to-Electrochemical Energy Storage in a Functionalized Covalent Organic Framework. *Angew. Chemie Int. Ed.* 57, 12716–12720 (**2018**).

333. Paolella, A., Faure, C., Bertoni, G., Marras, S., Guerfi, A., Darwiche, A., Hovington, P., Commarieu, B., Wang, Z., Prato, M., Colombo, M., Monaco, S., Zhu, W., Feng, Z., Vijh, A., George, C., Demopoulos, G. P., … Zaghib, K. Light-assisted delithiation of lithium iron phosphate nanocrystals towards photo-rechargeable lithium ion batteries. *Nat. Commun.* 8, 14643 (**2017**).
334. Chen, P., Li, G.-R., Li, T.-T., & Gao, X.-P. Solar-Driven Rechargeable Lithium–Sulfur Battery. *Adv. Sci.* 6, 1900620 (**2019**).
335. Kang, M., Jung, J., Lee, S.-Y., Ryu, J.-W., & Kim, S. W. Conductivity, carrier density, mobility, Seebeck coefficient, and power factor in V_2O_5. *Thermochim. Acta* 576, 71–74 (**2014**).
336. Deka Boruah, B., & De Volder, M. Vanadium dioxide–zinc oxide stacked photocathodes for photo-rechargeable zinc-ion batteries. *J. Mater. Chem. A* 9, 23199–23205 (**2021**).
337. Wang, Q., Brier, M., Joshi, S., Puntambekar, A., & Chakrapani, V. Defect-induced Burstein-Moss shift in reduced V_2O_5 nanostructures. *Phys. Rev. B* 94, 245305 (**2016**).
338. Harley-Mason, J. Some Aliphatic Thiols and their Derivates. Part I. Aliphatic Mercaptoamines. *J. Chem. Soc.* 74, 320–322 (**1947**).
339. Sun, M., Hong, C. Y., & Pan, C. Y. A unique aliphatic tertiary amine chromophore: Fluorescence, polymer structure, and application in cell imaging. *J. Am. Chem. Soc.* 134, 20581–20584 (**2012**).
340. Fotouhi, A., Auger, D., O'Neill, L., Cleaver, T., & Walus, S. Lithium-Sulfur Battery Technology Readiness and Applications—A Review. *Energies* 10, 1937 (**2017**).
341. Patel, K. Lithium-Sulfur Battery : Chemistry , Challenges , Cost , and Future. *J. Undergrad. Res.* 9, 39–42 (**2016**).
342. Meng, X., Comstock, D. J., Fister, T. T., & Elam, J. W. Vapor-phase atomic-controllable growth of amorphous Li_2S for high-performance lithium-sulfur batteries. *ACS Nano* 8, 10963–10972 (**2014**).
343. Ye, F., Liu, M., Yan, X., Li, J., Pan, Z., Li, H., & Zhang, Y. In Situ Electrochemically Derived Amorphous-Li_2S for High Performance Li_2S/Graphite Full Cell. *Small* 14, 1–7 (**2018**).
344. Jung, J. W., Lee, C. L., Yu, S., & Kim, I. D. Electrospun nanofibers as a platform

for advanced secondary batteries: A comprehensive review. *J. Mater. Chem. A* 4, 703–750 (**2016**).

345. Chen, X., Peng, L., Yuan, L., Zeng, R., Xiang, J., Chen, W., Yuan, K., Chen, J., Huang, Y., & Xie, J. Facile synthesis of Li_2S@C composites as cathode for Li–S batteries. *J. Energy Chem.* 37, 111–116 (**2019**).
346. Huang, X., Wang, Z., Knibbe, R., Luo, B., Ahad, S. A., Sun, D., & Wang, L. Cyclic Voltammetry in Lithium–Sulfur Batteries—Challenges and Opportunities. *Energy Technol.* 7, 1801001 (**2019**).
347. Yang, Y., Zheng, G., Misra, S., Nelson, J., Toney, M. F., & Cui, Y. High-capacity micrometer-sized Li 2S particles as cathode materials for advanced rechargeable lithium-ion batteries. *J. Am. Chem. Soc.* 134, 15387–15394 (**2012**).
348. Jung, Y., & Kang, B. Understanding abnormal potential behaviors at the 1st charge in Li_2S cathode material for rechargeable Li–S batteries. *Phys. Chem. Chem. Phys.* 18, 21500–21507 (**2016**).
349. Liu, J., Nara, H., Yokoshima, T., Momma, T., & Osaka, T. Li_2S cathode modified with polyvinylpyrrolidone and mechanical milling with carbon. *J. Power Sources* 273, 1136–1141 (**2015**).
350. Cai, K., Song, M.-K., Cairns, E. J., & Zhang, Y. Nanostructured Li 2 S–C Composites as Cathode Material for High-Energy Lithium/Sulfur Batteries. *Nano Lett.* 12, 6474–6479 (**2012**).
351. Seh, Z. W., Yu, J. H., Li, W., Hsu, P.-C., Wang, H., Sun, Y., Yao, H., Zhang, Q., & Cui, Y. Two-dimensional layered transition metal disulphides for effective encapsulation of high-capacity lithium sulphide cathodes. *Nat. Commun.* 5, 5017 (**2014**).
352. Lee, B.-J., Park, H.-Y., Yang, D.-S., Kang, T.-H., Hwang, S., & Yu, J.-S. Mesopore Channel Length Control in Ordered Mesoporous Carbon Hosts for High Performance Lithium-Sulfur Batteries. *J. Electrochem. Soc.* 166, A5244–A5251 (**2019**).
353. Fu, Y., & Manthiram, A. Orthorhombic Bipyramidal Sulfur Coated with Polypyrrole Nanolayers As a Cathode Material for Lithium–Sulfur Batteries. *J. Phys. Chem. C* 116, 8910–8915 (**2012**).
354. Yang, Y., Zheng, G., Misra, S., Nelson, J., Toney, M. F., & Cui, Y. High-Capacity Micrometer-Sized Li 2 S Particles as Cathode Materials for Advanced

Rechargeable Lithium-Ion Batteries. *J. Am. Chem. Soc.* 134, 15387–15394 (**2012**).

355. Fu, Y., Su, Y. S., & Manthiram, A. Li_2S-Carbon Sandwiched Electrodes with Superior Performance for Lithium-Sulfur Batteries. *Adv. Energy Mater.* 4, 1–5 (**2014**).
356. Diao, Y., Xie, K., Xiong, S., & Hong, X. Shuttle phenomenon – The irreversible oxidation mechanism of sulfur active material in Li–S battery. *J. Power Sources* 235, 181–186 (**2013**).
357. Wild, M., O'Neill, L., Zhang, T., Purkayastha, R., Minton, G., Marinescu, M., & Offer, G. J. Lithium sulfur batteries, a mechanistic review. *Energy Environ. Sci.* 8, 3477–3494 (**2015**).
358. Zhang, T., Marinescu, M., Walus, S., Kovacik, P., & Offer, G. J. What Limits the Rate Capability of Li-S Batteries during Discharge: Charge Transfer or Mass Transfer? *J. Electrochem. Soc.* 165, A6001–A6004 (**2018**).
359. Tao, Y., Wei, Y., Liu, Y., Wang, J., Qiao, W., Ling, L., & Long, D. Kinetically-enhanced polysulfide redox reactions by Nb_2O_5 nanocrystals for high-rate lithium–sulfur battery. *Energy Environ. Sci.* 9, 3230–3239 (**2016**).
360. Kurmaev, E. Z., Van Ek, J., Ederer, D. L., Zhou, L., Callcott, T. A., Perera, R. C. C., Cherkashenko, V. M., Shamin, S. N., Trofimova, V. A., Bartkowski, S., Neumann, M., Fujimori, A., & Moloshag, V. P. Experimental and theoretical investigation of the electronic structure of transition metal sulphides: CuS, FeS_2 and $FeCuS_2$. *J. Phys. Condens. Matter* 10, 1687–1697 (**1998**).
361. Liang, W., & Whangbo, M.-H. Conductivity anisotropy and structural phase transition in Covellite CuS. *Solid State Commun.* 85, 405–408 (**1993**).
362. Zhao-Karger, Z., Zhao, X., Fuhr, O., & Fichtner, M. Bisamide based non-nucleophilic electrolytes for rechargeable magnesium batteries. *RSC Adv.* 3, 16330–16335 (**2013**).
363. Zhan, Y., Zhang, W., Lei, B., Liu, H., & Li, W. Recent Development of Mg Ion Solid Electrolyte. *Front. Chem.* 8, (**2020**).
364. Yoshida, Y., Yamada, T., Jing, Y., Toyao, T., Shimizu, K., & Sadakiyo, M. Super Mg^{2+} Conductivity around 10^{-3} S cm^{-1} Observed in a Porous Metal–Organic Framework. *J. Am. Chem. Soc.* 144, 8669–8675 (**2022**).
365. Zhang, Y., Xie, J., Han, Y., & Li, C. Dual-Salt Mg-Based Batteries with Conversion Cathodes. *Adv. Funct. Mater.* 25, 7300–7308 (**2015**).

366. Deivanayagam, R., Ingram, B. J., & Shahbazian-Yassar, R. Progress in development of electrolytes for magnesium batteries. *Energy Storage Mater.* 21, 136–153 (**2019**).
367. Fan, T.-E., Tang, X., & Liu, S.-M. $CuFeS_2$ Nanosheets Assembled into Honeycomb-like Microspheres as Stable High-Capacity Anodes for Sodium-Ion Batteries. *ACS Appl. Nano Mater.* 5, 10392–10398 (**2022**).
368. Lokhande, A., Sharan, A., Nair, S. S., Shelke, A., Karade, V., Kim, J. H., Singh, N., & Choi, D. Self-supported graphene oxide encapsulated chalcopyrite electrode for high-performance Li-ion capacitor. *J. Energy Storage* 55, 105791 (**2022**).
369. Xu, B., Kong, W., Li, Q., Yang, Y., Jiang, T., & Liu, X. A Review of Thiosulfate Leaching of Gold: Focus on Thiosulfate Consumption and Gold Recovery from Pregnant Solution. *Metals* vol. 7 (**2017**).
370. Wang, Y., Li, X., Zhang, Y., He, X., & Zhao, J. Ether based electrolyte improves the performance of $CuFeS_2$ spike-like nanorods as a novel anode for lithium storage. *Electrochim. Acta* 158, 368–373 (**2015**).
371. Wu, X., Zhao, Y., Yang, C., & He, G. PVP-assisted synthesis of shape-controlled $CuFeS_2$ nanocrystals for Li-ion batteries. *J. Mater. Sci.* 50, 4250–4257 (**2015**).
372. Ye, Z., Jiang, Y., Li, L., Wu, F., & Chen, R. Synergetic Anion Vacancies and Dense Heterointerfaces into Bimetal Chalcogenide Nanosheet Arrays for Boosting Electrocatalysis Sulfur Conversion. *Adv. Mater.* 34, 2109552 (**2022**).
373. Yao, X., Huang, N., Han, F., Zhang, Q., Wan, H., Mwizerwa, J. P., Wang, C., & Xu, X. High-Performance All-Solid-State Lithium–Sulfur Batteries Enabled by Amorphous Sulfur-Coated Reduced Graphene Oxide Cathodes. *Adv. Energy Mater.* 7, 1602923 (**2017**).
374. Zhu, X., Jiang, W., Zhao, S., Huang, R., Ling, M., Liang, C., & Wang, L. Exploring the concordant solid-state electrolytes for all-solid-state lithium-sulfur batteries. *Nano Energy* 96, 107093 (**2022**).
375. Xi, L., Li, Y., Zhang, D., Liu, Z., Xu, X., & Liu, J. The Contact Interface Engineering of All-Sulfide-Based Solid State Batteries via Infiltrating Dissoluble Sulfide Electrolyte. *ENERGY Environ. Mater.* n/a, e12461 (**2022**).
376. Wu, J., Ye, T., Wang, Y., Yang, P., Wang, Q., Kuang, W., Chen, X., Duan, G., Yu, L., Jin, Z., Qin, J., & Lei, Y. Understanding the Catalytic Kinetics of Polysulfide Redox Reactions on Transition Metal Compounds in Li–S Batteries.

ACS Nano 16, 15734–15759 (**2022**).

377. Cheng, M., Ren, W., Zhang, D., Zhang, S., Yang, Y., Lv, X., Yang, J., Wang, J., & NuLi, Y. Efficient single-perfluorinated borate-based electrolytes for rechargeable magnesium batteries. *Energy Storage Mater.* 51, 764–776 (**2022**).
378. Wang, P., Trück, J., Häcker, J., Schlosser, A., Küster, K., Starke, U., Reinders, L., & Buchmeiser, M. R. A design concept for halogen-free Mg2+/Li+-dual salt-containing gel-polymer-electrolytes for rechargeable magnesium batteries. *Energy Storage Mater.* 49, 509–517 (**2022**).
379. Canepa, P., Bo, S.-H., Gautam, G. S., Key, B., Richards, W. D., Shi, T., Tian, Y., Wang, Y., Li, J., & Ceder, G. High magnesium mobility in ternary spinel chalcogenides. *Nat. Commun. 2017 81* 8, 1–8 (**2017**).
380. Wang, L.-P., Zhao-Karger, Z., Klein, F., Chable, J., Braun, T., Schür, A. R., Wang, C.-R., Guo, Y.-G., & Fichtner, M. $MgSc_2Se_4$—A Magnesium Solid Ionic Conductor for All-Solid-State Mg Batteries? *ChemSusChem* 12, 2286–2293 (**2019**).
381. Jaschin, P. W., Gao, Y., Li, Y., & Bo, S.-H. A materials perspective on magnesium-ion-based solid-state electrolytes. *J. Mater. Chem. A* 8, 2875–2897 (**2020**).
382. Zhao, Y., Li, X., Hou, N., Yuan, T., Huang, S., Li, L., Li, X., & Zhang, W. Self-powered sensor integration system based on thorn-like polyaniline composites for smart home applications. *Nano Energy* 104, 107966 (**2022**).
383. Tarascon, J.-M. Material science as a cornerstone driving battery research. *Nat. Mater.* 21, 979–982 (**2022**).
384. Wan, T. H., Saccoccio, M., Chen, C., & Ciucci, F. Influence of the Discretization Methods on the Distribution of Relaxation Times Deconvolution: Implementing Radial Basis Functions with DRTtools. *Electrochim. Acta* 184, 483–499 (**2015**).

10 Appendix

Erklärung

Hiermit versichere ich an Eides statt, dass ich die vorliegende Dissertation selbstständig und ohne die Benutzung anderer als der angegebenen Hilfsmittel und Literatur angefertigt habe. Alle Stellen, die wörtlich oder sinngemäß aus veröffentlichten und nicht veröffentlichten Werken dem Wortlaut oder dem Sinn nach entnommen wurden, sind als solche kenntlich gemacht. Ich versichere an Eides statt, dass diese Dissertation noch keiner anderen Fakultät oder Universität zur Prüfung vorgelegen hat; dass sie - abgesehen von unten angegebenen Teilpublikationen und eingebundenen Artikeln und Manuskripten - noch nicht veröffentlicht worden ist sowie, dass ich eine Veröffentlichung der Dissertation vor Abschluss der Promotion nicht ohne Genehmigung des Promotionsausschusses vornehmen werde. Die Bestimmungen dieser Ordnung sind mir bekannt. Darüber hinaus erkläre ich hiermit, dass ich die Ordnung zur Sicherung guter wissenschaftlicher Praxis und zum Umgang mit wissenschaftlichem Fehlverhalten der Universität zu Köln gelesen und sie bei der Durchführung der Dissertation zugrundeliegenden Arbeiten und der schriftlich verfassten Dissertation beachtet habe und verpflichte mich hiermit, die dort genannten Vorgaben bei allen wissenschaftlichen Tätigkeiten zu beachten und umzusetzen. Ich versichere, dass die eingereichte elektronische Fassung der eingereichten Druckfassung vollständig entspricht.

Köln, den 19.03.2023

_____

Michael Wilhelm

(Eingebundene Teilpublikationen siehe S. XII)

Conference presentations:

2022

- MRS Spring Meeting & Exhibit, Honolulu, Hawai'i, Title: *"Surface Modification of Few-Layered Graphene Nanoplatelets for Enhanced Energy Transportation in Nanofluids"*
- MRS Spring Meeting & Exhibit, Honolulu, Hawai'i, Title: *"Enzymes Immobilized Nanocarriers for the Selective Degradation of Synthetic Polymers"*
- Nanotage 2022, Hamburg, Germany, Title: *"Carbon coating on V_2O_5 nanofibers for increased performance of a photo-responsive lithium-ion battery"*
- MS&T 22 Pittsburgh, USA, Title: *"Electrospun Vanadium Pentoxide Nanofibers as a Photocathode in a Light Rechargeable LIB"*
- MS&T 22 Pittsburgh, USA, Title: "*Molecular Precursors for Li_2S as Cathode Material for Sustainable Energy Storage"*

2021

- CERAMICS 2021, 96th DKG Annual Meeting, Germany, Title: "*Innovative ceramic anode material based on $TiNb_2O_7$/carbon nanocomposites for lithium-ion batteries"* (virtual)
- CERAMICS 2021, 96th DKG Annual Meeting, Germany, Title: "*Rhenium Nitride Thin Films via Magnetic Field-Assisted CVD from Volatile Rhenium Precursors"* (virtual)
- 8th International Congress on Ceramics (ICC8), Bexco, Busan, Korea, Title: *"Ceramics in lithium-ion batteries $TiNb_2O_7$ a quick-charging anode material"* (virtual)
- Materials Challenges in Alternative & Renewable Energy (MCARE), OH, USA, Title: *"$TiNb_2O_7$ - a novel and fast-charging anode material for Li-ion batteries"* (virtual)
- MRS Fall Meeting & Exhibit, Boston, USA, Title: *"Don't Trust Fools when Looking for Gold – Iron Sulfide as Cathode Material for Mg-Batteries"* (virtual)
- MRS Fall Meeting & Exhibit, Boston, USA, Title: *"Copper Sulfide – A Conversion Cathode Material for Mg-Batteries"* (virtual)

- Cologne Graduate School Chemistry, PhD Symposium, Cologne, Germany, Title: *"House of cards"* (virtual, selected presenter)
- GDCh-Wissenschaftsforum Chemie, Title: *"Copper sulfide: A Conversion Cathode Material for Rechargeable Magnesium Batteries"* (virtual)

2020

- MRS Fall Meeting & Exhibit, Boston, USA, Title: *"Transition Metal Sulfide (MS, M = Mn, Zn) Nanoparticles as Conversion Cathode Materials for Rechargeable Magnesium-Sulfur Batteries"* (virtual)
- MRS Fall Meeting & Exhibit, Boston, USA, Title: *"Enhanced Heat Transfer of Functionalized Graphene Nanoplatelets in Nanofluids for Energy Conversion and Storage of Solar Power Plants"* (virtual)
- MSE, Darmstadt, Germany, Title: *"Surface modified graphene nanoplatelets in nanofluids for heat transfer applications"* (virtual)

2019

- Enhance, Cologne, Germany, Title: *"Thermal Conductivity Enhancement of Functionalized Graphene Nanoplatelets for the Application in Heat Transfer Fluids" (Poster)*
- German-Franco-Symposium, Cologne, Germany, Title: *"Graphene-based Additives for Controlling the Thermal Conductivity in Fluids"*
- International XPS User Meeting, Thüringen, Germany, Title: *"XPS analysis of nanomaterials for gas sensing and LIB applications"*

Organized Workshop and Events:

Winter 2020	**BrainDrops – DieJuniorUni, University of Cologne**
Winter 2021	**BrainDrops – DieJuniorUni, University of Cologne**
July 2022	**Cologne Summer School - Sustainable Future Strategies in Advanced Functional Ceramics for Human Well-Being, Krakow, Poland**
November 2021	**School meets University, Battery Day, University of Cologne**
Since 2020	**Sustainability workshop series**
Since 2020	**MRS lecture series** Includes: recruitment of international experts, organization of student discussion, lab tours
November 2021	**PowerPoint Karaoke, 2021 MRS Fall Meeting (virtual)**
May 2022	**PowerPoint Karaoke, 2022 MRS Spring Meeting**
November 2022	**PowerPoint Karaoke, 2022 MRS Fall Meeting**
November 2022	**Focus on Sustainability TF, hands-on activities, and video competition: Sustainability in Action, 2022 MRS Fall Meeting**

List of Publications

1. Hartl, F., Brune, V., Lüggert, S., Hegemann, C., van Gerven, D., **Wilhelm, M.**, Ji, S., Choi, H., Mathur, S. Direct Synthesis of Two Dimensional SnSe and $SnSe_2$ Through Molecular Scale Preorganization. *Submitted manuscript*.
2. Dmonte, D.J., Bhardwaj, A., **Wilhelm, M.**, Fischer, T., Kuřitka, I., Mathur, S. Sub ppm Detection of NO_2 Using Strontium Doped Bismuth Ferrite Nanostructures. Micromachines, 14, 644, (**2023**).
3. Drexelius, M., Arnold, R., Meinberger, D., **Wilhelm, M**., Mathur, S., Neundorf, I. Rational design of bifunctional chimeric peptides that combine antimicrobial and titanium binding activity. J. Pept. Sci., e3481 (**2023**).
4. **Wilhelm, M.**, Adam, R., Bhardwaj, A., Neumann, I., Cho, S. H., Yamada, Y., Sekino, T., Tao, J., Hong, Z., Fischer, T., & Mathur, S. Carbon-Coated Electrospun V_2O_5 Nanofibers as Photoresponsive Cathode for Lithium-Ion Batteries. *Adv. Eng. Mater.* 2200765, (**2022**).
5. Cuzzupè, D. T., Ünlü, F., Lê, K., Bernhardt, R., **Wilhelm, M.**, Grosch, M., Weißing, R., Fischer, T., van Loosdrecht, P. H. M., & Mathur, S. Thermally-induced drift of A-site cations at solid–solid interface in physically paired lead halide perovskites. *Sci. Rep.* 12, 10241 (**2022**).
6. Brune, V., Hegemann, C., **Wilhelm, M.**, Ates, N., & Mathur, S. Molecular Precursors to Group IV Dichalcogenides MS_2 (M=Ti, Zr, Hf). *Zeitschrift für Anorg. und Allg. Chemie* 648, e202200049 (**2022**).
7. Mukkavilli, R. S., Ichangi, A., Thiyagarajan, G. B., Vollnhals, F., **Wilhelm, M.**, Bhardwaj, A., Christiansen, S., Neelakantan, L., Mathur, S., & Kumar, R. Electrospun 1D Ta_3N_5 -(O) nanofibers as advanced electrocatalysts for hydrogen evolution reaction in proton exchange membrane water electrolyser. *Open Ceram.* 10, 100267 (**2022**).
8. Brune, V., Bohr, C., Ludwig, T., **Wilhelm, M.**, Hirt, S. D., Fischer, T., Wennig, S., Oberschachtsiek, B., Ichangi, A., & Mathur, S. A novel molecular synthesis route to Li_2S loaded carbon fibers for lithium–sulfur batteries. *J. Mater. Chem. A* 10, 9902–9910 (**2022**).
9. Yang, Y., Hoang, M. T., Bhardwaj, A., **Wilhelm, M.**, Mathur, S., & Wang, H. Perovskite solar cells based self-charging power packs: Fundamentals, applications and challenges. *Nano Energy* 94, 106910 (**2022**).

10. Thiyagarajan, G. B., Mukkavilli, R. S., Graf, D., Fischer, T., **Wilhelm, M.**, Christiansen, S., Mathur, S., & Kumar, R. Self-supported amorphous $TaN_x(O_y)$/nickel foam thin film as an advanced electrocatalyst for hydrogen evolution reaction. *Chem. Commun.* 58, 3310–3313 (**2022**).
11. Christoffels, R., Breitenbach (née Stastny), C., Weber, J. P., Körtgen, L., Tobeck, C., **Wilhelm, M.**, Mathur, S., Neudörfl, J.-M., Farid, M. S. Z., Maslo, M., Strub, E., & Ruschewitz, U. UoC-3: A Metal–Organic Framework with an Anionic Framework Based on Uranyl UO_2^{2+} Nodes and Partly Fluorinated Benzene-1,3,5-Tribenzoate Linkers. *Cryst. Growth Des.* 22, 681–692 (**2022**).
12. Brune, V., Raydan, N., Sutorius, A., Hartl, F., Purohit, B., Gahlot, S., Bargiela, P., Burel, L., **Wilhelm, M.**, Hegemann, C., Atamtürk, U., Mathur, S., & Mishra, S. Single source precursor route to nanometric tin chalcogenides. *Dalt. Trans.* 50, 17346–17360 (**2021**).
13. **Wilhelm, M.**, Ludwig, T., Fischer, T., Yu, W., Singh, D., & Mathur, S. Functionalized few-layered graphene nanoplatelets for superior thermal management in heat transfer nanofluids. *Int. J. Appl. Ceram. Technol.* 19, 803–812 (**2022**).
14. Krakor, E., Saniternik, S., Gessner, I., Frohnhoven, R., **Wilhelm, M.**, Drexelius, M., Tosun, N., Neundorf, I., & Mathur, S. Hollow mesoporous silica capsules loaded with copper, silver, and zinc oxide nanoclusters for sustained antibacterial efficacy. *J. Am. Ceram. Soc.* 105, 1685–1696 (**2022**).
15. Thiyagarajan, G. B., Shanmugam, V., **Wilhelm, M.**, Mathur, S., Moodakare, S. B., & Kumar, R. $TiNb_2O_7$-Keratin derived carbon nanocomposites as novel anode materials for high-capacity lithium-ion batteries. *Open Ceram.* 6, 100131 (**2021**).
16. Raauf, A., Leduc, J., Frank, M., Stadler, D., Graf, D., **Wilhelm, M.**, Grosch, M., & Mathur, S. Magnetic Field-Assisted Chemical Vapor Deposition of UO_2 Thin Films. *Inorg. Chem.* 60, 1915–1921 (**2021**).
17. Krakor, E., Gessner, I., **Wilhelm, M.**, Brune, V., Hohnsen, J., Frenzen, L., & Mathur, S. Selective degradation of synthetic polymers through enzymes immobilized on nanocarriers. *MRS Commun.* 11, 363–371 (**2021**).
18. Hong, Z., Maleki, H., Ludwig, T., Zhen, Y., **Wilhelm, M.**, Lee, D., Kim, K.-H., & Mathur, S. New insights into carbon-based and MXene anodes for Na and K-ion storage: A review. *J. Energy Chem.* 62, 660–691 (**2021**).

19. Frank, M., Bulut, Y., Czympiel, L., Weißing, R., Nahrstedt, V., **Wilhelm, M.**, Grosch, M., Raauf, A., Verma, A., Fischer, T., & Mathur, S. Piezo-enhanced activation of dinitrogen for room temperature production of ammonia. *Nanotechnology* 32, 465601 (**2021**).
20. Chernozem, R. V, Romanyuk, K. N., Grubova, I., Chernozem, P. V, Surmeneva, M. A., Mukhortova, Y. R., **Wilhelm, M.**, Ludwig, T., Mathur, S., Kholkin, A. L., Neyts, E., Parakhonskiy, B., Skirtach, A. G., & Surmenev, R. A. Enhanced piezoresponse and surface electric potential of hybrid biodegradable polyhydroxybutyrate scaffolds functionalized with reduced graphene oxide for tissue engineering. *Nano Energy* 89, 106473 (**2021**).
21. Bandar Abadi, M., Weissing, R., **Wilhelm, M.**, Demidov, Y., Auer, J., Ghazanfari, S., Anasori, B., Mathur, S., & Maleki, H. Nacre-Mimetic, Mechanically Flexible, and Electrically Conductive Silk Fibroin-MXene Composite Foams as Piezoresistive Pressure Sensors. *ACS Appl. Mater. Interfaces* 13, 34996–35007 (**2021**).
22. Schmidt-Verma, A.K., Renner, A.M., **Wilhelm, M.**, Bohr, C., Goenuellue, Y., Rudigier-Voigt, E. and Mathur, S., High-Temperature Ultrahydrophobic Ceramic Coatings from Surface-Functionalized $MgAl_2O_4$ Nanoparticles. Adv. Eng. Mater., 23, 2000738 (**2021**).
23. Sekhar, P. K., Ludwig, T., **Wilhelm, M.**, Graf, D., Riheen, M. A., & Mathur, S. Potentiometric Ethene Sensor for Postharvest Detection Applications. *J. Electrochem. Soc.* 166, B1477–B1482 (**2019**).

Short Curriculum Vitae

Michael Wilhelm
University of Cologne, Inorganic Chemistry
Greinstr. 6
50939 Cologne (Germany)
michael.wilhelm@uni-koeln.de

Education:

Since 04/2019	**Ph.D. Student in Chemistry** University of Cologne (UoC) – Germany
10/2016 – 03/2019	**M.Ed. in Chemistry and Physical Education** University of Cologne (UoC) – Germany, and German Sport University Cologne – Germany Thesis: “Graphene-based additives for the control of heat transfer in solutions.” Prof. Dr. Dr. (*h.c.*) Sanjay Mathur (Grade: 1.0)
10/2013 – 09/2016	**B.A. in Chemistry and Physical Education** University of Cologne (UoC) – Germany, and German Sport University Cologne – Germany Thesis: “Non-verbal communication in sport: Can emotionally intelligent people use the body language of athletes to better assess who is leading or lagging?” Dr. Philip Furley (Grade: 1.3)

Work experience:

Since 01/2023	**Junior Manager Advanced Analytics** Orion Engineered Carbons GmBH (Cologne, Germany)
04/2021 – 12/2022	**Scientific Assistant in Chemistry** University of Cologne (UoC) – Germany Project planning and management Head of X-Ray Photoelectron Spectroscopy team Operator SEM Teaching Assistant Leader of the battery research team
09/2017 – 03/2021	**Research Assistant in Chemistry** University of Cologne (UoC), Germany Redesign and organization a laboratory course/ module in chemistry Laboratory student assistance
02/2017 -09/2017	**Substitute Teacher** Bettine-von-Arnim Comprehensive School – Langenfeld, Germany

Awards:

2022	Macromolecular Journals Best Presentation Award for an oral presentation during Nanotage 2022, Hamburg, Germany
2021	1st Place as Slide Designer in the PPT Karaoke at ACerS MCARE 2021
2019	Poster award at the ENHANCE Conference 2019, Cologne, Germany

Academic Activities:

2020-2022	President of the MRS University Chapter Cologne
Since 2021	Ambassador of the MRS Student Engagement Subcommittee (Organizer of the MRS PowerPoint Karaoke at Fall (2021), Spring (2022), and Fall (2022) meetings)
Since 2021	Ambassador of the MRS Focus on Sustainability Subcommittee – Task Force
Since 2020	Ambassador of the Cross-Faculty Sustainability Initiative, University of Cologne
Since 2019	Ambassador of the ACerS Rhine Ceramics Chapter Germany
Since 2020	Ambassador of ‘My green lab’
2020-2021	BrainDrops – Die JuniorUni